

# Towards Creating the Perfect *In Vitro* Cell Model

Guest Editors: Malin K. B. Jonsson, Toon A. B. van Veen, Jane Synnergren,  
and Bruno Becker



---

**Towards Creating the Perfect *In Vitro*  
Cell Model**

## **Towards Creating the Perfect *In Vitro* Cell Model**

Guest Editors: Malin K. B. Jonsson, Toon A. B. van Veen,  
Jane Synnergren, and Bruno Becker



---

Copyright © 2016 Hindawi Publishing Corporation. All rights reserved.

This is a special issue published in “Stem Cells International.” All articles are open access articles distributed under the Creative Commons Attribution License, which permits unrestricted use, distribution, and reproduction in any medium, provided the original work is properly cited.

## Editorial Board

James Adjaye, Germany  
Nadire N. Ali, UK  
Kenneth R. Boheler, USA  
Dominique Bonnet, UK  
Marco Bregni, Italy  
Silvia Brunelli, Italy  
Bruce A. Bunnell, USA  
Kevin D. Bunting, USA  
B. Bussolati, Italy  
Yilin Cao, China  
Yuqingeugene Chen, USA  
Kyunghee Choi, USA  
Gerald A. Colvin, USA  
Christian Dani, France  
Varda Deutsch, Israel  
Leonard M. Eisenberg, USA  
Marina Emborg, USA  
Franca Fagioli, Italy  
Joel C. Glover, Norway  
Tong-Chuan He, USA  
Boon Chin Heng, Switzerland  
Toru Hosoda, Japan  
Xiao J. Huang, China  
Thomas Ichim, USA  
J. Itskovitz-Eldor, Israel  
P. Jendelova, Czech Republic

Arne Jensen, Germany  
Atsuhiko Kawamoto, Japan  
Armand Keating, Canada  
Mark D. Kirk, USA  
Valerie Kouskoff, UK  
Joanne Kurtzberg, USA  
Andrzej Lange, Poland  
Laura Lasagni, Italy  
Renke Li, Canada  
Tao-Sheng Li, Japan  
Susan Liao, Singapore  
Ching-Shwun Lin, USA  
Shinn-Zong Lin, Taiwan  
M. Lutolf, Switzerland  
Gary E. Lyons, USA  
Yupo Ma, USA  
Athanasios Mantalaris, UK  
Eva Mezey, USA  
C. Montero-Menei, France  
Karim Nayernia, UK  
Sue O'Shea, USA  
Bruno Péault, USA  
Stefan Przyborski, UK  
P. J. Quesenberry, USA  
Pranela Rameshwar, USA  
B. A.J Roelen, Netherlands

Peter Rubin, USA  
H. T. Ruohola-Baker, USA  
Donald S. Sakaguchi, USA  
Ghasem H. Salekdeh, Iran  
Heinrich Sauer, Germany  
C. Sengenès, France  
Ashok K. Shetty, USA  
Shimon Slavin, Israel  
Joost Sluijter, Netherlands  
Igor Slukvin, USA  
Shay Soker, USA  
W. L. Stanford, Canada  
Giorgio Stassi, Italy  
Ann Steele, USA  
A. Storch, Germany  
Corrado Tarella, Italy  
Yang D. Teng, USA  
Antoine Toubert, France  
Hung-Fat Tse, Hong Kong  
Marc Turner, UK  
Chia-Lin Wei, Singapore  
Dominik Wolf, Austria  
Qingzhong Xiao, UK  
Zhaohui Ye, USA  
Wen-Jie Zhang, China

# Contents

## **Towards Creating the Perfect *In Vitro* Cell Model**

Malin K. B. Jonsson, Toon A. B. van Veen, Jane Synnergren, and Bruno Becker  
Volume 2016, Article ID 3459730, 2 pages

## **Highly Synchronized Expression of Lineage-Specific Genes during *In Vitro* Hepatic Differentiation of Human Pluripotent Stem Cell Lines**

Nidal Ghosheh, Björn Olsson, Josefina Edsbagge, Barbara Küppers-Munther, Mariska Van Giezen, Annika Asplund, Tommy B. Andersson, Petter Björquist, Helena Carén, Stina Simonsson, Peter Sartipy, and Jane Synnergren  
Volume 2016, Article ID 8648356, 22 pages

## **Modulating the Substrate Stiffness to Manipulate Differentiation of Resident Liver Stem Cells and to Improve the Differentiation State of Hepatocytes**

Angela Maria Cozzolino, Valeria Noce, Cecilia Battistelli, Alessandra Marchetti, Germana Grassi, Carla Cicchini, Marco Tripodi, and Laura Amicone  
Volume 2016, Article ID 5481493, 12 pages

## **PTF1a Activity in Enriched Posterior Foregut Endoderm, but Not Definitive Endoderm, Leads to Enhanced Pancreatic Differentiation in an *In Vitro* Mouse ESC-Based Model**

Gopika G. Nair and Jon S. Odorico  
Volume 2016, Article ID 6939438, 15 pages

## **The Rise of CRISPR/Cas for Genome Editing in Stem Cells**

Bing Shui, Liz Hernandez Matias, Yi Guo, and Ying Peng  
Volume 2016, Article ID 8140168, 17 pages

## **Calcium/Cobalt Alginate Beads as Functional Scaffolds for Cartilage Tissue Engineering**

Stefano Focaroli, Gabriella Teti, Viviana Salvatore, Isabella Orienti, and Mirella Falconi  
Volume 2016, Article ID 2030478, 12 pages

## **High Content Analysis of Human Pluripotent Stem Cell Derived Hepatocytes Reveals Drug Induced Steatosis and Phospholipidosis**

Arvind Pradip, Daniella Steel, Susanna Jacobsson, Gustav Holmgren, Magnus Ingelman-Sundberg, Peter Sartipy, Petter Björquist, Inger Johansson, and Josefina Edsbagge  
Volume 2016, Article ID 2475631, 14 pages

## **Hematopoietic Stem and Progenitor Cell Expansion in Contact with Mesenchymal Stromal Cells in a Hanging Drop Model Uncovers Disadvantages of 3D Culture**

Olga Schmal, Jan Seifert, Tilman E. Schäffer, Christina B. Walter, Wilhelm K. Aicher, and Gerd Klein  
Volume 2016, Article ID 4148093, 13 pages

## **Stem Cell Models to Investigate the Role of DNA Methylation Machinery in Development of Neuropsychiatric Disorders**

K. Naga Mohan  
Volume 2016, Article ID 4379425, 8 pages

## **p53-Dependent Senescence in Mesenchymal Stem Cells under Chronic Normoxia Is Potentiated by Low-Dose $\gamma$ -Irradiation**

Ines Höfig, Yashodhara Ingawale, Michael J. Atkinson, Heidi Hertlein, Peter J. Nelson, and Michael Rosemann  
Volume 2016, Article ID 6429853, 11 pages

## Editorial

# Towards Creating the Perfect *In Vitro* Cell Model

Malin K. B. Jonsson,<sup>1</sup> Toon A. B. van Veen,<sup>2</sup> Jane Synnergren,<sup>3</sup> and Bruno Becker<sup>4</sup>

<sup>1</sup>Genome Institute of Singapore, 60 Biopolis Street, Genome, Singapore 138672

<sup>2</sup>Department of Medical Physiology, Division of Heart & Lungs, UMC Utrecht, 3584 CM Utrecht, Netherlands

<sup>3</sup>Systems Biology Research Center, University of Skövde, 541 28 Skövde, Sweden

<sup>4</sup>Department of Psychiatry and Neurochemistry, Sahlgrenska University Hospital, 431 80 Mölndal, Sweden

Correspondence should be addressed to Malin K. B. Jonsson; jonssonbm@gis.a-star.edu.sg

Received 13 December 2015; Accepted 13 December 2015

Copyright © 2016 Malin K. B. Jonsson et al. This is an open access article distributed under the Creative Commons Attribution License, which permits unrestricted use, distribution, and reproduction in any medium, provided the original work is properly cited.

Researchers both in academia and in industry regularly rely on *in vitro* models to study biological responses and mechanisms related to human health and disease. These models range from relatively simple overexpression systems in, for example, HEK293 or COS cells to more complex specialized cells/tissues/organs from animals or, in rare cases, humans (e.g., skin models, explanted organ materials) [1, 2]. Even though the results from these *in vitro* studies are further tested and validated in *in vivo* animal models before being extrapolated to the human situation, in general the translation of results from bench to bedside remains challenging due to poor species overlap. This is contributing to the high attrition rate that the pharmaceutical industry has been struggling with over the past years when trying to introduce new drugs into the market [3]. Nevertheless, *in vitro* models are one of the pillars of contemporary research, with the benefits of ease of pharmacological manipulation, genetic modifications, and analysis, small sample sizes, and relatively low cost. Although a complete abolishment of animal models is highly unlikely in the near future, the importance of cell models will increase as initiatives like the 3Rs (refining, reducing, and replacing animal models) are globally gaining importance. The US FDA is even planning to adapt its guidelines for preclinical cardiotoxicity studies by incorporating a computational integration of various individual ion channel assays as well as electrophysiological tests on stem cell-derived cardiomyocytes [4]. Needless to say, it stresses that a continuous improvement of our *in vitro* models is therefore warranted.

One of the reasons for the mentioned high attrition rates in the pharmaceutical industry is the lack of sufficiently predictive preclinical models of human origin. The discovery of human (induced) pluripotent stem cells (hPSC) and their ability to differentiate into a large variety of different cell types [5, 6] has therefore raised the hope for being able to create increasingly reliable *in vitro* models which includes the possibility of further exploring their potential in the field of personalized medicine. Extensive evaluation of these models has indeed shown great promise. For example, hPSC-derived hepatocytes that were exposed to hepatotoxic compounds over a long period of time (14 days) showed evidence of phospholipidosis and steatosis, which are signs of chronic long term toxicity [7]. Yet another example is the generation of functional hippocampal neurons from hPSC and their usefulness for studies on the onset and progression of diseases such as Alzheimer's disease and epilepsy [8]. Taking it one step further, researchers have also been able to test novel therapeutic options for the treatment of autosomal-dominant-negative disorders. This was elegantly shown through the use of RNA interference (RNAi) that rescued the diseased phenotype of hPSC-derived cardiomyocytes carrying a mutation causing the long QT syndrome [9] or carrying a mutation in phospholamban that results either in dilated or in arrhythmogenic cardiomyopathy [10].

Despite all these promising results, there are still severe limitations that currently hinder the implementation of stem cell models in routine assays. One of the most important and general challenges related to stem cell-derived models is the

immature or somewhat artificial phenotype of the derived cells which consequently leaves a considerable gap to the *in vivo* situation. This seems to hold true for all specialized cell types that are derived from hPSC and can be exemplified by, for example, hPSC-derived hepatocytes that persistently express fetal markers like alpha fetoprotein (AFP) and also lack key mature hepatocyte functions, as reflected by low levels of many detoxification enzymes (e.g., CYP2A6, CYP3A4) [11]. Another remaining challenge is to efficiently, and across different hPSC lines, control the directed differentiation into a specific subtype of a particular lineage, such as GABAergic cortical interneurons or pancreatic  $\beta$ -cells [12, 13].

For this special issue, investigators have contributed original research articles as well as review articles that will support the research community in approaching the goal of obtaining models for the lab that can mirror the *in vivo* situation. The published manuscripts in this special issue make use of stem cells to derive hepatocytes, cartilage, and pancreatic cells as well as utilize mesenchymal and hematopoietic stem cells under different conditions. Various methodologies have been employed to improve the cell phenotype generated, for example, by modulating of substrate stiffness, creating of functional scaffolds, and the addition of drugs. Furthermore, a range of topics, including cell cycle senescence, DNA methylation, and the use of CRISPR-Cas9 for genome editing, are covered. We hope that the readers will appreciate the contents of this issue and find scientific inspiration and new ideas for their future work.

Malin K. B. Jonsson  
Toon A. B. van Veen  
Jane Synnergren  
Bruno Becker

## References

- [1] M. K. B. Jonsson, T. A. B. van Veen, M.-J. Goumans, M. A. Vos, G. Duker, and P. Sartipy, "Improvement of cardiac efficacy and safety models in drug discovery by the use of stem cell-derived cardiomyocytes," *Expert Opinion on Drug Discovery*, vol. 4, no. 4, pp. 357–372, 2009.
- [2] J. W. Oh, T.-C. Hsi, C. F. Guerrero-Juarez, R. Ramos, and M. V. Plikus, "Organotypic skin culture," *Journal of Investigative Dermatology*, vol. 133, no. 11, pp. 1–4, 2013.
- [3] M. J. Waring, J. Arrowsmith, A. R. Leach et al., "An analysis of the attrition of drug candidates from four major pharmaceutical companies," *Nature Reviews Drug Discovery*, vol. 14, no. 7, pp. 475–486, 2015.
- [4] K. R. Chi, "Revolution dawning in cardiotoxicity testing," *Nature Reviews Drug Discovery*, vol. 12, no. 8, pp. 565–567, 2013.
- [5] K. Takahashi, K. Tanabe, M. Ohnuki et al., "Induction of pluripotent stem cells from adult human fibroblasts by defined factors," *Cell*, vol. 131, no. 5, pp. 861–872, 2007.
- [6] J. A. Thomson, J. Itskovitz-Eldor, S. S. Shapiro et al., "Embryonic stem cell lines derived from human blastocysts," *Science*, vol. 282, no. 5391, pp. 1145–1147, 1998.
- [7] G. Holmgren, A.-K. Sjögren, I. Barragan et al., "Long-term chronic toxicity testing using human pluripotent stem cell-derived hepatocytes," *Drug Metabolism and Disposition*, vol. 42, no. 9, pp. 1401–1406, 2014.
- [8] H. Sakaguchi, T. Kadoshima, M. Soen et al., "Generation of functional hippocampal neurons from self-organizing human embryonic stem cell-derived dorsomedial telencephalic tissue," *Nature Communications*, vol. 6, article 8896, 2015.
- [9] E. Matsa, J. E. Dixon, C. Medway et al., "Allele-specific RNA interference rescues the long-QT syndrome phenotype in human-induced pluripotency stem cell cardiomyocytes," *European Heart Journal*, vol. 35, no. 16, pp. 1078–1087, 2014.
- [10] I. Karakikes, F. Stillitano, M. Nonnenmacher et al., "Correction of human phospholamban R14del mutation associated with cardiomyopathy using targeted nucleases and combination therapy," *Nature Communications*, vol. 6, article 6955, 2015.
- [11] R. E. Schwartz, H. E. Fleming, S. R. Khetani, and S. N. Bhatia, "Pluripotent stem cell-derived hepatocyte-like cells," *Biotechnology Advances*, vol. 32, no. 2, pp. 504–513, 2014.
- [12] A. L. Goulburn, E. G. Stanley, A. G. Elefanty, and S. A. Anderson, "Generating GABAergic cerebral cortical interneurons from mouse and human embryonic stem cells," *Stem Cell Research*, vol. 8, no. 3, pp. 416–426, 2012.
- [13] B. Soria, B. R. Gauthier, F. Martin et al., "Using stem cells to produce insulin," *Expert Opinion on Biological Therapy*, vol. 15, no. 10, pp. 1469–1489, 2015.

## Research Article

# Highly Synchronized Expression of Lineage-Specific Genes during *In Vitro* Hepatic Differentiation of Human Pluripotent Stem Cell Lines

Nidal Ghosheh,<sup>1,2</sup> Björn Olsson,<sup>1</sup> Josefina Edsbage,<sup>3</sup> Barbara Küppers-Munther,<sup>3</sup> Mariska Van Giezen,<sup>3</sup> Annika Asplund,<sup>1</sup> Tommy B. Andersson,<sup>4,5</sup> Petter Björquist,<sup>6</sup> Helena Carén,<sup>7</sup> Stina Simonsson,<sup>2</sup> Peter Sartipy,<sup>1,8</sup> and Jane Synnergren<sup>1</sup>

<sup>1</sup>School of Bioscience, Systems Biology Research Center, University of Skövde, 541 28 Skövde, Sweden

<sup>2</sup>Institute of Biomedicine, Department of Clinical Chemistry and Transfusion Medicine, Sahlgrenska Academy, University of Gothenburg, 413 45 Gothenburg, Sweden

<sup>3</sup>Takara Bio Europe AB, Arvid Wallgrens Backe 20, 413 46 Gothenburg, Sweden

<sup>4</sup>AstraZeneca R&D, CVMD DMPK, 431 83 Mölndal, Sweden

<sup>5</sup>Department of Physiology and Pharmacology, Section of Pharmacogenetics, Karolinska Institutet, 171 77 Stockholm, Sweden

<sup>6</sup>NovaHep AB, Arvid Wallgrens Backe 20, 413 46 Gothenburg, Sweden

<sup>7</sup>Sahlgrenska Cancer Center, Department of Pathology, Institute of Biomedicine, Sahlgrenska Academy, University of Gothenburg, 405 30 Gothenburg, Sweden

<sup>8</sup>AstraZeneca R&D, GMD CVMD GMed, 431 83 Mölndal, Sweden

Correspondence should be addressed to Nidal Ghosheh; [nidal.ghosheh@his.se](mailto:nidal.ghosheh@his.se)

Received 31 July 2015; Accepted 1 December 2015

Academic Editor: Renke Li

Copyright © 2016 Nidal Ghosheh et al. This is an open access article distributed under the Creative Commons Attribution License, which permits unrestricted use, distribution, and reproduction in any medium, provided the original work is properly cited.

Human pluripotent stem cells- (hPSCs-) derived hepatocytes have the potential to replace many hepatic models in drug discovery and provide a cell source for regenerative medicine applications. However, the generation of fully functional hPSC-derived hepatocytes is still a challenge. Towards gaining better understanding of the differentiation and maturation process, we employed a standardized protocol to differentiate six hPSC lines into hepatocytes and investigated the synchronicity of the hPSC lines by applying RT-qPCR to assess the expression of lineage-specific genes (*OCT4*, *NANOG*, *T*, *SOX17*, *CXCR4*, *CER1*, *HHEX*, *TBX3*, *PROX1*, *HNF6*, *AFP*, *HNF4a*, *KRT18*, *ALB*, *AAT*, and *CYP3A4*) which serve as markers for different stages during liver development. The data was evaluated using correlation and clustering analysis, demonstrating that the expression of these markers is highly synchronized and correlated well across all cell lines. The analysis also revealed a distribution of the markers in groups reflecting the developmental stages of hepatocytes. Functional analysis of the differentiated cells further confirmed their hepatic phenotype. Taken together, these results demonstrate, on the molecular level, the highly synchronized differentiation pattern across multiple hPSC lines. Moreover, this study provides additional understanding for future efforts to improve the functionality of hPSC-derived hepatocytes and thereby increase the value of related models.

## 1. Introduction

The generation of a clinically relevant *in vitro* hepatocyte experimental model is challenging since the model has to mirror the diverse properties and functionality of its *in vivo* counterpart [1]. At present, primary cells isolated from human livers are considered to be the best *in vitro* hepatocyte

model [2]. However, these cells still have several limitations, such as shortage in availability, rapid phenotypical changes following their isolation, and *in vitro* manipulation including decreased hepatic enzyme functionality, short life span, substantial interindividual variations, and lack of bile collection [2–4]. Thus, the pursuit of a better candidate model is strongly motivated. In this regard, human pluripotent stem

cells (hPSCs), characterized by their unique capacities of self-renewal and differentiation, may provide an attractive alternative. These cells constitute an excellent human cell source for use in basic research and drug discovery and also potentially in future regenerative medicine and cell therapy applications. Moreover, the use of human induced pluripotent stem cells (hiPSCs), which are stem cells derived from reprogrammed somatic cells, enables the development of disease models and studies of interindividual diversity in safety pharmacology and toxicology [5, 6]. However, in order to fully realize the great potential of these cells, robust differentiation protocols are required to ensure reproducibility and recapitulation of the mature hepatic functionality in the final cell population [7]. Recent reports have indeed demonstrated efficient differentiation of hPSCs into hepatocytes that share many features of their *in vivo* counterparts, including the expression of hepatic markers and genes involved in drug metabolism and transport [8–11]. In addition, the cells have shown the ability to accurately predict and classify the toxicity of various compounds [6, 12].

Although the results from the hPSC-differentiation are encouraging, establishment of *in vivo*-like functionality of the *in vitro*-derived hepatocytes has still not been achieved, mainly due to impaired expression of key genes, which are critical for the metabolic functionality of the cells, a limitation that inhibits their utility in some applications in therapeutics and drug discovery [5]. Recently, Asplund and coworkers reported a standardized protocol to generate homogenous hepatocyte-like cell cultures from panel hPSC lines, which displayed metabolic diversity reminiscent of intraindividual variation found in the human population. That study showed notable similarities between the large number of cell lines analyzed but also variability of hepatic enzyme activity including CYP1A, CYP2C9, CYP2D6, and CYP3A [13]. The majority of previously reported protocols for differentiating hPSCs to hepatocyte-like cells recapitulate liver development, where the cells are first differentiated to definitive endoderm (DE) and subsequently to hepatoblast (the hepatic progenitor that gives rise to both hepatocytes and biliary cells) and finally to hepatocyte-like cells [7, 13–15]. The growth and differentiation of hepatocytes during embryonic liver organogenesis is known to be highly synchronized [16]. However, whether biological replicates from multiple hPSC lines are synchronized through an *in vitro* hepatocyte differentiation process has not been thoroughly investigated. Synchronicity accounts for the robustness of the differentiation protocol in recapitulating liver organogenesis *in vitro*, and thus the onset time of the different developmental stages for biological replicates should be consistent.

In this study, we have investigated the expression of a selected set of lineage-specific genes during the differentiation of six hPSC lines, including three hESC and three hiPSC lines, to hepatocyte-like cells applying a protocol further developed from the procedure reported by Asplund and coworkers [13]. Sixteen key genes were analyzed by reverse transcription quantitative real-time PCR (RT-qPCR): *OCT4* and *NANOG* as pluripotent markers; *T* (Brachyury) as primitive streak marker; *CXCR4*, *SOX17*, and *CER1* as definitive endoderm markers; *HHEX* as ventral foregut

endoderm marker [17]; *PROX1*, *TBX3*, and *HNF6* as hepatoblast markers; *AFP* as fetal hepatocyte marker; and *HNF4A* (HNF4a), *CYP3A4*, *SERPINA1* (AAT), *ALB* (albumin), and *KRT18* (CK18) as hepatic markers [14]. The RT-qPCR results were statistically analyzed using Spearman's rank correlation. A clustering analysis was also performed based on the gene expression values. The results presented here show highly synchronized and correlated gene expression profiles across the six cell lines. In addition, the functionality of mature hepatocytes-like cells was confirmed by measuring the drug metabolizing activity of Cytochrome P450 (CYP) enzymes CYP1A, CYP3A, CYP2C9, CYP2D6, and CYP2C19. Furthermore, these cells have the ability to store glycogen and they express the drug transporters MRP2, OATP1B1, NTCP, and BSEP. Interestingly, the hESC or hiPSC lines did not show any pattern indicating any specific correlation to each other. Furthermore, the clustering analysis shows the distribution of lineage-specific markers in groups, reflecting the differentiation stages of hepatocytes.

## 2. Materials and Methods

**2.1. Human Pluripotent Stem Cell Culture and Differentiation.** All hPSC lines used in this study are XY and were provided by Takara Clontech (<http://www.clontech.com>). The cells were thawed, maintained, and passaged in the feeder-free Cellartis DEF-CS culturing system (Takara Clontech) according to the manufacturer's recommendations. The cell lines were used in subsequent differentiation experiments at the following passages: Cellartis SA121 p.10, Cellartis SA181 p.11, Cellartis ChiPSC6b p.16, Cellartis AS034 p.10, Cellartis P11012 p.18, and Cellartis P11025 p.21. (Throughout this paper, the cell lines are referred to with their short names: SA121, SA181, ChiPSC6b, AS034, P11012, and P11025, resp.).

The hPSCs were differentiated into definitive endoderm (DE) cells by applying Cellartis DE differentiation kit (Takara Clontech) according to the manufacturer's recommendations.

At day 7, the cells were harvested according to the manufacturer's recommendations and differentiated into hepatocyte-like cells applying a prototype of the Cellartis Hep differentiation kit (available upon request from Takara Clontech) as illustrated in Figure 1.

**2.2. RNA Extraction and Real-Time Quantitative Polymerase Chain Reaction.** Cell samples were collected daily before performing medium change (if medium change was scheduled) during the differentiation process and preserved in RNAProtect Cell Reagent (Cat. number 76526, QIAGEN) at  $-20^{\circ}\text{C}$ . RNA was extracted using MagMAX-96 Total RNA Isolation Kit (Cat. number AM1830, Life Technologies) and quantified by using GeneQuantpro spectrophotometer. Eighty ng RNA of each sample was used to synthesize cDNA applying the iScript cDNA Synthesis Kit (Cat. number 170-8890, BIO-RAD).

TaqMan Fast Advanced Master Mix (Cat. number 4444557, Life Technologies) and TaqMan Gene Expression Assays were used in RT-qPCR. Table 1 summarizes the assays

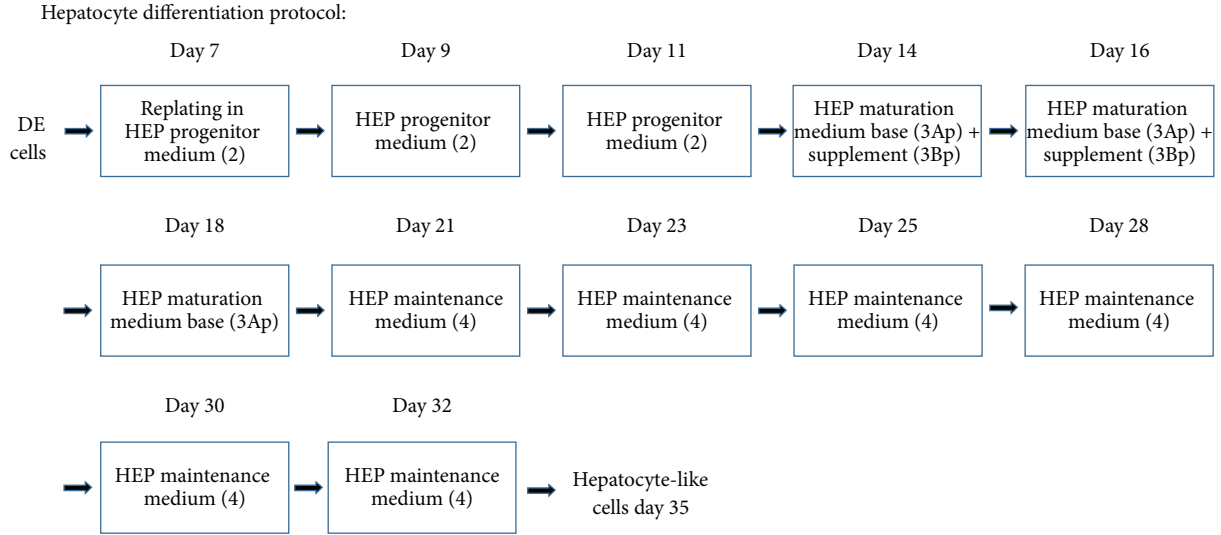


FIGURE 1: Schematic overview of the protocol used for the hepatic differentiation. The DE cells were harvested at day 7 and replated in HEP progenitor medium (2) on plates coated with the specific hepatocyte coating (1), which is included in the prototype of Cellartis Hep differentiation kit (Takara Clontech). Medium change with HEP progenitor medium (2) was performed at days 9 and 11. At days 14 and 16 the cells received HEP maturation medium base (3Ap) and supplement (3Bp). At day 18 the cells received HEP maturation medium base (3Ap). At days 21, 23, 25, 28, 30, and 32 the cells received HEP maintenance medium (4); thereafter they were maintained in culture until day 35.

TABLE 1: Summary of TaqMan Gene Expression Assays used in the study and on which days of the differentiation process they were applied.

Gene symbol	Product number	Days
ABCB11 (BSEP)	Hs00184824_m1	31, 34
ABCC2 (MRP2)	Hs00960494_m1	31, 34
AFP	Hs00173490_m1	10–35
ALB	Hs00910225_m1	19–35
T (Brachyury)	Hs00610080_m1	0–3
CER1	Hs00193796_m1	1–9
CREBBP	Hs00231733_m1	0–35
CXCR4	Hs00237052_m1	2–10
CYP3A4	Hs00604506_m1	21–35
HHEX	Hs00242160_m1	1–11
HNF4A	Hs00230853_m1	9–35
ONECUT1 (HNF6)	Hs00413554_m1	10–35
KRT18	Hs02827483_g1	13–35
KRT19	Hs00761767_s1	6–35
NANOG	HS2387400_g1	0–7
OCT4	Hs04260367_gH	0–7
PROX1	Hs00896294_m1	14–35
SERPINA1 (AAT)	Hs00165475_m1	19–35
SLCD1B1 (OATP1B1)	Hs00272374_m1	31, 34
SLC10A1 (NTCP)	Hs00161820_m1	31, 34
SOX17	Hs00751752_s1	2–10
TBX3	Hs00195621_m1	7–35

that were used and on which days they were applied. Each reaction included 1.6 ng cDNA and was run in duplicate. *CREBBP* was used as reference gene and an in-house

calibrator was used for sample normalization as well [13]. For hepatoblast, fetal, and mature hepatocytes markers an RNA pool of freshly isolated human primary hepatocytes from 5 different donors was used as a calibrator. Interplate controls were added for plate normalization.

The difference in quantification cycle ( $\Delta\Delta C_q$ ) and relative quantification (RQ) were calculated according to the following formulas:

$$\Delta C_q(\text{sample}) = C_q(\text{target}) - C_q(\text{reference}),$$

$$\Delta\Delta C_q = \Delta C_q(\text{sample}) - \Delta C_q(\text{calibrator}), \quad (1)$$

$$\text{RQ} = 2^{-\Delta\Delta C_q}.$$

**2.3. Statistical Analysis of Gene Expression Data.** For each gene, the expression data consisted of a matrix  $E_{ij}$  of RQ values, where  $i = 1, \dots, 6$  represents the six cell lines and  $j = d_{\min}, \dots, d_{\max}$  represents the days at which expression was measured for the particular gene. For each gene, the RQ vectors of every pair of cell lines were tested for association using Spearman rank correlation, which is a nonparametric test, not sensitive to extreme values, which can be used to detect nonlinear relationships [18]. Correlation coefficients were interpreted according to a scale where 0.8–1.0 was defined as “very strong,” 0.6–0.8 as “strong,” 0.4–0.6 as “moderate,” 0.2–0.4 as “weak,” and 0.0–0.2 as “very weak” or “no correlation.”

For the clustering analysis, the matrix  $E_{ij}$  was replaced with the vector median ( $E_j$ ), where each value is the median RQ for a particular day over all six cell lines. Groups of these RQ vectors, representing different combinations of genes, were hierarchically clustered with the HCL algorithm in the MultiExperiment Viewer software v4.9

(<http://www.tm4.org/mev.html>), using Spearman rank correlation as similarity metric and complete linkage as the linkage rule.

**2.4. Immunocytochemistry.** At days 0, 5, 7, 14, 24, 25, 29, and 30 of differentiation, the cells were washed with DPBS (+/+) (Cat. number 14040-, Life Technologies) and fixed by incubation for 10 min in 4% formaldehyde (Cat. number 02176, Histolab, Västra Frölunda, Sweden) and then washed and maintained in DPBS (+/+) until processing. TNB-blocking buffer was prepared by mixing 0.1 M Tris (Cat. number 10421-1, Kebo Lab AB) adjusted with hydrochloric acid 36.5%–38% (Cat. number H1758, Sigma) to pH 7.5 with 0.15 M NaCl (Cat. number S5886, Sigma) in dH<sub>2</sub>O. Blocking reagent from Perkin Elmer TSA-kit (Cat. number FP1012, Perkin Elmer) was slowly added to Tris-HCl/NaCl buffer under stirring to final concentration of 0.5%; then the solution was heated to 60°C until the blocking reagent was dissolved. The cells were washed once with DPBS (+/+), followed by incubation for 10 min in 0.3% Triton-X (Cat. number T8532, Sigma) in DPBS (+/+), and the cells were subsequently incubated in TNB-blocking buffer for 1 h. Primary antibodies diluted in 0.1% Triton-X in DPBS (+/+) were added to the cultures and incubated over night at 4°C. The following day, the cells were washed three times with DPBS (+/+); then the secondary antibodies and DAPI diluted in 0.1% Triton-X in DPBS (+/+) were added and the cells were incubated for 2 h at RT. Finally, the cells were washed three times with DPBS (+/+) before being imaged in a fluorescence microscope and photographed. The photos were processed using ImageJ software (<http://imagej.nih.gov/ij/>). Table 2 summarizes the different primary and secondary antibodies applied, the dilution ratios, and the days at which respective markers were analyzed.

**2.5. Cytochrome P450 (CYP) Enzymes Activity Assay.** The activities of the enzymes CYP1A, CYP3A, CYP2C9, CYP2C19, and CYP2D6 in hepatocyte-like cells differentiated from all hPSC lines used in this study and in cryoplateable human primary hepatocytes from four different donors (BioreclamationIVT, Frankfurt am Main, Germany) were measured as described previously with small modification [13]. Briefly, hPSC-derived hepatocyte-like cells at day 29 of the hepatic differentiation and primary human hepatocytes (cultured for in total 20 h after plating) were incubated in a cocktail of CYP substrates, 10 μM phenacetin a CYP1A substrate, 10 μM bufuralol a CYP2D6 substrate, 10 μM diclofenac a substrate of CYP2C9, 50 μM mephenytoin a substrate of CYP2C19, and 5 μM midazolam a substrate of CYP3A. The formation of the metabolites (paracetamol (CYP1A), 1-OH-bufuralol (CYP2D6), 4-OH-diclofenac (CYP2C9), 4-OH-mephenytoin (CYP2C19), and 3-OH-midazolam (CYP3A)) was determined by liquid chromatography/mass spectrometry (LC/MS) performed at Pharmacelsus GmbH (Saarbrücken, Germany). The samples were collected in duplicate for each cell line, and the metabolite concentration was normalized to the protein amount per well and incubation time and the results are presented as pmol metabolite/mg protein/min.

**2.6. PAS Staining.** The cells were fixed as described above. A PAS kit was applied (395B-1KT, Sigma Aldrich), in which the cells were incubated in periodic acid for 15 min on a shaker at RT. Then the cells were washed with dH<sub>2</sub>O and incubated in SCHIFF reagent for 30 min on a shaker at RT. Subsequently the cells were washed with dH<sub>2</sub>O and incubated in hematoxylin for 90 seconds and finally the cells were washed with dH<sub>2</sub>O again.

### 3. Results

**3.1. Human PSC Culturing and Hepatic Differentiation.** Human PSCs cultured in the Cellartis DEF-CS culturing system showed typical stem cell morphology (round cells with big nucleus) prior to harvesting at day 0 (Figure 2(a)). The cell morphology started to change with the application of Cellartis DE differentiation kit. At day 5 the cells showed some morphology indicative of DE, and on day 7 the shape of the cells became more spikey or triangular, which is the typical DE morphology having reached confluence (Figure 2(a)). The cells were dissociated and replated, and hepatocyte differentiation was performed by applying a prototype of Cellartis Hep differentiation kit. The hepatocyte differentiation protocol is schematically described in Figure 1. The typical DE cell morphology changed during the application of HEP progenitor medium (Figure 2(b)) and after the application of HEP maturation medium the cells gradually acquired the hepatocyte morphology (Figure 2(c)). Finally, when the cells were cultured in HEP maintenance medium, they acquired the typical hepatocyte morphology, and polygonal single- or binucleated cells were observed (Figure 2(d)).

**3.2. Gene Expression of Lineage-Specific Markers.** For each hPSC line, RNA was collected daily throughout the differentiation process and subsequently analyzed using RT-qPCR for the lineage-specific markers listed in Table 2. Figure 3 shows the relative quantification curves for the early stages markers, in addition to pairwise cell line correlation tables for each marker. The pluripotency markers *OCT4* and *NANOG* were distinctly downregulated early during the differentiation process; *OCT4* was expressed below the detection limit ( $C_q \geq 35$ ) already at day 4 and *NANOG* at day 7. The average pairwise correlation coefficients between cell lines for these two markers are > 0.9 (Figure 3), indicating very high synchronicity among the cell lines at this stage. The expression of *T* (Brachyury), a pan-mesoderm marker expressed in mesendoderm which is a precursor of both mesoderm and endoderm [19], peaks at day 2 in all cell lines (Figure 4). Figure 5 shows the onset of the DE markers *SOX17* and *CXCR4* at day 3 and the average correlation coefficients for these markers during day 2 to day 10 are very high (0.85 and 0.98, resp.). The expression of *SOX17* decreased gradually until it fell below the detection limit at day 10. The expression of *CXCR4* was upregulated until day 5 or day 6, and then it was downregulated and subsequently undetectable at day 9. The onset of the DE marker *CER1* occurred already at the mesendoderm stage (day 2), one day earlier than *SOX17* and *CXCR4*, and its expression increased until day 6 after which it started to

TABLE 2: Summary of primary and secondary antibodies used in the study.

Primary antibody	Class	Dilution	Distributor, catalogue number	Secondary antibody	Dilution	Distributor, catalogue number	Applied to cells day
Albumin (ALB)	Rabbit-IgG	1:500	DakoCytomation, A0001	Donkey anti-rabbit-IgG-Alexa 488	1:1000	ThermoFisher Scientific, A-21206	24, 25, 29, 30
CYP3A (4)	Rabbit-IgG	1:200	Cypex, PAP011	Donkey anti-rabbit-IgG-Alexa 488	1:1000	ThermoFisher Scientific, A-21206	29, 31
CK 18	Mouse-IgG1	1:100	DakoCytomation, M7010	Goat anti-mouse-IgG-Alexa 488	1:500	ThermoFisher Scientific, A-11029	24, 25, 29, 30
HNF4a	Rabbit-IgG	1:400	Santa Cruz, sc-8987	Donkey anti-rabbit-IgG-Alexa 488	1:1000	ThermoFisher Scientific, A-21206	14, 24, 25, 29, 30
Oct4	Mouse-IgG2b	1:200	Santa Cruz, sc-5279	Donkey anti-mouse-IgG-Alexa-488	1:1000	ThermoFisher Scientific, A-21202	0, 5, 7
Sox17	Goat-IgG	1:500	R&D Systems, AF1924	Donkey anti-goat-IgG Alexa 594	1:1000	ThermoFisher Scientific, A-11058	5, 7
SSEA-1	Mouse-IgM	1:200	Santa Cruz, sc-21702	Donkey anti-mouse-IgG-Alexa-488	1:1000	ThermoFisher Scientific, A-21202	0
AAT	Rabbit-IgG	1:200	DakoCytomation, A0012	Donkey anti-rabbit-IgG-Alexa 488	1:1000	ThermoFisher Scientific, A-21206	24, 25, 29, 30
$\alpha$ -fetoprotein (AFP)	Mouse-IgG1	1:500	Santa Cruz, sc-51506	Goat anti-mouse-IgG-Alexa 594	1:1000	ThermoFisher Scientific, A-11032	14, 24, 25, 29, 30
BSEP	Goat-IgG	1:100	Santa Cruz, sc-17292	Donkey anti-goat-IgG-Alexa-488	1:1000	ThermoFisher Scientific, A-11055	29
OATP-C (OATPIB1)	Rabbit-IgG	1:200	Santa Cruz, sc-33609	Donkey anti-rabbit-IgG-Alexa 488	1:1000	ThermoFisher Scientific, A-21206	29
NTCP	Goat-IgG	1:400	Santa Cruz, sc-107030	Donkey anti-goat-IgG-Alexa-594	1:1000	ThermoFisher Scientific, A-11058	29
MRP2	Rabbit-IgG	1:50	Santa Cruz, sc-20766	Donkey anti-rabbit-IgG-Alexa 488	1:1000	ThermoFisher Scientific, A-21206	29

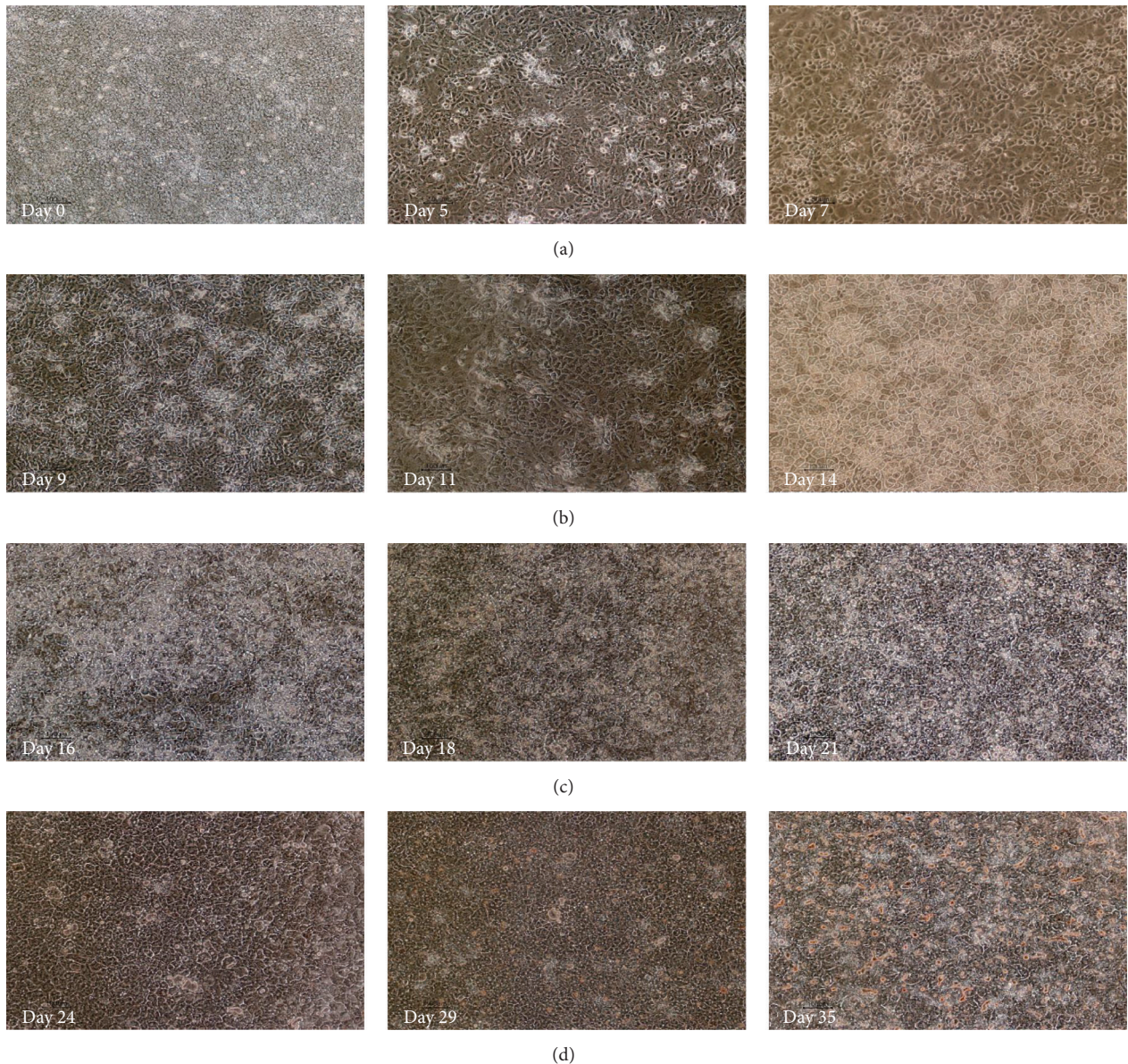


FIGURE 2: Morphology of cells during hepatic differentiation at days 0, 5, 7, 9 (ChiPSC6b), 11 (P11012), 14 (ChiPSC6b), 16 (P11012), 18 (P11012), 21 (P11012), 24 (SA121), 29 (AS034), and 35 (ChiPSC6b) magnification 10x. (a) Human PSCs cultured in Cellartis DEF-CS demonstrate stem cell morphology at day 0 (AS034). (b) At day 5 (P11025) and day 7 (SA181) the cells show a characteristic DE morphology. (c) Following the application of HEP progenitor medium, the DE cells transferred gradually to hepatoblasts. (d) The cells acquired the hepatocyte morphology (polygonal cells) following the application of HEP maturation medium (3Ap) and supplement (3Bp). In the HEP maintenance medium (4) the cells preserve typical hepatocyte morphology, polygonal cells with single- or binucleus.

decrease and, similar to *CXCR4*, it was below the detection limit at day 9. The average correlation coefficient for *CER1* is very strong (0.90) and there is no substantial difference in *CER1* expression between the cell lines. *HHEX*, a marker for ventral foregut endoderm, was also expressed at the DE stage and subsequently undetectable at day 11 (except for line AS034), with a very strong average correlation coefficient of 0.86 as shown in Figure 5. In general, the correlation analysis does not show any preference of hESC lines to correlate with each other rather than with hiPSC lines or vice versa (Figures 3, 4, and 5).

The correlation between cell lines regarding markers of stages following the DE phase of the hepatic differentiation is slightly lower compared to the early markers (Figures 6 and 7). Due to transient fluctuations in the RNA levels on the days after each medium change, days 8, 10, 12, 13, 15, 17, 19, 20, 22, 24, 26, 27, 29, 31, 33, and 34 were not included in the correlation analysis. The genes *TBX3*, *HNF4a*, *HNF6*, and *AFP* were expressed already at the hepatoblast stage. These genes demonstrated gene regulation synchronicity among all cell lines and, as shown in Figure 6, the average pairwise correlation ranges from moderate (0.52 for *HNF4a*) through

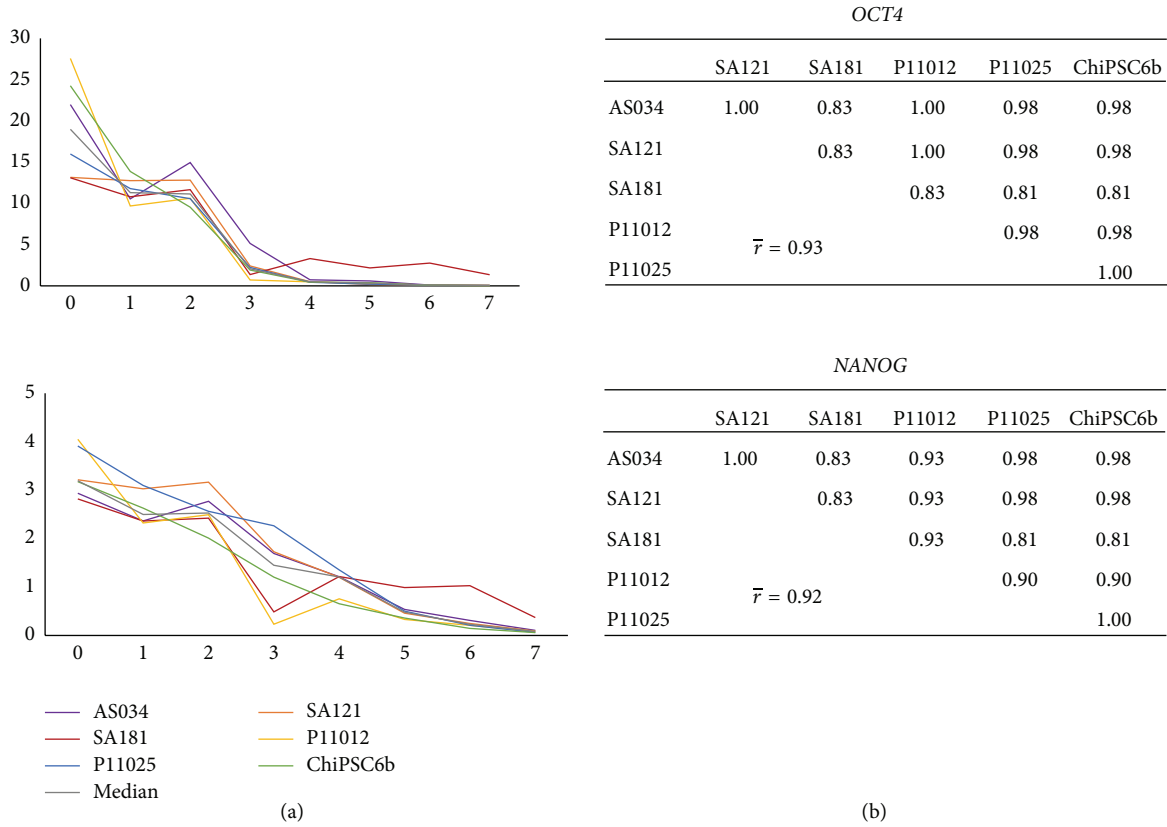


FIGURE 3: Gene expression profiles of the pluripotent markers *OCT4* and *NANOG*. (a) The x-axis indicates the days during differentiation and the y-axis indicates relative quantification (RQ) where the calibrator's RQ = 1. The colored lines show the results from each individual hPSC line and the grey line indicates the calculated median value of the RNA level. (b) Correlation tables show very strong correlations between the cell lines, with an average pairwise correlation of 0.93 for *OCT4* and 0.92 for *NANOG* for the interval of day 0 to day 7.

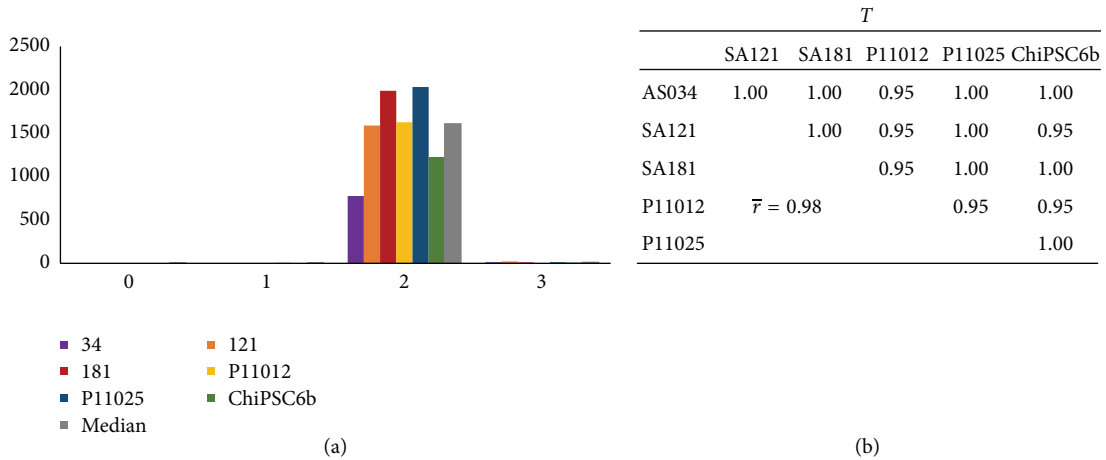
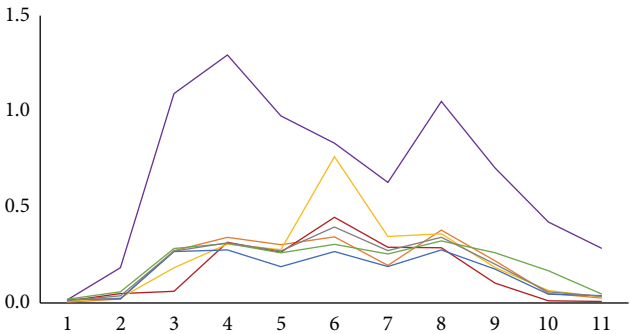
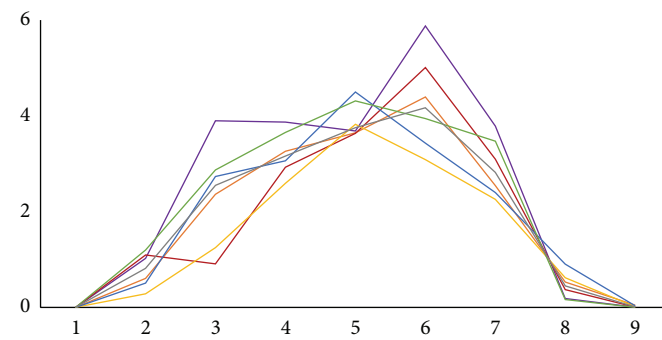
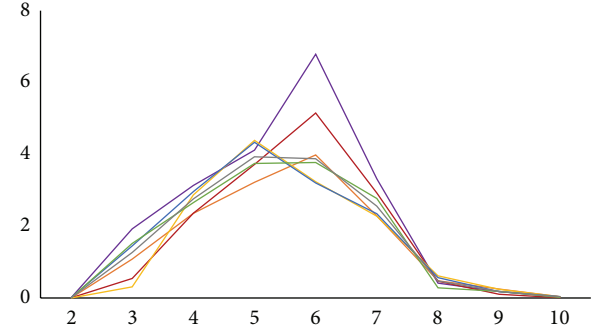
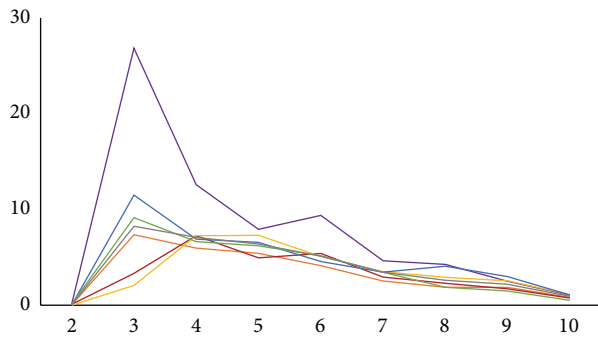


FIGURE 4: (a) Bar graph showing the RNA expression levels of the primitive streak marker *T*. The x-axis indicates the day of differentiation and the y-axis indicates RQ, where the calibrator's RQ = 1. All six cell lines express the *T* gene essentially only at day 2; therefore, the correlation between cell lines for the interval of day 0 to day 3 is very strong as indicated in (b).

strong (0.60 for *HNF6* and 0.63 for *AFP*) to very strong (0.83 for *TBX3*). The correlation of the mature hepatocyte markers ranges from weak (0.38 for *CYP3A4*), through moderate (0.41 for *PROX1* and 0.57 for *AAT*), to strong (0.75 for both *KRT18* and *ALB*) (Figure 7). Although the weakest average correlation was shown for *CYP3A4*, there are some strong

and very strong correlations between pairs of cell lines for this gene, for example, 0.89 between ChiPSC6b and P11025 (Figure 7). Interestingly, and as noted above for the DE stage, there is no preference for hESC lines to correlate with each other rather than with hiPSC lines at later stages either, and the same applies to the hiPSC lines. The expression profiles



— AS034                      — SA121  
 — SA181                      — P11012  
 — P11025                      — ChiPSC6b  
 — Median

(a)

<i>SOX17</i>					
	SA121	SA181	P11012	P11025	ChiPSC6b
AS034	0.98	0.90	0.60	0.97	0.98
SA121		0.88	0.63	0.98	1.00
SA181			0.85	0.87	0.88
P11012				0.62	0.63
P11025	$\bar{r} = 0.85$				0.98

<i>CXCR4</i>					
	SA121	SA181	P11012	P11025	ChiPSC6b
AS034	0.98	1.00	0.95	0.97	1.00
SA121		0.98	0.97	0.98	0.98
SA181			0.95	0.97	1.00
P11012				0.98	0.95
P11025	$\bar{r} = 0.98$				0.97

<i>CER1</i>					
	SA121	SA181	P11012	P11025	ChiPSC6b
AS034	0.85	0.77	0.77	0.80	0.78
SA121		0.97	0.97	0.95	0.98
SA181			0.92	0.87	0.95
P11012				0.98	0.98
P11025	$\bar{r} = 0.90$				0.97

<i>HHEX</i>					
	SA121	SA181	P11012	P11025	ChiPSC6b
AS034	0.88	0.68	0.69	0.92	0.91
SA121		0.81	0.89	0.93	0.95
SA181			0.92	0.85	0.80
P11012				0.87	0.83
P11025	$\bar{r} = 0.86$				0.95

(b)

FIGURE 5: Gene expression profiles for DE (*SOX17*, *CXCR4*, and *CER1*) and ventral foregut endoderm (*HHEX*) markers in the interval from day 1 to day 11. (a) The *x*-axis indicates the days during differentiation and the *y*-axis indicates RQ, where the calibrator's RQ = 1. The colored lines show the results from each individual hPSC line and the grey line indicates the calculated median value of the RNA level. Correlation tables are shown in (b). The time points before the onset of expression and after the RNA levels have decreased below the detection limit are not included in the analysis (e.g., day 1 and day 11 were excluded for *SOX17*). In general, the correlation between cell lines for all these markers is very strong. DE cells seem to emerge at day 3 and disappear at day 8.

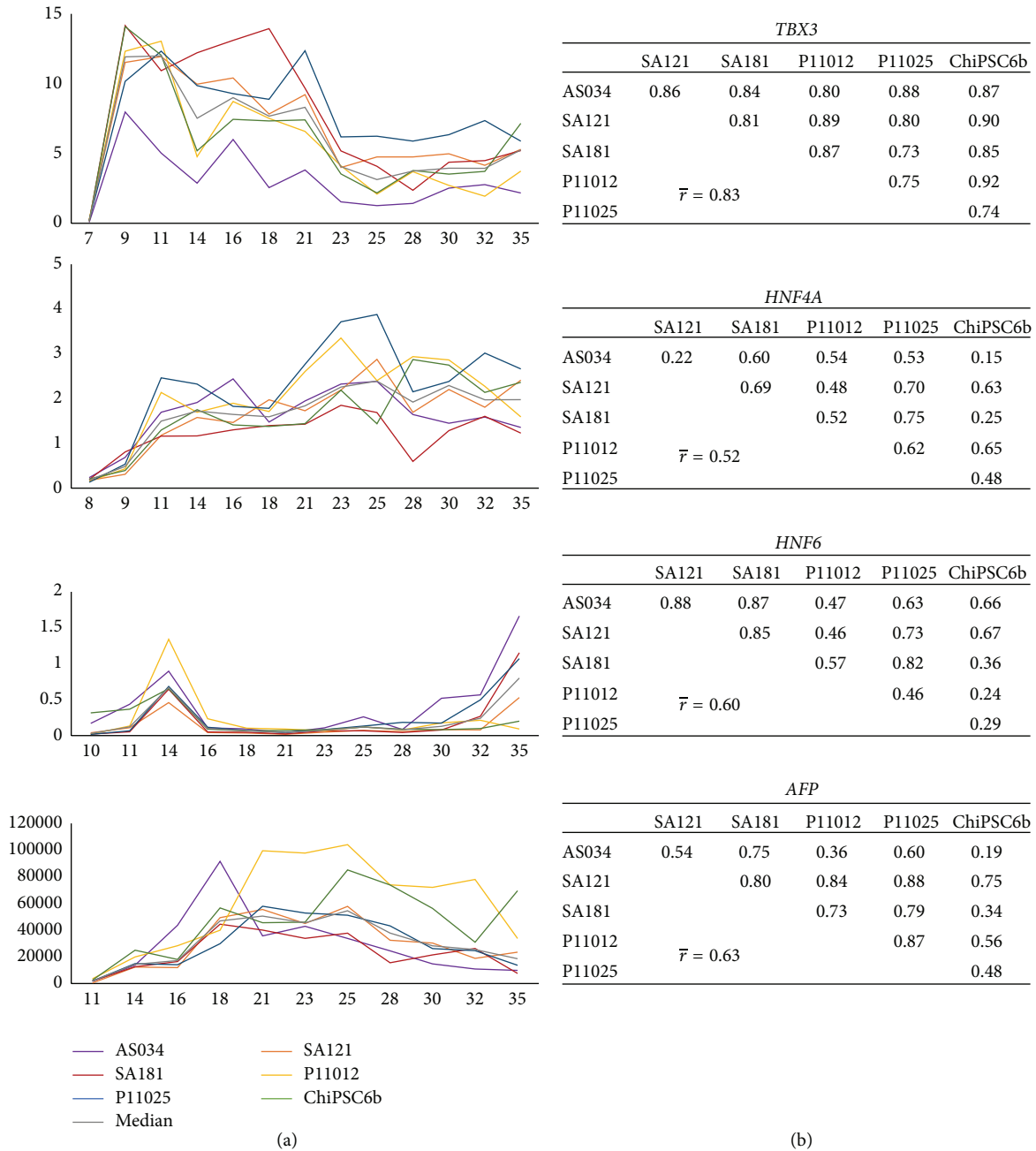


FIGURE 6: Gene expression profiles of early hepatic markers (*TBX3*, *HNF4A*, *HNF6*, and *AFP*) in the interval from day 7 to day 35. (a) The *x*-axis indicates the days during differentiation and the *y*-axis indicates RQ, where the calibrator's RQ = 1. The colored lines show the results from each individual hPSC line and the grey line indicates the calculated median value of the RNA level. Correlation tables are shown in (b). The graphs show synchronicity of onset as well as up- and downregulation among all cell lines for the genes *TBX3*, *HNF4A*, *HNF6*, and *AFP*. The average correlation between pairs of cell lines ranges from moderate (0.52 for *HNF4A*) to very strong (0.83 for *TBX3*).

for the different genes show minor fluctuations during the hepatic differentiation; however, the distinct changes in gene expression occurred in general at the same time for the different cell line, further underscoring the synchronized differentiation process across the cell lines.

**3.3. Immunocytochemical Analysis of Lineage-Specific Markers during Hepatic Differentiation.** The protein expression of selected markers from the different developmental stages

was analyzed by immunocytochemistry. Figure 8 shows the homogenous expression of the pluripotent marker Oct4 in hPSCs in addition to the absence of the differentiation marker SSEA-1 (Figures 8(a)–8(d)), demonstrating the undifferentiated state of the hPSC at the start of the differentiation protocol. At days 5 and 7, all cells expressed the DE marker Sox17 and the pluripotency marker Oct4 was absent (Figures 8(e)–8(h) and 8(i)–8(l), resp.), illustrating the high efficiency in generating DE cells using the differentiation kit.

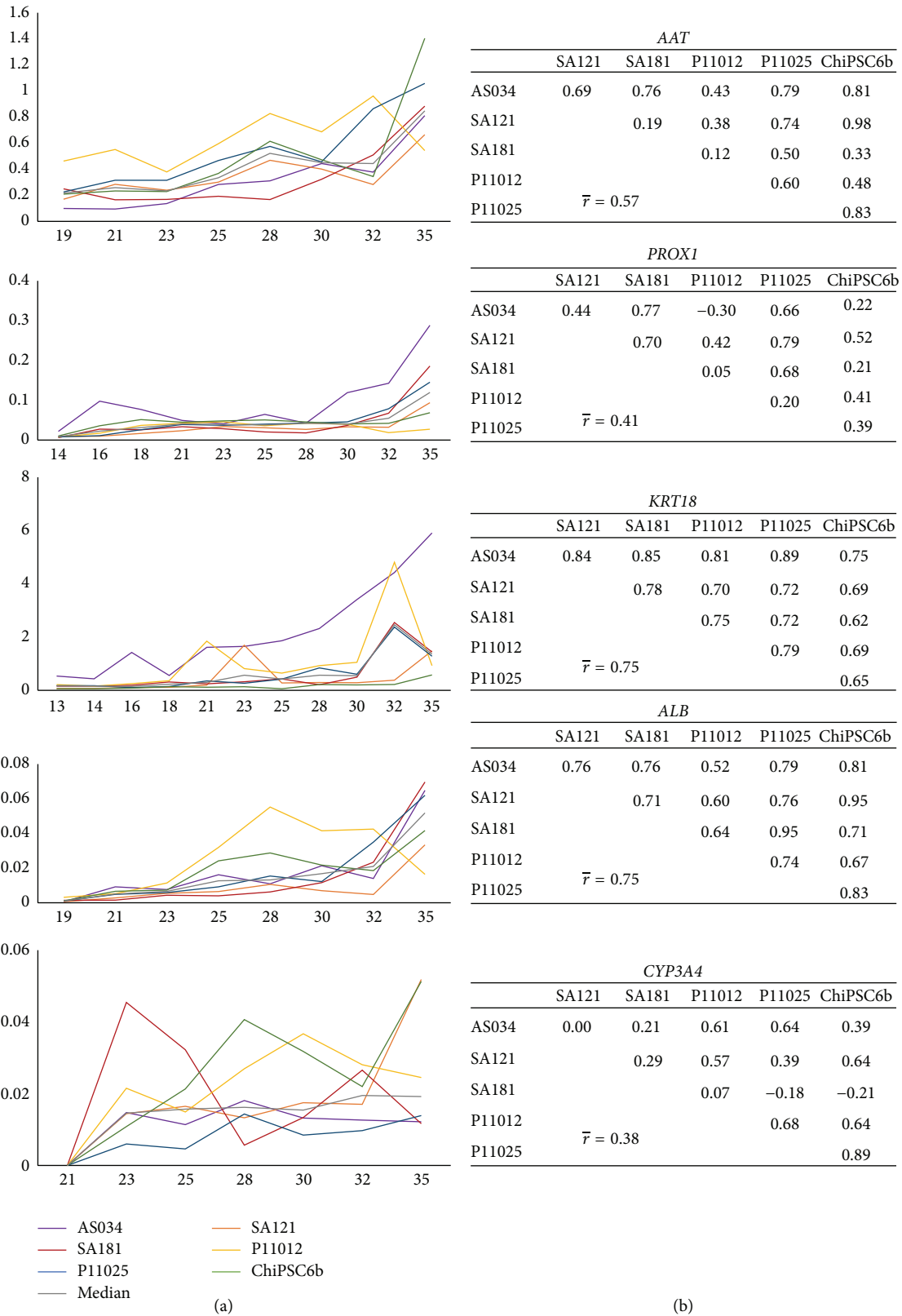


FIGURE 7: Gene expression profiles of later hepatic markers (*AAT*, *PROX1*, *KRT18*, *ALB*, and *CYP3A4*) in the interval from day 13 to day 35. (a) The *x*-axis indicates the days during differentiation and the *y*-axis indicates RQ, where the calibrator's RQ = 1. The colored lines show the results from each individual hPSC line and the grey line indicates the calculated median value of the RNA level. Correlation tables are shown in (b). The graphs show synchronicity of onset and up- and downregulation among all cell lines for the genes *AAT*, *PROX1*, *KRT18*, *ALB*, and *CYP3A4*. The average correlation between pairs of cell lines ranges from weak (0.38 for *CYP3A4*) to strong (0.75 for *KRT18* and *ALB*).

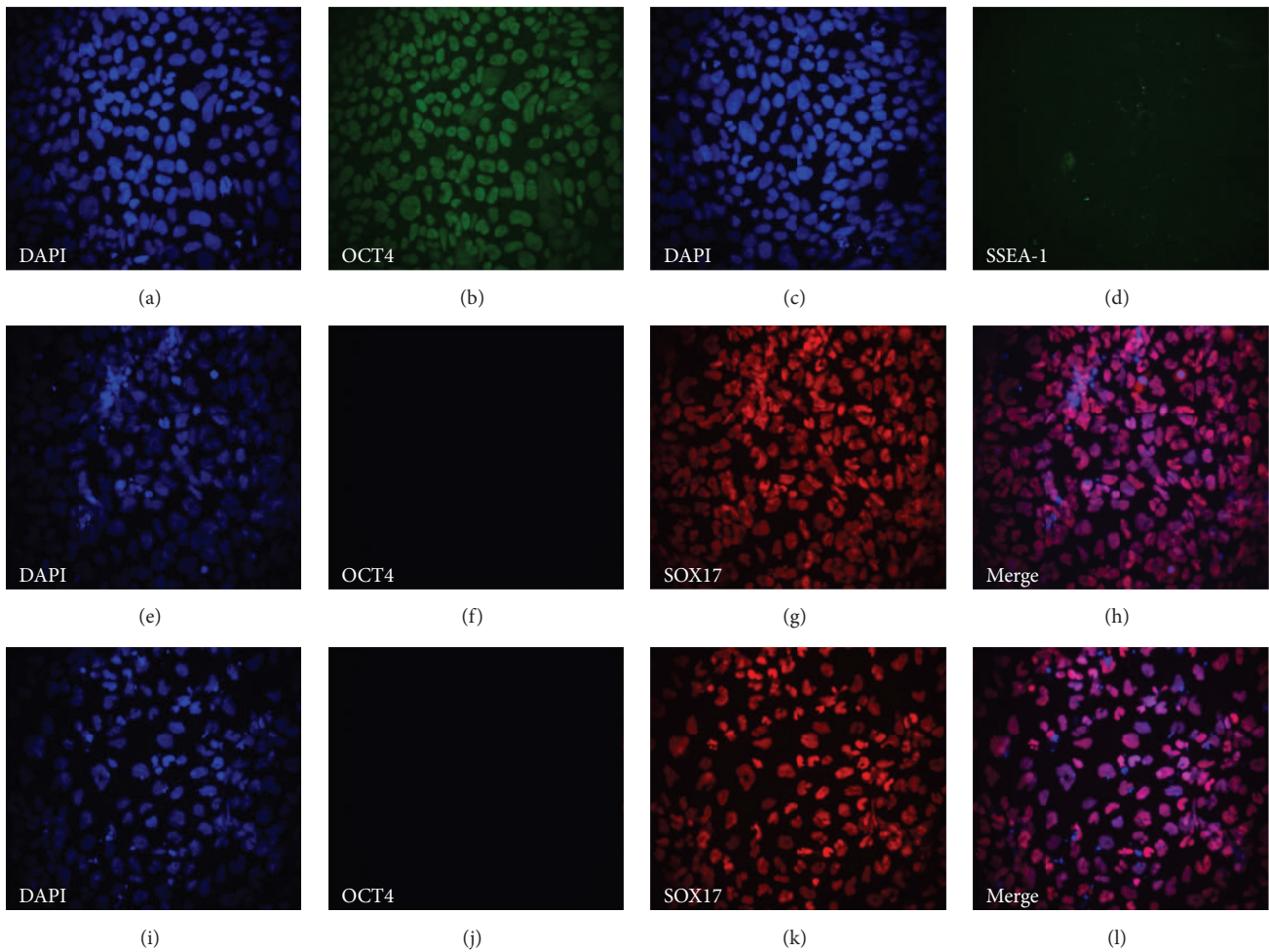


FIGURE 8: Representative micrographs from immunocytochemical analysis at days 0, 5, and 7 during hepatic differentiation of the cell line AS034. Magnification: 20x. Panels (a)–(d) show staining of undifferentiated hPSC at day 0: (a) and (c) show nuclear DAPI staining, (b) shows Oct4 staining, and (d) shows SSEA-1 staining. Panels (e)–(h) show staining of DE cells at day 5 of differentiation: (e) shows nuclear DAPI staining, (f) shows Oct4 staining, (g) shows Sox17 staining, and (h) shows a merge of DAPI and Sox17 staining. Panels (i)–(l) show staining of DE cells at day 7 of differentiation: (i) shows nuclear DAPI staining, (j) shows Oct4 staining, (k) shows Sox17 staining, and (l) shows a merge of DAPI and Sox17 staining.

During the differentiation from DE cells to hepatocytes, hepatic markers were gradually upregulated. Figure 9 shows the expression of CK18, AFP, and HNF4a at day 14. The hepatic marker CK18 was weakly expressed (Figure 9(a)), while AFP and HNF4a were strongly expressed in most of the cells (Figures 9(b) and 9(c), resp.).

At day 25, the differentiation has progressed and more mature hepatocyte markers were expressed in the cells. Figure 10(a) shows the expression of CK18, which was remarkably denser at day 25 than at day 14. HNF4a was still expressed at day 24 at a similar level as on day 14 (Figure 10(b)). Coexpression of ALB and AFP at day 25 was detected in some hepatocyte-like cells; however, the cell cultures were heterogeneous since in some cells only AFP was expressed, which indicated a fetal-like phenotype (Figure 10(c)).

At day 29, expression of AFP was still present although it was weaker than at day 25. At this stage, the cells were

still heterogeneous with about 50% of the cells expressing only ALB and the remaining 50% coexpressing AFP and ALB (Figure 11(a)) indicating the immaturity of some cells at this point. Coexpression of AAT and AFP was also detected (Figure 11(b)); however, there were still some cells that only expressed AFP. At day 30, mature hepatic markers were expressed, such as CYP3A4 (Figure 12(a)); however, not all cells were immunopositive. In addition, HNF4a was still expressed in all hepatocyte-like cells (Figure 12(b)).

Figure 13 shows an overview of the expression patterns of all the genes analyzed in this study, considering genes as being expressed if  $C_q < 35$ . The culturing medium of the different stages during hepatic differentiation as well as the days after start of differentiation is indicated in the upper bars. The pluripotency genes, *OCT4* and *NANOG*, were expressed from day 0 and their expression partly overlapped the DE stage. The *T* gene (Brachyury) was only expressed at day 2 indicating the mesendoderm stage. The genes *CER1*

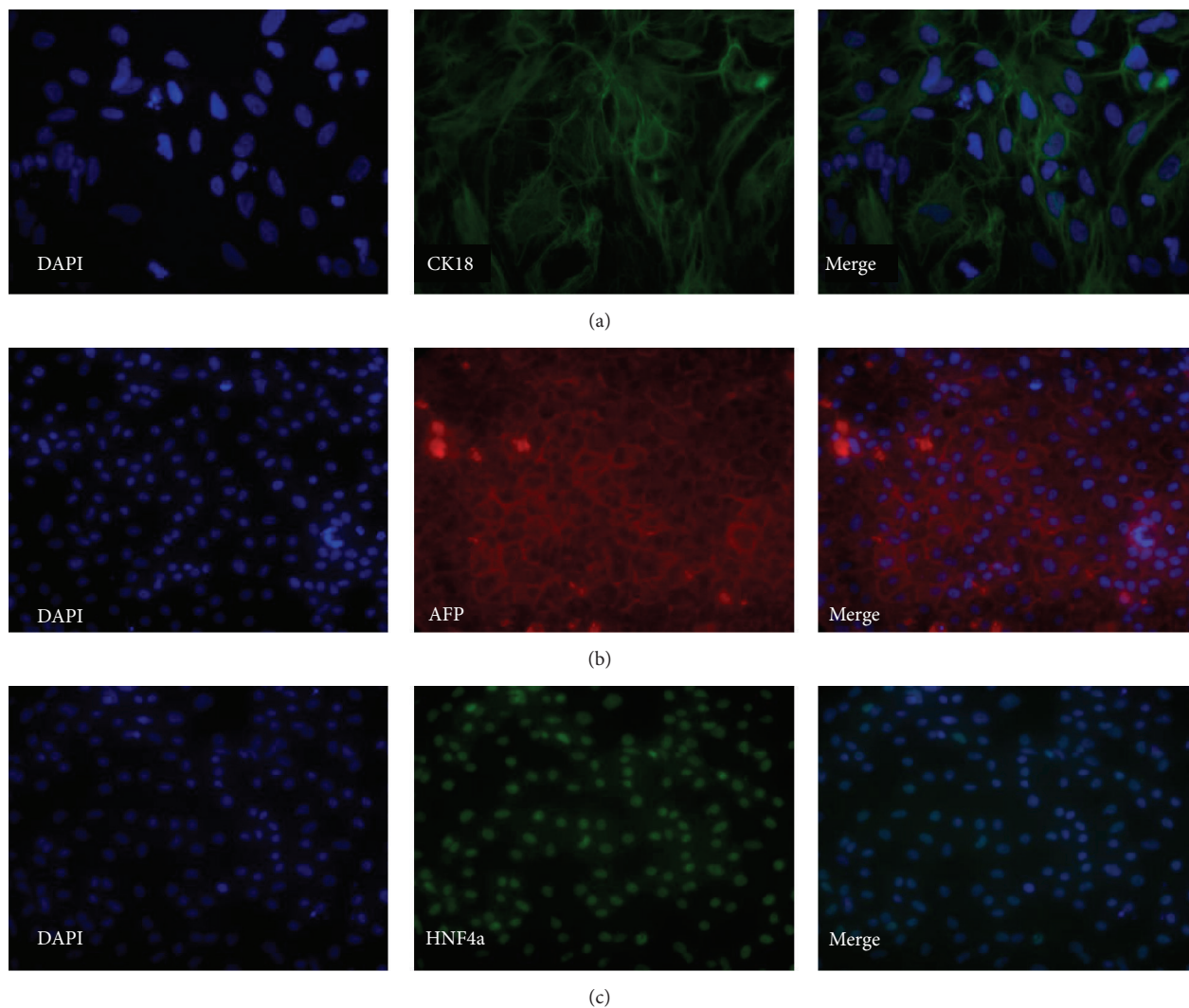


FIGURE 9: Representative micrographs illustrating the expression of selected markers at day 14 of the hepatic differentiation. Panel (a) shows staining for CK18 (SAI21, 40x magnification). Panel (b) shows staining for AFP (AS034, 20x magnification). Panel (c) shows staining for HNF4a (AS034, 20x magnification).

and *HHEX* were initiated already at day 2 and *CXCR4* and *SOX17* appeared at day 3, indicating the onset of the DE differentiation. Progenitor and hepatocyte markers were expressed gradually after adding HEP progenitor medium. *TBX3* and *HNF4A* were already present at day 8, which is one day after the shift to HEP progenitor medium (2). *HNF6* appeared on day 10 and the fetal hepatocyte marker *AFP* on day 11. The expression of *PROX1* and *KRT18* was detected at day 15, one day after the shift to HEP maturation medium base (3Ap) with supplement (3Bp). The hepatocyte maturation marker *AAT* was already expressed at day 18. *ALB* was present from day 20 and, notably, only a few days after the addition of HEP maintenance medium (4) the adult enzyme *CYP3A4* was expressed at day 23.

**3.4. Clustering Analysis.** In order to detect possible coregulation and similarities between all the genes that were analyzed in this study except transporters *SLC10A1* (NTCP),

*ABCB11* (BSEP), *SLCO1B1* (OATP1B1), and *ABCC2* (MRP2), clustering analyses of the gene expression were performed both globally and locally for different intervals during the hepatic differentiation. The clustering of genes was performed using each gene's median expression value over all cell lines, with Spearman's rank correlation as the similarity function. The clustering of days 0 to 11 shows a clear separation between two clusters, with one containing the pluripotency markers, *OCT4* and *NANOG*, and the primitive streak marker, *T*, and the other cluster containing the DE markers *SOX17*, *CXCR4*, *CER1*, and *HHEX*, the ventral foregut marker (Figure 14(a)). In the clustering of genes days 14 to 35 of the hepatic differentiation, the main separation is between a cluster containing the two genes *TBX3* and *AFP* and a second cluster containing the remaining genes. In the later cluster, *HNF4A* and *HNF6* are clearly separated from a subcluster containing *PROX1*, *CYP3A4*, *ALB*, *AAT*, and *KRT18* (Figure 14(b)). Notably, in the analysis of days 7 to 21, *HNF6* is clearly

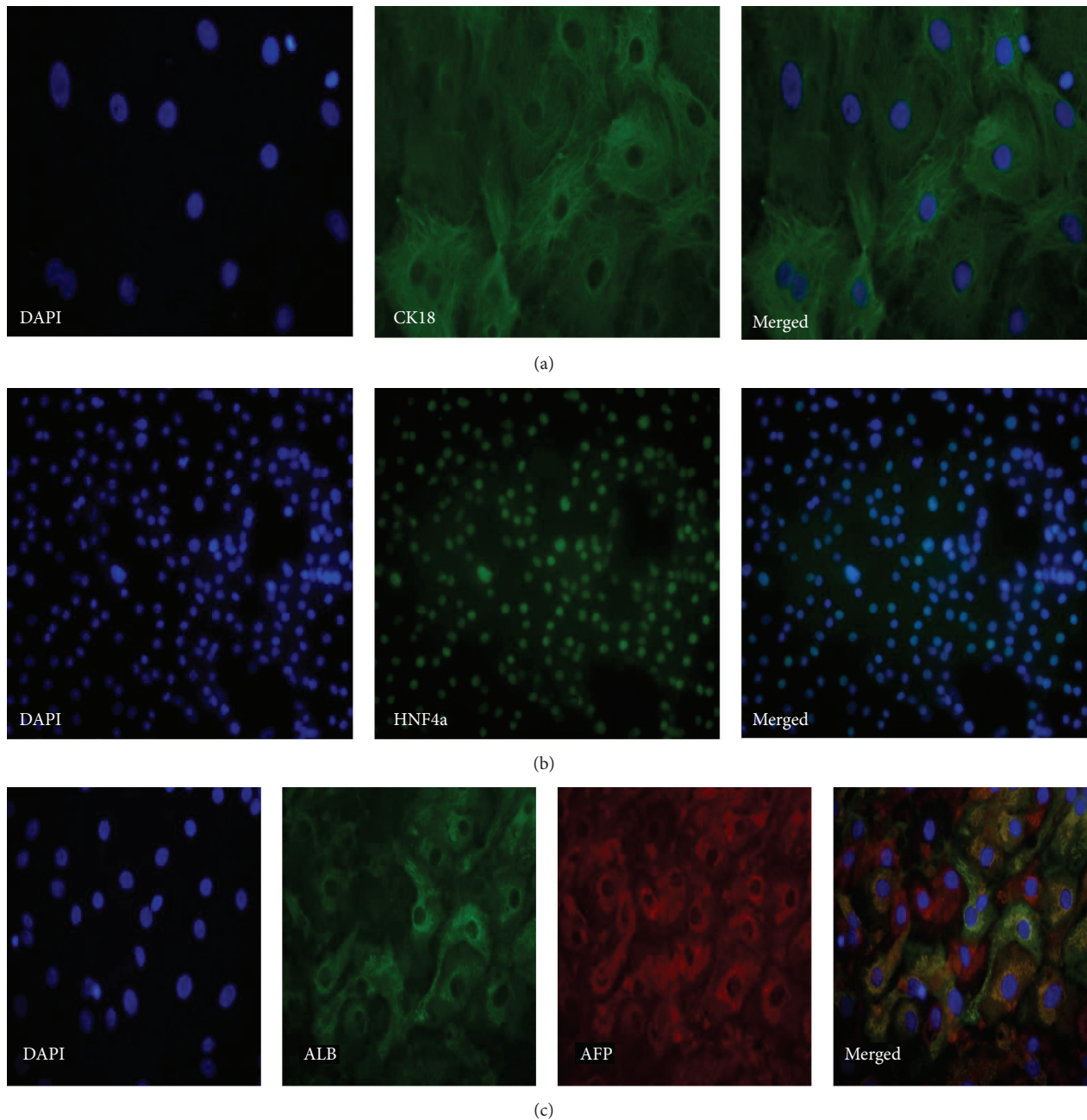


FIGURE 10: Representative micrographs illustrating the expression of markers at day 25. Panel (a) shows staining for CK18 (ChiPSC6b, 40x magnification). Panel (b) shows staining for HNF4a (AS034, 20x magnification). Panel (c) shows stainings for ALB and AFP (ChiPSC6b, 20x magnification).

separated from all other genes. For the remaining genes, there were one subcluster consisting of *HNF4A* and *AFP* and a second subcluster consisting of *TBX3*, *PROX1*, and *KRT18* (Figure 14(c)). For the maturation phase (days 21 to 35) two main clusters were identified, one containing *HNF4A*, *TBX3*, and *AFP* and the other containing *PROX1*, *AAT*, *HNF6*, *KRT18*, *ALB*, and *CYP3A4* (Figure 14(d)).

### 3.5. Gene Expression and Immunocytochemistry Analysis of Drug Transporters.

To determine the maturity of

the hepatocyte-like cells generated from the different hPSC used in this study, RT-qPCR was applied to analyze the expression of the drug transporters *SLC10A1* (NTCP), *ABCB11* (BSEP), *SLCO1B1* (OATP1B1), and *ABCC2* (MRP2). Figure 15 shows interindividual variation in drug transporters gene expression in hepatocyte-like cells derived from the different hPSC lines (Figure 15(a)–15(d)). In addition, the expression of NTCP (Figure 15(a)) and MRP2 (Figure 15(b)) was closer to the level of human freshly isolated primary hepatocytes (calibrator) than OATP1B1 (Figure 15(c)) and

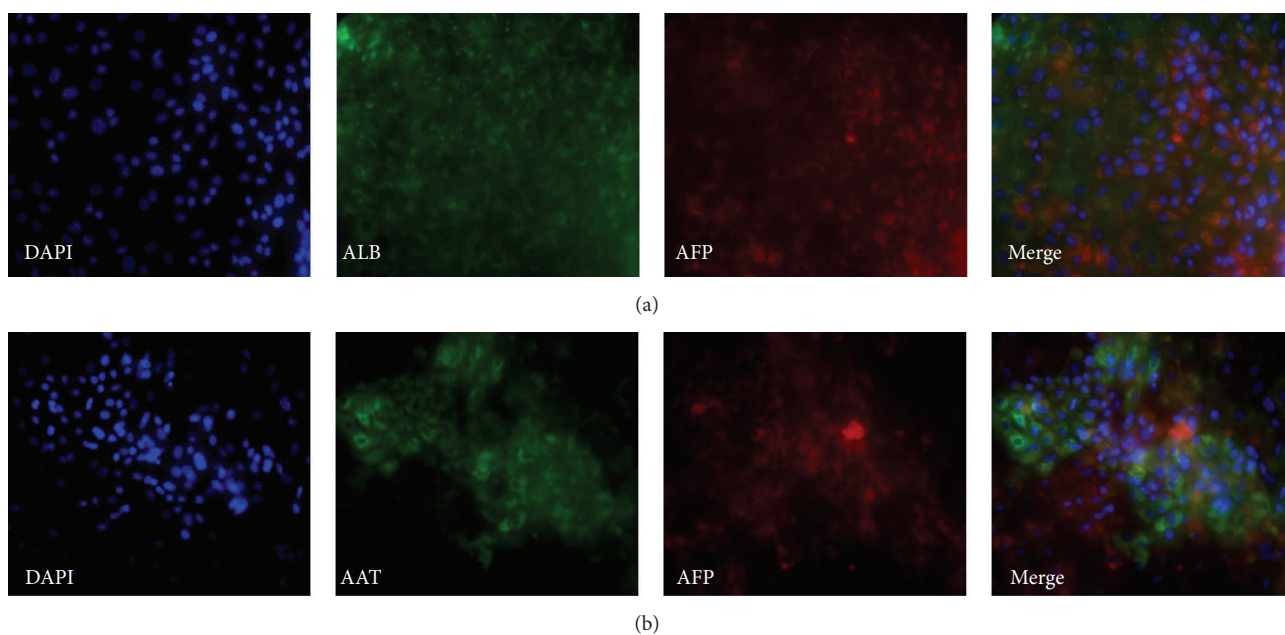


FIGURE 11: Representative micrographs illustrating the expression of markers at day 29 of the hepatic differentiation of the cell line ChiPSC6b. Magnification: 20x. Panel (a) shows stainings for ALB and AFP. Panel (b) shows stainings for AAT and AFP.

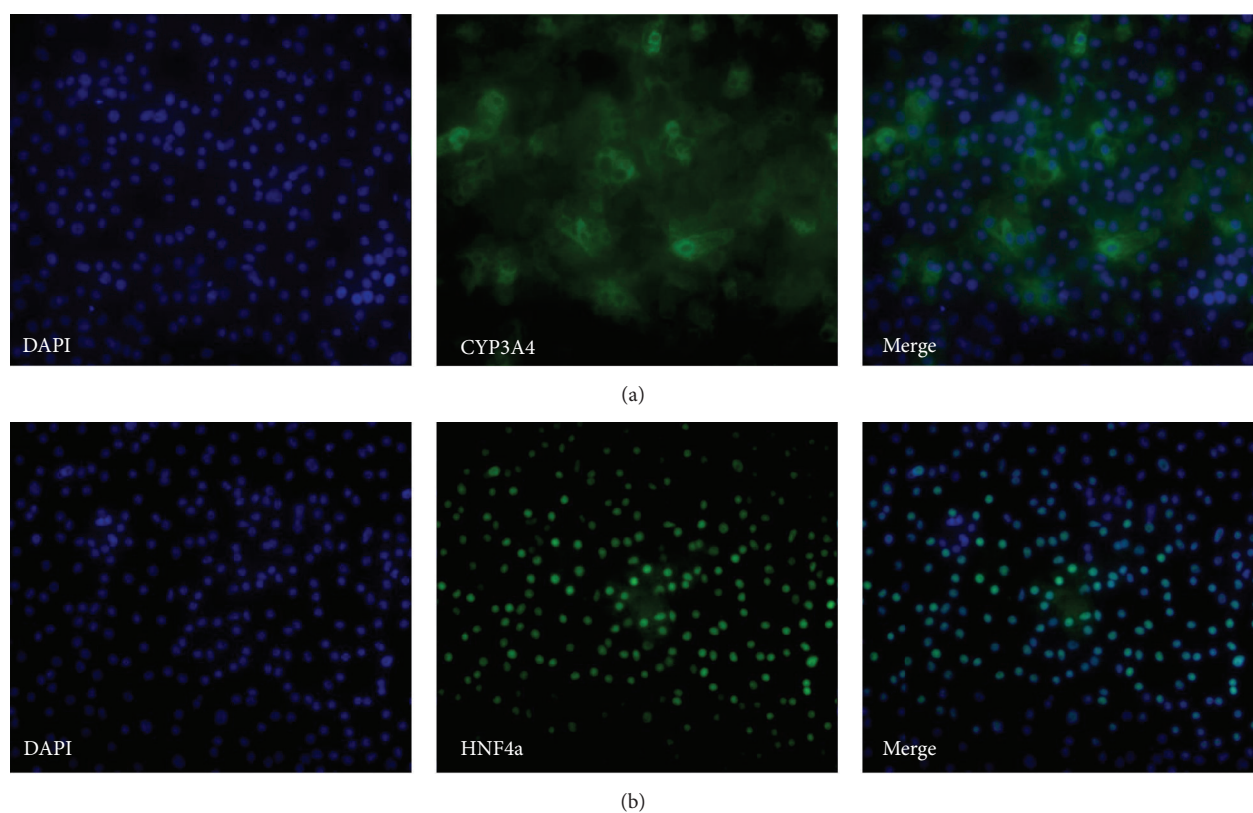


FIGURE 12: Representative micrographs illustrating the expression of markers at day 30. Panel (a) shows stainings for CYP3A4 (AS034, 20x magnification). Panel (b) shows stainings for HNF4a (AS034, 20x magnification).

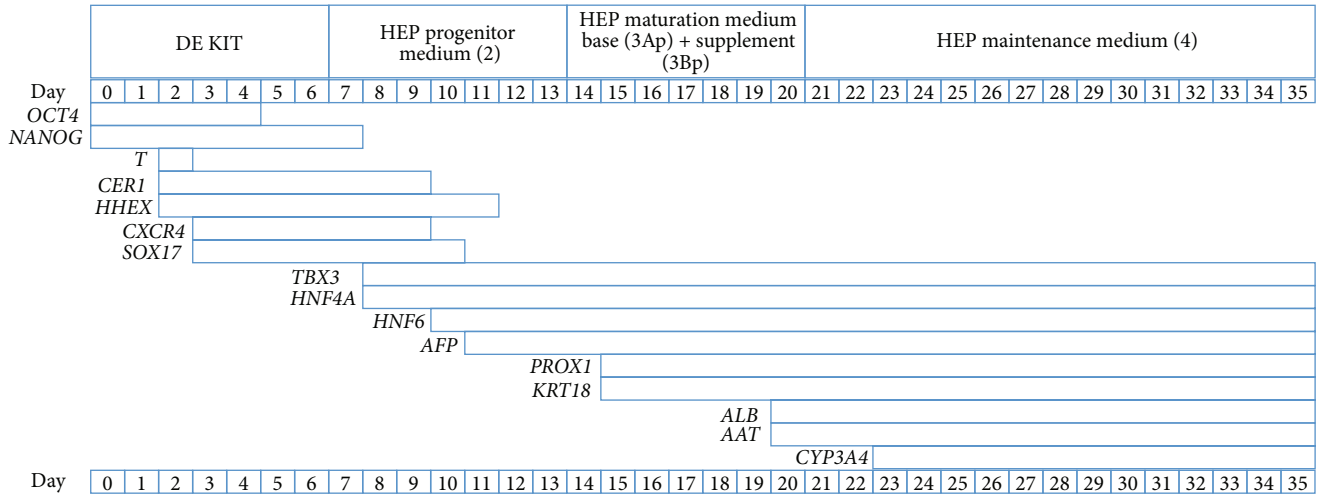


FIGURE 13: Overview of the expression patterns of all genes analyzed in this study. The header bar shows the medium in which the cells were incubated during the indicated days through hepatic differentiation. The bars below indicate the expression duration of the different genes during the hepatic differentiation. Gene expression after day 35 was not analyzed; hence end of expression for genes expressed at day 35 should not be assumed.

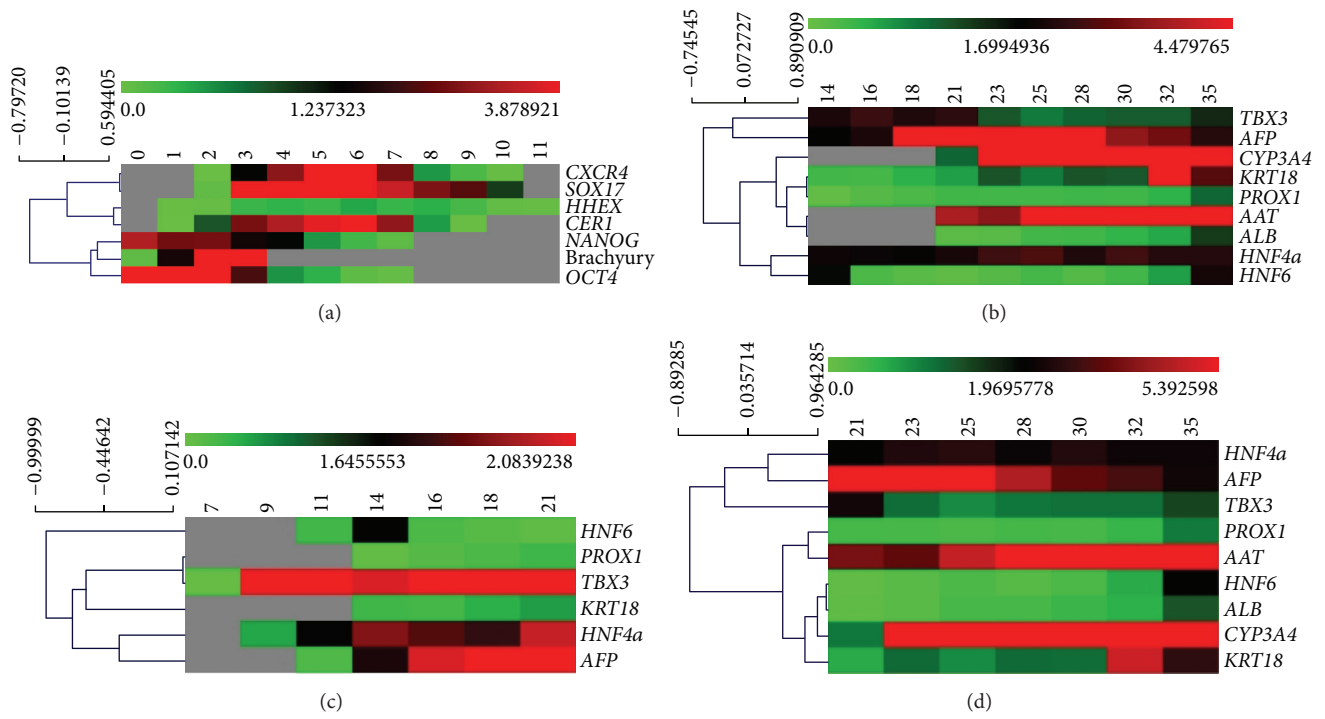


FIGURE 14: Clustering analysis. The genes included in the study were clustered applying Spearman rank correlation. Colors indicate RQ according to the scale shown above each heatmap. Missing values are indicated by gray color. (a) Clustering results for days 0 to 11, (b) days 14 to 35, (c) days 7 to 21, and (d) days 21 to 35.

BSEP (Figure 15(d)). Most of the interindividual variation was observed for BSEP (Figure 15(d)), where hepatocyte-like cells derived from AS034 at day 34 expressed BSEP at higher levels than any of the other hPSC-derived hepatocytes. OATP1B1 also showed high interindividual variation, where

hepatocytes derived from SA181 and P11012 at day 3 expressed OATP1B1 at higher levels than what were observed in the other cell lines.

Immunocytochemistry analyses were performed to confirm the expression of NTCP, BSEP, MRP2, and OATP1B1 at

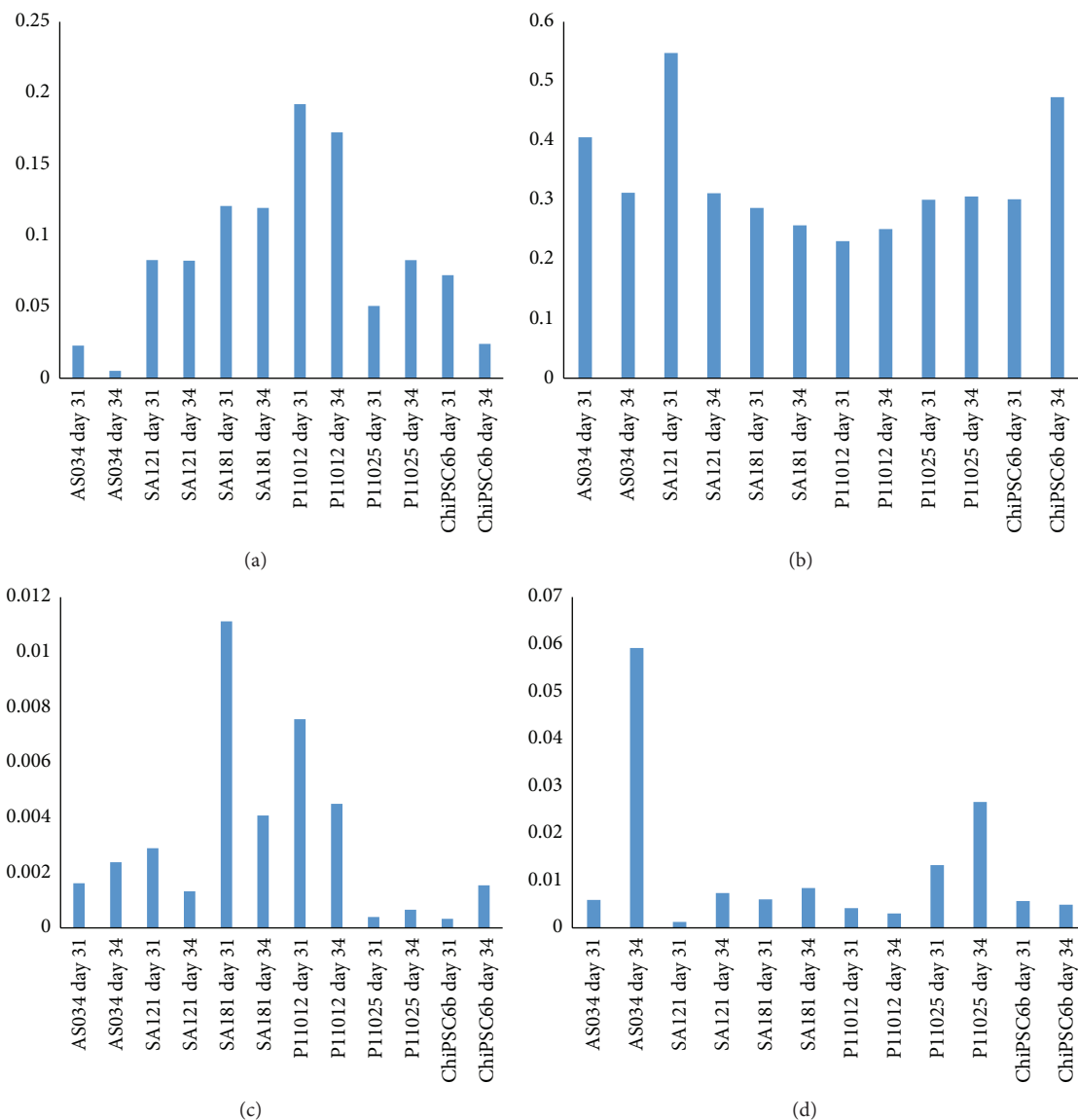


FIGURE 15: Bar graph showing the RNA expression levels of the drug transporters (a) *SLC10A1* (NTCP), (b) *ABCB2* (MRP2), (c) *SLCO1B1* (OATP1B1), and (d) *ABCB11* (BSEP). The x-axis indicates the hPSC lines at days 31 and 34 of the hepatic differentiation. The y-axis indicates RQ, where the calibrator's RQ = 1. The calibrator was an RNA pool of freshly isolated human primary hepatocytes from 5 different donors.

the protein level. Figure 16 shows the staining patterns for NTCP and OATP1B1 and Figure 17 shows the expression of BSEP and MRP2.

**3.6. Cytochrome P450 (CYP) Enzymes Activity Assay.** To investigate the drug metabolizing capacity, hepatocyte-like cells and cryoplateable human primary hepatocytes (hphep) were incubated in a cocktail of phenacetin (metabolized by CYP1A), bufuralol (metabolized by CYP2D6), diclofenac (metabolized by CYP2C9), midazolam (metabolized by CYP3A), and mephenytoin (metabolized by CYP2C19) at day 29 of the hepatic differentiation. The concentrations of the resulting metabolites paracetamol, 1-OH-bufuralol, 4-OH-diclofenac, 3-OH-midazolam, and 4-OH-mephenytoin

were determined by liquid chromatography/mass spectrometry. The metabolite concentrations were normalized to mg protein and incubation time. Figure 18 shows interindividual variation in the different CYP enzyme activities in the hepatocyte-like cells generated from the different hPSC lines. The activity of CYP1A in hphep is about 7 times higher than in AS034-derived hepatocytes (Figure 18(a)). However, the activity of CYP3A in SA034-derived hepatocytes was higher than in hphep (Figure 18(b)). The activity of CYP2C9 in hphep is about 4 times higher than in ChiPSC6b-derived hepatocytes (Figure 18(c)). The activity of CYP2D6 in hphep is much higher than in hPSC-derived hepatocytes (Figure 18(d)). Moreover, the activity of CYP2C19 in hphep is about 4 times higher than ChiPSC6b-derived hepatocytes (Figure 18(e)). In addition, hepatocyte-like cells from SA034

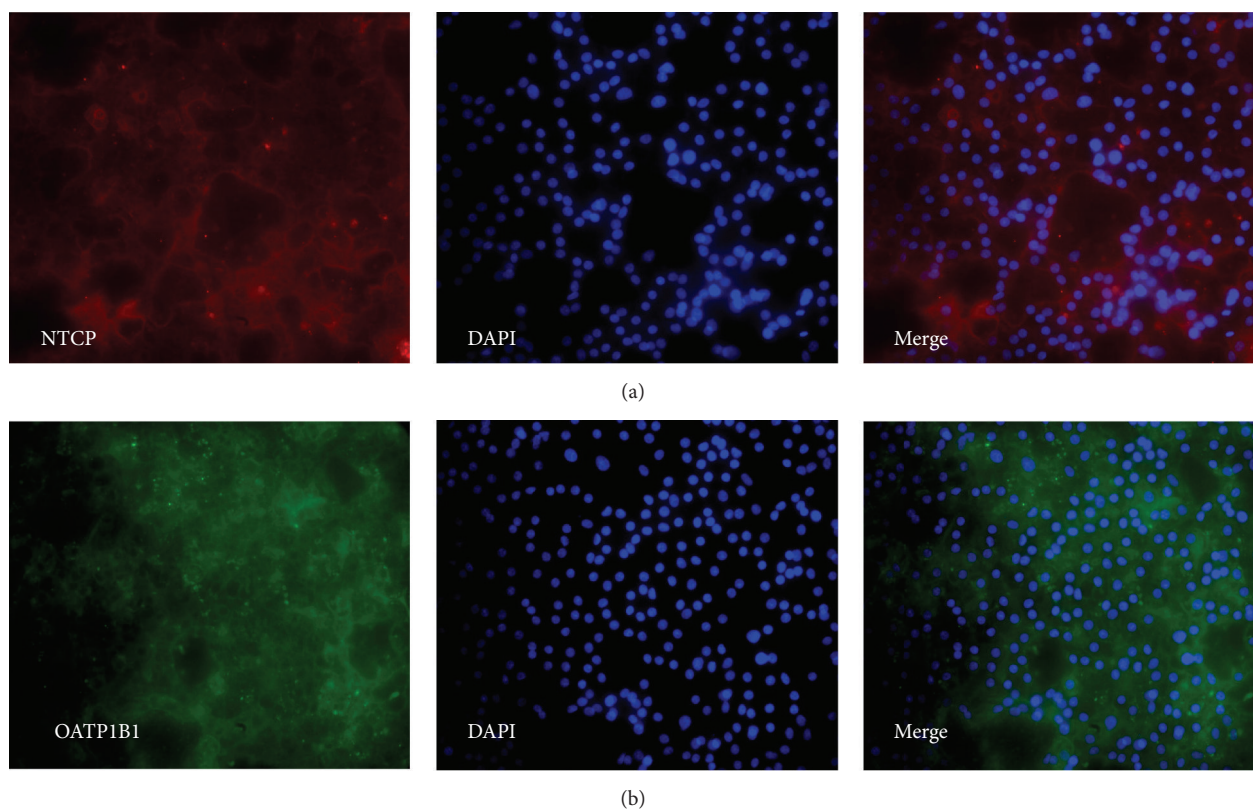


FIGURE 16: Representative micrographs illustrating the expression of drug transporters at day 29 of the hepatic differentiation of P11012. Magnification: 20x. Panel (a) shows stainings for NTCP. Panel (b) shows stainings for OATP1B1.

show much high CYP1A and CYP3A activity compared to other hPSC-derived hepatocytes (Figures 18(a) and 18(b), resp.). Hepatocyte-like cells derived from ChiPSC6b show higher CYP2C9 activity compared to hepatocytes-like cells derived from the other cell lines (Figure 18(c)). These results illustrate the interindividual variation in CYP activity of hPSC-derived hepatocytes.

**3.7. PAS Staining.** The ability to produce and store glycogen is a function of mature hepatocytes [11]. To investigate if hPSC-derived hepatocytes also have the ability to store glycogen PAS staining was performed. Figure 19 shows the detection of glycogen storage by PAS. Hepatocytes derived from both hESC (Figure 19(b)) and hiPSC (Figure 19(a)) show glycogen storage ability.

#### 4. Discussion

The unique properties of pluripotent stem cells, including their indefinite self-renewal and their capacity to differentiate to essentially all cell types in the body, make them an attractive source for human cells that can be applied in various cell models for drug discovery and future regenerative medicine applications [2, 4, 5, 7, 15, 20, 21]. *In vitro* differentiation of hepatocytes, recapitulating some of the properties and functionalities of their *in vivo* counterpart, has been reported by several groups using differentiation protocols that mimic

the hepatocyte development *in vivo* [4, 6–9, 15, 22]. A recent study reported a standardized hepatocyte differentiation protocol that does not require any further adjustments to produce near-homogenous hepatocytes from a large panel of different hPSC lines [13]. In the present study, we have differentiated six hPSC lines into hepatocyte-like cells applying a protocol developed further from the procedure published by Asplund and coworkers [13]. Using RT-qPCR, we analyzed the gene expression of several key lineage-specific genes that are markers for the different stages during hepatocyte differentiation to assess the synchronicity of the *in vitro* differentiation process. In addition, we applied statistical methods to mathematically analyze and quantify the correlation between the hPSC lines. The results revealed highly synchronized gene expression profiles, especially for key markers of the early differentiation stages, thus indicating the similarity of this *in vitro* differentiation process to the *in vivo* liver development. However, weak correlation of the mature hepatocyte marker *CYP3A4* could be explained by its high level of polymorphism [23]. We also noted that the correlation patterns among hESC and hiPSC lines appeared randomly distributed and no evidence of preferential similarity between specific cell lines was observed.

The hepatic differentiation process starts with the down-regulation of the stem cell markers *OCT4* and *NANOG* that are also clustered together indicating similar functionality, such as maintenance of pluripotency, and both genes have

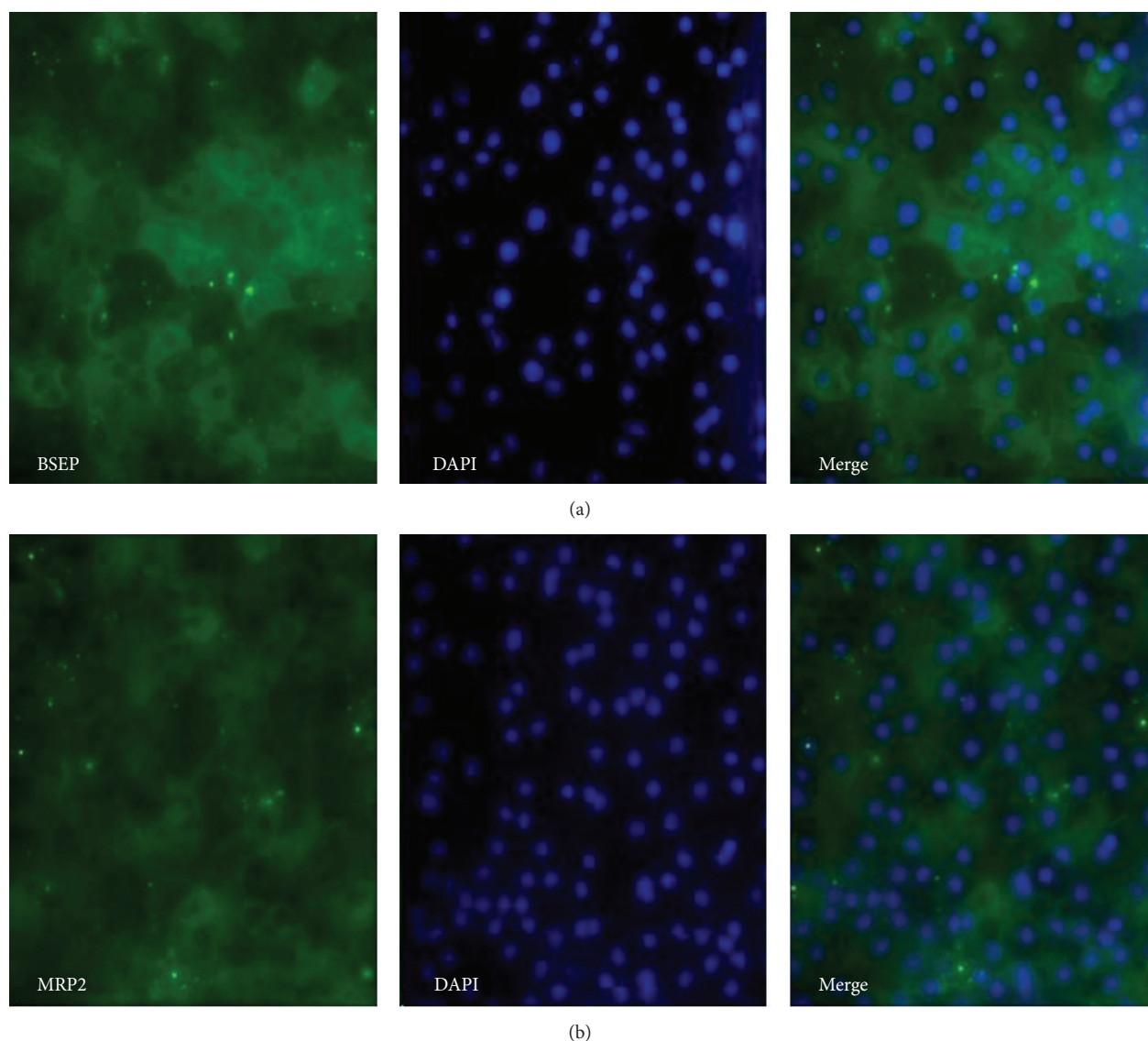


FIGURE 17: Representative micrographs illustrating the expression of drug transporters at day 29 of the hepatic differentiation. Magnification: 20x. Panel (a) shows stainings for BSEP in P11025 cell line. Panel (b) shows stainings for MRP2 in SA121 cell line.

been indeed reported to control the expression of each other [24]. *NANOG* clustered also with *T* (Brachyury), and *NANOG* has been reported to bind the promoter region of *T* [25]. Our results also show that *OCT4* is undetectable in DE cells while *NANOG* is downregulated but still present at low levels at the DE stage, which is also consistent with the results from other studies [26, 27]. The primitive streak stage appears at day 2 with a short peak expression of *T*, which is then undetectable already on day 3, in parallel with the onset of expression of *SOX17* and *CXCR4*, indicating the termination of the mesendoderm stage and the initiation of the DE stage [19, 27]. *SOX17* and *CXCR4* also clustered together at the DE stage, which is expected since *CXCR4* is regulated by *SOX17* [27]. *CER1* is typically used as DE marker in combination with other genes, since it is also expressed in mesoderm [28]. Our

results indicate that, unlike *SOX17* and *CXCR4*, the onset of *CER1* occurs in the primitive streak, which is in agreement with *in vivo* liver development [29]. *HHEX* promotes the further hepatic differentiation by terminating the DE stages, thereby initiating hepatoblast differentiation. The onset of *HHEX* expression is suggested to occur at the DE stage and continue through the hepatoblast stage [30]. Our results demonstrate the upregulation of *HHEX* in the mesendoderm and its expression is terminated at the hepatoblast stage. *HHEX* also cluster with *CER1*, and both of these genes are known to be induced by *SOX17*. This was, however, not reflected in our results, since *CER1* and *HHEX* were expressed before *SOX17*. In addition, *HHEX* is required for the normal expression of *CER1*, which may explain the clustering of this pair of genes with *SOX17* and *CXCR4* [28]. However,

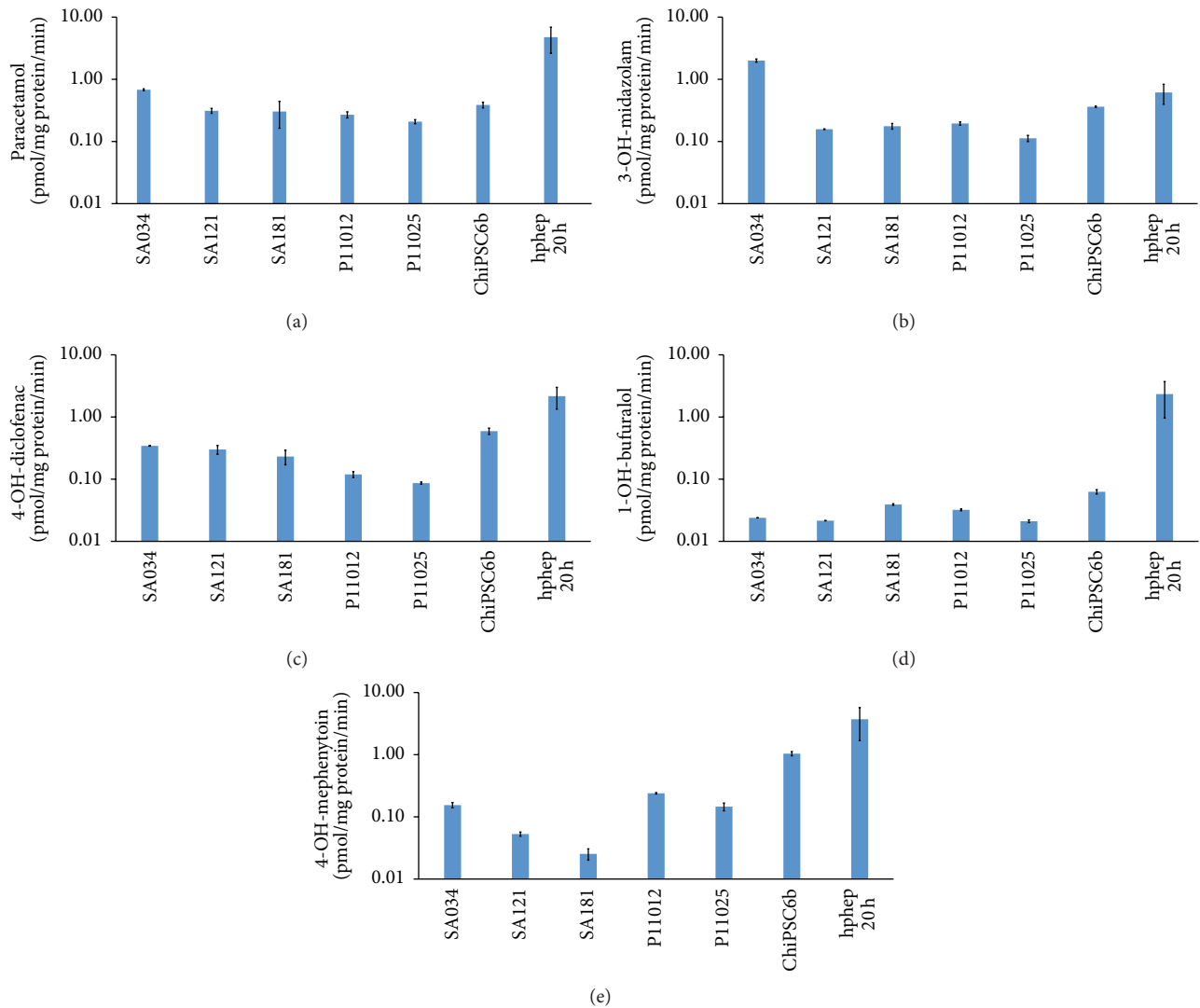


FIGURE 18: Cytochrome 450 enzymes (CYP) activities in hepatocytes derived from hPSCs (AS034, SA121, SA181, P11012, P11025, and ChiPSC6b) ( $N = 2$ ) and cryopreserved human primary hepatocytes plated for 20 hr (hphep 20 h) ( $N = 4$ ). CYP activities in hepatocyte cultures were measured after 29 days of differentiation by the following assay: the cells were incubated with CYP enzymes substrates phenacetin (CYP1A), midazolam (CYP3A), diclofenac (CYP2C9), bufuralol (CYP2D6), and mephenytoin (CYP2C19). The concentrations of the resulting metabolites paracetamol, 3-OH-midazolam, 3-OH-diclofenac, 4-OH-diclofenac, 1-OH-bufuralol, and 4-OH-mephenytoin were determined by liquid chromatography/mass spectrometry. The results were normalized to mg protein per well and the duration of CYP activity assay. The CYP activity is presented as pmol metabolite per mg protein per minute (mean  $\pm$  SEM). The  $y$ -axis in log scale. (a) CYP1A, (b) CYP3A, (c) CYP2C9, (d) CYP2D6, and (e) CYP2C19.

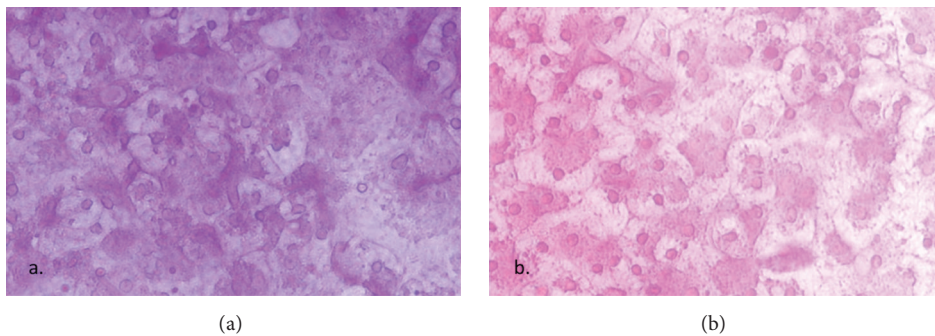


FIGURE 19: Representative PAS stainings. The cells were treated with periodic acid, SCHIFF, and hematoxylin as described in Materials and Methods. (a) P11025 and (b) AS034.

the expression of *HHEX* was terminated at the later hepatoblast stage, whereas *in vivo* expression of *HHEX* is maintained throughout the hepatic development [14].

Small fluctuations in the RNA levels were observed as an artifact at each medium change after the DE stage and these were not included in the gene expression and clustering analysis since they would mask the real effects when the gene expression is stabilized and introduce nonrelevant noise. The genes *TBX3* and *HNF4A* are known to be expressed in the hepatic endoderm stage [1, 4, 14, 31, 32]. Interestingly, these genes are induced directly after the application of HEP progenitor medium (2) indicating the efficiency of the medium in promoting the development into hepatoblasts. *TBX3* is proposed to promote hepatocyte differentiation from hepatoblasts and represses cholangiocytes by downregulating *HNF6* and *KRT18* and additionally promotes the expression of *HNF4A*, which is a key regulator of morphological and functional differentiation of hepatocytes [2], by repressing the transcriptional repressor of *HNF4A* [32]. *HNF6* is expressed at the hepatoblast stage and promotes the differentiation of hepatoblasts towards cholangiocytes [14, 32]. However, *HNF6* is required for proper liver development in the early stages [33]. Towards the end of the hepatoblast stage, *AFP* expression is detected, which is a fetal hepatocyte marker expressed until birth. Subsequently, it is downregulated but can still be detected in adult liver at very low levels [34]. Our results show that *AFP* is coexpressed in some hepatocyte-like cells with the mature hepatocyte markers *AAT* and *ALB* and is downregulated in the maturing hepatocyte-like cells, however, not to a level below the detection limit of the assay (Figure 6). *PROX1* and *KRT18* are upregulated at day 15 (Figure 7), directly after the switch to HEP maturation base medium (3Ap) and supplement (3Bp). *PROX1* together with *HNF6* was demonstrated to be crucial for complete hepatocyte programming including recapitulating the metabolic functionality *in vitro* [31]. *KRT18* is a hepatic marker which we observed to be weakly expressed in hepatoblasts and which was upregulated in later stages (Figure 7), which is in accordance with other studies [35]. *AAT* is detected at day 19 at low levels compared to freshly isolated primary hepatocytes. *ALB*, which is a mature hepatocyte marker, is detected at day 20. This gene could also be expressed in nonfunctional hepatocytes when the programming process fails to mimic liver organogenesis [31]. However, the detection of *CYP3A4* mRNA expression (Figure 7) and *CYP3A4* immunopositive hepatocyte-like cells (Figure 12) as well as CYP activity assay results that show comparable results to cryoplateable human primary hepatocytes (Figure 18) confirmed the hepatic functionality of the generated hepatocyte-like cells. In addition, the RNA and protein expression of the drug transporters MRP2, OATP1B1, BSEP, and NTCP (Figures 16 and 17), as well as the ability to store glycogen (Figure 19), also demonstrate the hepatic functionality of these cells. The interindividual variation in CYP activity and drug transporters expression in hPSC-derived hepatocytes show similarity to what is typically observed in their *in vivo* counterparts [11, 13]. However, unlike during the *in vivo* liver development [14], *ALB* is not detected in hepatoblasts in our study.

The clustering analysis of the later differentiation stages reveals the shift of the cluster *PROX1*, *TBX3*, *KRT18*, *HNF4A*, and *AFP* at days 7 to 21 to the cluster *HNF4A*, *AFP*, and *TBX3*, and the cluster *PROX1*, *AAT*, *HNF6*, *ALB*, *CYP3A4*, and *KRT18* at days 21 to 35. The clustering of *PROX1* and *KRT18* both between days 7 and 21 and between days 21 and 35 could be explained by the upregulation of both genes when switching to the HEP maturation base medium (3Ap) and supplement (3Bp). Importantly, *PROX1* and *HNF6* were described to be involved in the same gene regulatory network controlling the migration and adhesion of hepatocytes *in vivo* [33, 36]. Since *HNF6* and *KRT18* are both regulated by *TBX3* [32] it is plausible that *PROX1* and *KRT18* are involved in the same gene regulatory network. *HNF4a* is known to bind to more than 40% of liver active genes [2], and its expression is already upregulated at day 8, which could explain its clustering with *AFP* and *TBX3*, which are also upregulated early (Figure 13). At days 21 to 35 there is a clear distribution of mature hepatocyte markers (*AAT*, *ALB*, *KRT18*, and *CYP3A4*) into adjacent clusters separated from earlier markers (*AFP*, *TBX3*). Finally, the clustering of *HNF6* with *KRT18* could possibly be explained by the common regulation by *TBX3* [32]; however, the clustering of *ALB* with *HNF6* needs to be further investigated.

## 5. Conclusion

The process of differentiating hPSCs into hepatocytes used in the present study demonstrated highly synchronized gene expression profiles of several lineage-specific genes across 6 hPSC lines. Comparing these data to the results from previous studies of both *in vitro* and *in vivo* differentiated hepatocytes revealed important similarities but also some differences, such as the absence of coexpression of *PROX1* and *HNF6*, which promotes the induction of *HNF1A*. Furthermore, the silencing of *HHEX* at early stages also deviates from the *in vivo* situation. A successful correction of these deviations would have the potential to significantly improve the functionality of *in vitro* derived hepatocytes. Moreover, further investigation of the interaction between *ALB* and *HNF6* could also lead to improvements of future differentiation protocols. Taken together, this study adds yet another piece of information to the efforts of improving *in vitro* hepatic differentiation protocols, thereby bringing hPSC-derived hepatocyte based models to a wider practical use.

## Conflict of Interests

The authors Josefina Edsbacke and Barbara Küppers-Munther are employees of Takara Bio Europe AB. The author Mariska Van Giezen was employed by Takara Bio Europe AB during the course of this work.

## Acknowledgments

This work was supported by Takara Bio Europe AB (Gothenburg, Sweden) and the University of Skövde, Sweden, under

grants from the Knowledge Foundation [2012/0310] and [2013/89].

## References

- [1] T. Touboul, N. R. F. Hannan, S. Corbinau et al., "Generation of functional hepatocytes from human embryonic stem cells under chemically defined conditions that recapitulate liver development," *Hepatology*, vol. 51, no. 5, pp. 1754–1765, 2010.
- [2] C. Guguen-Guillouzo and A. Guillouzo, "General review on in vitro hepatocyte models and their applications," *Methods in Molecular Biology*, vol. 640, pp. 1–40, 2010.
- [3] D. Szkolnicka, W. Zhou, B. Lucendo-Villarín, and D. C. Hay, "Pluripotent stem cell-derived hepatocytes: potential and challenges in pharmacology," *Annual Review of Pharmacology and Toxicology*, vol. 53, pp. 147–159, 2013.
- [4] D. A. Chistiakov and P. A. Chistiakov, "Strategies to produce hepatocytes and hepatocyte-like cells from pluripotent stem cells," *Hepatology Research*, vol. 42, no. 2, pp. 111–119, 2012.
- [5] P. Sartipy and P. Björquist, "Concise review: human pluripotent stem cell-based models for cardiac and hepatic toxicity assessment," *STEM CELLS*, vol. 29, no. 5, pp. 744–748, 2011.
- [6] R. Yildirimman, G. Brolén, M. Vilardell et al., "Human embryonic stem cell derived hepatocyte-like cells as a tool for in vitro hazard assessment of chemical carcinogenicity," *Toxicological Sciences*, vol. 124, no. 2, pp. 278–290, 2011.
- [7] R. Kia, R. L. C. Sison, J. Heslop et al., "Stem cell-derived hepatocytes as a predictive model for drug-induced liver injury: are we there yet?" *British Journal of Clinical Pharmacology*, vol. 75, no. 4, pp. 885–896, 2013.
- [8] D. C. Hay, S. Pernagallo, J. J. Diaz-Mochon et al., "Unbiased screening of polymer libraries to define novel substrates for functional hepatocytes with inducible drug metabolism," *Stem Cell Research*, vol. 6, no. 2, pp. 92–102, 2011.
- [9] D. C. Hay, D. Zhao, J. Fletcher et al., "Efficient differentiation of hepatocytes from human embryonic stem cells exhibiting markers recapitulating liver development in vivo," *STEM CELLS*, vol. 26, no. 4, pp. 894–902, 2008.
- [10] C. M. Payne, K. Samuel, A. Pryde et al., "Persistence of functional hepatocyte-like cells in immune-compromised mice," *Liver International*, vol. 31, no. 2, pp. 254–262, 2011.
- [11] M. Ulvestad, P. Nordell, A. Asplund et al., "Drug metabolizing enzyme and transporter protein profiles of hepatocytes derived from human embryonic and induced pluripotent stem cells," *Biochemical Pharmacology*, vol. 86, no. 5, pp. 691–702, 2013.
- [12] G. Holmgren, A.-K. Sjögren, I. Barragan et al., "Long-term chronic toxicity testing using human pluripotent stem cell-derived hepatocytes," *Drug Metabolism and Disposition*, vol. 42, no. 9, pp. 1401–1406, 2014.
- [13] A. Asplund, A. Pradip, M. van Giezen et al., "One standardized differentiation procedure robustly generates homogenous hepatocyte cultures displaying metabolic diversity from a large panel of human pluripotent stem cells," *Stem Cell Reviews and Reports*, 2015.
- [14] A. M. Zorn, "Liver development," in *StemBook*, Aaron M. Zorn, Cambridge, Mass, USA, 2008.
- [15] H. Liu, Y. Kim, S. Sharkis, L. Marchionni, and Y.-Y. Jang, "In vivo liver regeneration potential of human induced pluripotent stem cells from diverse origins," *Science Translational Medicine*, vol. 3, no. 82, Article ID 82ra39, 2011.
- [16] A. Jochheim, A. Cieslak, T. Hillemann et al., "Multi-stage analysis of differential gene expression in BALB/C mouse liver development by high-density microarrays," *Differentiation*, vol. 71, no. 1, pp. 62–72, 2003.
- [17] A. K. K. Teo, S. J. Arnold, M. W. B. Trotter et al., "Pluripotency factors regulate definitive endoderm specification through eomesodermin," *Genes and Development*, vol. 25, no. 3, pp. 238–250, 2011.
- [18] M. Kotlyar, S. Fuhrman, A. Ableson, and R. Somogyi, "Spearman correlation identifies statistically significant gene expression clusters in spinal cord development and injury," *Neurochemical Research*, vol. 27, no. 10, pp. 1133–1140, 2002.
- [19] S. Tada, T. Era, C. Furusawa et al., "Characterization of mesoderm: a diverging point of the definitive endoderm and mesoderm in embryonic stem cell differentiation culture," *Development*, vol. 132, no. 19, pp. 4363–4374, 2005.
- [20] M. Vosough, M. Moslem, B. Pournasr, and H. Baharvand, "Cell-based therapeutics for liver disorders," *British Medical Bulletin*, vol. 100, no. 1, pp. 157–172, 2011.
- [21] R. Gramignoli, M. Vosough, K. Kannisto, R. C. Srinivasan, and S. C. Strom, "Clinical hepatocyte transplantation: practical limits and possible solutions," *European Surgical Research*, vol. 54, no. 3–4, pp. 162–177, 2015.
- [22] Z. Farzaneh, M. Pakzad, M. Vosough, B. Pournasr, and H. Baharvand, "Differentiation of human embryonic stem cells to hepatocyte-like cells on a new developed xeno-free extracellular matrix," *Histochemistry and Cell Biology*, vol. 142, no. 2, pp. 217–226, 2014.
- [23] K. Klein and U. M. Zanger, "Pharmacogenomics of cytochrome P450 3A4: recent progress toward the 'missing heritability' problem," *Frontiers in Genetics*, vol. 4, article 12, 2013.
- [24] T. Kalmar, C. Lim, P. Hayward et al., "Regulated fluctuations in Nanog expression mediate cell fate decisions in embryonic stem cells," *PLoS Biology*, vol. 7, no. 7, Article ID e1000149, 2009.
- [25] S. Mora-Castilla, J. R. Tejado, R. Tapia-Limonchi et al., "Transient downregulation of nanog and oct4 induced by DETA/NO exposure in mouse embryonic stem cells leads to mesodermal/endodermal lineage differentiation," *Stem Cells International*, vol. 2014, Article ID 379678, 11 pages, 2014.
- [26] H. Kim, M.-J. Jang, M.-J. Kang, and Y.-M. Han, "Epigenetic signatures and temporal expression of lineage-specific genes in hESCs during differentiation to hepatocytes in vitro," *Human Molecular Genetics*, vol. 20, no. 3, pp. 401–412, 2011.
- [27] M. Katoh and M. Katoh, "Integrative genomic analyses of CXCR4: transcriptional regulation of CXCR4 based on TGFβ, Nodal, Activin signaling and POU5F1, FOXA2, FOXC2, FOXH1, SOX17, and GFI1 transcription factors," *International Journal of Oncology*, vol. 36, no. 2, pp. 415–420, 2010.
- [28] Y. Liu, R. Kaneda, T. W. Leja et al., "Hhex and cer1 mediate the Sox17 pathway for cardiac mesoderm formation in embryonic stem cells," *STEM CELLS*, vol. 32, no. 6, pp. 1515–1526, 2014.
- [29] H. Iwashita, N. Shiraki, D. Sakano et al., "Secreted cerberus1 as a marker for quantification of definitive endoderm differentiation of the pluripotent stem cells," *PLoS ONE*, vol. 8, no. 5, Article ID e64291, 2013.
- [30] H. Watanabe, K. Takayama, M. Inamura et al., "HHEX promotes hepatic-lineage specification through the negative regulation of eomesodermin," *PLoS ONE*, vol. 9, no. 3, Article ID e90791, 2014.

- [31] D. Zhao, S. Chen, S. Duo et al., "Promotion of the efficient metabolic maturation of human pluripotent stem cell-derived hepatocytes by correcting specification defects," *Cell Research*, vol. 23, no. 1, pp. 157–161, 2013.
- [32] T. H.-W. Lüdtke, V. M. Christoffels, M. Petry, and A. Kispert, "Tbx3 promotes liver bud expansion during mouse development by suppression of cholangiocyte differentiation," *Hepatology*, vol. 49, no. 3, pp. 969–978, 2009.
- [33] S. Margagliotti, F. Clotman, C. E. Pierreux et al., "The Onecut transcription factors HNF-6/OC-1 and OC-2 regulate early liver expansion by controlling hepatoblast migration," *Developmental Biology*, vol. 311, no. 2, pp. 579–589, 2007.
- [34] D. K. Peyton, M.-C. Huang, M. A. Giglia, N. K. Hughes, and B. T. Spear, "The alpha-fetoprotein promoter is the target of Afr1-mediated postnatal repression," *Genomics*, vol. 63, no. 2, pp. 173–180, 2000.
- [35] D. Zhao, S. Chen, J. Cai et al., "Derivation and characterization of hepatic progenitor cells from human embryonic stem cells," *PLoS ONE*, vol. 4, no. 7, Article ID e6468, 2009.
- [36] Z. Burke and G. Oliver, "Prox1 is an early specific marker for the developing liver and pancreas in the mammalian foregut endoderm," *Mechanisms of Development*, vol. 118, no. 1-2, pp. 147–155, 2002.

## Research Article

# Modulating the Substrate Stiffness to Manipulate Differentiation of Resident Liver Stem Cells and to Improve the Differentiation State of Hepatocytes

Angela Maria Cozzolino,<sup>1</sup> Valeria Noce,<sup>1</sup> Cecilia Battistelli,<sup>1</sup> Alessandra Marchetti,<sup>1</sup> Germana Grassi,<sup>2</sup> Carla Cicchini,<sup>1</sup> Marco Tripodi,<sup>1,2</sup> and Laura Amicone<sup>1</sup>

<sup>1</sup>Department of Cellular Biotechnologies and Hematology, Section of Molecular Genetics, Sapienza University of Rome, Viale Regina Elena, 324, 00161 Rome, Italy

<sup>2</sup>National Institute for Infectious Diseases L. Spallanzani, IRCCS, Via Portuense 292, 00149 Rome, Italy

Correspondence should be addressed to Marco Tripodi; [tripodi@bce.uniroma1.it](mailto:tripodi@bce.uniroma1.it) and Laura Amicone; [amicone@bce.uniroma1.it](mailto:amicone@bce.uniroma1.it)

Received 28 July 2015; Revised 12 October 2015; Accepted 13 October 2015

Academic Editor: Malin Jonsson

Copyright © 2016 Angela Maria Cozzolino et al. This is an open access article distributed under the Creative Commons Attribution License, which permits unrestricted use, distribution, and reproduction in any medium, provided the original work is properly cited.

In many cell types, several cellular processes, such as differentiation of stem/precursor cells, maintenance of differentiated phenotype, motility, adhesion, growth, and survival, strictly depend on the stiffness of extracellular matrix that, *in vivo*, characterizes their correspondent organ and tissue. In the liver, the stromal rigidity is essential to obtain the correct organ physiology whereas any alteration causes liver cell dysfunctions. The rigidity of the substrate is an element no longer negligible for the cultivation of several cell types, so that many data so far obtained, where cells have been cultured on plastic, could be revised. Regarding liver cells, standard culture conditions lead to the dedifferentiation of primary hepatocytes, transdifferentiation of stellate cells into myofibroblasts, and loss of fenestration of sinusoidal endothelium. Furthermore, standard cultivation of liver stem/precursor cells impedes an efficient execution of the epithelial/hepatocyte differentiation program, leading to the expansion of a cell population expressing only partially liver functions and products. Overcoming these limitations is mandatory for any approach of liver tissue engineering. Here we propose cell lines as *in vitro* models of liver stem cells and hepatocytes and an innovative culture method that takes into account the substrate stiffness to obtain, respectively, a rapid and efficient differentiation process and the maintenance of the fully differentiated phenotype.

## 1. Introduction

The adult stem cell differentiation choices, as well as the maintenance of the differentiated phenotype, depend on many factors including diffusible molecules and cell/cell and cell/matrix interactions. In recent years an increasing importance has been attributed to the elasticity and the stiffness of the extracellular matrix (ECM), which are physical elements characterizing each adult organ and tissue. These parameters are expressed as resistance to deformation or elastic modulus ( $E$ ) and reported in Pascal units ( $\text{Pa} = \text{newtons/m}^2$ ) [1].

The ECM stiffness is particularly relevant in the liver, the physiology and pathology of this organ being strictly correlated to specific modules of elasticity. In general, it is known that a healthy liver has a low ECM elasticity (0.3–6 kPa),

which allows the polarization and the proper functioning of hepatocytes and maintains the quiescence of stellate cells and the optimal fenestration of sinusoidal endothelium. A fibrocirrhotic liver, conversely, is characterized by a significant increase of the matrix elasticity (20 kPa or higher when fibrosis and cirrhosis progress) that, in addition to negatively affecting the microcirculation, can alter the state of differentiation/quiescence of mature liver cells and/or of the stem cell compartment [2]. It has been reported that an increase of liver stiffness may precede the matrix deposition [3], which represents the first response of the organ to several injuries. Therefore, the increase of liver stiffness may also play an important role in the early stages of fibrosis, in addition to characterizing the more advanced disease.

The importance of the substrate elasticity cannot be neglected even in cell cultures. Recently, the impact of the mechanotransduction on many aspects of the behavior of cultured cells has been unveiled. Several cell functions have been proven to be strictly depending on mechanical forces exerted by the extracellular environment, including the execution of the differentiation program, the maintenance of the differentiated phenotype, motility, adhesion, growth, and survival [4, 5]. The effects of an alteration of ECM elasticity on cell behavior are extensive, also affecting the efficiency of DNA uptake [6] (which is particularly important when cells are manipulated for therapeutic approaches or basic research) and the basal transcriptional activity [7].

All these considerations lead to a reassessment of many acquisitions deriving from the studies on cells grown on plastic (with  $E > 1$  GPa), since this culture condition would not allow a proper execution of the mechanosensitive biological processes. One of the most common problems of the traditionally performed cell cultures (for all cell types and, in particular, for hepatocytes) is the loss of the fully differentiated phenotype [8] that could be overcome by more physiological culture conditions. Moreover, with respect to stem/precursor cells, the challenge is to find the optimal conditions for their *in vitro* maintenance and expansion, as well as for their quick and correct differentiation [9]. These elements are particularly important in attempting to use cultured liver cells in protocols of cell therapy and liver tissue engineering.

In the recent years, several methods have been developed to culture mammalian cells in a more physiological and efficient setting and important results have been obtained using natural or synthetic substrates with different  $E$  values.

Gels based on natural ECM components, such as type I collagen, Matrigel, and fibrin, whose stiffness can be modulated by modifying the density of ECM proteins or by chemical crosslinking, allowed impacting tumor growth [10–12] as well as regulating the differentiation and proliferation of normal cells [13].

Recently, to overcome the main limitation of natural ECM (i.e., the limited range of the obtainable stiffness), fully synthetic and covalently cross-linked hydrogels with tunable stiffness have been developed. In a study reported by Pelham Jr. and Wang, polyacrylamide gels of variable stiffness were used for fibroblast cultures [14]. More recently, other synthetic substrates with different  $E$  values have been utilized [15, 16] to study the effects of mechanical stimuli on the growth and differentiation of several cell types.

Here, we propose the optimization of culture conditions of both liver stem cells and differentiated hepatocytes, using the cellular models deriving from murine livers that we had previously established in line livers and widely characterized both *in vitro* and *in vivo*. The Resident Liver Stem Cells (RLSCs) are immortalized stem cells able to spontaneously acquire features of hepatocytes within several weeks of standard culture [17]. A fully differentiated phenotype was obtained when RLSCs were orthotopically inoculated in growing livers, where they correctly integrated the liver architecture, giving rise to both hepatocytes and mesenchymal liver cells [18]. Concerning the lines of immortalized hepatocytes, they were isolated from livers of both transgenic

(MMH/E14) [19] and wild-type (WT/3A) mice [20] and are not tumorigenic, well differentiated, and able to express a wide range of liver functions and products [21–25].

In the attempt to improve the performance of our cells in culture we set up a protocol that, taking into account the stiffness of the substrate, permitted an early and homogeneous differentiation of liver stem cells and, consequently, the analysis, in a restricted time frame, of the molecular events involved. In particular, the use of hydrogels of acrylamide and bisacrylamide with stiffness of 0.4 kPa produced the differentiation of RLSCs into hepatocytes just after 24 hours, whereas higher matrix stiffness (80 kPa) resulted in a substantial maintenance of the fibroblastoid phenotype showing only an initial hepatocyte-specific transcriptional activity. The rapid acquisition of a hepatocyte-like morphology and of a specific gene expression profile on 0.4 kPa hydrogels is correlated with consistent epigenetic modifications on the promoter of the hepatocyte differentiation master gene *HNF4 $\alpha$*  and with the lack of activation of molecular pathways, the latter ones being known to respond to mechanic stimuli and involved in cell growth and stemness. Furthermore, the use of a soft hydrogel also allowed hepatocyte cell lines to assume a full epithelial morphology and to express the repertoire of epithelial genes and hepatic functions more effectively, compared to the traditional culture on plastic.

## 2. Materials and Methods

**2.1. Polyacrylamide Hydrogels.** Polyacrylamide hydrogels with two different stiffness values (0.4 kPa and 80 kPa) were prepared on 25 mm glass coverslips (Menzel-Glaser, Thermo Fisher Scientific Inc., MA, USA) using the method described by Li et al. [26] with small changes. In brief, the glass coverslips were treated for 1 hour with 0.2 M HCl and washed four times with water. The same glass coverslips were treated for 10 minutes with 0.1 M NaOH and washed in water four times. 0.5%<sub>v/v</sub> 3-aminopropyltrimethoxysilane (APTMS 97%; Sigma-Aldrich, St. Louis, MO) was added on glass coverslips for 30 minutes and followed by four water washes. Next, the coverslips were treated with 0.5%<sub>v/v</sub> glutaraldehyde in PBS (glutaraldehyde solution 25%; Sigma-Aldrich, St. Louis, MO) for 1 hour, then washed for 1 hour in water, and air-dried.

In order to obtain hydrogels with 0.4 kPa and 80 kPa, we prepared the following mixture (final concentrations): 3% (for 0.4 kPa) and 16% (for 80 kPa) of Acrylamide (Bio-Rad Laboratories, Inc., Hercules, CA, USA), 0.06% (for 0.4 kPa) and 0.96% (for 80 kPa) of *N,N'*-methylene bisacrylamide (Sigma-Aldrich), 0.1% APS (ammonium persulfate) (Sigma-Aldrich, St. Louis, MO), and 0.1% of *TEMED* (*N,N,N',N'*-tetramethylethylenediamine) (Sigma-Aldrich, St. Louis, MO) in water.

61  $\mu$ L of this mixture was pipetted on a glass previously treated with hydrophobic silicon polymer (Rain-X) and a coverslip of 25 mm (treated as above) was placed upside down onto the gel droplet. After 30 minutes the coverslip was carefully removed and the polymerized gel in adhesion on it was washed twice with 50 mM HEPES pH 8, cross-linked using 0.05% Sulpho-SANPAH Photoreactive Crosslinker (Thermo

Fisher Scientific Inc., MA, USA) in 20 mM HEPES pH 8 under UV<sub>365 nm</sub> light, and then washed twice with 20 mM HEPES pH 8.

A thin layer of collagen I (GIBCO Life Technology, Monza, Italy) was placed on the hydrogels as follows: 1 mL of collagen 10 µg/mL (in 20 mM acetic acid) was added to the hydrogel in 35 mm plates. After 1 hour of incubation at room temperature the solution was aspirated and the hydrogels were rinsed three times with 1x PBS to remove the acid and cross-linked under UV<sub>365 nm</sub> light. The hydrogels were then washed once with cold water and blocked with 1% ethanolamine (Sigma-Aldrich, St. Louis, MO) in 50 mM HEPES pH 8 for 30 minutes at 4°C. Finally, gels were sterilized under UV light and incubated with serum-free culture media (Dulbecco's Modified Eagle's Medium and RPMI 1640; GIBCO Life Technology, Monza, Italy).

**2.2. Cell Cultures.** RLSCs [17] were grown in DMEM (Dulbecco's Modified Eagle's Medium) (GIBCO Life Technology, Monza, Italy) with 10% FBS (Sigma Aldrich, St. Louis, MO), 2 mM L-glutamine (Sigma-Aldrich, St. Louis, MO), and antibiotics on collagen I (GIBCO Life Technology, Monza, Italy) coated dishes (BD Falcon, Franklin Lakes, NJ, USA) and on 0.4 kPa and 80 kPa hydrogels obtained as described above. Nontumorigenic murine MMH/E14 and WT/3A hepatocytes [19, 20] were grown in RPMI 1640 with 10% FBS (GIBCO Life Technology, Monza, Italy), 50 ng/mL EGF, 30 ng/mL IGF II (PeproTech Inc., Rocky Hill, NJ, USA), 10 µg/mL insulin (Roche, Mannheim, Germany), and antibiotics, on collagen I (GIBCO Life Technology, Monza, Italy) coated dishes (BD Falcon, Franklin Lakes, NJ, USA) and on 0.4 kPa and 80 kPa hydrogels obtained as described above. 200,000 cells were seeded on each 25 mm coverslip with hydrogel. The morphological analysis was performed by phase-contrast microscopy.

**2.3. Immunofluorescence.** Cells were fixed with 4% paraformaldehyde, permeabilized with 0.2% Triton-X-100 in phosphate-buffered saline, and incubated over night at 4°C with the following antibodies: 1:50 goat polyclonal anti-HNF4α (C-19 sc-6556, Santa Cruz Biotechnology, USA), 1:50 mouse monoclonal anti-E-cadherin (610181, BD Biosciences Pharmingen, USA), 1:400 rabbit monoclonal anti-Vimentin (2707-1, Eptomics, USA), and 1:50 mouse monoclonal anti-YAP (sc-101199, Santa Cruz Biotechnology, USA). Secondary antibodies are as follows: anti-goat Alexa Fluor 594, anti-mouse Alexa Fluor 488, anti-rabbit Alexa Fluor 488, and anti-mouse Alexa Fluor 594 (all from Molecular Probes, Eugene, OR, USA), diluted to 1:500. The nuclei were stained with DAPI (Molecular Probes D1306). Preparations were examined using Nikon Eclipse E600 fluorescent microscope equipped with a 40x objective and a coolSNAP HQ2 CCD camera (Photometrics). Digital images were processed with Adobe Photoshop 7 software (Adobe Systems, Mountain View, CA).

**2.4. RNA Extraction, Reverse Transcription, and Real-Time Polymerase Chain Reaction (RT-qPCR).** Total RNA was extracted with miRNeasy Mini Kit (Quiagen-GmbH, Hilden, Germany) and reverse-transcribed with iScript cDNA Synthesis Kit (Bio-Rad Laboratories, Inc., Hercules, CA, USA).

cDNA was amplified by RT-qPCR using Mini Opticon Real-Time PCR detection system (Bio-Rad) with GoTaq qPCR Master Mix (Promega, Madison, WI, USA). Relative amounts were obtained with 2<sup>-ΔΔCt</sup> method and normalized to Rpl34.

The list of specific primers is as follows: HNF4α: For 5'-TGCGACTCTCTAAAACCCCTTGCCG-3', Rev 5'-GCC-CATGGTCAACACCTGCACA-3'; Albumin: For 5'-ACAGACCGGAGGGCTTATCT-3', Rev 5'-TGGTGTAGACAGGTCAGGATGT-3'; Ttr (Transthyretin): For 5'-GTC-CTCTGATGGTCAAAGTC-3', Rev 5'-CTCCTTCTACAACTTCTCATCTG-3'; HNF1α: For: 5'-AGACCATGTTGATCACAGAC-3', Rev: 5'-GGGTGGAGATAAAAGTCTCG-3'; Apoc3: For 5'-GGACGCTCCTCACTGTGG-3', Rev 3'-CACGACTCAATAGCTGGAG-3'; E-cadherin (Cdh1): For 5'-CTACTGTTTCTACGGAGGAG-3', Rev 5'-CTCAAA-TCAAAGTCCTGGTC-3'; Snail: For 5'-CCACTGCAACCGTGCTTTT-3', Rev 5'-CACATCCGAGTGGGTTTGG-3'; Vimentin: For 5'-AGCAGTATGAAAGCGTGGCT-3', Rev 5'-CTCCAGGGACTCGTTAGTGC-3'; Cyp2b10: For 5'-CAAAGTCCCGTGGCAACTTC-3', Rev 5'-TCTCCA-TATTTTTCTCGAAGCTGAA-3'; and Rpl34: For 5'-GGA-GCCCCATCCAGACTC-3', Rev 5'-CGCTGGATATGG-CTTTCCTA-3'.

**2.5. Western Blotting.** Cells were lysed in Laemmli buffer 1x (Tris 60 µM pH 6.8, 2% SDS, 10% glycerol, and 5% 2-β mercaptoethanol). Equal volumes of extracts were separated by SDS-PAGE and transferred to nitrocellulose membranes (Millipore, MA, USA). Blots were blocked for 1 hour in 5% nonfat milk (Bio-Rad Laboratories, Inc., Hercules, CA, USA) prepared in TBST 1x and incubated overnight with the following primary antibodies: α-ERK1 (K23; 1:1000) and α-CDK4 (c-22; 1:1000) (Santa Cruz Biotechnology, Inc., CA, USA), phospho-p44/42 MAPK ERK1/2 (4370; 1:1000) (Cell Signalling Technology Boston, USA), and α-Vimentin (Clone V9; 1:1000) (Millipore, MA, USA). Blots were incubated with HRP-conjugated anti-rabbit secondary antibody (Bio-Rad Laboratories, Inc., Hercules, CA, USA). Immunoreactivity was detected by Enhanced Chemiluminescence Reaction (WESTAR NOVA 2011, Cyanagen, Bologna, Italy) following the manufacturer's instructions.

**2.6. Cell Cycle Analysis.** 5 × 10<sup>5</sup> cells were washed with PBS, fixed in 4:1 methanol:acetone, and incubated with RNase A (2 ng/mL) (Sigma-Aldrich, St. Louis, MO) and with propidium iodide (PI) for 30 min at room temperature. The DNA content was evaluated by flow cytometry with a FACS Calibur (BD Biosciences, USA).

**2.7. Chromatin Immunoprecipitation (ChIP) Analysis.** ChIP analysis was performed as previously reported [27] by using 5 µg of the following antibodies: rabbit anti-H3K4me3 (07473), rabbit anti-H3K27me3 (07449), rabbit anti-H3AcK9 (07352), or rabbit IgG as a negative control (12307) (all from Millipore, MA, USA). 5 ng of immunoprecipitated DNA and the relative control were used as templates for RT-qPCR analysis, performed in duplicate. Primers utilized to amplify

the HNF1/6 consensus on HNF4 $\alpha$  promoter are as follows: forward 5'-TCCGAAAGACCCAAGTGTGG-3' and reverse 5'-GCCAATCACGTCCCAGATCA-3'.

**2.8. Urea Production/Secretion Analysis.** Urea production was analysed in 24 h and 48 h culture supernatants of RLSCs, MMH/E14, and WT/3A cultured on plastic and on 0.4 kPa hydrogels. Urea levels were quantified with a colorimetric urea assay kit (Abnova, CA, USA), according to the manufacturer's instructions. Fresh culture medium was used as negative control.

**2.9. Statistical Analysis.** Data are expressed as the mean  $\pm$  standard deviation of mean (SD) of three independent experiments (unless stated otherwise) and Student's *t*-test was used for statistical analyses. All the tests were two-tailed and a *p* value  $< 0.05$  was considered statistically significant (*p* value  $< 0.05 = *$ , *p* value  $< 0.01 = **$ , and *p* value  $< 0.001 = ***$ ).

### 3. Results and Discussion

**3.1. Soft Substrate Promotes a Rapid and Homogeneous Differentiation of RLSCs toward Hepatocytes.** Firstly, we explored the role of substrate stiffness on RLSC self-renewal and differentiation. To this aim, we plated RLSCs on substrate of polyacrylamide gel (hereafter referred to as "gels") with elastic modulus of 0.4 kPa, matching the intrinsic health liver stiffness, and of 80 kPa, corresponding to the stiffness of fibrocirrhotic parenchyma [2]. As control, RLSCs were grown on the high rigidity substrate of polystyrene dishes (stiffness  $> 1$  GPa). All substrates were coated with type I collagen, which has been proven to facilitate adhesion of both stem cells and hepatocytes under the standard culture conditions [17, 19].

Since the cell morphology recapitulates the molecular events controlling specific differentiation programs, we first evaluated the morphological changes of RLSCs grown on substrates with different elasticity. The analysis by phase-contrast optical microscopy has revealed that, just after 24 hours of culture on 0.4 kPa gel, cells underwent homogeneous differentiation acquiring a cuboidal shape, establishing tight cell-cell interactions, and being arranged in well-defined epithelial islands surrounding empty spaces (Figure 1(a)). Differently, cells on 80 kPa matrix, as well as cells cultured on plastic, grew interdispersed, maintaining a fibroblastoid shape.

The immunofluorescence analysis confirmed the alternative programs executed by the cells on different stiffness (Figure 1(b)). RLSCs grown on the low-stiffness matrix expressed, just after 24 hours and consistently, the liver-specific transcriptional factor HNF4 $\alpha$  in the nucleus and the epithelial marker E-cadherin at the membrane (reinforced at 48 hours); at the same time, they lost the expression of the mesenchymal/stem marker Vimentin. Cells cultured on higher stiffness (80 kPa and plastic), instead, did not acquire epithelial/hepatocyte specific markers (only few cells showed a faint HNF4 $\alpha$  expression) and maintained the expression of Vimentin.

We excluded that the change in Vimentin fluorescence signal was due to the different solubility of the protein

when cells grow on surfaces with different stiffness [28], by confirming the immunofluorescence data with a western blot analysis (Figure 1(c)).

A broader analysis of epithelial/hepatocyte and mesenchymal/stemness markers in cells cultured on different stiffness was performed at transcriptional level by RT-qPCR. On a low-stiffness substrate, the epithelial gene E-cadherin (Cdh1) and the hepatocyte-specific genes HNF4 $\alpha$ , HNF1 $\alpha$ , Albumin, Ttr, and Cyp2b10 had been strongly expressed just after 24 hours and further upregulated at 48 hours (Figure 2(a)); two additional experiments are shown in Supplementary Figure 1 and the level expression of Cyp2b10 is reported in Supplementary Figure 2A (Supplementary Material available online at <http://dx.doi.org/10.1155/2016/5481493>). Coherently, the mesenchymal/stem markers Vimentin and Snail were found to be downregulated. On the other hand, the expression of the same genes in cells grown on high-stiffness substrate was only slightly modulated compared to the culture on plastic (Figure 2(a) and Supplementary Figure 1).

Finally, we assessed the differentiation state of RLSCs grown on soft hydrogel evaluating the ability of these cells to synthesize and secrete urea in the culture medium; in fact one of the most important liver functions is the ability to detoxify ammonia transforming this toxic compound into urea.

The levels of urea in supernatants of RLSCs grown on soft hydrogel at 24 and 48 hours were found to be strongly increased compared to the control (RLSCs grown on plastic) (Figure 2(b)).

On the whole, these data reveal that RLSCs already execute an effective program of epithelial/hepatocyte differentiation after 24 hours of culture on a matrix with a low modulus of elasticity and without specific instructive stimuli. Conversely, a hydrogel with high stiffness mostly maintains the RLSC phenotype, delaying the onset of hepatocyte differentiation process.

**3.2. Soft Substrate Impacts on Signaling Pathways of Mechanotransduction Involved in Hepatocyte Differentiation.** The causal link between gel rigidity and differentiation is suggested by early modifications of pathways responsive to extracellular matrix stiffness and involved in stemness/differentiation.

The high ECM stiffness is sensed by the focal adhesions/integrin system and consequently activates ERKs, MAP kinases playing a crucial role in regulating many cell functions, including the maintenance of stemness and the dedifferentiation of mature epithelial cells [29–31]. Starting from this evidence, we explored the ERK1/2 activation state in our experimental conditions by means of the survey of its phosphorylated form. As shown in Figure 3(a), the sustained high ERK1/2 phosphorylation levels, observed in RLSCs grown on stiff gel and in standard conditions, appeared to be dramatically reduced in cells cultured on soft gel just after 3 hours and at least until 24 hours of culture.

In accordance with the acquisition of the differentiated phenotype and with the ERK inactivation, the flow cytometry analysis revealed a significant accumulation in the G1 phase of the cell cycle of RLSCs grown on low stiffness, compared

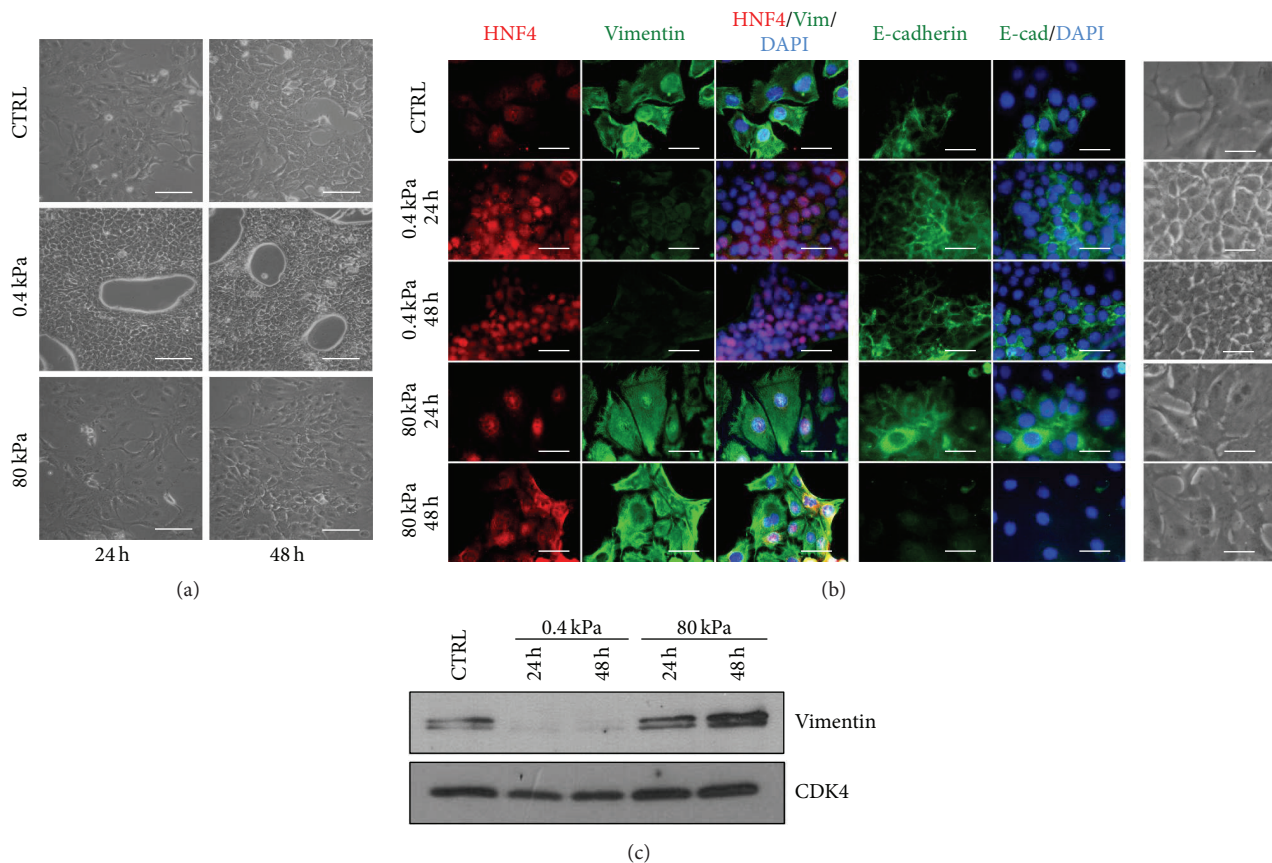


FIGURE 1: Soft substrate induces a rapid and homogeneous epithelial differentiation of RLSCs. (a) Phase-contrast micrographs of RLSCs grown on Petri plastic dish (CTRL;  $E > 1$  GPa) and on hydrogels with  $E = 0.4$  kPa and 80 kPa, for 24 and 48 hours. Images are representative of three independent experiments. Scale bar:  $100 \mu\text{m}$ . (b) Phase-contrast micrographs and immunofluorescence of cells cultured on plastic (CTRL), 0.4 kPa and 80 kPa for 24 and 48 hours, stained for HNF4 $\alpha$ , Vimentin, and E-cadherin. The nuclei were stained with DAPI. Images are representative of three independent experiments. Scale bar:  $50 \mu\text{m}$ . (c) Western blot analysis of Vimentin at 24 and 48 hours after seeding on substrates with the indicated  $E$  values. CDK4 was used as a loading control.

to stiff gel or plastic (Figure 3(b)), together with a reduction of the percentage of cells in S phase.

Recently, the identification of the Yorkie-homologues YAP (Yes-associated protein) and TAZ (transcriptional coactivator with PDZ-binding motif) as nuclear relay of mechanical signals exerted by ECM rigidity and cell shape has been reported [32].

Moreover, several data associated these transcriptional factors with the expression of a large number of stemness genes, establishing a critical role of YAP/TAZ in maintaining stem cell pluripotency [33, 34]. Interestingly, recent important reports attributed a crucial role to these molecules also in the liver cell fate: YAP regulates HNF4 $\alpha$  transcriptional activity during hepatocyte differentiation [35] and its inhibition restores hepatocyte differentiation in advanced HCC [36]. Moreover, an acute inactivation of Hippo pathway signaling *in vivo*, resulting in an elevated YAP activity, has been proven to dedifferentiate adult hepatocytes and to drive liver overgrowth and “oval” cell appearance [37]. Starting from these observations, we analysed the localization of YAP

and, accordingly, we observed a nuclear localization of this factor when RLSCs were cultivated on plastic or on high stiffness (where they maintained a fibroblastoid phenotype), while a clear cytoplasmic localization occurred on soft stiffness (where the cells started their epithelial differentiation program) (Figure 3(c)). Consistently with YAP localization, the strong downregulation of its target gene *Ctgf* [38] was observed in cells cultured on soft gel (Figure 3(d)).

These results correlate the epithelial/hepatocyte differentiation of RLSCs grown on soft substrate with the cytoplasmic localization of YAP and with an inactive ERKs signaling, extending to the liver stem cells what has been observed in other cell systems concerning the role of ECM stiffness in the mechanotransduction and cellular behavior.

**3.3. Soft Substrate Promotes Early Epigenetic Modifications on HNF4 $\alpha$  Promoter.** Starting from recent reports describing new relationships between biophysical microenvironment, mechanotransduction and epigenetic modifications in cell reprogramming [39–41] and aiming at the identification

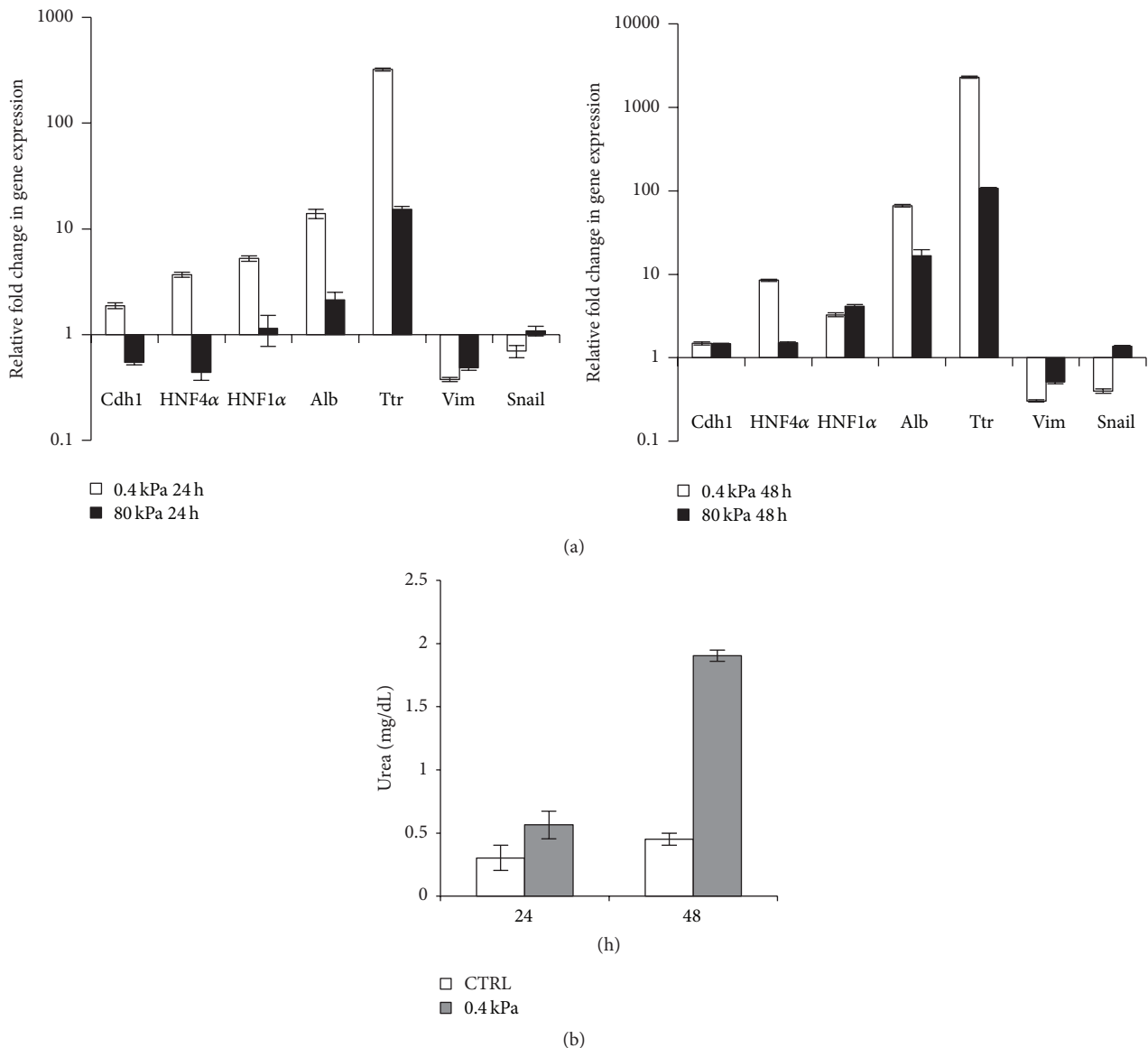
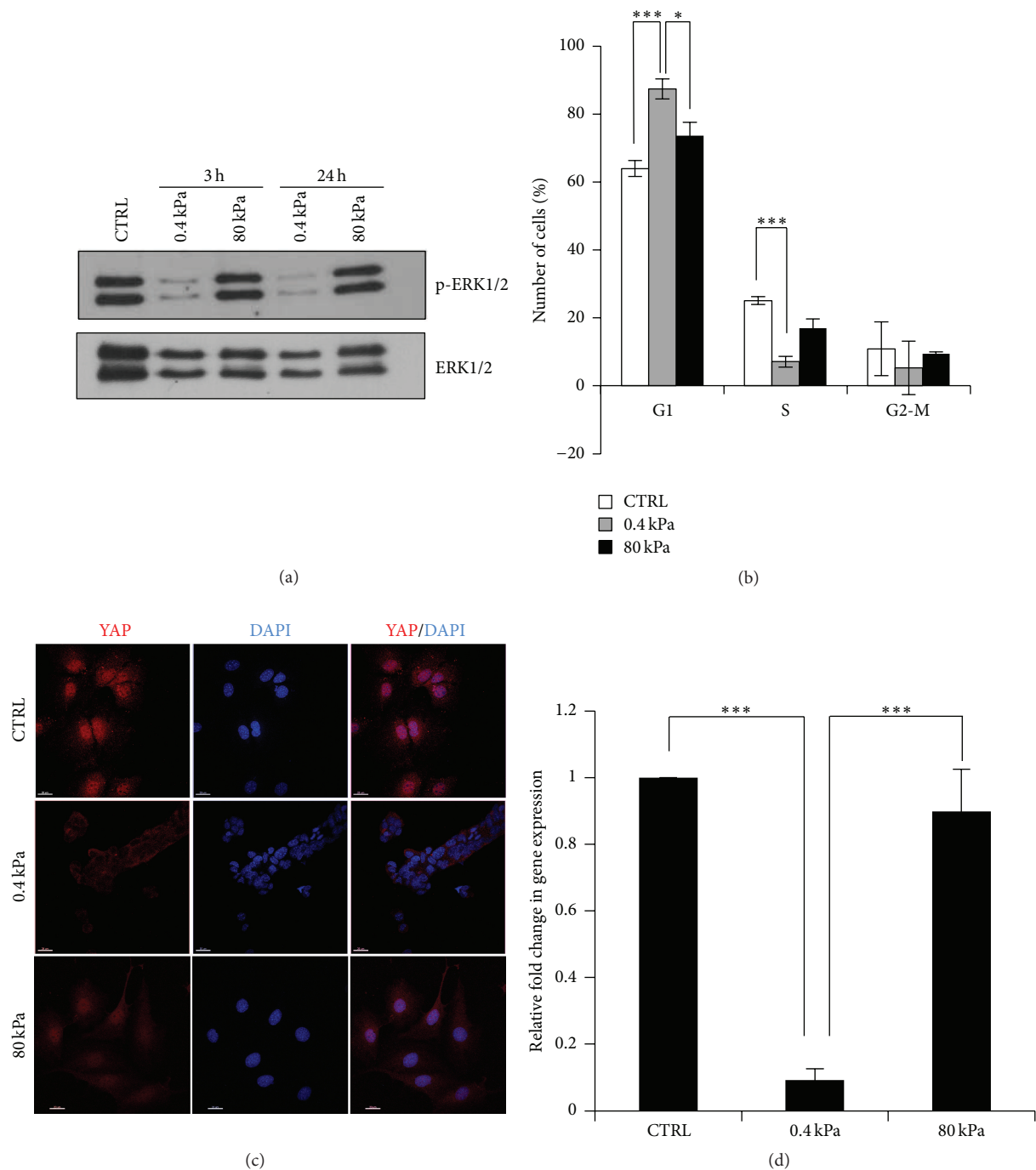


FIGURE 2: RLSCs grown on soft substrate display epithelial/hepatic gene expression and hepatic function. (a) RT-qPCR analysis for the indicated genes of RLSCs grown on 0.4 kPa and 80 kPa at 24 hours (left panel) and 48 hours (right panel). Data are expressed as fold change in gene expression in cells grown on hydrogels versus CTRL (arbitrary value = 1). The graphics are representative of three independent experiments. Note the logarithmic scale. (b) Urea production in RLSCs. Urea levels in supernatant of cells grown on plastic (CTRL) and on 0.4 kPa hydrogel were analysed at 24 and 48 hours. The mean  $\pm$  SD of two independent experiments is shown.

of new molecular tools for monitoring and/or inducing a rapid and efficient hepatocyte differentiation *in vitro*, we explored the stiffness-induced chromatin modifications on the promoter of HNF4 $\alpha$  in our cellular model.

As shown in Figure 4, the activation of the hepatocyte differentiation program in RLSCs is linked to the early epigenetic modifications of HNF4 $\alpha$  promoter. In particular, by ChIP assays, we detected an increase in the level of the acetylation of lysine 9 of histone H3 (H3K9Ac, known to be an activating chromatin modification) at the binding site for the transcriptional activators HNF1 and HNF6 [42], at

48 hours from the cell seeding on soft substrate, compared to cells grown on plastic. At the same site, and even earlier (at 24 hours), we have highlighted the increase of histone H3 Lys4 trimethylation (H3K4me3), a histone modification associated with active transcription. Conversely, in the same region, we observed a significant decrease in the level of histone H3 Lys27 trimethylation (H3K27me3), an epigenetic modification known to be correlated with a transcriptional inhibition. This decrease was also observed at 24 hours after seeding on low stiffness, thus preceding the increase of H3K9Ac level.



**FIGURE 3:** Substrate rigidity controls pathways of mechanotransduction involved in hepatocyte differentiation. (a) Western blot analysis of phospho-ERK1/2 and total ERK1/2 (used as a loading standard) at 3 and 24 hours after seeding on substrates with the indicated  $E$  values. Images are representative of three independent experiments. (b) Flow cytometric analysis of cell cycle in RLSCs cultured at the indicated conditions for 24 hours. The values, obtained from three independent experiments, are reported as mean  $\pm$  SD; \*\*\* $p \leq 0.001$ , \* $p \leq 0.05$ . (c) Immunofluorescence analysis of RLSCs cultured on Petri dish (CTRL), 0.4 kPa and 80 kPa for 12 hours, stained for YAP protein. The nuclei were stained with DAPI. Images are representative of three independent experiments. Scale bar: 20  $\mu$ m. (d) RT-qPCR analysis of the YAP target gene, *Ctgf*. Data are expressed as fold change in gene expression in cells grown on 0.4 kPa and 80 kPa for 24 hours versus CTRL (arbitrary value = 1). The mean  $\pm$  SD of three independent experiments is shown; \*\*\* $p \leq 0.001$ .

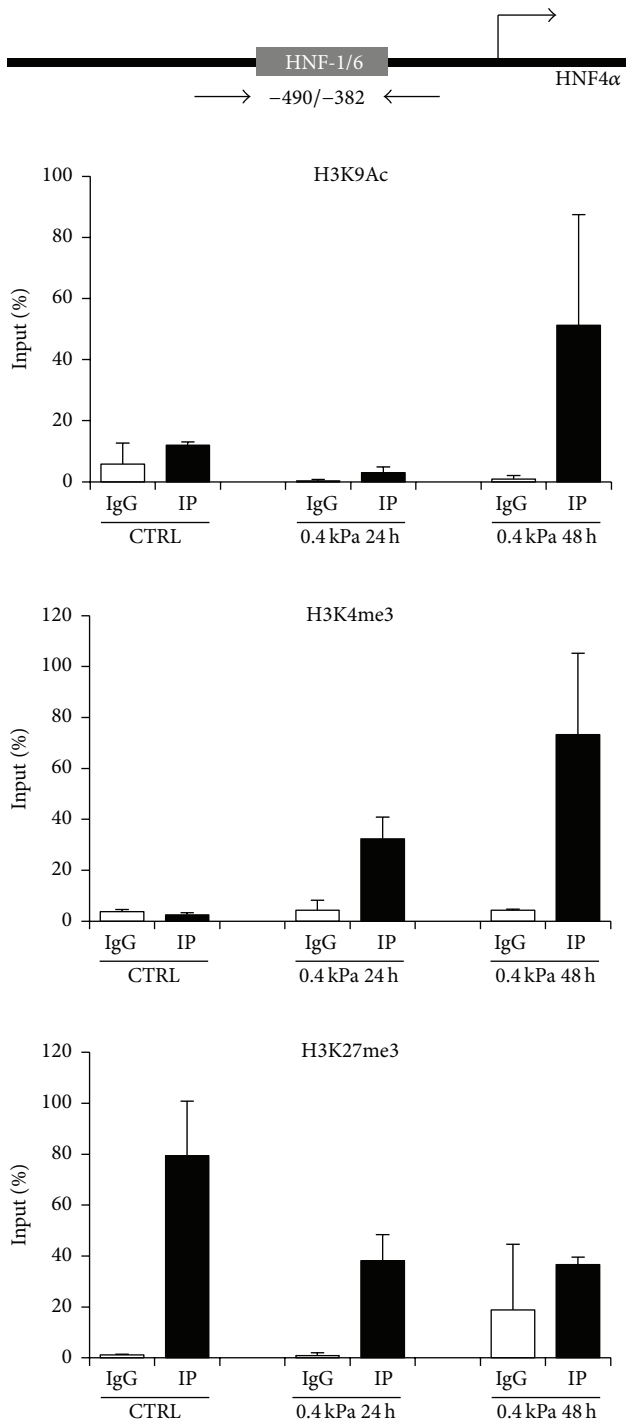


FIGURE 4: Differentiation of RLSCs towards hepatocytes correlates with early chromatin modifications on HNF4 $\alpha$  promoter. qPCR analysis of ChIP assay performed to quantify H3K9Ac, H3K4me3, and H3K27me3, on the HNF1/HNF6 binding site of HNF4 $\alpha$  promoter in RLSCs grown on plastic (CTRL) and on 0.4 kPa hydrogel for 24 and 48 hours. Amplification signals of specific immunoprecipitated samples (IP) and IgG are normalized versus total chromatin (Input) and expressed as % of Input. The mean  $\pm$  SD of two independent experiments is shown. The upper part of the figure shows a schematic representation of murine HNF4 $\alpha$  promoter indicating the binding site for HNF1/HNF6 and the relative positions of the qPCR primers.

These results are in accordance with the early transcriptional activation of HNF4 $\alpha$  observed in soft substrate and confirm that matrix stiffness can impact the epigenetic regulation during stem cell differentiation. Furthermore, the identification of early chromatin modifications involved in differentiation of precursor cells can contribute to the development of new protocols of cell reprogramming and differentiation based on the use of small molecules able to inhibit or activate specific chromatin modifiers, as discussed by Lin and Wu [43].

**3.4. Soft Substrate Efficiently Sustains the Differentiation State of Cultured Hepatocytes.** Obtaining a fully differentiated phenotype of immortalized hepatocytes in culture, together with the maintenance of differentiation of freshly isolated hepatocytes, represents a further challenge for the cellular biologists. It has been largely observed, indeed, that a number of liver-specific functions are progressively lost when hepatocytes are cultivated. These phenotypic modifications are primarily the result of fundamental changes in gene expression concomitant with a decreased transcription of the relevant liver-specific genes and can be interpreted as a “dedifferentiation” of the isolated hepatocytes [8]. To investigate whether soft substrate can sustain or improve the differentiation state of hepatocytes, we utilized hepatocyte cell lines derived both from livers of MMH mice (MMH/E14) [19] and from WT murine livers (WT/3A) [20].

As shown in Figure 5, hepatocytes MMH/E14 (Figure 5(a)) and WT/3A (Figure 5(d)) cultured on 0.4 kPa acquired a more noticeable and homogeneous epithelial phenotype just at 24 hours after seeding; the cells are organized in epithelial islands with the typical cobblestone appearance and delimited sharply bounded empty spaces. Remarkably, hepatocytes showed a significant change in the expression profile of hepatospecific genes that appeared to be strongly upregulated and a significant downregulation of mesenchymal genes that were still expressed in cells cultured on plastic (Figures 5(b) and 5(e); levels of expression of Cyp2b10 are reported in Supplementary Figures 2B and 2C). The detoxification hepatic function was also analysed evaluating the ability of hepatocytes to synthesize and secrete urea. In both MMH/E14 (Figure 5(c)) and WT/3A (Figure 5(f)) cell lines grown on soft hydrogel, the levels of urea production appeared to be increased compared to the control (hepatocytes grown on plastic).

Thus, while a lot of liver functions are lost when hepatocytes are cultivated in standard conditions, a large repertoire of genes for liver products and hepatic functions (e.g., urea production) can be efficiently expressed and maintained when the cells are cultivated on soft extracellular matrix. These results appeared particularly relevant because they could contribute to the improvement of the reliability of liver cell lines and to the promotion of the culture of differentiated hepatocytes, allowing the maintenance of a functional differentiated state.

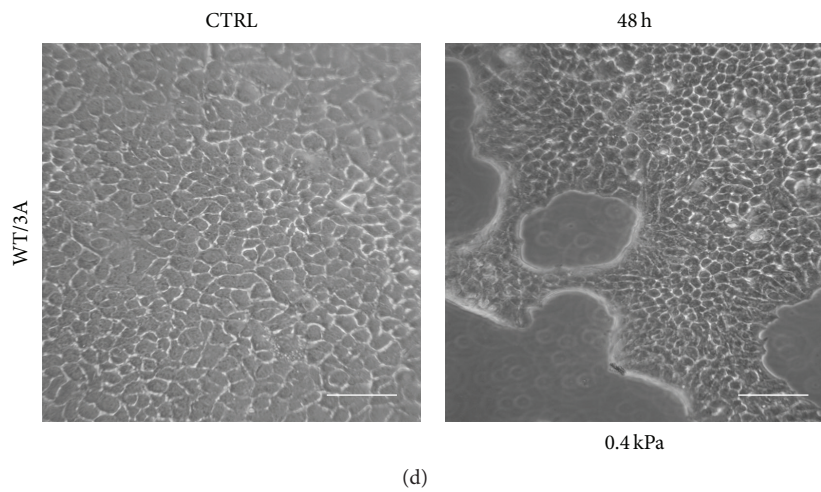
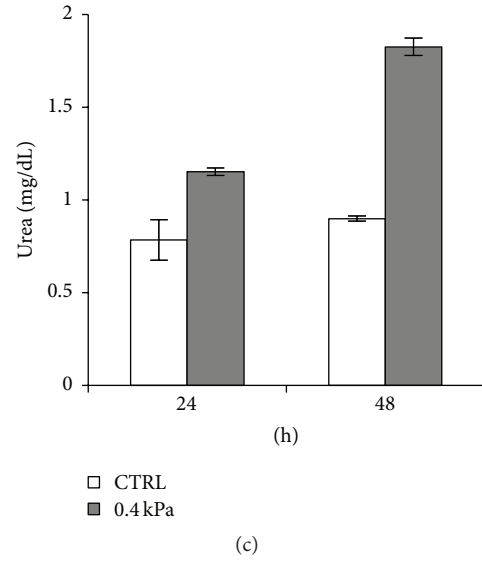
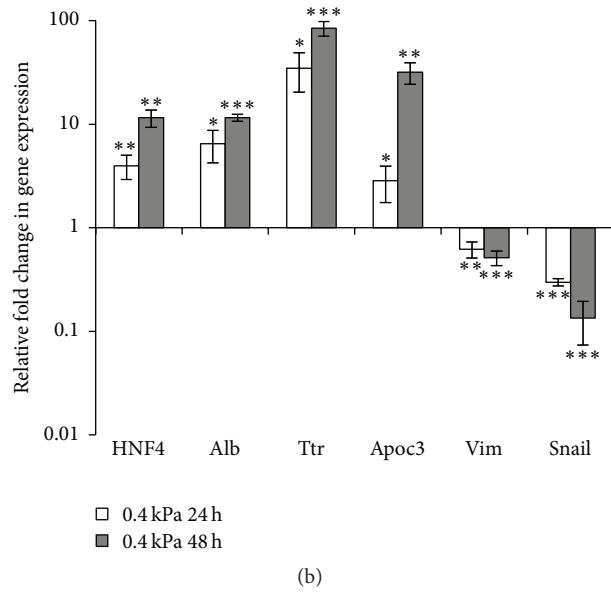
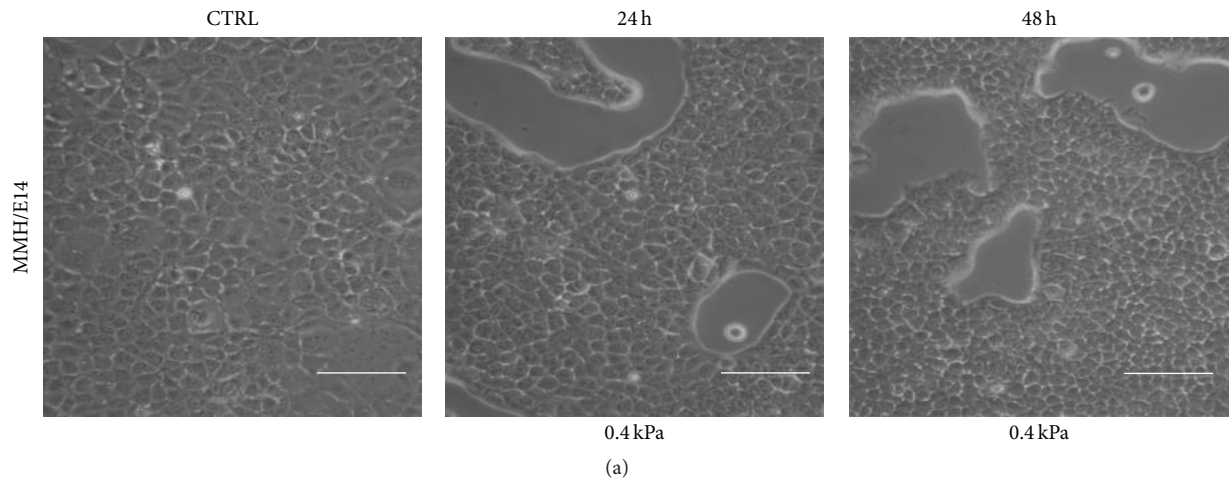


FIGURE 5: Continued.

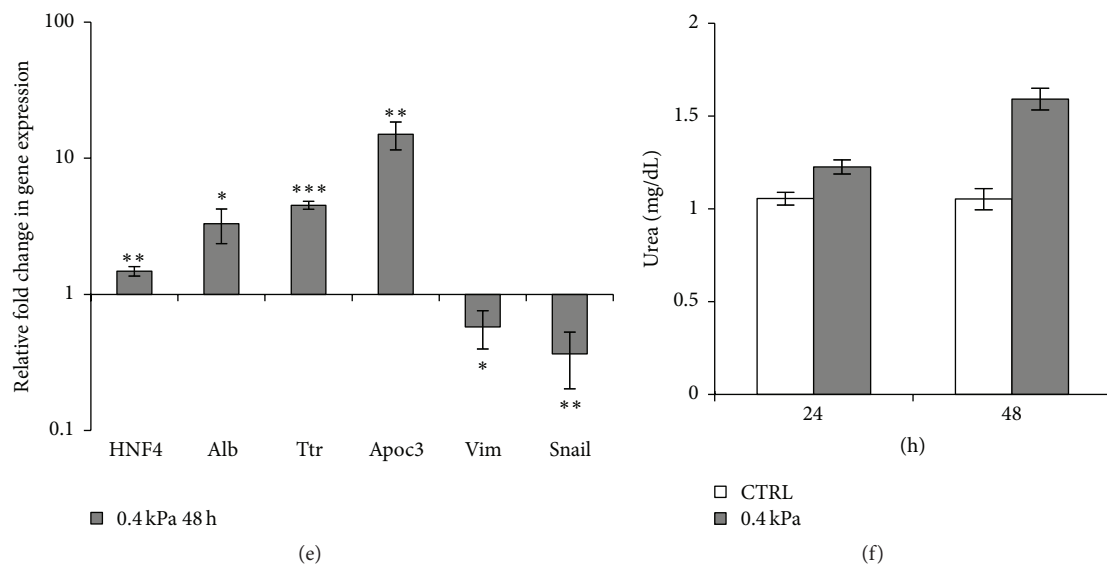


FIGURE 5: Soft substrate improves the differentiation state of hepatocyte cell lines. (a) Phase-contrast micrographs of MMH/E14 hepatocyte cell lines grown on plastic (CTRL) and on 0.4 kPa hydrogel for 24 and 48 hours. Images are representative of three independent experiments. Scale bar: 100  $\mu\text{m}$ . (b) RT-qPCR analysis for the indicated genes. Data are expressed as fold change in gene expression in cells grown on 0.4 kPa versus CTRL (arbitrary value = 1). The graphic represents the mean of three independent experiments  $\pm$  SD. Asterisks indicate  $p$  values in Student's  $t$ -test (\* $p$  < 0.05, \*\* $p$  < 0.01, and \*\*\* $p$  < 0.001). Note the logarithmic scale. (c) Urea production in MMH/E14 hepatocytes. Urea levels in supernatant of cells grown on plastic (CTRL) and on 0.4 kPa hydrogel at 24 and 48 hours were analysed. The mean  $\pm$  SD of two independent experiments is shown. (d) Phase-contrast micrographs of WT/3A hepatocyte cell lines grown on plastic (CTRL) and on 0.4 kPa hydrogel for 48 hours. Images are representative of three independent experiments. Scale bar: 100  $\mu\text{m}$ . (e) RT-qPCR analysis for the indicated genes. Data are expressed as fold change in gene expression in cells grown on 0.4 kPa versus CTRL (arbitrary value = 1). The graphic represents the mean of three independent experiments. \* $p$  < 0.05, \*\* $p$  < 0.01, and \*\*\* $p$  < 0.001. Note the logarithmic scale. (f) Urea production in WT/3A hepatocytes. Urea levels in supernatant of cells grown on plastic (CTRL) and on 0.4 kPa hydrogel at 48 hours were analysed. The mean  $\pm$  SD of two independent experiments is shown.

#### 4. Conclusions

The intent of this work is to contribute to addressing the pressing needs of cell biology to reproduce in culture, as closely as possible, the physiological conditions that, *in vivo*, sustain the biology of each cell type. In particular, we have developed a method for the cultivation of liver cells that takes into account the influence of the rigidity of the substrate. Indeed, it is now clear that the cultivation of cells on substrates whose elasticity is too different from that of the correspondent organ or tissue may alter their gene expression and, consequently, their morphological and molecular phenotype. The use of hydrogels of acrylamide/bisacrylamide with a finely adjustable rigidity has allowed us to study the cells belonging to a soft tissue, such as the liver parenchyma, in a more mechanically physiologic context. Although the polyacrylamide gels may interfere with the adhesion of proteins within the serum or secreted by cells (which might, otherwise, act as adhesive anchors and, consequently, control cell behavior), the comparison between cells grown on the same type of hydrogel but with different stiffness demonstrated the relevance of substrate rigidity in the hepatocyte differentiation process.

Firstly, by manipulating the stiffness of the substrate, we were able to induce a quick and efficient hepatocyte differentiation of stem/precursor cells. This protocol also allowed analysis and identification, in a restricted time frame, of the molecular events involved in the early phase of the differentiation process. The identified molecules could represent useful tools to guide and control the *in vitro* biological processes, such as differentiation and stemness. In fact, although the real involvement of liver resident stem/precursor cells in hepatic regeneration after chronic injury is still debated [44–49], it remains extremely important to handle *in vitro* the differentiation fate of these cells to obtain a source of functional hepatocytes to be used in protocols of cell therapy and tissue engineering.

Moreover, the new culture protocol is useful for inducing/restoring a fully differentiated phenotype of hepatocyte cell lines. This allows giving a new value to the cell lines as models of their counterparts *in vivo*. In fact, given the difficulty in isolating mature hepatic cells from liver explants and maintaining long term cultures of freshly isolated hepatocytes, the improvement of the methods for the cultivation of immortalized cells has become an urgent need. The culture method and the cell lines shown here represent new tools that

can be useful to carry out studies on liver physiology and to realize efficient biological modules of bioartificial livers.

Therefore, the rapid amplification of liver cells (obtainable by standard culture) and their following rapid and efficient differentiation (obtainable by shifting cultivation on soft matrix) could represent an innovative method to culture both progenitor and differentiated liver cell lines.

### Conflict of Interests

The authors declare that there is no conflict of interests regarding the publication of this paper.

### Acknowledgments

The authors thank Claudio Cavallari for technical support. They acknowledge Grant support from Associazione Italiana per la Ricerca sul Cancro (IG 14114), Ministry for Health of Italy (“Ricerca Corrente”), Ministry of University, and Scientific Research of Italy (PRIN 2010LC747T\_003, FIRB RBIN06E9Z8).

### References

- [1] T. R. Cox and J. T. Ertler, “Remodeling and homeostasis of the extracellular matrix: implications for fibrotic diseases and cancer,” *Disease Models and Mechanisms*, vol. 4, no. 2, pp. 165–178, 2011.
- [2] S. Mueller and L. Sandrin, “Liver stiffness: a novel parameter for the diagnosis of liver disease,” *Hepatic Medicine*, vol. 2, pp. 49–67, 2010.
- [3] P. C. Georges, J.-J. Hui, Z. Gombos et al., “Increased stiffness of the rat liver precedes matrix deposition: implications for fibrosis,” *American Journal of Physiology: Gastrointestinal and Liver Physiology*, vol. 293, no. 6, pp. G1147–G1154, 2007.
- [4] D. E. Discher, P. Janmey, and Y.-L. Wang, “Tissue cells feel and respond to the stiffness of their substrate,” *Science*, vol. 310, no. 5751, pp. 1139–1143, 2005.
- [5] C. Jean, P. Gravelle, J.-J. Fournie, and G. Laurent, “Influence of stress on extracellular matrix and integrin biology,” *Oncogene*, vol. 30, no. 24, pp. 2697–2706, 2011.
- [6] H. J. Kong, J. Liu, K. Riddle, T. Matsumoto, K. Leach, and D. J. Mooney, “Non-viral gene delivery regulated by stiffness of cell adhesion substrates,” *Nature Materials*, vol. 4, no. 6, pp. 460–464, 2005.
- [7] A. Mammoto, T. Mammoto, and D. E. Ingber, “Mechanosensitive mechanisms in transcriptional regulation,” *Journal of Cell Science*, vol. 125, no. 13, pp. 3061–3073, 2012.
- [8] J. P. Miranda, S. B. Leite, U. Muller-Vieira, A. Rodrigues, M. J. T. Carrondo, and P. M. Alves, “Towards an extended functional hepatocyte *in vitro* culture,” *Tissue Engineering C: Methods*, vol. 15, no. 2, pp. 157–167, 2009.
- [9] N. R. F. Hannan, C.-P. Segeritz, T. Touboul, and L. Vallier, “Production of hepatocyte-like cells from human pluripotent stem cells,” *Nature Protocols*, vol. 8, no. 2, pp. 430–437, 2013.
- [10] K. R. Levental, H. Yu, L. Kass et al., “Matrix crosslinking forces tumor progression by enhancing integrin signaling,” *Cell*, vol. 139, no. 5, pp. 891–906, 2009.
- [11] M. S. Samuel, J. I. Lopez, E. J. McGhee et al., “Actomyosin-mediated cellular tension drives increased tissue stiffness and beta-catenin activation to induce epidermal hyperplasia and tumor growth,” *Cancer Cell*, vol. 19, no. 6, pp. 776–791, 2011.
- [12] J. Liu, Y. Tan, H. Zhang et al., “Soft fibrin gels promote selection and growth of tumorigenic cells,” *Nature Materials*, vol. 11, no. 8, pp. 734–741, 2012.
- [13] J. Alcaraz, R. Xu, H. Mori et al., “Laminin and biomimetic extracellular elasticity enhance functional differentiation in mammary epithelia,” *The EMBO Journal*, vol. 27, no. 21, pp. 2829–2838, 2008.
- [14] R. J. Pelham Jr. and Y.-L. Wang, “Cell locomotion and focal adhesions are regulated by substrate flexibility,” *Proceedings of the National Academy of Sciences of the United States of America*, vol. 94, no. 25, pp. 13661–13665, 1997.
- [15] C. E. Kadow, P. C. Georges, P. A. Janmey, and K. A. Benigno, “Polyacrylamide hydrogels for cell mechanics: steps toward optimization and alternative uses,” *Methods in Cell Biology*, vol. 83, pp. 29–46, 2007.
- [16] J. R. Tse and A. J. Engler, “UNIT 10.16 Preparation of hydrogel substrates with tunable mechanical properties,” in *Current Protocols in Cell Biology*, chapter 10, John Wiley & Sons, 2010.
- [17] A. Conigliaro, M. Colletti, C. Cicchini et al., “Isolation and characterization of a murine resident liver stem cell,” *Cell Death and Differentiation*, vol. 15, no. 1, pp. 123–133, 2008.
- [18] A. Conigliaro, L. Amicone, V. Costa et al., “Evidence for a common progenitor of epithelial and mesenchymal components of the liver,” *Cell Death and Differentiation*, vol. 20, no. 8, pp. 1116–1123, 2013.
- [19] L. Amicone, F. M. Spagnoli, G. Späth et al., “Transgenic expression in the liver of truncated Met blocks apoptosis and permits immortalization of hepatocytes,” *The EMBO Journal*, vol. 16, no. 3, pp. 495–503, 1997.
- [20] B. Guantario, A. Conigliaro, L. Amicone, Y. Sambuy, and D. Bellovino, “The new murine hepatic 3A cell line responds to stress stimuli by activating an efficient Unfolded Protein Response (UPR),” *Toxicology in Vitro*, vol. 26, no. 1, pp. 7–15, 2012.
- [21] A. Aiuti, C. Cicchini, S. Bernardini et al., “Hematopoietic support and cytokine expression of murine-stable hepatocyte cell lines (MMH),” *Hepatology*, vol. 28, no. 6, pp. 1645–1654, 1998.
- [22] D. Bellovino, Y. Lanyau, I. Garaguso et al., “MMH cells: an *in vitro* model for the study of retinol-binding protein secretion regulated by retinol,” *Journal of Cellular Physiology*, vol. 181, no. 1, pp. 24–32, 1999.
- [23] M. Napolitano, R. Rivabene, M. Avella et al., “Oxidation affects the regulation of hepatic lipid synthesis by chylomicron remnants,” *Free Radical Biology and Medicine*, vol. 30, no. 5, pp. 506–515, 2001.
- [24] V. Bordoni, T. Alonzi, C. Agrati et al., “Murine hepatocyte cell lines promote expansion and differentiation of NK cells from stem cell precursors,” *Hepatology*, vol. 39, no. 6, pp. 1508–1516, 2004.
- [25] M. G. Sacco, L. Amicone, E. M. Catò, D. Filippini, P. Vezzoni, and M. Tripodi, “Cell-based assay for the detection of chemically induced cellular stress by immortalized untransformed transgenic hepatocytes,” *BMC Biotechnology*, vol. 4, article 5, 2004.
- [26] Z. Li, J. A. Dranoff, E. P. Chan, M. Uemura, J. Sévigny, and R. G. Wells, “Transforming growth factor-beta and substrate stiffness regulate portal fibroblast activation in culture,” *Hepatology*, vol. 46, no. 4, pp. 1246–1256, 2007.

- [27] A. Busanello, C. Battistelli, M. Carbone, C. Mostocotto, and R. Maione, "MyoD regulates p57kip2 expression by interacting with a distant cis-element and modifying a higher order chromatin structure," *Nucleic Acids Research*, vol. 40, no. 17, pp. 8266–8275, 2012.
- [28] M. E. Murray, M. G. Mendez, and P. A. Janmey, "Substrate stiffness regulates solubility of cellular vimentin," *Molecular Biology of the Cell*, vol. 25, no. 1, pp. 87–94, 2014.
- [29] P. P. Provenzano, D. R. Inman, K. W. Eliceiri, H. E. Beggs, and P. J. Keely, "Mammary epithelial-specific disruption of focal adhesion kinase retards tumor formation and metastasis in a transgenic mouse model of human breast cancer," *The American Journal of Pathology*, vol. 173, no. 5, pp. 1551–1565, 2008.
- [30] P. P. Provenzano, D. R. Inman, K. W. Eliceiri, and P. J. Keely, "Matrix density-induced mechanoregulation of breast cell phenotype, signaling and gene expression through a FAK-ERK linkage," *Oncogene*, vol. 28, no. 49, pp. 4326–4343, 2009.
- [31] J. Li, G. Wang, C. Wang et al., "MEK/ERK signaling contributes to the maintenance of human embryonic stem cell self-renewal," *Differentiation*, vol. 75, no. 4, pp. 299–307, 2007.
- [32] S. Dupont, L. Morsut, M. Aragona et al., "Role of YAP/TAZ in mechanotransduction," *Nature*, vol. 474, no. 7350, pp. 179–184, 2011.
- [33] H. Qin, K. Blaschke, G. Wei et al., "Transcriptional analysis of pluripotency reveals the hippo pathway as a barrier to reprogramming," *Human Molecular Genetics*, vol. 21, no. 9, Article ID dds023, pp. 2054–2067, 2012.
- [34] T. A. Beyer, A. Weiss, Y. Khomchuk et al., "Switch enhancers interpret TGF- $\beta$  and hippo signaling to control cell fate in human embryonic stem cells," *Cell Reports*, vol. 5, no. 6, pp. 1611–1624, 2013.
- [35] O. Alder, R. Cullum, S. Lee et al., "Hippo signaling influences HNF4A and FOXA2 enhancer switching during hepatocyte differentiation," *Cell Reports*, vol. 9, no. 1, pp. 261–271, 2014.
- [36] J. Fitamant, F. Kottakis, S. Benhamouche et al., "YAP inhibition restores hepatocyte differentiation in advanced HCC, leading to tumor regression," *Cell Reports*, vol. 10, no. 10, pp. 1692–1707, 2015.
- [37] D. Yimlamai, C. Christodoulou, G. G. Galli et al., "Hippo pathway activity influences liver cell fate," *Cell*, vol. 157, no. 6, pp. 1324–1338, 2014.
- [38] B. Zhao, X. Ye, J. Yu et al., "TEAD mediates YAP-dependent gene induction and growth control," *Genes and Development*, vol. 22, no. 14, pp. 1962–1971, 2008.
- [39] T. L. Downing, J. Soto, C. Morez et al., "Biophysical regulation of epigenetic state and cell reprogramming," *Nature Materials*, vol. 12, no. 12, pp. 1154–1162, 2013.
- [40] E. J. Arnsdorf, P. Tummala, A. B. Castillo, F. Zhang, and C. R. Jacobs, "The epigenetic mechanism of mechanically induced osteogenic differentiation," *Journal of Biomechanics*, vol. 43, no. 15, pp. 2881–2886, 2010.
- [41] Z. Tong, A. Solanki, A. Hamilos et al., "Application of biomaterials to advance induced pluripotent stem cell research and therapy," *The EMBO Journal*, vol. 34, no. 8, pp. 987–1008, 2015.
- [42] N. Briançon, A. Bailly, F. Clotman, P. Jacquemin, F. P. Lemaigre, and M. C. Weiss, "Expression of the alpha7 isoform of hepatocyte nuclear factor (HNF) 4 is activated by HNF6/OC-2 and HNF1 and repressed by HNF4alpha1 in the liver," *The Journal of Biological Chemistry*, vol. 279, no. 32, pp. 33398–33408, 2004.
- [43] T. Lin and S. Wu, "Reprogramming with small molecules instead of exogenous transcription factors," *Stem Cells International*, vol. 2015, Article ID 794632, 11 pages, 2015.
- [44] M. B. Herrera, V. Fonsato, S. Bruno et al., "Human liver stem cells improve liver injury in a model of fulminant liver failure," *Hepatology*, vol. 57, no. 1, pp. 311–319, 2013.
- [45] M. B. Herrera, S. Bruno, S. Buttiglieri et al., "Isolation and characterization of a stem cell population from adult human liver," *Stem Cells*, vol. 24, no. 12, pp. 2840–2850, 2006.
- [46] Y. Y. Dan, K. J. Riehle, C. Lazaro et al., "Isolation of multipotent progenitor cells from human fetal liver capable of differentiating into liver and mesenchymal lineages," *Proceedings of the National Academy of Sciences of the United States of America*, vol. 103, no. 26, pp. 9912–9917, 2006.
- [47] C. Duret, S. Gerbal-Chaloin, J. Ramos et al., "Isolation, characterization, and differentiation to hepatocyte-like cells of non-parenchymal epithelial cells from adult human liver," *Stem Cells*, vol. 25, no. 7, pp. 1779–1790, 2007.
- [48] K. Yanger, D. Knigin, Y. Zong et al., "Adult hepatocytes are generated by self-duplication rather than stem cell differentiation," *Cell Stem Cell*, vol. 15, no. 3, pp. 340–349, 2014.
- [49] J. R. Schaub, Y. Malato, C. Gormond, and H. Willenbring, "Evidence against a stem cell origin of new hepatocytes in a common mouse model of chronic liver injury," *Cell Reports*, vol. 8, no. 4, pp. 933–939, 2014.

## Research Article

# PTF1a Activity in Enriched Posterior Foregut Endoderm, but Not Definitive Endoderm, Leads to Enhanced Pancreatic Differentiation in an *In Vitro* Mouse ESC-Based Model

Gopika G. Nair<sup>1,2</sup> and Jon S. Odorico<sup>1</sup>

<sup>1</sup>Division of Transplantation, Department of Surgery, University of Wisconsin-Madison School of Medicine and Public Health, Madison, WI 53792, USA

<sup>2</sup>Diabetes Research Center, University of California-San Francisco, San Francisco, CA 94143, USA

Correspondence should be addressed to Jon S. Odorico; [jon@surgery.wisc.edu](mailto:jon@surgery.wisc.edu)

Received 30 July 2015; Revised 7 November 2015; Accepted 26 November 2015

Academic Editor: Bruno Becker

Copyright © 2016 G. G. Nair and J. S. Odorico. This is an open access article distributed under the Creative Commons Attribution License, which permits unrestricted use, distribution, and reproduction in any medium, provided the original work is properly cited.

Transcription factors are tools repetitively used by the embryo to generate a variety of lineages. Hence, their context of activation is an important determinant of their ability to specifically trigger certain cell fates, but not others. The context is also consequential when considering directing differentiation of embryonic stem cells (ESCs). In this study, we sought to assess the context of pancreatic transcription factor 1a (PTF1a) activation in reference to its propancreatic effects in mouse ESCs (mESCs). We hypothesized that an enriched endodermal population would respond to PTF1a and trigger the pancreatic program more effectively than a spontaneously differentiated population. Using an *in vitro* model of pancreas development that we recently established, we found that inducing PTF1a in highly enriched definitive endoderm did not promote pancreatic differentiation but induction in more differentiated endoderm, specifically posterior foregut endoderm, did form pancreatic progenitors. These progenitors never underwent terminal differentiation to endocrine or acinar phenotype. However, a short 3D culture period, prior to PTF1a induction, led to the generation of monohormonal insulin<sup>+</sup> cells and amylase-expressing cells. Our findings suggest that enriched posterior foregut endoderm is competent to respond to PTF1a's propancreatic activity; but a 3D culture environment is essential for terminal differentiation of pancreatic progenitors.

## 1. Introduction

ESCs hold great potential in regenerative medicine due to their unlimited ability to self-renew and differentiate to a repertoire of lineages and hence have been the focus of many differentiation studies to obtain transplantable cell types. For example, making functional  $\beta$  cells successfully promises a cure for Type 1 Diabetes. Definitive endoderm (DE) is the gastrulation-derived cell population that ultimately gives rise to the respiratory and digestive tract organs, including the pancreas. Therefore, efforts to generate functional  $\beta$  cells involve directed differentiation of ESCs to DE followed by stepwise differentiation to pancreatic cells, inspired by processes from normal pancreatic development.

Several studies have used TGF- $\beta$  family molecules such as Activin A, Nodal, and BMP4 [1–6] or small molecules

[7, 8] that mimic endogenous nodal signaling to specify endodermal fate in mouse and human ESCs. Transcription factors that are activated by Nodal signaling include Mix-like homeodomain proteins, Gata zinc finger factors, Sox HMG domain proteins, and Fox forkhead factors [9]. Many genes expressed in DE are also expressed in mesoderm, neuroectoderm, and extraembryonic endoderm (EE). For example, *Foxa2* is expressed in both DE and mesoderm; *Sox 17* is expressed in DE and EE, and hence there is no single marker to identify DE. Nonetheless, the DE population is marked by the coexpression of FOXA2 [10] and SOX17 [11] though individually both of these markers are not specific for DE. Due to heterogeneity in ESC differentiation cultures, the presence of DE markers and the absence of markers of nontarget cell types are used to determine DE-enriched populations. Further differentiation of DE to pancreatic cell

types has been reported using a cocktail of growth factors, including FGF10, FGF7, and RA, and inhibitors of key signaling pathways, including Noggin, KAAD-cyclopamine, SANT-1, and Alk5 inhibitor [12–16].

However, current ESC to  $\beta$  cell differentiation protocols are limited by low efficiency and generation of immature polyhormonal cells as well as a formation of not-so-robust glucose responsive cells [12, 17–21]. This leads us to believe that some important transcriptional events that are necessary for proper pancreatic development are missing. PTF1a, a critical determinant of pancreatic fate, is not rigorously expressed/is lacking in many of the published differentiation protocols [12, 13, 18, 20, 22]. The significance of the role of PTF1a in committing foregut endodermal cells to pancreatic lineage was elucidated by acquisition of a duodenal fate by pancreatic progenitors that lacked PTF1a in murine transgenic lineage tracing systems [23]. We have previously shown that ectopic expression of PTF1a in mouse ESCs can be used to model pancreas development *in vitro* and results in the generation of monohormonal endocrine cells embedded in exocrine tissue [24]. However, the correct context of PTF1a signaling that is sufficient to direct differentiation to the pancreatic lineage has not been investigated in ESCs until now, and it would be of interest to test if PTF1a signaling can overcome the deficiencies in the current methods of differentiation. In this study, we addressed this question using our *in vitro* model of pancreas development, wherein PTF1a was induced in populations of cells exclusively differentiated to DE or its derivatives.

## 2. Materials and Methods

**2.1. Cell Lines.** The generation and characterization of *Tet-Ptfla* line that was used in this study are described in [24].

**2.2. mESC Maintenance and Differentiation.** *Tet-Ptfla* ESCs were maintained in an undifferentiated state on MEF feeder layers with LIF in DMEM-high glucose with 15% FBS, 100 U penicillin/streptomycin, 2 mM L-glut, 2 mM NEAA, 1 mM Sodium pyruvate, and 0.05 mM  $\beta$ -mercaptoethanol and cultured in differentiation media as previously described [26], with the following modifications. Media compositions of various differentiation protocols that we tested are enumerated in Table 1. Initial cell seeding density is also indicated for every protocol. The growth factors are abbreviated as Activin A (A), BMP4 (B), and bFGF (F) and their respective concentrations are indicated by the numbers that follow in ng/mL. To induce PTF1a expression, cultures were exposed to 1  $\mu$ g/mL doxycycline (Dox) renewed every 24 hrs for 3 or 4 days as indicated for the individual experiments. Cells were seeded on two different ECM substrates, Matrigel and Gelatin, for some of the experiments. Methodology for the protocol in Figure 8: Cells were seeded at a density of 60,000 cells/cm<sup>2</sup> in mESC media containing ROCK Inhibitor (Y-27632) either on Gelatin or on Matrigel. Cells were allowed to attach overnight and DE treatment was started the next day. PTF1a was induced by adding 1  $\mu$ g/mL Dox for 4 days overlapping with the end of primitive foregut endoderm stage (PF) and pancreatic endoderm stage (PE).

Following the PE stage, cultures were further treated with Alk5 inhibitor and Nicotinamide (a maturation factor) for 8 days. The source of the growth factors/inhibitors that were used in these experiments is tabulated in Supplementary Table 3 in Supplementary Material available online at <http://dx.doi.org/10.1155/2016/6939438>.

**2.3. Quantitative Real-Time PCR.** Cells were harvested at various stages by dissolution and homogenization in 0.5 mL of Buffer RLT (Qiagen), and RNA was isolated and purified using Qiagen RNeasy Mini kits. QPCR was performed using Applied Biosystems gene expression assays. Assay IDs are given in Supplementary Table 1. *Gapdh* was used as an internal control and the comparative threshold method was used to quantify transcript abundance.

**2.4. Immunofluorescent Staining.** Immunostaining was performed as previously described by Kahan et al. [27]. The antibodies and dilutions are listed in Supplementary Table 2. Secondary antibodies were 488, 568, and 647 Alexa Fluors of anti-goat, anti-mouse, anti-rabbit raised in either goat or donkey. Cells were counterstained with DAPI to mark nuclei. Coverslips with adherent stained cells were mounted on glass slides with Prolong Gold Antifade reagent (Invitrogen). Images were generated using A1R-Si Nikon Confocal or a Zeiss Axiovert 200M microscope.

Immunofluorescent staining was also used to qualitatively measure expression of key transcription factors during differentiation. Flow cytometry was not compatible in many samples involving 3D structures that were hard to digest to single cells for FACS analysis. Hence, it was decided that costaining and manual counting method would be used to quantify all the samples to maintain consistency. After differentiating mESCs using a multitude of protocols, the cultures were costained for *Foxa2* and *Sox17* at the definitive endoderm stage and for *Pdx1* and *Nkx6.1* at the pancreatic endoderm stage. Single expressing and coexpressing cells were counted for  $N = 3$  biological replicates and tabulated in Table 1. Table 1 also indicates seeding densities, format of culture plates, and presence of clustered or scattered expression of markers.

## 3. Results

**3.1. Cell Seeding Density Has a Significant Effect on Definitive Endoderm Generation.** Our published EB-based differentiation protocol that involves culturing mouse ESCs in suspension as embryoid bodies and plating them in 1% SR results in a heterogeneous culture that has only some cells coexpressing SOX17 and FOXA2, two markers of DE (Supplementary Figure 1) [24]. To explore the question of PTF1a induction in an endoderm context, we pursued generating DE efficiently. Numerous DE-induction protocols were tested using growth factors of the TGF- $\beta$  family, including Nodal, Activin A, and BMP4, and small molecules (Table 1). A universal theme among the various protocols was the impact of cell seeding density on differentiation outcome. Low cell densities promoted DE differentiation irrespective of the protocol or the format of the plate used for cell culture. Adaptation of

TABLE 1: Summary of the experimental procedure and results of several endoderm differentiation protocols that were tested on the *Tet-Pf/la* cells indicating the degree of differentiation to definitive endoderm, Pdx1<sup>+</sup> cells, and Nkx6.1<sup>+</sup> cells.

Protocol	Media	Growth factor conc.	Cell seeding number/culture format	Sox17 <sup>+</sup> Foxa2 <sup>+</sup> cells	PTFla induced/days	Pdx1 <sup>+</sup> cells	Pdx1 <sup>+</sup> cells on prolonged culture
EB in 15% FBS [24]	15% FBS, DMEM for 7 days + 1% SR, DMEM for 2 days	None	3 × 10 <sup>6</sup> cells in 60 mm dish	10%- EB7+2 25%- EB7+4 Not all EBs have co-positive cells	Yes. Sequential/3 d	Begin to see at EB7+7	Yes
Bernardo protocol in monolayer [28]	DMEM (Iscove's modified DM plus Ham's F12 medium at a 1:1 ratio), L-Glut, BSA 5 g/L, lipids lx, 2x ITS, BME lx.	A100B10 for 3 days A100B10 for 3 days + A100 for 2 days	500,000 per 24 well	Very few and cells unhealthy 5% co-positive cells around the edges of colonies	Yes. Sequential/3 days	None 2 clusters (50 cells each)	None None
Low serum	0.5% serum, DMEM, 1% L-glut, 1% penstrep 2% serum, DMEM, 1% L-glut, 1% penstrep	A100B10 for 3 days A100B10 for 3 days + A100 for 2 days A100B10 for 3 days A100B10 for 3 days + A100 for 2 days	500,000 per 24 well	Almost none Few cells but culture looks unhealthy Few cells and culture looks little better 5-8% co-positive cells where density was low	Yes. Sequential/3 days	None None None None	None None None None
Xu protocol w/o Matrigel [17]	DMEM high glucose, 2 g/L BSA, 1% penstrep, 1% L-Glut	A100F100B10 A100F100B50 A100B10 A100B50 A100F100B10 A100F100B50 A100B100 A100B50	300,000 per 24 well 100,000 per 24 well	2-3% 1-2% 1-2% <1% 10% 3-4% 10% 5%	No No No No No No No No	None None None None None None None None	None None None None None None None None
Hansson protocol [5]	KO DMEM + 1x-N2 lx-B27 + 1% L-glut + 1% penstrep + Bme + NEAA for 5 days	A100 A30 A30	1000 per 96 well 5000 per 96 well	50-60% 40-50% 10% 10%	Yes, (a) overlapping (b) sequential/3 d No No	Yes, (a) scattered cells (b) scattered cells Yes, scattered cells	Yes, (a) scattered cells (b) scattered cells Yes, scattered cells
Melton protocol in 96 well [7]	ARPMI + 0.2% FBS + 1% L-glut-penstep	Nodal1000 IDE 800 nM IDE 5 μM Nodal1000 IDE 800 nM IDE 5 μM	1000 per 96 well 5000 per 96 well	>90% 30% High 40-50% >80% >60% 40-50%	Yes, (a) overlapping (b) sequential/3 d No Yes, (a) overlapping (b) sequential/3 d No	(a) No (b) 15 cell clusters with 20-100 cells each (a) and (b) No (a) Scattered cells (b) No (a) No (b) Scattered cells	Did not see Pdx1 <sup>+</sup> cells on prolonged culture

TABLE 1: Continued.

Protocol	Media	Growth factor conc.	Cell seeding number/culture format	Sox17 <sup>+</sup> Foxa2 <sup>+</sup> cells	PTF1a induced/days	Pdx1 <sup>+</sup> cells	Pdx1 <sup>+</sup> cells on prolonged culture
Melton protocol on 24 well	ARPMI + 0.2% FBS + 1% L-glut-penstep	IDE 800 nM	7500 per 24 well 15000 per 24 well	10% 5%	Yes/3 d Yes/3 d	None None	
Melton protocol on 24 well w Matrigel	ARPMI + 0.2% FBS + 1% L-glut-penstep on Matrigel	IDE 800 nM Nodal1000 A100	7500	25% 25% 1%	No No No		
Melton modified (obtained from [7])	Definitive endoderm: Activin A (50 ng/mL) or Nodal (1000 ng/mL) in 0.2% FBS in ARPMI for 4–6 days Primitive gut tube: FGF10 (50 ng/mL), KAAD-cyc (0.25 μM) in 2% FBS in ARPMI for 2 days Pancreatic endoderm: FGF10 (50 ng/mL), KAAD-cyc (0.25 μM), RA (2 μM) in B27 DMEM for 4 days PTF1a induction for 4 days in B27 DMEM or 1% SR for Additional culture for 4 more days in same media		2000 per 96 well fed every other day	Activin ~70%, Nodal: 80–90%. After treatment with further factors, some Pdx1 seen in nodal cultures before PTF1a induction	Yes. Sequential/4 d	Activin A: Yes, scattered Pdx1 <sup>+</sup> cells Nodal-yes, Pdx1 in bud-like clusters.	Did not see Pdx1 on culturing for 4 more days not become insulin <sup>+</sup> even on ra + nic treatment.

Nkx6.1

expression was seen in some of the Pdx1<sup>+</sup> cells but these cells did not become insulin<sup>+</sup> even on ra + nic treatment.

FAB protocol [17], originally devised for hESCs, to mESC differentiation on 24-well plates was more effective in generating DE at an initial cell seeding of 100,000 cells/well versus 300,000 cells/well (corresponding to a cell density of  $\sim 50,000$  cells/cm<sup>2</sup> and  $\sim 150,000$  cells/cm<sup>2</sup>, resp.), as evaluated by *Foxa2*, *T*, and *Sox17* transcripts, and staining for FOXA2 and SOX17 (Table 1). AB10 (Activin 100 ng/mL and BMP4 10 ng/mL) and FAB10 (bFGF 100 ng/mL, Activin 100 ng/mL, and BMP4 10 ng/mL) conditions produced significantly more *Foxa2*, *T*, and *Sox17* transcripts in cultures seeded with 100,000 cells/well than their counterparts seeded with 300,000 cells/well (Figure 1(a)). Similarly, another protocol by Hansson et al. [5] utilizing Activin A in a defined N2B27 medium was more successful in 96-well plates at a lower cell density of 1000 cells/well ( $\sim 3000$  cells/cm<sup>2</sup>) compared with 5000 cells/well (15000 cells/cm<sup>2</sup>). This pattern was, again, observed for two different concentrations of Activin A (Figure 1(b)). Immunofluorescent costaining for FOXA2 and SOX17 was consistent with the transcript profile showing that cultures with low starting cell density formed more DE than high density cultures. Moreover, SOX17<sup>+</sup>FOXA2<sup>+</sup> cells were always observed at the edges of the colonies (Figure 1(c)) possibly suggesting that DE formation requires less cell-cell contact.

**3.2. Inducing PTF1a in Monolayer Endodermal-Derived Cells Generated Pdx1<sup>+</sup>Nkx6.1<sup>+</sup> Pancreatic Progenitors.** Achieving DE differentiation from mESC monolayer cultures has been challenging with low yields and poor cell survival. *Tet-Ptfla* mESCs were subjected to several DE differentiation protocols that were published over the course of several years. Initial protocols that were tested had very low efficiency of forming SOX17<sup>+</sup>FOXA2<sup>+</sup> cells. Subsequent protocols made modifications to the basal media and additives and/or concentration of growth factors and reported improved DE formation [5, 17], and these also led to robust DE generation by the *Tet-Ptfla* cells. The results of these protocols are summarized in Table 1. Treatment with Activin A, Nodal, and IDE1 gave rise to DE as marked by SOX17<sup>+</sup>FOXA2<sup>+</sup> cells (Supplementary Figure 1) and ECADH<sup>+</sup>FOXA2<sup>+</sup> cells and some ECADH<sup>-</sup>FOXA2<sup>+</sup> mesodermal cells (Supplementary Figure 2) at differing frequencies. Nodal was the most effective in converting the majority of cells to DE as indicated by the number of SOX17<sup>+</sup>FOXA2<sup>+</sup> and ECADH<sup>+</sup>FOXA2<sup>+</sup> cells. Ectopic PTF1a expression was induced in DE obtained from many of these protocols to test the hypothesis that PTF1a activity triggers the pancreatic developmental program more efficiently in an endoderm enriched population compared to spontaneously differentiated EB cultures and ultimately leads to enhanced pancreatic differentiation. Pdx1 activation was designated as the first landmark of pancreatic differentiation, in particular pancreas specification of the naïve endoderm. A short PTF1a induction for 3 days (1  $\mu$ g/mL Dox addition), either sequentially following DE generation or overlapping with the last 2 days of DE generation, was performed. PDX1 expression was evaluated shortly after (ranging from 3 to 4 days) PTF1a induction. Scattered Pdx1<sup>+</sup> cells were found in cultures that

were grown using the Hansson protocol [5], whereas nodal-generated DE [7] produced Pdx1<sup>+</sup> bud-like clusters after sequential PTF1a induction (data not shown). However, when these cultures were analyzed a week later, PDX1 expression was absent (results compiled in Table 1). These observations suggested that unpatterned SOX17<sup>+</sup>FOXA2<sup>+</sup> DE population does not have the right cellular context to respond to PTF1a activity.

Hence, we pursued further differentiation of naïve endoderm into primitive gut (PG) and posterior foregut endoderm (PF) (modified Melton protocol) to establish the right cell types before inducing PTF1a. Activin A (50 ng/mL) or Nodal (1000 ng/mL) in low serum media was used to generate endoderm. DE markers, *Sox17* and *Foxa2*, were significantly upregulated in both Activin A- and Nodal-DE compared to control cultures (cells that did not receive growth factors but were cultured in the same base media indicating spontaneous differentiation) (Figure 2(a)). Activin A- and Nodal-DE had more SOX17<sup>+</sup>FOXA2<sup>+</sup> cells than control cultures, and the control cultures also had large numbers of SOX17<sup>-</sup>FOXA2<sup>+</sup> mesodermal cells (Figure 2(b)). As these two transcription factors are also present in extraembryonic endoderm (EE), it is important to determine the expression of *Sox7*, a marker of EE. Notably, *Sox7* expression was reduced in DE cultures. In addition, *Sox1*, a regulator of ectoderm lineage, and *Meox1*, an indicator of mesoderm differentiation, were significantly lower in Activin A- and Nodal-DE than in controls (Figure 2(a)). After subsequent differentiation to PG and PF, cultures were analyzed for markers of PF. There were significantly higher levels of *Hlxb9* and *Hnf6* transcripts in Activin A-PF ( $P < 0.05$  and  $P < 0.001$ , resp.) and Nodal-PF ( $P < 0.01$  and  $P < 0.001$ , resp.) compared to control cultures that did not receive any growth factors. *Hnf4a*, a liver progenitor maker, was downregulated in both Activin A-PF and Nodal-PF cultures indicating that they have been specified to the pancreatic lineage ( $P < 0.01$ ). *HnflB* and *Pdx1* were significantly elevated in the Nodal cultures ( $P < 0.05$ ) (Figure 3(a)). Immunofluorescent staining of Nodal-PF cultures confirms the gene expression profile (Figure 3(b)). PDX1<sup>+</sup> areas, however, were very few and typically appeared as a subset of HNF6<sup>+</sup> domains (Figure 3(b)).

FGF10 is involved in the proliferation of pancreatic progenitors [29, 30] and in the maintenance of PTF1a expression in the dorsal pancreatic bud [31]. Therefore, we treated the Activin A-PF and Nodal-PF with FGF10 during the induction of PTF1a. PTF1a induction in both Activin A-PF and Nodal-PF cultures resulted in many PDX1<sup>+</sup>NKX6.1<sup>+</sup> areas. For example, larger domains of PDX1 expression containing small clusters of NKX6.1<sup>+</sup> cells can be seen (Figure 4(a)). Nkx6.1 is initially expressed in the pancreatic epithelium, but it is a marker of the trunk domain that is poised to become endocrine/duct lineage at later stages. Next, we wanted to investigate whether the formation of pancreatic epithelium was specific to the PTF1a-induced cultures or was caused by FGF10. Nodal-PF cultures that were induced with Dox but not treated with FGF10 also gave rise to PDX1<sup>+</sup>NKX6.1<sup>+</sup> cells, though lower in number than combined treatment (Figure 4(b), top row). More importantly, Nodal-PF cultures treated with FGF10 alone did not produce any NKX6.1<sup>+</sup>

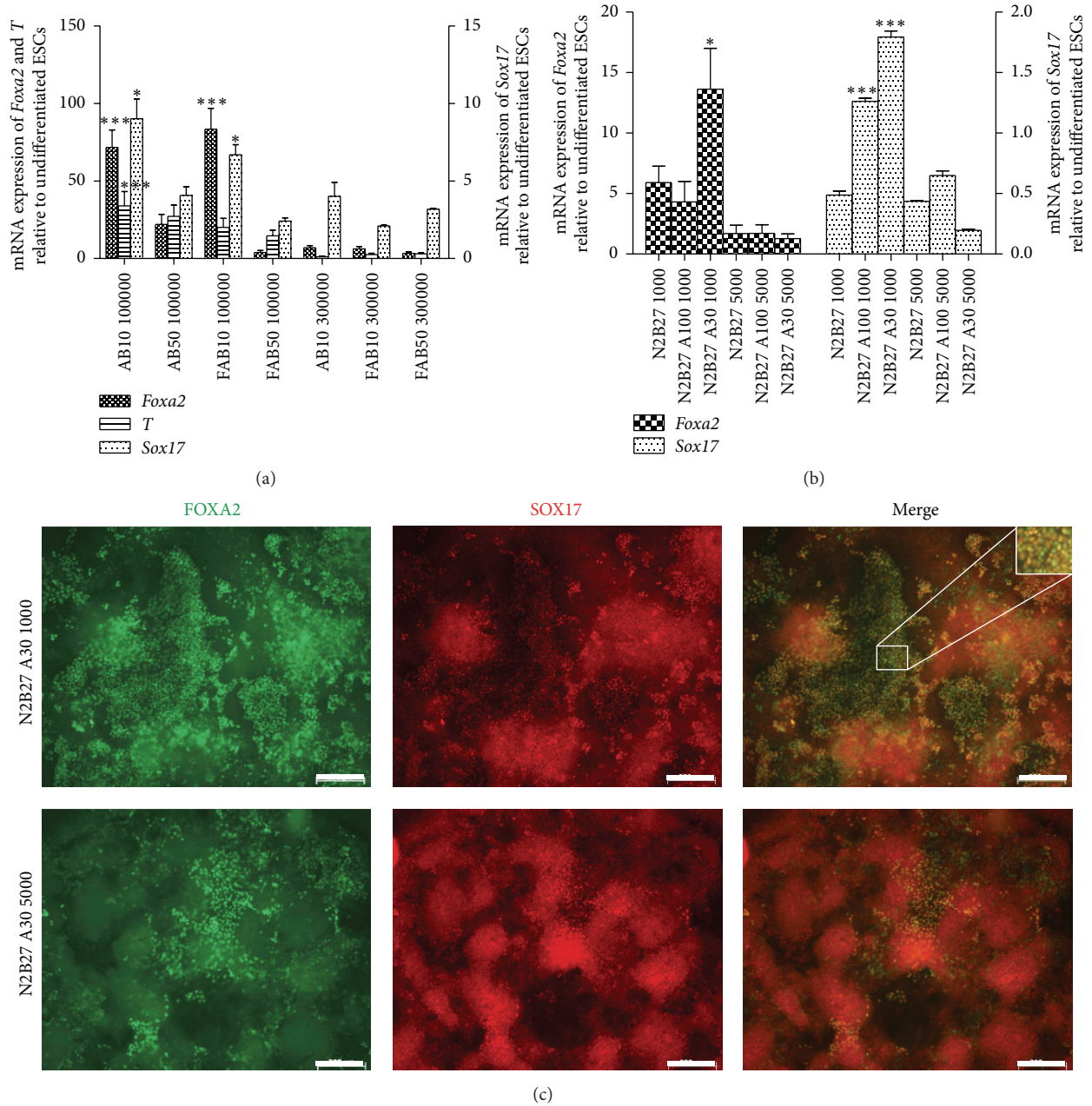


**FIGURE 1:** Cell seeding density influences definitive endoderm generation. (a) Cultures seeded with two different mESC densities (100,000 cells/well or 300,000 cells/well of a 24-well plate) were subjected to a 3-day endoderm differentiation protocol containing 100 ng/mL bFGF, 100 ng/mL Activin A, and 10 ng/mL or 50 ng/mL of BMP4. (b) Cells cultured using another endoderm protocol containing Activin A 100 ng/mL or 30 ng/mL for 5 days in N2B27 but seeded with two starting cell densities (1000 cells/well or 5,000 cells/well of a 96 well plate). Relative mRNA expression of *Sox17*, *T*, and *Foxa2* indicates low densities led to higher expression of DE markers.  $N = 2$ . Data are presented as mean  $\pm$  SEM. Asterisks indicate  $P$  values on comparison with corresponding high density cultures: \* $P < 0.05$ , \*\* $P < 0.01$ , and \*\*\* $P < 0.001$  determined by one-way ANOVA with Tukey's multiple comparison test. (c) Immunofluorescent costaining for FOXA2 and SOX17 confirms that cultures that started with low cell density (N2B27 A30 1000) had higher numbers of FOXA2<sup>+</sup>SOX17<sup>+</sup> definitive endoderm than cultures seeded with high density (N2B27 A30 5000). Images at 5x. Higher magnification inset to indicate coexpression at the cellular level. Scale bars, 200  $\mu\text{m}$ .

cells (Figure 4(b), second row). These results suggest that PTF1a induction is important to generate a true pancreatic epithelial progenitor phenotype (PDX1<sup>+</sup>NKX6.1<sup>+</sup>), and that it acts synergistically with FGF10. Above all, it is to be noted that inducing PTF1a in the non-Nodal-PF cultures (i.e.,

not endodermal enriched cultures) resulted in a few small isolated PDX1<sup>+</sup> clusters and wide-spread scattered NKX6.1 expression (Figure 4(b), third row) with the PDX1<sup>+</sup> cells expressing NKX6.1 but with many NKX6.1<sup>+</sup>PDX1<sup>-</sup> cells as well. These NKX6.1<sup>+</sup>PDX1<sup>-</sup> cells are not pancreatic and could

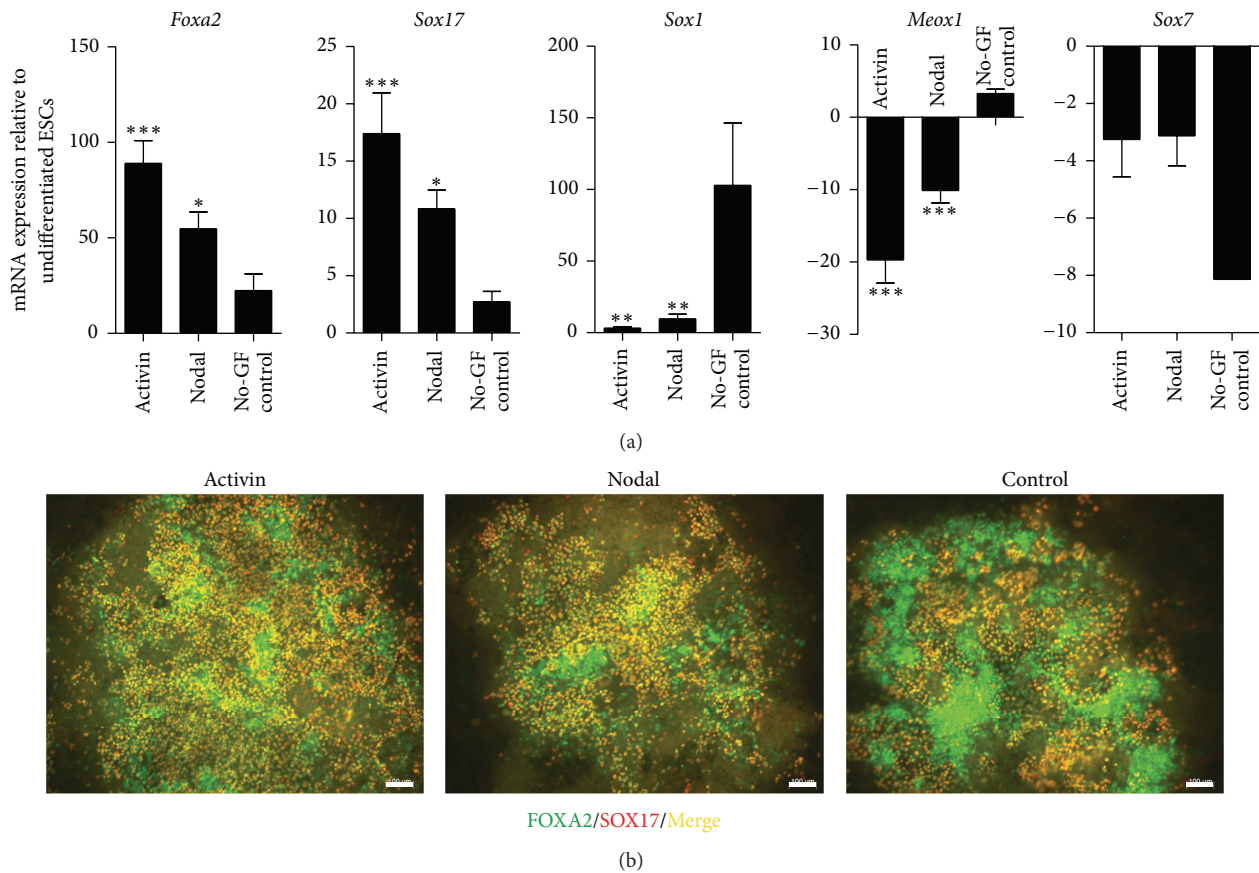


FIGURE 2: Markers of DE are highly expressed in Nodal and Activin A treated cells, whereas markers of other lineages, including ectoderm, mesoderm, and extraembryonic endoderm are repressed. (a) DE markers, *Sox17* and *Foxa2*, are upregulated in contrast to the genes of other germ layers, ectoderm (*Sox1*), mesoderm (*Meox1*), and extraembryonic endoderm (*Sox7*) in Nodal and Activin A treated cultures.  $N = 3$ . Data are presented as mean  $\pm$  SEM. Asterisks indicate  $P$  values on comparison with no-growth factor treated (No-GF) control cultures: \*  $P < 0.05$ , \*\*  $P < 0.01$ , and \*\*\*  $P < 0.001$  determined by one-way ANOVA with Tukey's multiple comparison test. (b) Activin A and Nodal treatment lead to substantial number of FOXA2<sup>+</sup>SOX17<sup>+</sup> cells, whereas the No-GF control cultures generate FOXA2<sup>+</sup>SOX17<sup>-</sup> populations. Scale bars, 100  $\mu$ m.

potentially be of neural lineage, as shown by elevated levels of *Sox1* in control (no growth factor treated) cultures early in differentiation (Figure 2(a)). In other words, PTF1a activity in an endodermal context, specifically in prepatterned posterior foregut endoderm, improves the formation of pancreatic progenitor cells compared to induction in spontaneously differentiated cultures.

**3.3. Differentiation to Adult Pancreatic Cell Types Is Enhanced by 3D Culturing in the DE/PE Stage.** On further differentiation of monolayer cultures of PTF1a-induced Activin A/Nodal-PF, we did not observe a concomitant increase in terminally differentiated pancreatic cell types, including insulin<sup>+</sup>, glucagon<sup>+</sup>, somatostatin<sup>+</sup>, or amylase<sup>+</sup> cells; in fact, only rare insulin<sup>+</sup> cells were found. Monolayer cultures, though homogenous, lack complex morphogenesis and paracrine signaling present in 3D cultures [32, 33] and hence may not be the optimal way to direct differentiation efficiently into adult cell types. While testing monolayer differentiations on two different ECM substrates, Gelatin or Matrigel, using a protocol adapted from Sneddon et al. [25] (Figure 5),

we observed an interesting phenomenon. Floating EB-like subpopulations emerged in both DE and PG stages from Gelatin-coated dishes. These spheres arose only from Gelatin-coated dishes possibly due to differences in integrin signaling mediating cell-ECM interactions on those two substrates. It has been shown that E-cadherin is more stable in cells on Matrigel than on Gelatin resulting in more stable attachment to Matrigel [34]. Serendipitously, the floating spheres were collected, replated, and differentiated as per the protocol till the end stage.

It is to be noted that the two ECMs differed in their propensities to generate DE: cells seeded on Gelatin expressed significantly more *Foxa2* than ones seeded on Matrigel, whereas *Sox17* expression was comparable between the two groups (Supplementary Figure 3). PTF1a was induced for 4 days overlapping with the end of PF stage and the beginning of pancreatic endoderm (PE) differentiation as shown in Figure 5. Cells were further cultured for 8 days in Alk5 inhibitor and Nicotinamide, and terminal differentiation to adult pancreatic cell types was assessed. Transcript profiles of endocrine hormones, namely, *Insulin*, *Gcg* and

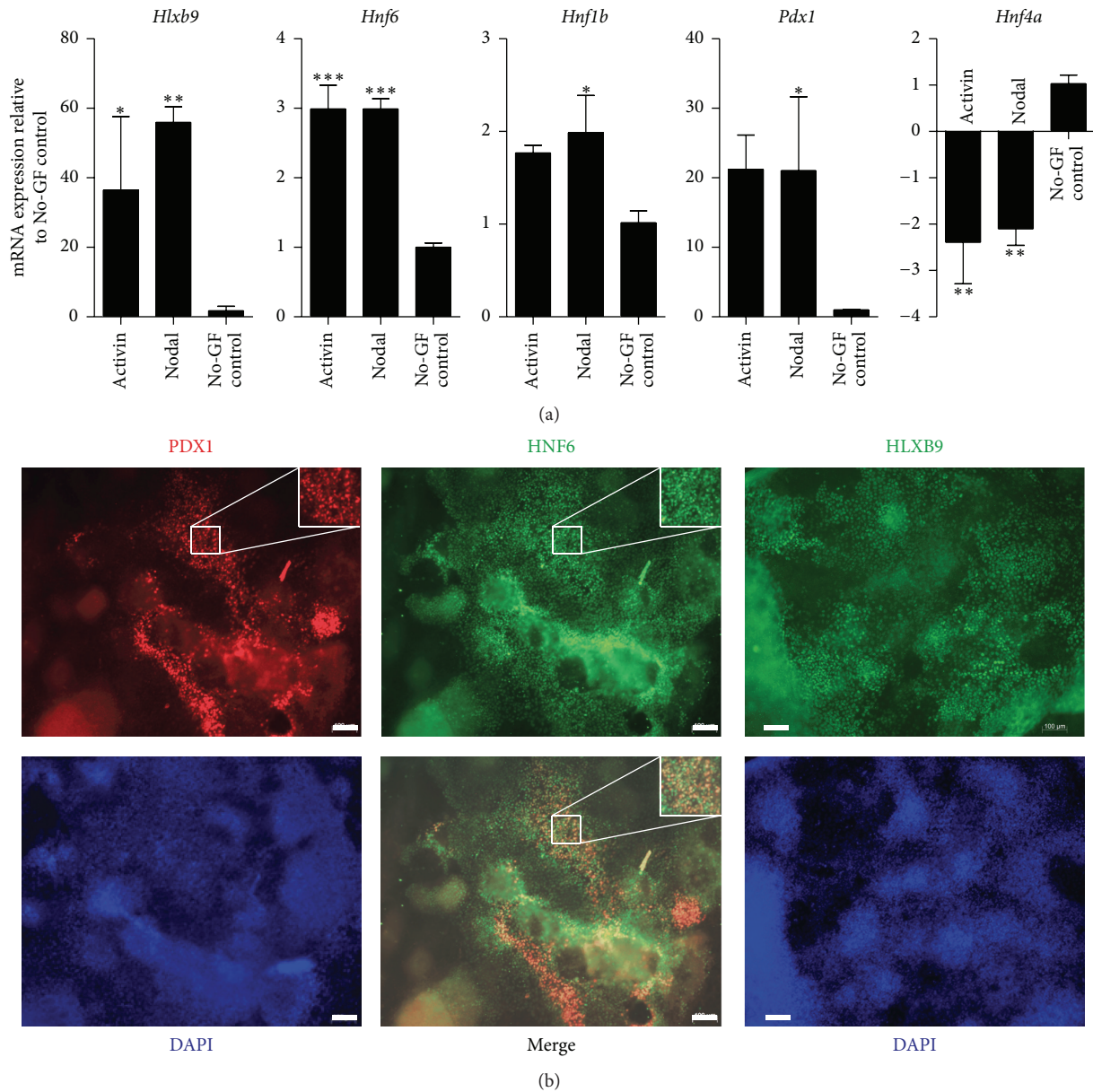


FIGURE 3: Analysis of mESC-derived posterior foregut endoderm. (a) Posterior foregut endoderm markers, *Hlxb9*, *Hnf6*, *Hnf1b*, and *Pdx1*, were significantly higher in Nodal- and Activin-derived cultures than in no growth factor treated (No-GF) control cultures. On the other hand, *Hnf4a* that is expressed in liver progenitors was reduced.  $N = 2-3$ . Data are presented as mean  $\pm$  SEM. Asterisks indicate  $P$  values on comparison with No-GF control cultures: \* $P < 0.05$ , \*\* $P < 0.01$ , and \*\*\* $P < 0.001$  determined by one-way ANOVA with Tukey's multiple comparison test. (b) Immunofluorescent staining of Nodal-derived posterior foregut endoderm cultures indicates the expression of the above-mentioned markers at the single-cell protein level. *Pdx1* is expressed in *Hnf6*-expressing cells. Scale bars, 100  $\mu$ m.

*Sst*, and exocrine digestive enzyme, *Amy2a*, were analyzed in the different cultures. Upon induction of PTF1a, subpopulations that were in suspension (floating) in DE or PG stages (Suspension-DE/Suspension-PG) expressed more endocrine- and exocrine-specific genes than those that were differentiated throughout in adherent cultures (Figure 6). Suspension-DE group had the maximum level of *Insulin*, *Gcg*, and *Amy2a*, whereas Suspension-PE group had maximum *Sst* expression (Figure 6). Cultures that were in suspension for a brief period of time responded better to PTF1a activity and showed enhanced terminal differentiation. Among the

adherent cultures, we found that Gelatin performed better than Matrigel as an ECM substrate in the differentiation of Dox-treated cells as judged by significantly higher expression of *Amy2a*, *Gcg*, *Sst*, and *Insulin*. Matrigel, however, seemed to promote the expression of endocrine transcripts in undifferentiated cultures (Supplementary Figure 4).

In concert with gene expression, staining for amylase- and hormone-expressing cells (antibody cocktail against insulin, glucagon, and somatostatin) also revealed extensive differentiation of PTF1a-induced Suspension-DE/Suspension-PG cultures to both endocrine and acinar lineage (Figure 7,

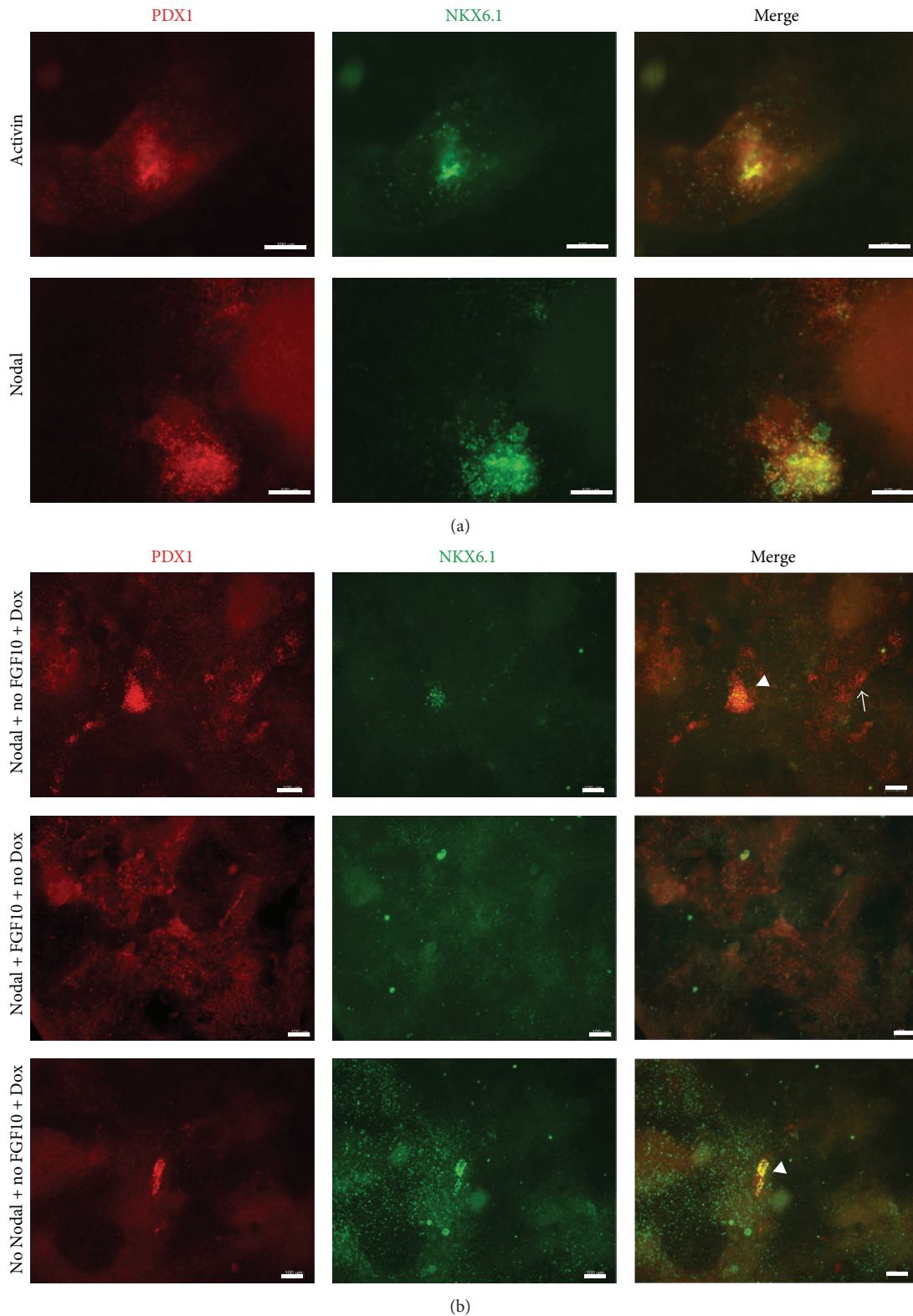


FIGURE 4: PTF1a induction in combination with FGF10 led to the formation of pancreatic epithelial progenitors. (a) Both Nodal and Activin A derived posterior foregut endoderm generated PDX1<sup>+</sup>NKX6.1<sup>+</sup> pancreatic progenitors on induction of PTF1a along with FGF10 treatment. Uninduced cultures did not have any such copositive area (data not shown). (b) Nkx6.1 and Pdx1 copositive pancreatic progenitors were unique to PTF1a induced cultures (top and bottom row). FGF10 was not necessary to generate PDX1<sup>+</sup>NKX6.1<sup>+</sup> population, although it increased the numbers of such progenitors (top row). Notably, FGF10 alone did not produce any NKX6.1<sup>+</sup> cells (middle row), and hence PTF1a induction is essential for the formation of this pancreatic progenitor population. Arrowheads indicate PDX1 and NKX6.1 double positive costained population. Arrows indicate PDX1 single positive cells. Scale bars, 100  $\mu$ m.

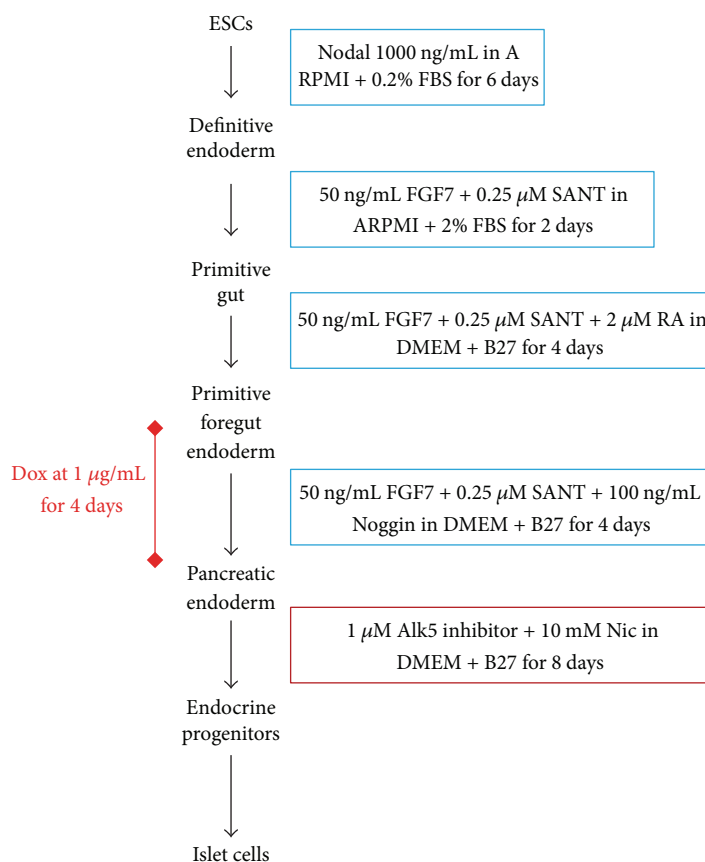


FIGURE 5: Pancreatic differentiation protocol adapted from Sneddon et al. [25]. Cells were seeded at a density of 60,000 cells/cm<sup>2</sup> either on Gelatin or on Matrigel. PTF1a was induced by adding 1 μg/mL Dox for 4 days overlapping with the end of primitive foregut endoderm stage (PF) and pancreatic endoderm stage (PE). Following the PE stage, cultures were further treated with Alk5 inhibitor and Nicotinamide (a maturation factor) for 8 days and analyzed for markers specific to adult pancreatic cell types.

middle and lower rows). Qualitatively, it appeared that the Suspension-DE cultures produced more endocrine and acinar cells than Suspension-PG cultures. High magnification images of Suspension-DE cultures demonstrated that the amylase<sup>+</sup> and the hormone<sup>+</sup> cells were distinct (Figures 8(a) and 8(b)) and that the insulin<sup>+</sup> cells in the cultures do not express glucagon (Figure 8(c)), while most express nuclear PDX1 (Figure 8(d)).

There was another difference in the way the suspension and the adherent cultures were treated. To enable reattachment, the floating EB-like population was plated in 15% FBS overnight and subjected to subsequent steps in the differentiation protocol as usual. Thus, to rule out that transient serum exposure might be the cause for enhanced pancreatic differentiation, a control experiment was performed where the adherent cultures received overnight serum-bolus mimicking the period of attachment of the floaters. mRNA expression analysis from these cultures (adherent DE/PG) did not show comparable expression of *Amy2a*, *insulin*, *Gcg*, or *Sst* transcripts as the cultures that underwent suspension culturing (Supplementary Figure 5) and immunofluorescent staining (data not shown) confirmed these results, suggesting that the physical state of suspension was responsible for the enhanced pancreatic differentiation that we observed.

## 4. Discussion

The pancreas is an organ of endodermal origin, arising from a narrow *Shh* signaling-excluded region in the posterior foregut endoderm. Therefore, the context of expression of key pancreatic transcription factors (PDX1 and PTF1a) involved in pancreas specification is extremely unique and is important for the successful activation of the pancreatic program. Previously we have shown that ectopic expression of PTF1a in EB-based cultures leads to the formation of all pancreatic lineages: endocrine, acinar, and duct cells. In particular, *in vitro* cultures recapitulated major morphological and molecular events that occur during pancreas organogenesis. In these studies, we hypothesized that induction of PTF1a in an enriched endodermal context would lead to better pancreatic differentiation and that PTF1a could potentially be the missing element in the current β cell differentiation protocols that fail to generate monohormonal insulin<sup>+</sup> cells.

To this end, we generated DE using numerous published protocols as illustrated in Table 1. Many of these protocols showed abysmal performance with low efficiency and/or low cell viability. In contrast to the efficient differentiation of hESC to DE in monolayers using high Activin A and low serum supplementation, mESCs have proven to be rather

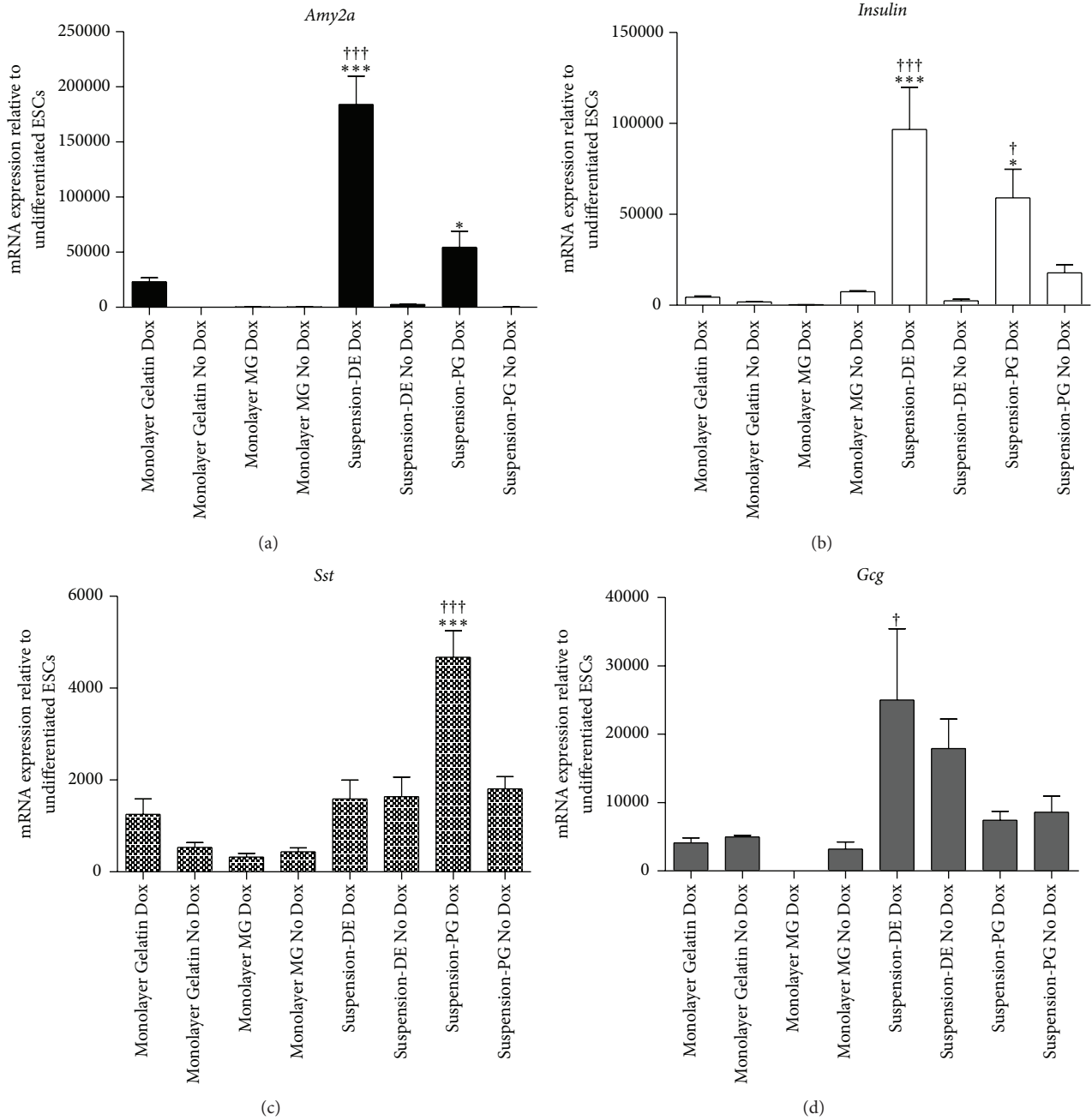


FIGURE 6: A short 3D culture period at the beginning of differentiation promotes PTF1a-induced pancreatic differentiation. Populations that formed EB-like floating bodies either in DE or in PG stage, when replated and subjected to the differentiation protocol, expressed significantly more *Amy2a* (a), *Insulin* (b), *Sst* (c), and *Gcg* (d) transcripts than those cultures grown as monolayers throughout. Growing in suspension also improved endocrine differentiation in general (Suspension-DE No dox and Suspension-PG No dox) indicated by elevated *Insulin*, *Sst*, and *Gcg* transcripts.  $N = 3$ . Data are presented as mean  $\pm$  SEM. Asterisks indicate  $P$  values on comparison with Gelatin-No Dox cultures: \* $P < 0.05$ , \*\*\* $P < 0.001$ , and Obelisks indicate  $P$  values on comparison with Gelatin-Dox cultures: † $P < 0.05$  and ††† $P < 0.001$  determined by one-way ANOVA with Tukey’s multiple comparison test.

difficult [1, 3–5, 16]. During our various trials, we observed a common trend: cell seeding density influenced the success of endoderm generation. Cultures that started with low cell densities differentiated to DE more readily than ones with high densities. Our findings correlate well with similar observations that low cell densities promoted RA-induced PDX1

expression in hESCs in culture [35], where cell-cell contact was found to be inhibitory for pancreatic differentiation. It has also been shown that mESCs grown at high densities have their  $\beta$ -catenin pool localized at the plasma membrane [36] and membrane association of  $\beta$ -catenin with Oct4/E-cadherin is associated with pluripotency [37]. These studies

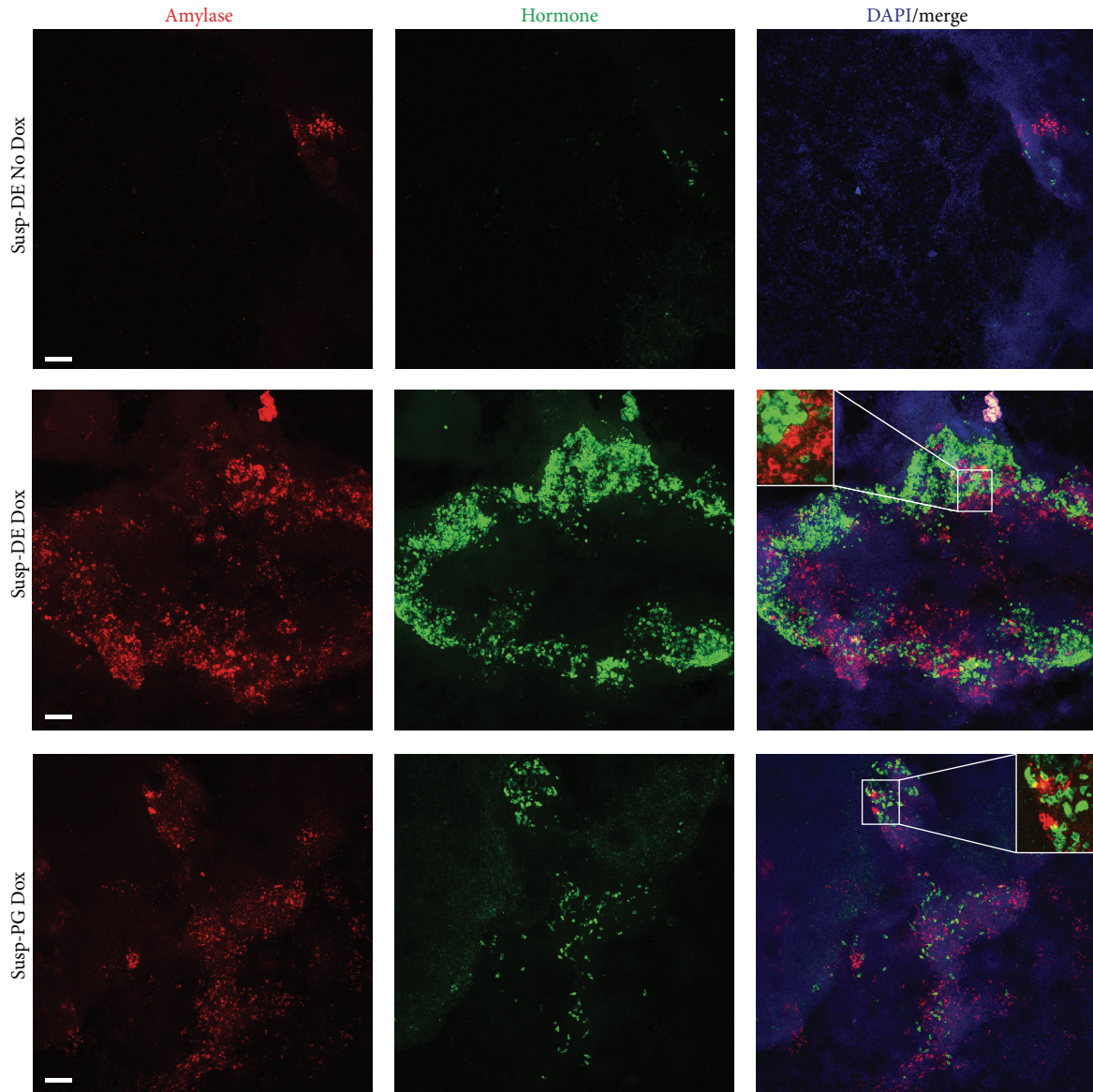


FIGURE 7: Cultures that were in suspension during either DE or PG stage when induced with PTF1a showed enhanced differentiation to pancreatic cell types. Confocal Z-stacks images at low magnification shown along with DAPI to demonstrate the extent of differentiation between conditions. Susp-DE Dox and Susp-PG Dox cultures had large numbers of Amy<sup>+</sup> and Horm<sup>+</sup> cells compared to No Dox cultures and attachment cultures (data not shown). Susp-DE Dox cultures had more Amy<sup>+</sup> and Horm<sup>+</sup> cells than Susp-PG Dox cultures. High magnification insets are shown to indicate cytoplasmic staining of hormones and amylase. Scale bars, 50  $\mu$ m.

imply that high cell densities may even inhibit differentiation in general. On the contrary, recent reports show contradictory outcomes; high densities promoted pancreatic differentiation [38, 39]. Nonetheless, high/low is a relative term: the seeding density in high density cultures (100,000 cells/cm<sup>2</sup>) in the study by Chetty et al. [39] was midway between low and high density cultures in our experiment (Figure 1(a)) and hence suggests a normal relationship (bell-curve) between seeding density versus DE formation.

Induction of PTF1a in naïve monolayer DE (SOX17<sup>+</sup>FOXA2<sup>+</sup>) populations resulted in only rare Pdx1<sup>+</sup>

cell clusters that were more prominent in Nodal-derived than Activin A-derived DE. It has been suggested that Nodal-derived DE is competent for morphogenesis and organ specification, and hence Nodal is a more relevant molecule for ESC differentiation [6]. But these cells never activated the expression of downstream pancreatic genes, indicating that unpatterned endoderm is not a sufficient context for PTF1a activity. Hence, we differentiated the monolayer DE further to PF and then induced the expression of PTF1a. Importantly, inducing PTF1a in the PF population permitted the generation of PDX1<sup>+</sup>NKX6.1<sup>+</sup> pancreatic

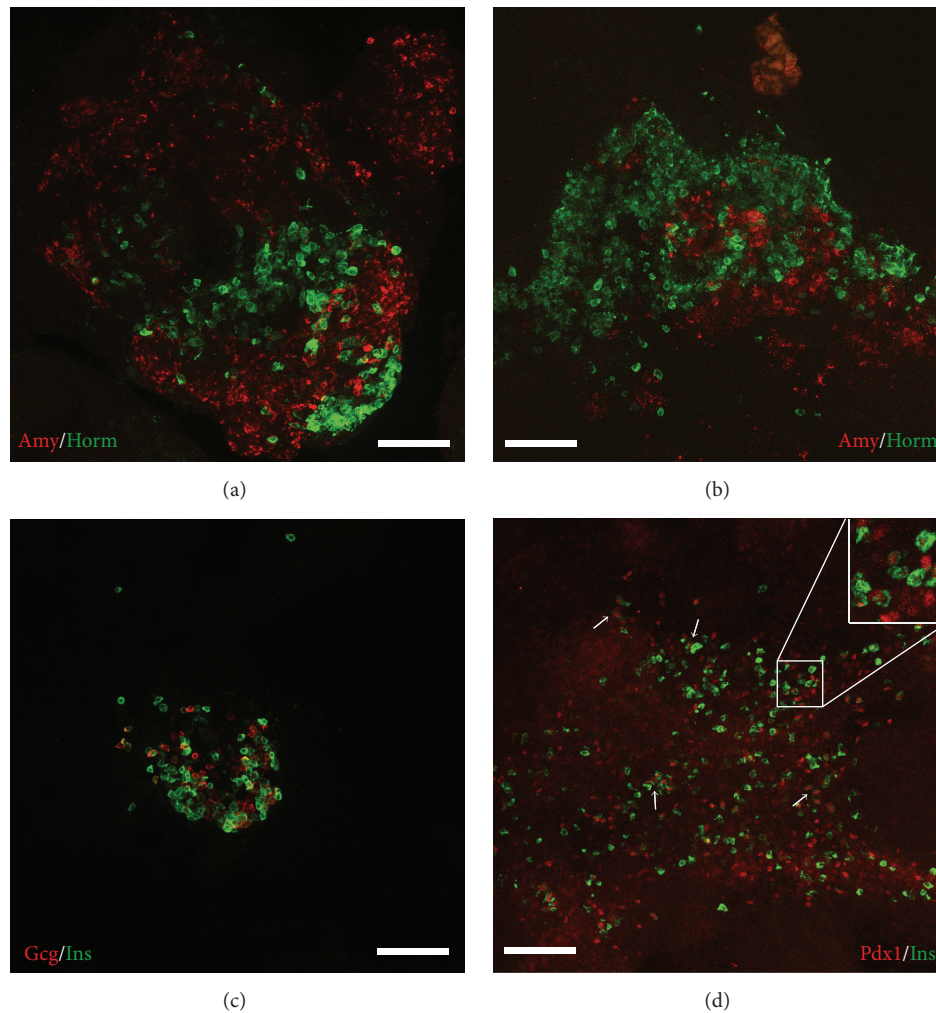


FIGURE 8: High magnification images of Suspension-DE Dox cultures. (a, b) Horm<sup>+</sup> and Amy<sup>+</sup> cells are intermingled with each other. In particular amylase and hormone expression are cytoplasmic and do not overlap. (c) Insulin<sup>+</sup> cells are mostly monohormonal but comingled with glucagon<sup>+</sup> cells. (d) Insulin<sup>+</sup> cells express PDX1 in the nucleus. Inset shows higher magnification to indicate nuclear PDX1 in insulin<sup>+</sup> cells. Arrows point to many insulin<sup>+</sup> cell clusters that have nuclear PDX1. Scale bars, 50  $\mu$ m.

progenitors. FGF10 was found to increase the numbers of PDX1<sup>+</sup>NKX6.1<sup>+</sup> cells synergistically with PTF1a activity, and FGF10 alone produced isolated PDX1<sup>+</sup> cells that did not express NKX6.1. Thus, we have demonstrated the necessity of PTF1a expression in the posterior foregut endoderm cells in order to acquire a true pancreatic fate. However, PF-derived PDX1<sup>+</sup>NKX6.1<sup>+</sup> cells in these cultures did not undergo terminal differentiation. This could be attributed to several factors, one of them being the presence of FGF10 as FGF10 has been shown to force progenitor arrest maintaining them in a proliferative state and abolishes terminal differentiation [30, 40].

While differentiating mESCs in monolayers, we observed some cells spontaneously detaching from the plate and forming floating EB-like populations in suspension especially during the DE and PG stages. Collecting, replating, inducing PTF1a, and differentiating these populations led to considerable adult pancreatic cell types in the cultures, including acinar and hormone-expressing cells. Cells that

were in suspension during the DE stage most efficiently generated pancreatic cells. In addition, the insulin<sup>+</sup> cells that were produced expressed nuclear PDX1 and did not coexpress glucagon suggesting that they represent mature  $\beta$  cells. Growing cells in suspension for a short period of time, somehow, enhanced the potential of PTF1a-induced mESCs to progress toward terminal differentiation. 3D aggregates of ESCs or ESC-derived cells possess complex assembly of cellular adhesions, essential for morphogenesis and juxtacrine/paracrine signaling, which are missing in monolayer cultures [32, 33]. Furthermore, additional “inductive” cell type(s) from other germ layers may be generated in 3D cultures that are essential for proper pancreas development. Moreover, EB-based mESC cultures have been differentiated into DE more successfully than monolayer mESCs [2, 41], with maximum DE markers peaking at Day 4. However, EBs also express SHH, an inhibitor of pancreatic fate, from Day 7 [42]. The findings from these studies could be used to explain our results: cells that are in suspension in both

Activin A and in low serum differentiate efficiently to DE and are subsequently plated before SHH induction thereby circumventing pancreatic inhibition. Moreover, the plated EB-derived cells are exposed to SANT-1, a SHH signaling inhibitor, in the PG stage reinforcing the elimination of SHH activity.

## 5. Conclusions

In essence, we have demonstrated that PTF1a activity in an endodermal context, specifically in patterned posterior foregut endoderm, improves the formation of pancreatic progenitor cells in mESCs. Additionally, we found that cell density and ECM substrate affect the output of DE and pancreatic cell types. Above all, PTF1a induction in combination with suspension culture formats significantly enhanced differentiation to all adult pancreatic cell types, including insulin<sup>+</sup> cells that were monohormonal. This study asserts the importance of PTF1a expression in highly enriched endodermal-derived populations to drive the differentiation of ESCs to  $\beta$ -like cells efficiently.

## Abbreviations

1% SR:	1% serum replacement
DE:	Definitive endoderm
ECADH:	E-cadherin
EB:	Embryoid body
FOXA2:	Forkhead box protein A2
mESC:	Mouse embryonic stem cells
NKX6.1:	NK6 homeobox 1
No-GF:	No growth factor treated
PDX1:	Pancreatic and duodenal homeobox 1
PE:	Pancreatic endoderm
PF:	Posterior foregut endoderm
PG:	Primitive gut
PTF1a:	Pancreas specific transcription factor 1a
SOX17:	Sex determining region Y-box17
<i>Tet-Ptfla</i> :	Tetracycline/doxycycline inducible mouse embryonic stem cell line.

## Conflict of Interests

The authors declare that there is no conflict of interests regarding the publication of this paper.

## Authors' Contribution

Gopika G. Nair designed and performed experiments, wrote the paper, and analyzed data. Jon S. Odorico designed the experiments, analyzed data, and wrote and edited the paper.

## Acknowledgments

The authors would like to thank the following individuals for providing access to important reagents: Chris Wright for anti-PDX1 antibody, Ray Macdonald for anti-PTF1a antibody, Samuel Pfaff for anti-HLXB9 antibody, and Michael Kyba for

Ainv15 cell line. The authors would also like to acknowledge the CMN Waisman Core facility for training and use of their AIR-Si Nikon Confocal and FACS Calibur machines. Financial support for this project was provided by the following funding: NIH ARRA DK-78889-1A2, JDRF Research Grant no. 2007-75, ADA Innovative Award, Department of Surgery Surgical Associates Award, Vilas Associate Professorship Award, and ROTRF/JDRF Award no. 71612962.

## References

- [1] K. A. D'Amour, A. D. Agulnick, S. Eliazar, O. G. Kelly, E. Kroon, and E. E. Baetge, "Efficient differentiation of human embryonic stem cells to definitive endoderm," *Nature Biotechnology*, vol. 23, no. 12, pp. 1534–1541, 2005.
- [2] A. Kubo, K. Shinozaki, J. M. Shannon et al., "Development of definitive endoderm from embryonic stem cells in culture," *Development*, vol. 131, no. 7, pp. 1651–1662, 2004.
- [3] S. Tada, T. Era, C. Furusawa et al., "Characterization of mesendoderm: a diverging point of the definitive endoderm and mesoderm in embryonic stem cell differentiation culture," *Development*, vol. 132, no. 19, pp. 4363–4374, 2005.
- [4] M. Yasunaga, S. Tada, S. Torikai-Nishikawa et al., "Induction and monitoring of definitive and visceral endoderm differentiation of mouse ES cells," *Nature Biotechnology*, vol. 23, no. 12, pp. 1542–1550, 2005.
- [5] M. Hansson, D. R. Olesen, J. M. L. Peterslund et al., "A late requirement for Wnt and FGF signaling during activin-induced formation of foregut endoderm from mouse embryonic stem cells," *Developmental Biology*, vol. 330, no. 2, pp. 286–304, 2009.
- [6] A. E. Chen, M. Borowiak, R. I. Sherwood, A. Kweudjeu, and D. A. Melton, "Functional evaluation of ES cell-derived endodermal populations reveals differences between Nodal and Activin A-guided differentiation," *Development*, vol. 140, no. 3, pp. 675–686, 2013.
- [7] M. Borowiak, R. Maehr, S. Chen et al., "Small molecules efficiently direct endodermal differentiation of mouse and human embryonic stem cells," *Cell Stem Cell*, vol. 4, no. 4, pp. 348–358, 2009.
- [8] H. K. Bone, A. S. Nelson, C. E. Goldring, D. Tosh, and M. J. Welham, "A novel chemically directed route for the generation of definitive endoderm from human embryonic stem cells based on inhibition of GSK-3," *Journal of Cell Science*, vol. 124, no. 12, pp. 1992–2000, 2011.
- [9] A. M. Zorn and M. J. Wells, "Molecular basis of vertebrate endoderm development," in *International Review of Cytology*, W. J. Kwang, Ed., pp. 49–111, Academic Press, 2007.
- [10] D. Dufort, L. Schwartz, K. Harpal, and J. Rossant, "The transcription factor HNF3 $\beta$  is required in visceral endoderm for normal primitive streak morphogenesis," *Development*, vol. 125, no. 16, pp. 3015–3025, 1998.
- [11] M. Kanai-Azuma, Y. Kanai, J. M. Gad et al., "Depletion of definitive gut endoderm in Sox17-null mutant mice," *Development*, vol. 129, no. 10, pp. 2367–2379, 2002.
- [12] M. C. Nostro, F. Sarangi, S. Ogawa et al., "Stage-specific signaling through TGF $\beta$  family members and WNT regulates patterning and pancreatic specification of human pluripotent stem cells," *Development*, vol. 138, no. 5, pp. 861–871, 2011.
- [13] A. Rezanian, J. E. Bruin, M. J. Riedel et al., "Maturation of human embryonic stem cell-derived pancreatic progenitors

- into functional islets capable of treating pre-existing diabetes in mice," *Diabetes*, vol. 61, no. 8, pp. 2016–2029, 2012.
- [14] E. Kroon, L. A. Martinson, K. Kadoya et al., "Pancreatic endoderm derived from human embryonic stem cells generates glucose-responsive insulin-secreting cells in vivo," *Nature Biotechnology*, vol. 26, no. 4, pp. 443–452, 2008.
- [15] K. A. D'Amour, A. G. Bang, S. Eliazar et al., "Production of pancreatic hormone-expressing endocrine cells from human embryonic stem cells," *Nature Biotechnology*, vol. 24, no. 11, pp. 1392–1401, 2006.
- [16] Y. Kunisada, N. Tsubooka-Yamazoe, M. Shoji, and M. Hosoya, "Small molecules induce efficient differentiation into insulin-producing cells from human induced pluripotent stem cells," *Stem Cell Research*, vol. 8, no. 2, pp. 274–284, 2012.
- [17] X. Xu, V. L. Browning, and J. S. Odorico, "Activin, BMP and FGF pathways cooperate to promote endoderm and pancreatic lineage cell differentiation from human embryonic stem cells," *Mechanisms of Development*, vol. 128, no. 7, pp. 412–427, 2011.
- [18] H. A. Russ, A. V. Parent, J. J. Ringler et al., "Controlled induction of human pancreatic progenitors produces functional beta-like cells in vitro," *The EMBO Journal*, vol. 34, no. 13, pp. 1759–1772, 2015.
- [19] G. Nair and M. Hebrok, "Islet formation in mice and men: lessons for the generation of functional insulin-producing  $\beta$ -cells from human pluripotent stem cells," *Current Opinion in Genetics & Development*, vol. 32, pp. 171–180, 2015.
- [20] F. W. Pagliuca, J. R. Millman, M. Gürtler et al., "Generation of functional human pancreatic  $\beta$  cells in vitro," *Cell*, vol. 159, no. 2, pp. 428–439, 2014.
- [21] A. Rezanian, J. E. Bruin, P. Arora et al., "Reversal of diabetes with insulin-producing cells derived in vitro from human pluripotent stem cells," *Nature Biotechnology*, vol. 32, no. 11, pp. 1121–1133, 2014.
- [22] O. G. Kelly, M. Y. Chan, L. A. Martinson et al., "Cell-surface markers for the isolation of pancreatic cell types derived from human embryonic stem cells," *Nature Biotechnology*, vol. 29, no. 8, pp. 750–756, 2011.
- [23] Y. Kawaguchi, B. Cooper, M. Gannon, M. Ray, R. J. MacDonald, and C. V. E. Wright, "The role of the transcriptional regulator Ptf1a in converting intestinal to pancreatic progenitors," *Nature Genetics*, vol. 32, no. 1, pp. 128–134, 2002.
- [24] G. G. Nair, R. K. Vincent, and J. S. Odorico, "Ectopic ptf1a expression in murine ESCs potentiates endocrine differentiation and models pancreas development in vitro," *Stem Cells*, vol. 32, no. 5, pp. 1195–1207, 2014.
- [25] J. B. Sneddon, M. Borowiak, and D. A. Melton, "Self-renewal of embryonic-stem-cell-derived progenitors by organ-matched mesenchyme," *Nature*, vol. 491, no. 7426, pp. 765–768, 2012.
- [26] R. Vincent, N. Treff, M. Budde, Z. Kastenberg, and J. Odorico, "Generation and characterization of novel tetracycline-inducible pancreatic transcription factor-expressing murine embryonic stem cell lines," *Stem Cells and Development*, vol. 15, no. 6, pp. 953–962, 2006.
- [27] B. W. Kahan, L. M. Jacobson, D. A. Hullett et al., "Pancreatic precursors and differentiated islet cell types from murine embryonic stem cells," *Diabetes*, vol. 52, no. 8, pp. 2016–2024, 2003.
- [28] A. S. Bernardo, C. H.-H. Cho, S. Mason et al., "Biphasic induction of Pdx1 in mouse and human embryonic stem cells can mimic development of pancreatic  $\beta$ -cells," *STEM CELLS*, vol. 27, no. 2, pp. 341–351, 2009.
- [29] A. Hart, S. Papadopoulou, and H. Edlund, "Fgf10 maintains notch activation, stimulates proliferation, and blocks differentiation of pancreatic epithelial cells," *Developmental Dynamics*, vol. 228, no. 2, pp. 185–193, 2003.
- [30] G. A. Norgaard, J. N. Jensen, and J. Jensen, "FGF10 signaling maintains the pancreatic progenitor cell state revealing a novel role of Notch in organ development," *Developmental Biology*, vol. 264, no. 2, pp. 323–338, 2003.
- [31] P. Jacquemin, H. Yoshitomi, Y. Kashima, G. G. Rousseau, F. P. Lemaigre, and K. S. Zaret, "An endothelial-mesenchymal relay pathway regulates early phases of pancreas development," *Developmental Biology*, vol. 290, no. 1, pp. 189–199, 2006.
- [32] A. M. Bratt-Leal, R. L. Carpenedo, and T. C. McDevitt, "Engineering the embryoid body microenvironment to direct embryonic stem cell differentiation," *Biotechnology Progress*, vol. 25, no. 1, pp. 43–51, 2009.
- [33] D. ten Berge, W. Koole, C. Fuerer, M. Fish, E. Eroglu, and R. Nusse, "Wnt signaling mediates self-organization and axis formation in embryoid bodies," *Cell Stem Cell*, vol. 3, no. 5, pp. 508–518, 2008.
- [34] Y. Xu, X. Zhu, H. S. Hahm et al., "Revealing a core signaling regulatory mechanism for pluripotent stem cell survival and self-renewal by small molecules," *Proceedings of the National Academy of Sciences of the United States of America*, vol. 107, no. 18, pp. 8129–8134, 2010.
- [35] J. Cai, C. Yu, Y. Liu et al., "Generation of homogeneous PDX1+ pancreatic progenitors from human ES cell-derived endoderm cells," *Journal of Molecular Cell Biology*, vol. 2, no. 1, pp. 50–60, 2010.
- [36] J. J. Otero, W. Fu, L. Kan, A. E. Cuadra, and J. A. Kessler, " $\beta$ -Catenin signaling is required for neural differentiation of embryonic stem cells," *Development*, vol. 131, no. 15, pp. 3545–3557, 2004.
- [37] A. M. Arias, F. Faunes, P. Hayward et al., "A membrane-associated  $\beta$ -catenin/Oct4 complex correlates with ground-state pluripotency in mouse embryonic stem cells," *Development*, vol. 140, no. 6, pp. 1171–1183, 2013.
- [38] B. K. Gage, T. D. Webber, and T. J. Kieffer, "Initial cell seeding density influences pancreatic endocrine development during *in vitro* differentiation of human embryonic stem cells," *PLoS ONE*, vol. 8, no. 12, Article ID e82076, 2013.
- [39] S. Chetty, F. W. Pagliuca, C. Honore, A. Kweudjeu, A. Rezanian, and D. A. Melton, "A simple tool to improve pluripotent stem cell differentiation," *Nature Methods*, vol. 10, no. 6, pp. 553–556, 2013.
- [40] S. Kobberup, M. Schmerr, M.-L. Dang et al., "Conditional control of the differentiation competence of pancreatic endocrine and ductal cells by Fgf10," *Mechanisms of Development*, vol. 127, no. 3–4, pp. 220–234, 2010.
- [41] F. Li, Z. He, Y. Li et al., "Combined Activin A/LiCl/Noggin treatment improves production of mouse embryonic stem cell-derived definitive endoderm cells," *Journal of Cellular Biochemistry*, vol. 112, no. 4, pp. 1022–1034, 2011.
- [42] J. K. Mfopou, V. De Groot, X. Xu, H. Heimberg, and L. Bouwens, "Sonic Hedgehog and other soluble factors from differentiating embryoid bodies inhibit pancreas development," *Stem Cells*, vol. 25, no. 5, pp. 1156–1165, 2007.

## Review Article

# The Rise of CRISPR/Cas for Genome Editing in Stem Cells

Bing Shui,<sup>1</sup> Liz Hernandez Matias,<sup>2</sup> Yi Guo,<sup>3,4</sup> and Ying Peng<sup>3</sup>

<sup>1</sup>Department of Biology, Carleton College, Northfield, MN 55057, USA

<sup>2</sup>Department of Biology, University of Puerto Rico, Rio Piedras, San Juan, PR 00931, USA

<sup>3</sup>Department of Biochemistry and Molecular Biology, Mayo Clinic, Rochester, MN 55905, USA

<sup>4</sup>Division of Gastroenterology and Hepatology, Mayo Clinic, Rochester, MN 55905, USA

Correspondence should be addressed to Yi Guo; [guo.yi@mayo.edu](mailto:guo.yi@mayo.edu) and Ying Peng; [peng.ying@mayo.edu](mailto:peng.ying@mayo.edu)

Received 3 August 2015; Revised 3 November 2015; Accepted 5 November 2015

Academic Editor: Jane Synnergren

Copyright © 2016 Bing Shui et al. This is an open access article distributed under the Creative Commons Attribution License, which permits unrestricted use, distribution, and reproduction in any medium, provided the original work is properly cited.

Genetic manipulation is a powerful tool to establish the causal relationship between a genetic lesion and a particular pathological phenotype. The rise of CRISPR/Cas9 genome-engineering tools overcame the traditional technical bottleneck for routine site-specific genetic manipulation in cells. To create the perfect *in vitro* cell model, there is significant interest from the stem cell research community to adopt this fast evolving technology. This review addresses this need directly by providing both the up-to-date biochemical rationale of CRISPR-mediated genome engineering and detailed practical guidelines for the design and execution of CRISPR experiments in cell models. Ultimately, this review will serve as a timely and comprehensive guide for this fast developing technology.

## 1. Introduction

Genome-engineering tools facilitate site-specific DNA deletions, insertions, inversions, and replacements. These manipulations of the complex eukaryotic genome help researchers understand the function of genes in a given cellular context, explore the mode of gene regulation at the endogenous locus, and, most importantly, model human disease conditions using *in vitro* cellular models or *in vivo* model organisms.

Since the emergence of designer nucleases based on DNA base recognition by modular protein motifs, such as Zinc Fingers in Zinc Finger Nucleases (ZFNs) [1–3], as well as TALE domains in transcription activator-like effector nucleases (TALENs) [4, 5], site-specific DNA manipulations in eukaryotic cells have passed a critical efficiency and specificity threshold to enable routine applications in a laboratory. The recently developed, explosively popular CRISPR/Cas9 (clustered regularly interspaced palindromic repeats/CRISPR-associated) genome-engineering system has transformed discovery in this exciting era. CRISPR/Cas was first discovered in prokaryote adaptive immunity [6–8] and has now been more extensively adapted for eukaryotic genome engineering than ZFNs and TALENs [9]. The

most widely utilized class, the type II CRISPR/Cas9 system from *Streptococcus pyogenes*, offers users the greatest ease and modularity for design and execution of any genome-engineering experiments [10–13]. However, limitations and common practical pitfalls of the CRISPR/Cas9 system have not been sufficiently and systematically summarized and emphasized for the emerging population of potential users, in large part due to the great enthusiasm accompanying the system's amazing rise in popularity.

In this review, practical issues associated with the design and execution of a typical CRISPR experiment will be discussed, especially in the context of modeling human diseases using stem cells. Due to the limitation of the current scope, this paper will discuss neither earlier designer nucleases (ZFNs and TALENs) nor applications of CRISPR on model organisms, although similar rationale and general principles discussed in the following sections would also apply to these applications.

## 2. The Discovery of CRISPR/Cas System

The CRISPR system was first discovered in bacteria as an “adaptive immune system” against plasmids, viral DNA, or

RNA [6–8]. This “memory system” can destroy DNA or RNA if reinfection occurs in the same bacteria or in its descendants [14–19]. Three types of CRISPR loci exist, all of which acquire short pieces of DNA called spacers from foreign DNA elements [20]. Spacers are integrated into the bacterial genome during the process of CRISPR adaptation. They are usually inserted into the CRISPR locus that contains short, partially palindromic DNA repeats to form loci that alternate repeated elements (CRISPR repeats). These loci are subsequently transcribed and processed into small interfering RNA that guides nucleases for sequence-specific cleavage of complementary sequences. Through these stepwise but continuous evolutions of adaptation, CRISPR repeat RNA (crRNA) biogenesis and foreign DNA targeting generated sophisticated CRISPR-based adaptive immune systems in nearly half of the bacterial species, as well as in most archaea [21].

The sequence in the exogenous nucleic acid element corresponding to a CRISPR spacer was defined as a protospacer [22]. For proper targeting by type I and II CRISPR systems, the protospacer is usually flanked by a system-specific, highly conserved CRISPR motif, namely, a protospacer adjacent motif (PAM) [23]. Most PAMs are typically 2 to 5 highly conserved nucleotides, either on the 5' end of protospacer (type I system) or on the 3' side (most type II systems). A significant feature of the PAM for the CRISPR system is to distinguish the foreign DNA against the host genome; thus, only the PAM-bearing invading sequence will be targeted for destruction.

### 3. Different Classes of CRISPR/Cas

Among the three different types of CRISPR loci, type I and III loci involve a complex panel of multiple Cas proteins that form ribonucleoprotein (RNP) complexes with CRISPR RNA to target foreign sequences [15]. However, the type II CRISPR system uses a much smaller number of Cas proteins to perform this core function. Type II CRISPR loci have three subdivisions. The most commonly used CRISPR system for eukaryotic genome engineering is adopted from a type II A system from *S. pyogenes*, where a single Cas9 protein (spCas9) is responsible for both forming the CRISPR-RNP complex and subsequent DNA cleavage. For the practical reason of simplicity, most genome-engineering applications use one hybrid RNA (guide RNA, gRNA) combining the essential structural features of the transactivating RNA (tracrRNA) and crRNA duplex [10]. The single-chain gRNA is used here in subsequent discussions.

Besides spCas9, a few other orthologous Cas9 proteins from similar type II CRISPR systems share the core feature as the sole protein component for RNA-guided targeting. The Cas9 proteins of *Streptococcus thermophilus*, *Neisseria meningitidis*, and *Treponema denticola* demonstrated comparable genome-editing efficiency to spCas9 (Table 1) [24–27]. These Cas9 proteins have different sizes, mostly due to their target recognition domains (REC) [28]. Significantly, orthologous Cas9 proteins differ in the specific PAM sequences used for targeting; thus, they can be used in the same cell when paired with their corresponding crRNA to recognize their corresponding targets without interfering with each other [29–31].

TABLE 1: Orthogonal type II Cas9 and their optimal PAM preference.

Bacteria	PAM	CRISPR type	Reference
<i>S. thermophilus</i> **	NNAGAAW (CRISPR1)	IIA	[28, 29]
<i>N. meningitidis</i>	NNNNGATT NNNNGCTT	IIC	[28, 47, 145]
<i>T. denticola</i>	NAAAAN	IIA	[29]
<i>S. mutans</i>	NGG	IIA	[47]
<i>L. innocua</i>	NGG	IIA	[47]
<i>L. buchneri</i>	NAAAAN	IIA	[47]
<i>C. jejuni</i>	NNNNACA	IIC	[47]
<i>P. multocida</i>	GNNNCNNA	IIC	[47]
<i>S. aureus</i> **	NNGRRT	IIA	[31]
<i>N. cinerea</i>	GAT*	IIC	[31]
<i>C. lari</i>	GGG*	IIC	[31]
<i>P. lavamentivorans</i>	CAT*	IIC	[31]
<i>C. diphtheriae</i>	GG*	IIC	[31]
<i>S. pasteurianus</i>	GTGA*	IIA	[31]
<i>S. pyogenes</i>	NGG (NAG as minor)	IIA	[10]
<i>S. pyogenes</i> (D1135E)	NGG (does not recognize NAG)	IIA	[35]
<i>S. pyogenes</i> VQR (D1135V/R1335Q/T1337R)	NGAN NGCG	IIA	[35]
<i>S. pyogenes</i> EQR (D1135E/R1335Q/T1337R)	NGAG	IIA	[35]

\*Putative PAM; \*\*significantly smaller than spCas9. Bottom rows are engineered spCas9 proteins with different PAM preferences.

This characteristic enables sequence flexibility of CRISPR experiments by offering a variety of Cas9 proteins to target virtually any particular sequence [25]. This orthogonality was best demonstrated by recent work that allowed the labeling of distinct genomic regions using different inactivated Cas9-fluorescent fusion proteins simultaneously in a single live cell [32, 33]. Although most Cas9 proteins from type II CRISPR system have one or more optimal PAMs, there is also considerable flexibility in terms of PAM recognition. For example, spCas9 recognizes NGG as its optimal PAM sequence, while NAG can also be recognized with lower frequency ([12] and subsequent). This plasticity might arise from continuous selection pressure on bacterium to target evolving viral sequences [34]. In practice, this plasticity poses considerable challenges due to the off-targeted recognition of alternative PAM sequences [12]. On the other hand, this flexibility allows further engineering of different Cas9 proteins to optimize or modify PAM preference. Initial progress has been made toward generation of spCas9 with more rigid NGG PAM recognition and modification of the PAM preferences [35]. In a few years further biochemical characterization of native orthogonal Cas9 proteins with their PAM preferences and protein engineering efforts on characterized Cas9 proteins

will likely generate a full repertoire of Cas9 proteins with high specificity covering virtually any 2~5-nucleotide PAMs.

A recent important addition to the CRISPR toolbox is the characterization of Cpf1, a class II CRISPR effector that is distinct from Cas9. Cpf1 is a single RNA-guided endonuclease that uses T-rich PAMs and generates staggered DNA double-stranded breaks instead of blunt ends [36]. Its smaller protein size and single RNA guide requirement may make future CRISPR applications simpler and with more precise control.

#### 4. Cas9 Enzymology

The Cas9 protein contains two independent endonuclease domains: one is homologous to the HNH endonuclease and the other one to the RuvC endonuclease (Figure 1) [10]. Each domain cleaves one strand of double-stranded DNA (dsDNA) at the target recognition site: the HNH domain cleaves the complementary DNA strand (the strand forming the duplex with gRNA), and the RuvC-like domain cleaves the noncomplementary DNA strand [10]. Recent CRISPR/Cas9 complex structural analysis [37, 38] revealed a two-lobed structure for Cas9: a recognition (REC) lobe and a nuclease (NUC) lobe. Cas9 interacts with the RNA-DNA duplex using the REC lobe in a largely sequence-independent manner, implying that the Cas9 protein itself does not confer significant target sequence preference. One caveat of the CRISPR/Cas9 system is that gRNA-loaded Cas9 endonuclease cleavage is not completely dependent on a linear guide sequence, since some off-target sequences were shown to be cut with similar or even higher efficiency than the designed target sites [12, 39–42]. In general, mismatches between the first 12 nucleotides (nts) of the gRNA (seed sequence in gRNA spacer, Figure 1) and the DNA target are not well tolerated, suggesting high sequence specificity in the PAM-proximal region. However, mismatches beyond the first 12 nts can be compatible with efficient cleavage (tail region in gRNA spacer, Figure 1) [12]. Structural biology insights into the Cas9-gRNA RNP complex revealed that the 12-nt sequence is in a fixed “seed” configuration even prior to the DNA substrate binding, whereas the 5' end of gRNA remains unstructured. While generally true, it is an oversimplification, and the sequence recognition specificity of the CRISPR system is a topic of active investigation [39–44]. Notably, shorter gRNA with up to a 5000-fold reduction in off-target effects was recently described [45]. Adding two additional Guanine (G) nucleotides at the 5' end of gRNA in some circumstances modestly improves the specificity of the CRISPR/Cas9 system [46], possibly by altering gRNA stability, concentration, or secondary structure. The relaxation of sequence specificity of the RNA-guided endonuclease system remains the biggest challenge for its usage in genome engineering. A recent biophysical study [37] for the thermodynamic properties of Cas9 binding provided a likely explanation for the features of specificity outlined above, and further analyses along these lines will be valuable to further refine design guidelines.

A degree of structural flexibility was found from the DNA-gRNA duplex-loaded Cas9 crystallography structure [38], which was substantiated by an independent crystallography and single-particle electron microscopy study on both

*S. pyogenes* and *A. naeslundii* Cas9 [37]. This study demonstrated that a conformational rearrangement is induced by gRNA binding to Cas9, shaping a central channel to accommodate the DNA substrate (Figure 1, gRNA binding) [37]. Detailed structural information is lacking for how Cas9 recognizes targeted sequences within the genome and triggers the specific DNA cleavage after sequence recognition. However, the RNA-loaded Cas9 protein reads the PAM in its base-paired configuration (Figure 1, scan for PAM). The recognition of dinucleotide GG in PAM simultaneously allows for the local stabilization of the unwound target DNA immediately upstream of the PAM sequence, which might compensate for the energy cost of local DNA strand separation starting immediately upstream of PAM (Figure 1, Cas9 recognizes PAM) [47]. A recent biophysics study for Cas9-mediated DNA recognition *in vitro* further revealed that Cas9 does not behave as a typical nuclease [48]. First, gRNA-loaded Cas9 enzymatic activity does not follow Michaelis-Menten kinetics, since Cas9 protein stably associates with target sites on DNA even after inducing a double-strand break. Thus, the key requirement for successful CRISPR-mediated genome engineering is efficient and precise target locating. Secondly, gRNA-loaded Cas9 finds the target sequence using 3D diffusion without obvious sliding on the DNA substrate. Cas9 pauses on DNA for interrogation once it recognizes a PAM sequence. Many of these reactions are transient and do not lead to DNA cleavage. In agreement with this “pausing” behavior of the gRNA-loaded Cas9 on the DNA substrate *in vitro*, this mode of transient DNA binding on a non-matching target is stable enough in cells to be detected using genome-wide CHIP-Seq (Chromatin Immunoprecipitation Sequencing) [43]. Besides the highly enriched binding of Cas9 at its on-target site, numerous binding events with lower frequency can be observed around a short motif of 5~10 nucleotides matching the PAM-proximal region on a gRNA plus NGG PAM sequence [43]. Thus these “off-targeted” bindings likely involve partial base pairing between gRNA and the PAM-proximal sequence. Without intrinsic DNA helicase activity, how Cas9 facilitates the strand replacement on its DNA substrate by the gRNA is not known. It is suggested to be a thermodynamically favorable process upon PAM recognition, and the unwinding of local DNA base pairing was suggested to be in a directional and sequential manner, starting at the 3' end of the target sequence adjacent to PAM and progressing in the 5' direction of the DNA substrate (Figure 1, base-pairing extension) [47, 48]. The Cas9 protein likely stabilizes the locally unwound DNA, allowing further stabilization of the single-stranded DNA chain by continuous formation of Watson-Crick base pairing with the gRNA (Figure 1, base-pairing extension). If base pairing is blocked due to a mismatch between the DNA substrate and the gRNA, the thermodynamic energy of the DNA-Cas9 interaction might be insufficient to maintain a significant portion of unwound DNA. In this case, partially unwound DNA will return to its duplex state, and the DNA-Cas9 interaction will attenuate simultaneously (Figure 1, mismatch and DNA release). These observations provide an attractive stepwise substrate-unwinding model for target recognition and cleavage by the gRNA-loaded Cas9 protein. This model

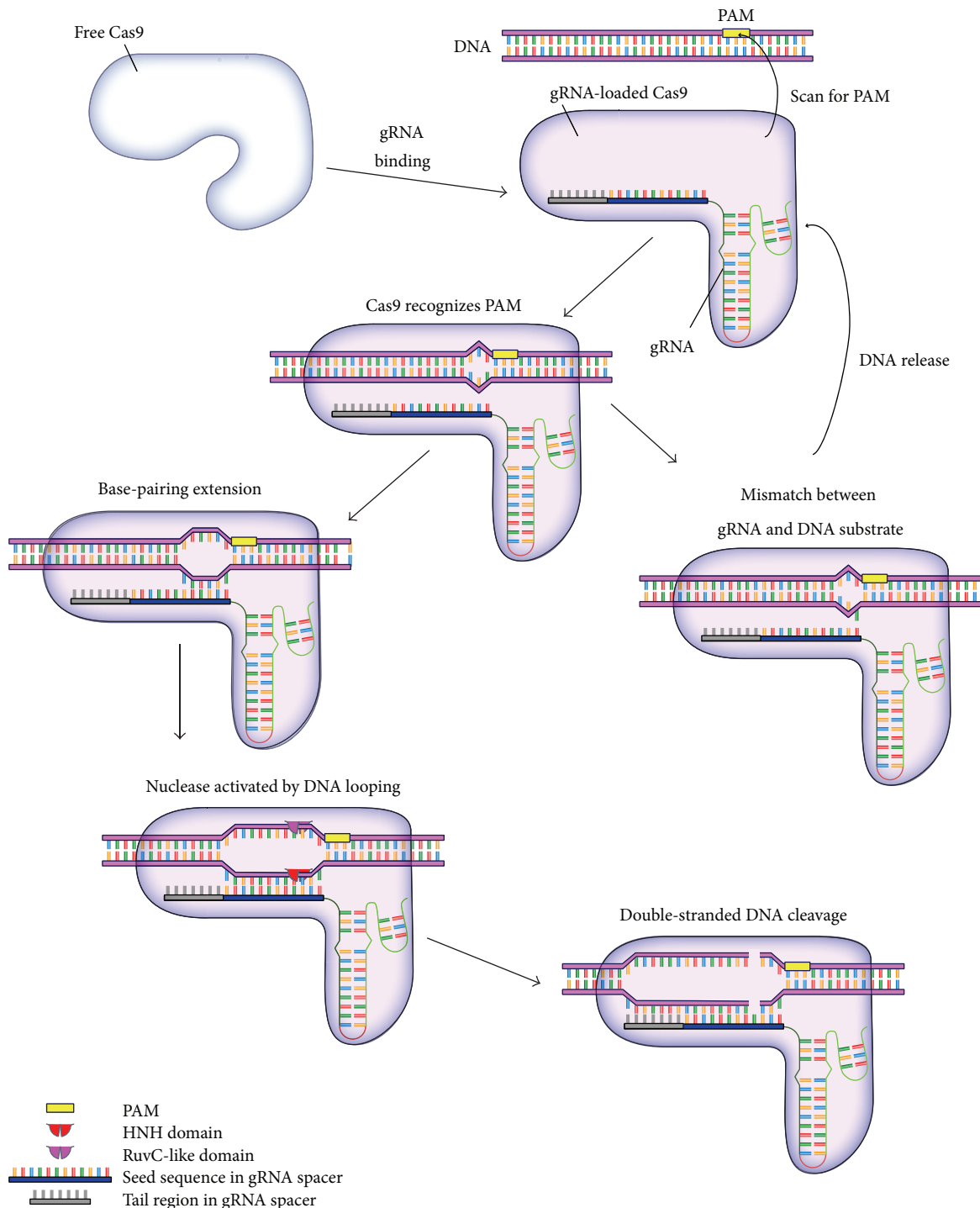


FIGURE 1: A proposed model for Cas9 endonuclease to trigger DNA cleavage. A conformational change is induced once the Cas9 protein binds to gRNA, allowing it to search for the DNA substrate. The REC lobe of Cas9 scans for the PAM in the genome. PAM recognition helps local unwinding of dsDNA 5' to the PAM region. The unwound DNA is transiently stabilized by protein/ssDNA interaction. Successful base pairing between the ssDNA portion and the gRNA further extends the ssDNA loop. A critical loop size may trigger the enzymatic activity of Cas9 to make the double-stranded cut. Afterwards, Cas9 remains bound to the DNA substrate. If the base pairing between ssDNA and gRNA is blocked by mismatches, the ssDNA loop collapses to release the Cas9 protein.

predicts that only perfectly or nearly perfectly paired DNA-RNA hybrids can lead to significant DNA unwinding, upon which Cas9 will cleave both DNA strands (Figure 1, nuclease activation and cleavage). This explains the high sequence specificity in the PAM-proximal region observed for CRISPR-mediated gene editing [49], as well as the recent finding that off-targeted Cas9 binding through the beginning of the PAM-proximal sequence only rarely leads to off-targeted enzymatic activity *in vivo* [43]. Because unwinding the DNA duplex across the first-10~12-nt preconfigured seed sequence might be the critical thermodynamic hurdle to establish stable Cas9 interaction with DNA and subsequent cleavages, a high degree of sequence fidelity in this seed sequence might be both sufficient and necessary via strand replacement to trigger Cas9 conformational changes and remodeling of the active sites. In theory, based on this model, the mismatch of a DNA-gRNA hybrid occurring closest to the PAM sequence should be the least tolerated and is indeed the least common among observed off-targeted bindings [43]. Further thermodynamic modeling based on this model and structural information will likely improve both the efficiency and specificity of CRISPR applications.

## 5. On-Target and Off-Target Considerations

Similar to most other engineering applications, specificity and efficiency are the main factors ensuring a rational CRISPR-experiment design. In subsequent discussions, specificity is defined as the probability that Cas9 will target the designed locus compared to other undesirable loci (off-target effects). Efficiency is defined as the probability that the locus of interest will be modified by Cas9 nuclease in the context of a pool of available target chromosomes from the cell population. In a word, vigorous CRISPR design tends to minimize the off-target effect and maximize the on-target effect of the designer nuclease to achieve both high specificity and efficiency.

The 18~20-nt spacer region, designed as the protospacer sequence in the gRNA, is the main determinant for both off-target and on-target effects of CRISPR experiments. Together with a given adjacent PAM sequence, a gRNA with a 20-nt protospacer region can achieve, in theory, unique sequence recognition in a random sequence space of roughly 17 TB (tera-base pairs) if a perfectly base-paired match is required for targeting. While this theoretical upper limit of resolution exceeds the size of most eukaryotic genomes, the practical specificity of Cas9 was found to be magnitudes lower than the theoretical expectation. It was discovered that the “NGG” PAM sequence requirement of spCas9 was not absolutely necessary since a “NAG” PAM is frequently tolerated with a lower efficiency [12]. The scientific community also quickly realized, since the onset of development of CRISPR genome engineering, that mismatches between the protospacer and targeting DNA are tolerated at a surprisingly high frequency, especially for the 5' sequence of the protospacer [41, 42, 44, 50]. Further elucidation of Cas9 enzymology revealed that this bias might be due to the unidirectional (3' to 5') DNA double-strand melting coupled with DNA-RNA duplex formation upon PAM recognition by Cas9 nuclease. While

the gross 3' to 5' relaxation gradient of the base-pairing requirement of Cas9 targeting generally holds true, it was found that sometimes sequences with mismatches to the 12-nt seed sequence in the gRNA spacer can be efficiently targeted [39, 41, 42]. This suggests that proper base pairing with the gRNA seed sequence alone does not guarantee specificity. Furthermore, targeting efficiency at some off-target sites could be even higher than the desired locus with perfectly matched spacer-protospacer sequences [39, 41, 42]. This phenomenon might be caused by additional factors beyond the RNA-based sequence recognition used by Cas9 nucleases.

Compared to the considerable knowledge for the basis of Cas9 off-target effects, relatively little is known about how to design a gRNA to make the desired targeting event more efficient. Multiple factors determine the success of any given CRISPR experiments, such as the quantity of Cas9 proteins and gRNA, chromatin accessibility of the targeting loci, and cellular response to CRISPR-induced DNA lesions. Most of these issues are beyond experimental controls when a CRISPR experiment is designed. A few recent studies [51–53] attempted to debug the sequence preference of effective gRNA by retrieving the successful targeting gRNA sequences in a large, randomly selected gRNA pool. This statistical approach is limited by current capability to generate a gRNA pool with sufficient diversity and the difficulties avoiding artificial bias when selecting the efficiently targeted cell pools. Nevertheless, a few statistically significant rules have been revealed by these pioneering studies on common traits of efficient gRNA for spCas9. (a) Guanine (G) is strongly favored at the 3' position most proximal to the PAM sequence (especially the –1 position). This preference might be due to Cas9 loading [51]. (b) A series of thymine (T) is disfavored at the four positions (–1 to –4) closest to the PAM, which might be related to the fact that RNA polymerase III recognizes a series of uracil (U) as a pausing/termination signal [54], causing a lower level of gRNA expression [51]. (c) Cytosine (C) is preferred at the DNA cleavage site (–3 position). (d) In the PAM region, the +1 position favors C while disfavoring T [52]. (e) The CRISPR activity correlates with gRNA stability, which can be influenced by the nucleotide composition of the spacer: G-rich spacers are more stable especially when comparing with A-rich ones [55].

The emerging gRNA design rationale discussed above was continuously incorporated into available bioinformatics toolboxes as weight matrices for calculating the off-target or on-target scores for any gRNA [52, 55–59]. Although these scores are informative in facilitating the experimental design process, potential CRISPR users should be cautious about interpreting gRNA ranking based on these scores, since it does not necessarily indicate superior specificity and efficiency.

## 6. CRISPR/Cas9 Delivery Methods

As an efficient, RNA-guided, specific gene-modification tool, CRISPR was widely used in many experimental settings to achieve desired mutations. However, the delivery of the required Cas9 protein and gRNA is a long-standing challenge

[60]. Three methods of CRISPR delivery, including plasmids, viruses, and ribonucleoproteins (RNPs), were shown to successfully introduce Cas9 and gRNA into target cells and accomplish guided gene editing [11, 49, 61]. With their various merits and limitations, these three delivery methods offer researchers an opportunity to optimize their gene-editing procedures based on various experimental needs.

**6.1. Delivery Using Plasmid Vectors.** Delivery using the plasmid vector system is the conventional and most popular method for CRISPR introduction. It has the main advantage of being simple to make *in vitro*. In order to introduce a functional CRISPR system into target cells, cells need to be transfected with plasmids encoding the Cas9 protein, crRNA, and tracrRNA while simultaneously using electroporation or cationic lipid-mediated delivery to achieve assembly of the CRISPR complex in cells [11].

The plasmid system procedure was continually simplified, and its application range expanded to *in vivo* animal studies. Instead of cloning three different plasmids encoding three different components, researchers showed that plasmid encoding gRNA, a fusion transcript of crRNA and tracrRNA, is sufficient for Cas9 binding and DNA target-site recognition [10]. Recently, plasmids encoding both Cas9 and gRNA became commercially available. Therefore, transfection of a single plasmid is the sole requirement for a CRISPR experiment. Multiplex edition of target loci can be accomplished through simultaneous introduction of multiple gRNA species by a single plasmid or by cotransfection of multiple plasmids [13]. Plasmid delivery was also applied in a tissue-specific CRISPR application in murine liver [60, 62]. Through hydrodynamic tail-vein injection, plasmids were efficiently delivered to ~20% of hepatocytes for transient expression. This study demonstrated successful gene editing with limited efficiency *in vivo* through direct plasmid delivery.

However, compared to successful delivery *in vitro*, the plasmid delivery system still faces significant challenges for *in vivo* applications, such as low delivery efficiency and frequent epigenetic silencing on episomal DNA [63]. Conversely, plasmid delivery offers the dual possibility of both long-term and transient CRISPR delivery *in vitro*. In a small proportion of transfected cells, random but stable integration of all or part of plasmid DNA into the host genome occurs. This is possibly due to low levels of spontaneous DNA damage, which in turn provide continuous Cas9 and gRNA sources [11, 49, 61, 64]. When this feature is not desirable, delivered plasmids usually become diluted and gradually lost over a few cell cycles. This limited time window of genome engineering is critical for obtaining genetic homogenous cell populations for downstream functional studies.

**6.2. Delivery Using Lenti-, Adeno-, and Adeno-Associated Viral Vectors.** The plasmid system introduces CRISPR into established cell lines efficiently. However, to expand CRISPR's application range, viral vectors are used to deliver CRISPR into primary cells or cells refractory to plasmid transfection. Lentiviral vectors stably integrate into the host genome, making it the preferred means of delivery if the targeting information needs to be retrieved after functional selection

processes [51, 65–67]. It is now feasible to carry out genome-wide, CRISPR-based, functional genomic screens by delivering complex pools of CRISPR reagents into a relevant cell type via lentiviral packaging. One significant limitation of lentiviral-based delivery is that the random integration of a viral genome may cause unwanted insertional mutagenesis at undesired host loci. Use of nonintegrating viral vectors (NIVVs), including adenoviral vectors and adeno-associated vectors, can efficiently circumvent this problem because they do not incorporate viral DNA into the host genome [11, 60]. Moreover, viral DNA dilutes during mitosis due to the lack of a replication signal [60]. Among NIVVs, adenoviral and adeno-associated vectors are both potentially suitable CRISPR delivery candidates because of their episomal nature, large cloning capacity, high-titers, capability of long-term *in vivo* expression, and ability to transduce many cell lines [39, 49, 61, 62].

While a viral vector encompassing Cas9 and gRNA expression cassettes can be produced at high-titers, the negative correlation of packaging efficiency versus vector size also poses challenges for single-vector delivery of both Cas9 protein and gRNA. Successful gene editing was achieved using adenovirus-delivered CRISPR in multiple mammalian cells. Using different gRNA and Cas9 virus concentrations, researchers showed that the editing efficiency is dosage dependent [10, 61]. Besides transfection of stable cell lines, adenoviral vector-mediated CRISPR delivery can also be applied *in vivo*. Through tail-vein injection, adenoviruses carrying Cas9 and gRNA expression cassettes can be introduced into murine liver. Resulting Cas9-mediated gene editing is stable even after extensive regeneration of liver tissue [13, 68]. Compared to hydrodynamic tail-vein injection of plasmids, tail-vein injection of adenoviruses achieved 5- to 8-fold greater editing frequency [69]. This high efficiency makes virus-delivered CRISPR an attractive option for *in vivo* genome modification. However, systematic delivery using the adenovirus vector *in vivo* could induce immune responses that eliminate infected cells and eventually impair CRISPR genome-editing efficiency. In one recent study using adenoviral vector delivery, the transduction rate of liver cells drops from 80.8% one day after injection to 1.4% fourteen days after injection. This is most likely due to the immune response of the host, including elevated expression of inflammatory cytokines [31, 69]. In contrast, the adeno-associated virus (AAV) induces a mild immune response *in vivo* and can provide long-term expression in nondividing cells. The recent study using *Staphylococcus aureus* Cas9 (SaCas9) solved the viral packaging limit problem for spCas9, making the AAV-mediated delivery an ideal method for *in vivo* genome editing [31].

**6.3. Delivery Using Cas9-gRNA Ribonucleoproteins (RNPs).** In addition to plasmid vector and viral vector delivery, CRISPR delivery using Cas9-gRNA RNPs is another established method [64]. Both plasmid and viral delivery encountered the problem of high off-target editing rates due to prolonged expression of Cas9 and gRNA in cells. Using direct delivery of RNPs can effectively circumvent this problem. When injected directly into cells, RNPs induce editing at

target sites immediately after delivery and degrade rapidly, reducing off-target effects [70, 71]. Additionally, using RNPs avoids the possibility of undesired DNA integration into the genome due to its DNA-free mode of delivery.

Application of RNP delivery led to successful genome editing in multiple human cell lines [64, 72]. The RNP complex can be readily made through incubating *in vitro* purified Cas9 protein with either a single-chain guide RNA (sgRNA) or dual RNA that consists of crRNA and tracrRNA. Under certain circumstances, dual RNA was shown to be more effective than single gRNA [73]. Direct injection of RNP complexes into cells can lead to efficient CRISPR-mediated genome editing with high specificity and low off-target rates compared to plasmid delivery [64]. RNPs are traditionally delivered by direct microinjection in a low-throughput manner. Recently, the feasibility of transfecting CRISPR RNPs into cells efficiently using electroporation was demonstrated [72], as well as using cationic lipid-mediated liposome delivery [74]. Delivery of RNPs into cell-cycle-synchronized cells also yielded a significantly higher rate of editing compared to delivery in nonsynchronized cells. More importantly, researchers can maximize the utilization a particular mode of double-strand break (DSB) repair by delivering RNPs into cells arrested at a particular cell-cycle phase [72]. Continual improvement of RNP delivery makes it a prominent method for not only gene editing in an experimental setting, but also clinical gene therapy development.

## 7. CRISPR Efficiency Test

**7.1. Test of Indel (Local Point Mutation, Insertion, and Deletion).** When assembled with gRNA, Cas9 nuclease cleaves dsDNA and induces DSBs. DSBs can be repaired by either nonhomologous end joining (NHEJ) or homologous recombination (HR). NHEJ is an error-prone process that generates random insertion or deletion (indel) mutations at the DNA rejoining sites. Sanger sequencing is the most accurate way of confirming indel mutations (Figure 2(a)). However, due to the random nature of indels, a wide variety of mutated DNA might be present after a CRISPR-induced NHEJ process. Separating these molecule species using molecular cloning coupled with Sanger sequencing is time-consuming and cost-inefficient [75]. Recent progress in bioinformatics tools (such as TIDE, Tracking of Indels by DEcomposition) enabled successful digital decoding of Sanger sequencing from a mixture of complex indels, generated by a unique CRISPR-targeting event into separate mutant species [76–78]. Although this method is still of limited sensitivity and remains to be validated on a larger scale, Sanger sequencing of a locally amplified, targeted locus offers a quick and reliable readout confirming the efficiency of any given CRISPR experiment. Without sequencing, the separation of DNA with minor differences of length (resulting from some indels) on a Sanger sequencer can be used to quickly access the success of a genome-editing experiment. IDAA (Indel Detection by Amplicon Analysis) was recently developed to fill this niche [79]. Through the use of target-specific primers flanking the target site, the different sizes of amplicons can be

detected [79]. Furthermore, several other methods that take advantage of NHEJ-induced indels were developed to efficiently assess the cleaving efficiency of CRISPR through the detection of indel mutations at target loci regardless of DNA length change; these include the Surveyor nuclease assay, the T7 Endonuclease I (T7E1) assay, the High Resolution Melting Analysis (HRMA), and PAGE electrophoresis [80–85].

Surveyor, T7E1, and other nuclease-based mutation detection assays rely on the formation of a locally mismatched heteroduplex DNA, a byproduct of sequence variation caused by NHEJ following the designated nuclease target (Figure 2(b)). If CRISPR-mediated cleavage is successful, indels will be generated at the DSB sites through NHEJ. Heteroduplex DNA can be formed after melting and rehybridizing mutant and wild-type alleles. The mismatch-recognizing enzymes, such as Surveyor and T7E1 nucleases, can detect heteroduplex DNA. Bacteriophage resolvase T7E1 recognizes and cleaves distorted dsDNA undergoing conformational changes [86]. Surveyor nuclease is a single-stranded nuclease that recognizes a nucleotide mismatch induced by indels. It not only cleaves DNA one strand at a time on the 3' end, but also contains 5' exonuclease activity [87, 88]. Both enzymes recognize indels and induce DSBs at mismatch sites, resulting in shortened DNA fragments of various sizes. The digested DNA fragments can then be visualized using gel electrophoresis or DNA fragment analysis [82, 88]. However, both enzymes exhibit low levels of random single-stranded nuclease activity, leading to unspecific cleavage. This problem can be partially resolved through addition of Ampligase during the enzyme nuclease reaction [89], which reduces the nonspecific nuclease activity.

HRMA is another tool for indel detection, utilizing the different denaturation profile of heteroduplex DNA compared to that of homoduplex DNA (Figure 2(c)) [90]. If CRISPR-induced indel is present in template DNA, heteroduplex and homoduplex DNA will be formed after melting and rehybridizing mutant and WT alleles. Different duplex species exhibit different denaturation patterns. HRMA records the temperature-dependent denaturation profile of the sample and determines the existence of heteroduplex DNA based on different melting patterns from the sample mixture. Due to its sensitivity, HRMA requires proper optimization of PCR conditions to ensure high specificity of target amplification.

The polyacrylamide gel electrophoresis- (PAGE-) based method was recently proven to be efficient in detecting the presence of heteroduplex DNA (Figure 2(d)) [85]. This method takes advantage of the migration speed difference between heteroduplex and homoduplex DNA during native PAGE. Heteroduplex DNA generally migrates at a much slower rate due to its indel-induced open angle between matched and mismatched DNA strands and therefore can be visualized using PAGE. However, whether the PAGE assay provides sufficient sensitivity across the spectrum of indel mutation variation remains to be verified.

**7.2. Sensitivity Issues and Reporter.** While CRISPR is considered an accurate genome-editing method, the efficiency of CRISPR varies significantly when applied to distinct loci

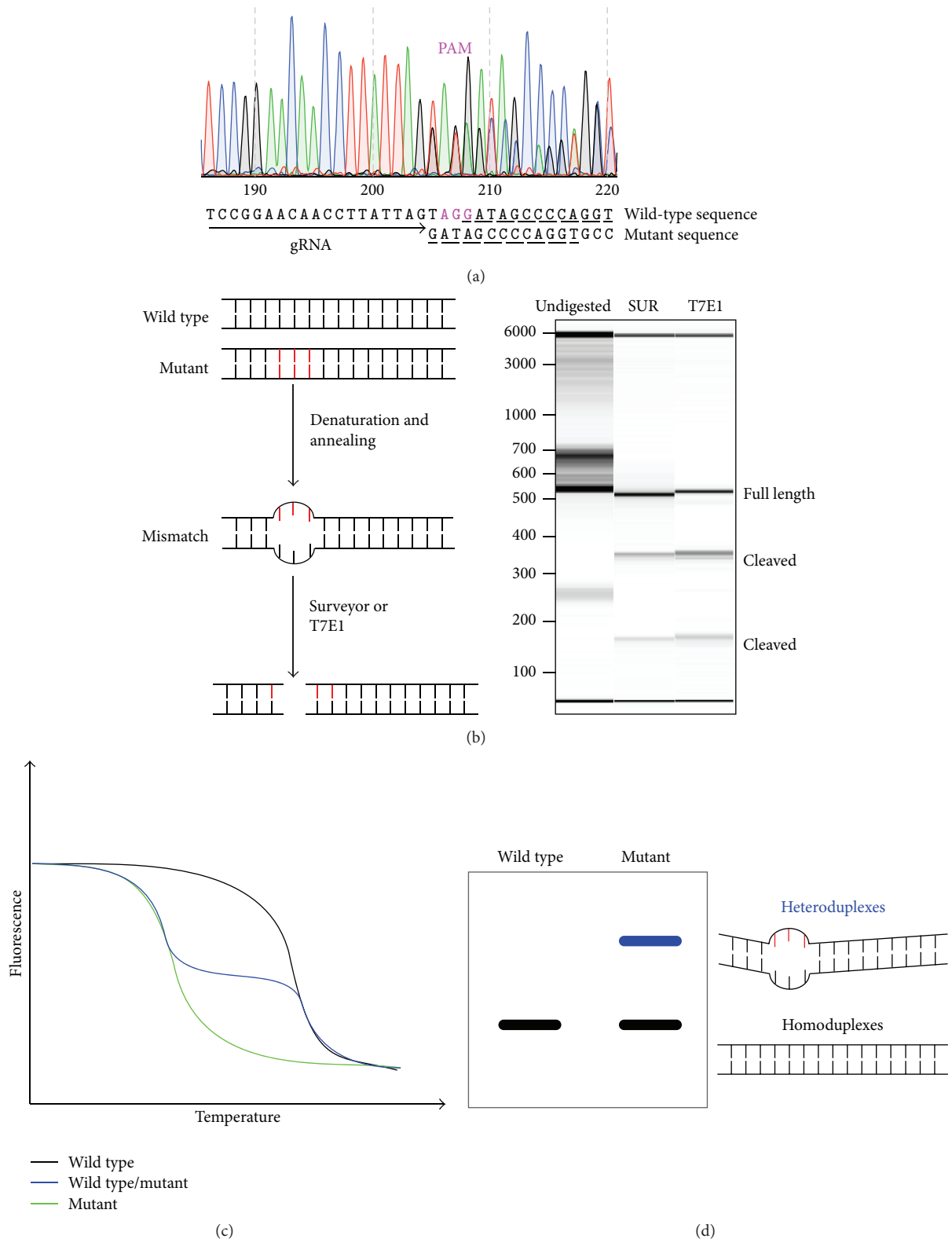


FIGURE 2: Major methodologies for mutation detection. (a) Sequence decoding from Sanger sequencing. An example of a Sanger sequencing read was shown to illustrate the significant decrease of read quality from the predicted CRISPR cut site (PAM position labeled by magenta). This is due to the inclusion of the mutated DNA (decoded as the bottom sequence) with the wild-type DNA sequence (decoded as the top sequence). Underlined sequence reveals identical nucleotides between the wild-type and mutant sequences, which indicates the major mutation is a 3-nucleotide (TAG) deletion. (b) Recognizing mismatched dsDNA using the single-stranded specific nucleases. Mixed sequences with local sequence polymorphisms (CRISPR-induced indel mutations) form a mismatch when rehybridizing. The result from the mismatch-recognizing nuclease assay is visualized using fragment analysis as a digital nucleic acid size profile. (c) High Resolution Melting Analysis. (d) PAGE electrophoresis of a DNA hybrid.

and different cell types. In induced pluripotent stem (iPS) cells and human embryonic stem cells (hESCs), for example, CRISPR-editing efficiency frequently drops below 1% [91, 92]. This low frequency increases demand for more sensitive rare mutation detection methods. Sanger sequencing is the gold standard for determining on-target edition efficiency, yet it is a time- and resource-consuming process. When the mutation rate falls below a given threshold (usually ~1%), routine mutagenesis detection methodologies (Sanger sequencing, nuclease-based heteroduplex cleavage assay, HRMA, and PAGE) are of limited use due to their sensitivity restraints. High-throughput sequencing was developed for accurate measurement of rare indels that happen at a frequency of 0.01–1%. However, because this method is considerably more sensitive than traditional methods (such as mismatch-recognizing enzymes) the false-positive frequency is also elevated [75].

Single molecule real-time (SMRT) DNA sequencing was developed as a unique high-throughput sequencing platform [93]. It has the advantage of both high sensitivity and long reading length. A regular PCR amplified region of interest is ligated with SMRT adaptors to create a single molecule SMRTbell template to generate sequence reads. This method not only examines the existence of an editing event, but also quantifies the frequency of editing through either NHEJ or HR. With an average sequencing length of 3 kb and up to 15 kb, SMRT sequencing provides a reliable method for assessing both on-target and off-target rare editing effects. Similarly, other high-throughput sequencing platforms can be applied to quantitate indels in the targeted amplicon.

To further assess CRISPR-editing efficiency using accurate quantification for very rare editing events, digital droplet PCR (ddPCR) can be applied to CRISPR-edited genome testing [94]. Depending on the assay format, ddPCR assay has theoretical mutation detection limits in the range of 0.01~0.001%. To achieve individual assessment of the edited genome, sample DNA is partitioned into small droplets through emulsion. One set of primers flanking the region of interest and two competitive fluorescence-tagged probes targeting wild-type and mutant sequences, respectively, are included in the reaction. An individual PCR reaction is carried out in each droplet, and fluorescence signals from each droplet are subsequently recorded. The wild-type and mutant sequences are differentiated, and the frequency of editing can be calculated based on the number of droplets with different fluorescence signals [91]. This method allows extremely sensitive detection of rare mutations as well as accurate quantification of CRISPR-editing efficiency. Novel ddPCR application was explored in other studies, including differentiating wild type and mutants based on the size of amplicons using the nonspecific, double-strand DNA binding dye EvaGreen (EG) [95].

Besides quantifying CRISPR-induced indels, live reporters based on HR can be used to visualize CRISPR activity. Typically, a reporter plasmid vector can be designed to include the identical target-site sequence as the targeting locus. The CRISPR target is flanked by two separate halves of a fluorescent protein reporter, with a stretch of an identical sequence included in both halves. Thus, this reporter is

inactive since the fluorescent protein gene is interrupted by the inserted sequence. CRISPR components and the reporter plasmid are cotransfected. Efficient gRNA loads Cas9 to cleave both the chromosomal targeting locus and the episomal reporter-targeting site. In the reporter, the DSB will be repaired through HR between the two halves of the fluorescent protein, thus rendering a fully functional fluorescent protein. Hence, the “on” status of the reporter plasmid, exhibited by the gain of the cellular fluorescence signal, can give a real-time readout of CRISPR efficiency in live cells independent of additional molecular assays.

## 8. Selection of Mutant Clones

Pure clonal isolation from a single progenitor cell is a critical step in the genetic and functional characterization of mutations achieved by the CRISPR/Cas9 system. While it is usually the most laborious and time-consuming step in CRISPR-based genome engineering using cell models, generating clonal mutant cell lines is absolutely required to draw any solid conclusions correlating a given mutation and cellular behavior. Each single cell, upon the introduction of activated Cas9 nuclease, is an independent unit that undergoes stochastic genetic changes dependent on both the nuclease-induced DNA lesion and the subsequent cellular DNA-repair response. In the case of transient introduction of CRISPR agents, it is desirable to establish clonogenic cultures by the conclusion of CRISPR action. In the stem cell research field, a clonogenic culture is frequently confused with the sphere generating culture, such as formation of embryonic bodies from ES cells or neurospheres from neuronal stem cells [96]. While these sphere-forming assays are frequently used to estimate the capability of stem cells to self-renew and differentiate, the individual spheres formed in standard stem cell culture conditions do not necessarily rise from single cells [97], since sphere aggregation and fusion were frequently found even at low seeding densities [98–100]. The requirement of clonogenicity after CRISPR action usually calls for more rigorous culture conditions to ensure proper clonal separation of distinct isogenic pools.

There are multiple methods to achieve clonogenicity. To prevent sphere fusion, single cells can be encapsulated into a semisolid matrix to form embedded sphere cultures [101]. This approach greatly improves the clonogenicity of the spheres generated and offers greater advantage when cell proliferation is strictly dependent on high cell density in the culture [98]. However, single-cell encapsulation usually requires specific microfluidics devices [102]. Furthermore, maintaining capsule integrity and retrieving encapsulated cells remain challenging. Aside from cell encapsulation, cells grown in semisolid media, such as those containing methylcellulose or soft agar, are less likely to migrate [103]. When seeded at low density, single cells in semisolid media can grow into individual colonies over time. Manual or robotic selection of these colonies can subsequently establish isogenic clones. The traditional labor-intensive ways to establish cultures from single cells include cloning rings, serial dilution and plating, and fluorescent-based single-cell sorting [104, 105]. Regardless of the methodology, establishing and maintaining

a large number of isogenic cell clones are costly and labor-intensive. For most genome-engineering experiments, the optimally desired approach should minimize the number of isogenic cell clones needed to achieve the desired genetic modification. In the following sections, the factors to achieve this goal will be discussed.

*8.1. Overall Strategy, NHEJ or HR.* DSBs in the eukaryote genome can be repaired mainly by two different mechanisms: NHEJ or HR. The NHEJ repair mechanism joins broken chromosomal ends directly without the guidance of a homologous sequence. Because it lacks a reference template, this repair pathway is usually error-prone due to local DNA sequence alterations at the repaired junction (the so-called indels) [106]. In contrast, the HR repair mechanism is aided by using a homologous sequence as the repair template. This homologous sequence can be a sister chromatid duplicated during the synthesis (S) phase of cell cycle, the homologous chromosome in diploid cells, or foreign DNA introduced bearing regions of sequence homology with the targeted locus. Due to the flexibility of donor choice in HR repair, a given locus with desirable features (such as restriction enzyme recognition sites, protein fusion tags, antibiotic selection markers, or recombination sites) can be engineered by incorporating these features with a piece of introduced homologous DNA. Either plasmid construct or synthesized DNA oligos can be used as the donor template [40]. A plasmid donor can be used when long insertions need to be introduced [107, 108]. For small insertions or deletions, single-stranded DNA containing 80 bp homologous arms at 5' and 3' ends is preferred [107]. This method is similar to traditional HR-based gene targeting. However, since the introduced DSBs occur in the chromosomal DNA instead of epichromosomal DNA, the HR efficiency is usually several orders of magnitude higher than traditional HR triggered by breaking the foreign donor [3, 108–111].

While the choice of DNA-repair pathways is largely beyond experimental control, the cell-cycle phase upon which DSB occurs plays an important role in repair mechanism determination. In general, HR takes place in the synthesis (S) and the premitotic (G2) phases when there are sister chromatids available [112]. NHEJ is the predominant repair mechanism in the growth 1 (G1) and the mitotic (M) phases [113]. Although this general guideline holds true in most cases, precautions are warranted for any particular cell type for its capability on HR- or NHEJ-based DNA-repair pathways.

Regardless of the preferred DNA-repair mechanisms to get a particular or a range of desired mutations, similar clonogenic selection processes are needed. Since HR usually happens at a lower frequency than NHEJ for most cell types, it is an efficient strategy to include a selection marker on the donor construct so that successfully engineered cells can be easily traced by fluorescence or drug resistance. The marker is integrated onto the targeted loci. In some cases this feature is not ideal for downstream functional analysis, even when the majority of the selection markers can be subsequently excised by recombinases.

A few seamless genome-engineering applications emerged in the last few years to overcome this hurdle. This elegant approach aims to introduce only the desired genetic modification without leaving additional footprints at the engineered loci (including indels at the CRISPR cut sites, any selection markers, or short residual recombination sites after marker excision) (Figure 3) [24, 114, 115]. To facilitate clonal selection, a selection marker is included in the DNA donor similar to traditional HR. However, instead of using a recombinase to induce flanking recombination sites around the marker, which would leave behind at least one recombination site (Figure 3(a)), an optimized PiggyBac transposon is used for all exogenous sequences between the homology arms. Only a “TA” dinucleotide sequence is left on each side flanking the exiting PiggyBac (Figure 3(b)). To make this truly seamless, the left and right homology sequences start with a “TA” motif, which is abundant in most genomic loci. If there is no endogenous “TA” around the intended mutation, it is usually feasible to introduce one without changing the translated protein sequence in exons or make this change in mutation-tolerating introns. A negative selection marker is usually included in the PiggyBac cassette in the designed DNA donor to facilitate screening the loss of the PiggyBac cassette by the transposase. This method holds great promise for CRISPR-mediated site-specific gene therapy, since avoiding any additional sequence modification is highly desirable.

Regardless of the choice of methods, clonogenic clone isolation and identification are labor-intensive. To design the most effective screening strategy, it is crucial to realistically estimate the chance of obtaining the desired mutant cells in the pool undergoing CRISPR-mediated genome engineering. A critical factor is the efficiency of CRISPR targeting the locus of interest, which can be tested by a small-scale pilot experiment using the mutation detection methodologies discussed in the previous section. Depending on the mode of DNA-repair pathway chosen, further consideration can be made regarding whether it is feasible to first reduce the size of the cell pool by selection to enrich the targeted cells before clonal assay. Isolating cells positive for the HR-mediated live-cell cleavage reporter could enrich NHEJ-mediated indel mutations [116]. Although these are achieved by different mechanism of DNA repair, the reporter assay may indicate the subpopulation of cells where CRISPR is more active. Similarly, if the desired mutation was introduced using HR repair, inclusion of the selection marker in the DNA donor could be an efficient way to reduce the size of clonal selection pool. Frequently, the intended mutation might be predicted with high confidence to cause a specific cellular phenotype in the target-cell type. If the specific cellular phenotype can reliably be used for selection, target-cell enrichment can be achieved by applying this selection pressure [117]. Without highly efficient CRISPR reagents, a target selection scheme is required to move the mutation frequency above 0.1%, in order to make clonal single-cell selection feasible.

In cases of low mutagenesis frequency and no suitable selection strategy available for mutant enrichment, a random cell partition scheme named sib-selection can be employed to facilitate enrichment of the desired mutation before clonal

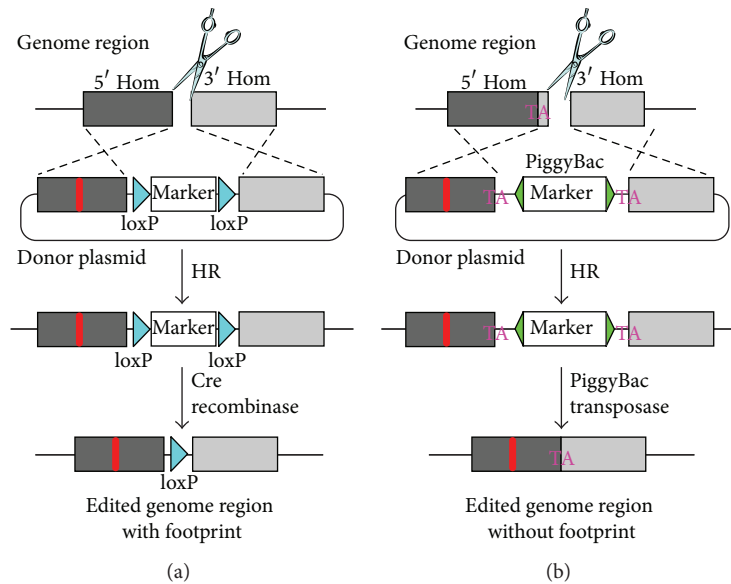


FIGURE 3: The comparison of seamless genome editing with traditional HR-based marker selection. (a) Traditional HR. (b) Seamless genome editing. Homology arms (dark grey and light grey boxes) bearing the desired mutation (red bar) are used to flank an excisable selection marker cassette. This is achieved by using the tandem loxP sites as in (a) and a PiggyBac transposon as in (b). Successful HR will insert the selection marker cassette into the genome (middle panels). Removing the loxP cassette with Cre recombinase will leave one loxP site at the locus of interest (blue triangle) in (a). The remobilization of the PiggyBac transposon will only leave a “TA” dinucleotide in (b), which initially can be found in the locus of interest, or can be tolerated without any undesired changes to the protein sequence.

isolation [91, 118]. Sib-selection is based on precise measurements of mutation frequencies in pools of cells even when the rate is extremely low. The ddPCR method was used for this purpose to gain a reliable quantitative mutation rate. When a pool of cell mixtures with a rare mutant is sequentially partitioned randomly into smaller pools (such as different wells in a 96-well plate), the mutation rate in one or a few small pools will increase significantly due to the overall significant decrease of cells in a pool following a Poisson distribution. The capability to locate these enriched wells using a quantitative mutation measurement can facilitate serial pool partition and mutant identification, until the rate of desired mutants surpasses the practical threshold for clonal identification. Although a powerful and quick way to enrich mutation, sib-selection is not a clonogenic process *per se*. Thus subsequent clonal mutant strain identification is needed to isolate the intended mutant cell.

**8.2. Estimation of Off-Target Mutations in Isolated Cell Clones.** Acquiring pure cell populations with the desired genetic modifications should not be considered as the final step before using these cell models for functional studies. No matter how carefully the experiment was designed, it is likely that some off-target modifications were introduced into the cell pool by CRISPR. If any of these are carried on into the final selected clones, these additional genetic modifications might complicate further functional analysis.

Whole genome sequencing of the isolated cell clones remains the most rigorous standard to estimate the off-target lesions [119–121]. It remains expensive, especially for human cells, since the complete genome requires a significant

sequencing depth to detect the occurrence of low frequency indels. While its costs prohibit routine use to examine all isolated cell clones in a typical lab, a reasonable approximation can usually be made by targeted sequencing of predicted off-target sites. This can be done in a low-throughput manner using PCR and Sanger sequencing of a number of individual predicted off-target sites with significant targeting probability. Alternatively, multiplexed next-generation targeted sequencing can be achieved by covering a large number of off-target sites simultaneously from multiple single-cell clones with significant sequencing depth [46, 122]. In the case of targeted sequencing, the choice of examined genomic region becomes critical. While various *in silico* platforms give a rough estimate of potential off-target sites, recent advances on genome-wide breakpoint sequencing technology (such as CHIP-Seq [43, 122], Digenome-seq [123] and GUIDE-seq [124], and genome-wide translocation sequencing [125]) offer a more realistic range of potential off-target sites in any given genome. While these platforms collectively can aid targeted genome sequencing of the engineered cells, precautions are still warranted since off-target CRISPR targeting can be influenced by the different cell types used and minor differences of genome sequence [126]. Some additional practical precautions should be taken into consideration, especially when the undesirable off-target lesions are not sufficiently characterized or hard to avoid.

**8.3. Correlating Phenotype and Genotype Controls.** When a certain phenotype is displayed after CRISPR-mediated editing in the clonogenically isolated mutant cells, the phenotype is not necessarily caused by the intended target due

to the possibility of poorly characterized off-target lesions. The genotype/phenotype association can be strengthened by verification using additional clonogenic clones carrying independent mutations generated by different CRISPR agents targeting the same locus. Because identical off-target lesions might be generated by the same gRNA, it is not possible to strictly exclude this possibility by relying on additional clones generated by a single gRNA. Therefore, additional gRNA is desired to target the same region of interest to achieve the identical phenotypic outcome. With limited overlapping of off-target sites, multiple gRNA designs ensure that any shared phenotype exhibited after editing using all gRNA correlates with the genotype of interest with high confidence. Aside from establishing proper controls for CRISPR targeting, genetic rescue is considered the gold standard to formally establish the causal relationship between phenotype and genotype. For loss of function mutations, introducing the intact target genes or gene products into the engineered cells should serve the purpose. Introducing the gene of interest back into the endogenous engineered locus is readily achievable by CRISPR [127–129] and is preferable, since the rescue genetic material is under endogenous transcriptional control. In the case of gain-of-function mutations where genetic rescue is difficult to achieve, pharmaceutical genetic approaches are useful in functional validations. Fine-tuning the functionality of a given target or relevant pathways using well-characterized specific drugs could provide independently supported evidence.

## 9. A Much Brighter Future for Stem Cell Models

The accumulation of large-scale human genome-sequencing efforts in the past few years greatly accelerated genetic discovery by linking genetic variations discovered in human populations or disease-associated somatic tissue to a disease state. Stem cell models, on the other hand, are traditionally extremely powerful in establishing the mechanistic linkage between genotype and phenotype. The recent explosion of applications of CRISPR/Cas9 genome-editing techniques now establishes the causal relationship between genotype and cellular behaviors with great flexibility and efficiency. While our current review can grasp neither the full extent nor the rapid evolution of these applications, a few prominent examples are highlighted below to demonstrate the range and depth of these applications.

One of the earliest successful applications of CRISPR in stem cell research was to correct the CTCF mutation in cultured intestinal stem cells from cystic fibrosis (CF) patients [130]. Besides fixing local sequence errors, CRISPR was recently used to correct a chromosomal structural abnormality (a chromosomal inversion over a several-hundred-kilo-base-pair) associated with Hemophilia A [131]. Using stem cell models (especially patient-derived iPSCs), CRISPR was used to correct more than a dozen disease-associated genetic lesions across a wide spectrum [115, 130–143], including metabolic disorders, immunological deficiencies, and neuromuscular disorders. These genetically corrected,

patient-derived stem cells might be the critical vehicle for future cell and gene therapies, with further improvement on its safety.

Regardless of its therapeutic potential, CRISPR is an invaluable tool in establishing the causal relationship between genes and stem cell behavior. Clevers group recently modeled the occurrence of the 4 most frequent mutations identified in human colorectal cancer within the context of a human intestinal stem cell organoid culture. This analysis enabled them to pinpoint the driver mutations causing extensive aneuploidy within this cancer stem cell model [117]. CRISPR also helped to pinpoint a specific single-nucleotide polymorphism (SNP) in the human FTO locus as the critical effector for obesity [144]. Previous genome-wide association studies indicated the FTO region harbors the strongest genetic association with obesity, while no mechanistic association could be drawn. A SNP in the FTO locus was further nailed down as the obesity-causing variant. Modeling the conversion of this one nucleotide using CRISPR in the context of isogenic, patient-derived preadipocytes provided the critical link between this single-nucleotide substitution and distinct adipocyte differentiation programs: thermogenic beige adipocytes versus fat-storing white adipocytes. This stem cell model, combined with the power of CRISPR-mediated genome editing to change one particular nucleotide in the human genome, helped resolve one of the longest standing mysteries in human genetics. Thus, we are extremely enthusiastic for a much brighter future for making and using stem cell models for similar mechanistic studies.

## Abbreviations and Acronyms

ZFN:	Zinc Finger Nucleases
TALEN:	TALE domains in transcription activator-like effector nucleases
CRISPR/Cas:	Clustered regularly interspaced palindromic repeats/CRISPR-associated
tracrRNA:	Transactivating CRISPR RNA
crRNA:	CRISPR repeat RNA
PAM:	Protospacer adjacent motif
RNP:	Ribonucleoprotein
gRNA:	Guide RNA
dsDNA:	Double-stranded DNA
DSB:	Double-strand break
NHEJ:	Nonhomologous end joining
HR:	Homologous recombination
PAGE:	Polyacrylamide gel electrophoresis
HRMA:	High Resolution Melting Analysis
CHIP-Seq:	Chromatin Immunoprecipitation Sequencing.

## Conflict of Interests

The authors declare that there is no conflict of interests regarding the publication of this paper.

## Authors' Contribution

Bing Shui and Liz Hernandez Matias contributed equally.

## Acknowledgments

The authors thank Lisa M. Anttila, Kristi Simons, and Alison Seemann for assistance with paper preparation. They thank Dr. Jeong Heon Lee and the Mayo Clinic Center for Individualized Medicine Epigenetics Development Laboratory for reagents and technical support. This work was supported in part by the Mayo Clinic Center for Individualized Medicine. The work was funded by a Mayo Clinic Summer Undergraduate Research Fellowship to Bing Shui, a LSAMP Bridge to the Doctorate Cohort X NSF Grant Award (HRD-1400870) to Liz Hernandez Matias, a Mayo Clinic New Investigator Startup Fund, a Richard F. Emslander Career Development Award, and a Mayo Clinic Center for Biomedical Discovery Platform Award to Dr. Yi Guo.

## References

- [1] M. Bibikova, K. Beumer, J. K. Trautman, and D. Carroll, "Enhancing gene targeting with designed zinc finger nucleases," *Science*, vol. 300, no. 5620, p. 764, 2003.
- [2] Y.-G. Kim, J. Cha, and S. Chandrasegaran, "Hybrid restriction enzymes: zinc finger fusions to Fok I cleavage domain," *Proceedings of the National Academy of Sciences of the United States of America*, vol. 93, no. 3, pp. 1156–1160, 1996.
- [3] M. H. Porteus and D. Baltimore, "Chimeric nucleases stimulate gene targeting in human cells," *Science*, vol. 300, no. 5620, p. 763, 2003.
- [4] J. Boch, H. Scholze, S. Schornack et al., "Breaking the code of DNA binding specificity of TAL-type III effectors," *Science*, vol. 326, no. 5959, pp. 1509–1512, 2009.
- [5] M. J. Moscou and A. J. Bogdanove, "A simple cipher governs DNA recognition by TAL effectors," *Science*, vol. 326, no. 5959, p. 1501, 2009.
- [6] A. Bolotin, B. Quinquis, A. Sorokin, and S. D. Ehrlich, "Clustered regularly interspaced short palindrome repeats (CRISPRs) have spacers of extrachromosomal origin," *Microbiology*, vol. 151, no. 8, pp. 2551–2561, 2005.
- [7] F. J. M. Mojica, C. Díez-Villaseñor, J. García-Martínez, and E. Soria, "Intervening sequences of regularly spaced prokaryotic repeats derive from foreign genetic elements," *Journal of Molecular Evolution*, vol. 60, no. 2, pp. 174–182, 2005.
- [8] C. Pourcel, G. Salvignol, and G. Vergnaud, "CRISPR elements in *Yersinia pestis* acquire new repeats by preferential uptake of bacteriophage DNA, and provide additional tools for evolutionary studies," *Microbiology*, vol. 151, no. 3, pp. 653–663, 2005.
- [9] M. Boettcher and M. T. McManus, "Choosing the right tool for the job: RNAi, TALEN, or CRISPR," *Molecular Cell*, vol. 58, no. 4, pp. 575–585, 2015.
- [10] M. Jinek, K. Chylinski, I. Fonfara, M. Hauer, J. A. Doudna, and E. Charpentier, "A programmable dual-RNA-guided DNA endonuclease in adaptive bacterial immunity," *Science*, vol. 337, no. 6096, pp. 816–821, 2012.
- [11] M. Jinek, A. East, A. Cheng, S. Lin, E. Ma, and J. Doudna, "RNA-programmed genome editing in human cells," *eLife*, vol. 2013, no. 2, Article ID e00471, 2013.
- [12] L. Cong, F. A. Ran, D. Cox et al., "Multiplex genome engineering using CRISPR/Cas systems," *Science*, vol. 339, no. 6121, pp. 819–823, 2013.
- [13] P. Mali, L. Yang, K. M. Esvelt et al., "RNA-guided human genome engineering via Cas9," *Science*, vol. 339, no. 6121, pp. 823–826, 2013.
- [14] W. Jiang and L. A. Marraffini, "CRISPR-cas: new tools for genetic manipulations from bacterial immunity systems," *Annual Review of Microbiology*, vol. 69, no. 1, pp. 209–228, 2015.
- [15] E. J. Sontheimer and R. Barrangou, "The bacterial origins of the crispr genome-editing revolution," *Human Gene Therapy*, vol. 26, no. 7, pp. 413–424, 2015.
- [16] K. S. Makarova, N. V. Grishin, S. A. Shabalina, Y. I. Wolf, and E. V. Koonin, "A putative RNA-interference-based immune system in prokaryotes: computational analysis of the predicted enzymatic machinery, functional analogies with eukaryotic RNAi, and hypothetical mechanisms of action," *Biology Direct*, vol. 1, article 7, 2006.
- [17] J. E. Garneau, M.-È. Dupuis, M. Villion et al., "The CRISPR/cas bacterial immune system cleaves bacteriophage and plasmid DNA," *Nature*, vol. 468, no. 7320, pp. 67–71, 2010.
- [18] R. E. Haurwitz, M. Jinek, B. Wiedenheft, K. Zhou, and J. A. Doudna, "Sequence- and structure-specific RNA processing by a CRISPR endonuclease," *Science*, vol. 329, no. 5997, pp. 1355–1358, 2010.
- [19] F. V. Karginov and G. J. Hannon, "The CRISPR system: small RNA-guided defense in bacteria and archaea," *Molecular Cell*, vol. 37, no. 1, pp. 7–19, 2010.
- [20] R. Barrangou and L. A. Marraffini, "CRISPR-Cas systems: prokaryotes upgrade to adaptive immunity," *Molecular Cell*, vol. 54, no. 2, pp. 234–244, 2014.
- [21] I. Grissa, G. Vergnaud, and C. Pourcel, "The CRISPRdb database and tools to display CRISPRs and to generate dictionaries of spacers and repeats," *BMC Bioinformatics*, vol. 8, article 172, 2007.
- [22] H. Deveau, R. Barrangou, J. E. Garneau et al., "Phage response to CRISPR-encoded resistance in *Streptococcus thermophilus*," *Journal of Bacteriology*, vol. 190, no. 4, pp. 1390–1400, 2008.
- [23] F. J. M. Mojica, C. Díez-Villaseñor, J. García-Martínez, and C. Almendros, "Short motif sequences determine the targets of the prokaryotic CRISPR defence system," *Microbiology*, vol. 155, no. 3, pp. 733–740, 2009.
- [24] K. Yusa, S. T. Rashid, H. Strick-Marchand et al., "Targeted gene correction of alpha1-antitrypsin deficiency in induced pluripotent stem cells," *Nature*, vol. 478, no. 7369, pp. 391–394, 2011.
- [25] H. Yin, W. Xue, S. Chen et al., "Genome editing with Cas9 in adult mice corrects a disease mutation and phenotype," *Nature Biotechnology*, vol. 32, no. 6, pp. 551–553, 2014.
- [26] K. Yoshimi, T. Kaneko, B. Voigt, and T. Mashimo, "Allele-specific genome editing and correction of disease-associated phenotypes in rats using the CRISPR-Cas platform," *Nature Communications*, vol. 5, article 4240, 2014.
- [27] Y. Wu, D. Liang, Y. Wang et al., "Correction of a genetic disease in mouse via use of CRISPR-Cas9," *Cell Stem Cell*, vol. 13, no. 6, pp. 659–662, 2013.
- [28] P. D. Hsu, E. S. Lander, and F. Zhang, "Development and applications of CRISPR-Cas9 for genome engineering," *Cell*, vol. 157, no. 6, pp. 1262–1278, 2014.
- [29] K. M. Esvelt, P. Mali, J. L. Braff, M. Moosburner, S. J. Yaung, and G. M. Church, "Orthogonal Cas9 proteins for RNA-guided gene regulation and editing," *Nature Methods*, vol. 10, no. 11, pp. 1116–1121, 2013.

- [30] I. Fonfara, A. Le Rhun, K. Chylinski et al., "Phylogeny of Cas9 determines functional exchangeability of dual-RNA and Cas9 among orthologous type II CRISPR-Cas systems," *Nucleic Acids Research*, vol. 42, no. 4, pp. 2577–2590, 2014.
- [31] F. A. Ran, L. Cong, W. X. Yan et al., "In vivo genome editing using *Staphylococcus aureus* Cas9," *Nature*, vol. 520, no. 7546, pp. 186–191, 2015.
- [32] B. Chen, L. A. Gilbert, B. A. Cimini et al., "Dynamic imaging of genomic loci in living human cells by an optimized CRISPR/Cas system," *Cell*, vol. 155, no. 7, pp. 1479–1491, 2013.
- [33] H. Ma, A. Naseri, P. Reyes-Gutierrez, S. A. Wolfe, S. Zhang, and T. Pederson, "Multicolor CRISPR labeling of chromosomal loci in human cells," *Proceedings of the National Academy of Sciences of the United States of America*, vol. 112, no. 10, pp. 3002–3007, 2015.
- [34] D. Carroll, "Staying on target with CRISPR-Cas," *Nature Biotechnology*, vol. 31, no. 9, pp. 807–809, 2013.
- [35] B. P. Kleinstiver, M. S. Prew, S. Q. Tsai et al., "Engineered CRISPR-Cas9 nucleases with altered PAM specificities," *Nature*, vol. 523, no. 7561, pp. 481–485, 2015.
- [36] B. Zetsche, J. S. Gootenberg, O. O. Abudayyeh et al., "Cpf1 is a single RNA-guided endonuclease of a class 2 CRISPR-cas system," *Cell*, vol. 163, no. 3, pp. 759–771, 2015.
- [37] M. Jinek, F. Jiang, D. W. Taylor et al., "Structures of Cas9 endonucleases reveal RNA-mediated conformational activation," *Science*, vol. 343, no. 6176, Article ID 1247997, 2014.
- [38] H. Nishimasu, F. A. Ran, P. D. Hsu et al., "Crystal structure of Cas9 in complex with guide RNA and target DNA," *Cell*, vol. 156, no. 5, pp. 935–949, 2014.
- [39] P. Mali, K. M. Esvelt, and G. M. Church, "Cas9 as a versatile tool for engineering biology," *Nature Methods*, vol. 10, no. 10, pp. 957–963, 2013.
- [40] F. A. Ran, P. D. Hsu, C.-Y. Lin et al., "Double nicking by RNA-guided CRISPR cas9 for enhanced genome editing specificity," *Cell*, vol. 154, no. 6, pp. 1380–1389, 2013.
- [41] P. D. Hsu, D. A. Scott, J. A. Weinstein et al., "DNA targeting specificity of RNA-guided Cas9 nucleases," *Nature Biotechnology*, vol. 31, no. 9, pp. 827–832, 2013.
- [42] V. Pattanayak, S. Lin, J. P. Guilinger, E. Ma, J. A. Doudna, and D. R. Liu, "High-throughput profiling of off-target DNA cleavage reveals RNA-programmed Cas9 nuclease specificity," *Nature Biotechnology*, vol. 31, no. 9, pp. 839–843, 2013.
- [43] X. Wu, D. A. Scott, A. J. Kriz et al., "Genome-wide binding of the CRISPR endonuclease Cas9 in mammalian cells," *Nature Biotechnology*, vol. 32, no. 7, pp. 670–676, 2014.
- [44] Y. Fu, J. A. Foden, C. Khayter et al., "High-frequency off-target mutagenesis induced by CRISPR-Cas nucleases in human cells," *Nature Biotechnology*, vol. 31, no. 9, pp. 822–826, 2013.
- [45] Y. Fu, J. D. Sander, D. Reyon, V. M. Cascio, and J. K. Joung, "Improving CRISPR-Cas nuclease specificity using truncated guide RNAs," *Nature Biotechnology*, vol. 32, no. 3, pp. 279–284, 2014.
- [46] S. W. Cho, S. Kim, Y. Kim et al., "Analysis of off-target effects of CRISPR/Cas-derived RNA-guided endonucleases and nickases," *Genome Research*, vol. 24, no. 1, pp. 132–141, 2014.
- [47] C. Anders, O. Niewoehner, A. Duerst, and M. Jinek, "Structural basis of PAM-dependent target DNA recognition by the Cas9 endonuclease," *Nature*, vol. 513, no. 7519, pp. 569–573, 2014.
- [48] S. H. Sternberg, S. Redding, M. Jinek, E. C. Greene, and J. A. Doudna, "DNA interrogation by the CRISPR RNA-guided endonuclease Cas9," *Nature*, vol. 507, no. 7490, pp. 62–67, 2014.
- [49] S. W. Cho, J. Lee, D. Carroll, J.-S. Kim, and J. Lee, "Heritable gene knockout in *Caenorhabditis elegans* by direct injection of Cas9-sgRNA ribonucleoproteins," *Genetics*, vol. 195, no. 3, pp. 1177–1180, 2013.
- [50] P. Mali, J. Aach, P. B. Stranges et al., "CAS9 transcriptional activators for target specificity screening and paired nickases for cooperative genome engineering," *Nature Biotechnology*, vol. 31, no. 9, pp. 833–838, 2013.
- [51] T. Wang, J. J. Wei, D. M. Sabatini, and E. S. Lander, "Genetic screens in human cells using the CRISPR-Cas9 system," *Science*, vol. 343, no. 6166, pp. 80–84, 2014.
- [52] J. G. Doench, E. Hartenian, D. B. Graham et al., "Rational design of highly active sgRNAs for CRISPR-Cas9-mediated gene inactivation," *Nature Biotechnology*, vol. 32, no. 12, pp. 1262–1267, 2014.
- [53] H. Xu, T. Xiao, C.-H. Chen et al., "Sequence determinants of improved CRISPR sgRNA design," *Genome Research*, 2015.
- [54] S. Nielsen, Y. Yuzenkova, and N. Zenkin, "Mechanism of eukaryotic RNA polymerase III transcription termination," *Science*, vol. 340, no. 6140, pp. 1577–1580, 2013.
- [55] M. A. Moreno-Mateos, C. E. Vejnar, J. Beaudoin et al., "CRISPRscan: designing highly efficient sgRNAs for CRISPR-Cas9 targeting in vivo," *Nature Methods*, vol. 12, no. 10, pp. 982–988, 2015.
- [56] C. Ronda, L. E. Pedersen, H. G. Hansen et al., "Accelerating genome editing in CHO cells using CRISPR Cas9 and CRISPy, a web-based target finding tool," *Biotechnology and Bioengineering*, vol. 111, no. 8, pp. 1604–1616, 2014.
- [57] H. Xu, T. Xiao, C.-H. Chen et al., "Sequence determinants of improved CRISPR sgRNA design," *Genome Research*, vol. 25, no. 8, pp. 1147–1157, 2015.
- [58] M. Stemmer, T. Thumberger, M. del Sol Keyer, J. Wittbrodt, J. L. Mateo, and S. Maas, "CCTop: an intuitive, flexible and reliable CRISPR/Cas9 target prediction tool," *PLoS ONE*, vol. 10, no. 4, Article ID e0124633, p. e0124633, 2015.
- [59] S. K. Upadhyay and S. Sharma, "SSFinder: high throughput CRISPR-Cas target sites prediction tool," *BioMed Research International*, vol. 2014, Article ID 742482, 4 pages, 2014.
- [60] Q. U. Ain, J. Y. Chung, and Y.-H. Kim, "Current and future delivery systems for engineered nucleases: ZFN, TALEN and RGEN," *Journal of Controlled Release*, vol. 205, pp. 120–127, 2015.
- [61] I. Maggio, M. Holkers, J. Liu, J. M. Janssen, X. Chen, and M. A. F. V. Gonçalves, "Adenoviral vector delivery of RNA-guided CRISPR/Cas9 nuclease complexes induces targeted mutagenesis in a diverse array of human cells," *Scientific Reports*, vol. 4, article 5105, 2014.
- [62] W. Xue, S. Chen, H. Yin et al., "CRISPR-mediated direct mutation of cancer genes in the mouse liver," *Nature*, vol. 514, no. 7522, pp. 380–384, 2014.
- [63] Z.-Y. Chen, C.-Y. He, A. Ehrhardt, and M. A. Kay, "Minicircle DNA vectors devoid of bacterial DNA result in persistent and high-level transgene expression in vivo," *Molecular Therapy*, vol. 8, no. 3, pp. 495–500, 2003.
- [64] S. Kim, D. Kim, S. W. Cho, J. Kim, and J.-S. Kim, "Highly efficient RNA-guided genome editing in human cells via delivery of purified Cas9 ribonucleoproteins," *Genome Research*, vol. 24, no. 6, pp. 1012–1019, 2014.
- [65] H. Koike-Yusa, Y. Li, E.-P. Tan, M. D. C. Velasco-Herrera, and K. Yusa, "Genome-wide recessive genetic screening in mammalian cells with a lentiviral CRISPR-guide RNA library," *Nature Biotechnology*, vol. 32, no. 3, pp. 267–273, 2014.

- [66] O. Shalem, N. E. Sanjana, E. Hartenian et al., "Genome-scale CRISPR-Cas9 knockout screening in human cells," *Science*, vol. 343, no. 6166, pp. 84–87, 2014.
- [67] Y. Zhou, S. Zhu, C. Cai et al., "High-throughput screening of a CRISPR/Cas9 library for functional genomics in human cells," *Nature*, vol. 509, no. 7501, pp. 487–491, 2014.
- [68] R. Cheng, J. Peng, Y. Yan et al., "Efficient gene editing in adult mouse livers via adenoviral delivery of CRISPR/Cas9," *FEBS Letters*, vol. 588, no. 21, pp. 3954–3958, 2014.
- [69] D. Wang, H. Mou, S. Li et al., "Adenovirus-mediated somatic genome editing of *Pten* by CRISPR/Cas9 in mouse liver in spite of Cas9-specific immune responses," *Human Gene Therapy*, vol. 26, no. 7, pp. 432–442, 2015.
- [70] X. Liang, J. Potter, S. Kumar et al., "Rapid and highly efficient mammalian cell engineering via Cas9 protein transfection," *Journal of Biotechnology*, vol. 208, pp. 44–53, 2015.
- [71] A. Hendel, R. O. Bak, J. T. Clark et al., "Chemically modified guide RNAs enhance CRISPR-Cas genome editing in human primary cells," *Nature Biotechnology*, vol. 33, no. 9, pp. 985–989, 2015.
- [72] S. Lin, B. T. Staahl, R. K. Alla, and J. A. Doudna, "Enhanced homology-directed human genome engineering by controlled timing of CRISPR/Cas9 delivery," *eLife*, vol. 3, Article ID e04766, 2014.
- [73] P. K. Mandal, L. M. R. Ferreira, R. Collins et al., "Efficient ablation of genes in human hematopoietic stem and effector cells using CRISPR/Cas9," *Cell Stem Cell*, vol. 15, no. 5, pp. 643–652, 2014.
- [74] J. A. Zuris, D. B. Thompson, Y. Shu et al., "Cationic lipid-mediated delivery of proteins enables efficient protein-based genome editing in vitro and in vivo," *Nature Biotechnology*, vol. 33, no. 1, pp. 73–80, 2015.
- [75] T. Koo, J. Lee, and J. Kim, "Measuring and reducing off-target activities of programmable nucleases including CRISPR-Cas9," *Molecules and Cells*, vol. 38, no. 6, pp. 475–481, 2015.
- [76] E. K. Brinkman, T. Chen, M. Amendola, and B. van Steensel, "Easy quantitative assessment of genome editing by sequence trace decomposition," *Nucleic Acids Research*, vol. 42, no. 22, article e168, 2014.
- [77] J. T. Hill, B. L. Demarest, B. W. Bisgrove, Y.-C. Su, M. Smith, and H. J. Yost, "Poly peak parser: method and software for identification of unknown indels using sanger sequencing of polymerase chain reaction products," *Developmental Dynamics*, vol. 243, no. 12, pp. 1632–1636, 2014.
- [78] M. C. Porter, K. Murray-Leisure, and P. Dalbey, "Aeromonas hydrophila cellulitis. A case report," *Journal of the American Podiatric Medical Association*, vol. 78, no. 5, pp. 259–261, 1988.
- [79] Z. Yang, C. Steentoft, C. Hauge et al., "Fast and sensitive detection of indels induced by precise gene targeting," *Nucleic Acids Research*, vol. 43, no. 9, article e59, 2015.
- [80] D. Y. Guschin, A. J. Waite, G. E. Katibah, J. C. Miller, M. C. Holmes, and E. J. Rebar, "A rapid and general assay for monitoring endogenous gene modification," *Methods in Molecular Biology*, vol. 649, pp. 247–256, 2010.
- [81] J. C. Miller, M. C. Holmes, J. Wang et al., "An improved zinc-finger nuclease architecture for highly specific genome editing," *Nature Biotechnology*, vol. 25, no. 7, pp. 778–785, 2007.
- [82] Y. Niu, B. Shen, Y. Cui et al., "Generation of gene-modified cynomolgus monkey via Cas9/RNA-mediated gene targeting in one-cell embryos," *Cell*, vol. 156, no. 4, pp. 836–843, 2014.
- [83] T. Sakurai, S. Watanabe, A. Kamiyoshi, M. Sato, and T. Shindo, "A single blastocyst assay optimized for detecting CRISPR/Cas9 system-induced indel mutations in mice," *BMC Biotechnology*, vol. 14, article 69, 2014.
- [84] Y. H. Sung, Y. Jin, S. Kim, and H.-W. Lee, "Generation of knockout mice using engineered nucleases," *Methods*, 2014.
- [85] X. Zhu, Y. Xu, S. Yu et al., "An efficient genotyping method for genome-modified animals and human cells generated with CRISPR/Cas9 system," *Scientific Reports*, vol. 4, article 6420, 2014.
- [86] A.-C. Déclais and D. M. Lilley, "New insight into the recognition of branched DNA structure by junction-resolving enzymes," *Current Opinion in Structural Biology*, vol. 18, no. 1, pp. 86–95, 2008.
- [87] P. Qiu, H. Shandilya, J. M. D'Alessio, K. O'Connor, J. Durocher, and G. F. Gerard, "Mutation detection using Surveyor nuclease," *BioTechniques*, vol. 36, no. 4, pp. 702–707, 2004.
- [88] L. Vouillot, A. Thelie, and N. Pollet, "Comparison of T7E1 and surveyor mismatch cleavage assays to detect mutations triggered by engineered nucleases," *G3: Genes—Genomes—Genetics*, vol. 5, no. 3, pp. 407–415, 2015.
- [89] M. C. Huang, W. C. Cheong, L. S. Lim, and M.-H. Li, "A simple, high sensitivity mutation screening using Ampligase mediated T7 endonuclease I and Surveyor nuclease with microfluidic capillary electrophoresis," *Electrophoresis*, vol. 33, no. 5, pp. 788–796, 2012.
- [90] T. J. Dahlem, K. Hoshijima, M. J. Jurynek et al., "Simple methods for generating and detecting locus-specific mutations induced with TALENs in the zebrafish genome," *PLoS Genetics*, vol. 8, no. 8, Article ID e1002861, 2012.
- [91] Y. Miyaoka, A. H. Chan, L. M. Judge et al., "Isolation of single-base genome-edited human iPSC cells without antibiotic selection," *Nature Methods*, vol. 11, no. 3, pp. 291–293, 2014.
- [92] F. Soldner, J. Laganière, A. W. Cheng et al., "Generation of isogenic pluripotent stem cells differing exclusively at two early onset Parkinson point mutations," *Cell*, vol. 146, no. 2, pp. 318–331, 2011.
- [93] A. Hendel, E. J. Kildebeck, E. J. Fine et al., "Quantifying genome-editing outcomes at endogenous loci with SMRT sequencing," *Cell Reports*, vol. 7, no. 1, pp. 293–305, 2014.
- [94] B. J. Hindson, K. D. Ness, D. A. Masquelier et al., "High-throughput droplet digital PCR system for absolute quantitation of DNA copy number," *Analytical Chemistry*, vol. 83, no. 22, pp. 8604–8610, 2011.
- [95] L. Miotke, B. T. Lau, R. T. Rumma, and H. P. Ji, "High sensitivity detection and quantitation of DNA copy number and single nucleotide variants with single color droplet digital PCR," *Analytical Chemistry*, vol. 86, no. 5, pp. 2618–2624, 2014.
- [96] R. S. Weisman, D. Price, and P. H. Wald, "Outpatient management of acute and chronic poisoning," *Primary Care*, vol. 13, no. 1, pp. 151–156, 1986.
- [97] E. Pastrana, V. Silva-Vargas, and F. Doetsch, "Eyes wide open: a critical review of sphere-formation as an assay for stem cells," *Cell Stem Cell*, vol. 8, no. 5, pp. 486–498, 2011.
- [98] B. L. K. Coles-Takabe, I. Brain, K. A. Purpura et al., "Don't look: growing clonal versus nonclonal neural stem cell colonies," *Stem Cells*, vol. 26, no. 11, pp. 2938–2944, 2008.
- [99] I. Singec, R. Knoth, R. P. Meyer et al., "Defining the actual sensitivity and specificity of the neurosphere assay in stem cell biology," *Nature Methods*, vol. 3, no. 10, pp. 801–806, 2006.

- [100] H. Mori, K. Ninomiya, M. Kino-Oka et al., “Effect of neurosphere size on the growth rate of human neural stem/progenitor cells,” *Journal of Neuroscience Research*, vol. 84, no. 8, pp. 1682–1691, 2006.
- [101] G. Orive, E. Santos, J. L. Pedraz, and R. M. Hernández, “Application of cell encapsulation for controlled delivery of biological therapeutics,” *Advanced Drug Delivery Reviews*, vol. 67–68, pp. 3–14, 2014.
- [102] A. Kang, J. Park, J. Ju, G. S. Jeong, and S.-H. Lee, “Cell encapsulation via microtechnologies,” *Biomaterials*, vol. 35, no. 9, pp. 2651–2663, 2014.
- [103] H. C. Kluijn-Nelemans, H. W. J. Hakvoort, J. H. Jansen et al., “Colony growth of normal and neoplastic cells in various concentrations of methylcellulose,” *Experimental Hematology*, vol. 16, no. 11, pp. 922–928, 1988.
- [104] P. S. Hoppe, D. L. Coutu, and T. Schroeder, “Single-cell technologies sharpen up mammalian stem cell research,” *Nature cell Biology*, vol. 16, no. 10, pp. 919–927, 2014.
- [105] K. Hope and M. Bhatia, “Clonal interrogation of stem cells,” *Nature Methods*, vol. 8, no. 4, supplement, pp. S36–S40, 2011.
- [106] K. Rodgers and M. McVey, “Error-prone repair of DNA double-strand breaks,” *Journal of Cellular Physiology*, vol. 231, no. 1, pp. 15–24, 2016.
- [107] K. J. Beumer and D. Carroll, “Targeted genome engineering techniques in *Drosophila*,” *Methods*, vol. 68, no. 1, pp. 29–37, 2014.
- [108] K. J. Beumer, J. K. Trautman, K. Mukherjee, and D. Carroll, “Donor DNA utilization during gene targeting with zinc-finger nucleases,” *G3: Genes—Genomes—Genetics*, vol. 3, no. 4, pp. 657–664, 2013.
- [109] K. J. Beumer, J. K. Trautman, A. Bozas et al., “Efficient gene targeting in *Drosophila* by direct embryo injection with zinc-finger nucleases,” *Proceedings of the National Academy of Sciences of the United States of America*, vol. 105, no. 50, pp. 19821–19826, 2008.
- [110] M. Bibikova, D. Carroll, D. J. Segal et al., “Stimulation of homologous recombination through targeted cleavage by chimeric nucleases,” *Molecular and Cellular Biology*, vol. 21, no. 1, pp. 289–297, 2001.
- [111] L. A. Baena-Lopez, C. Alexandre, A. Mitchell, L. Pasakarnis, and J.-P. Vincent, “Accelerated homologous recombination and subsequent genome modification in *Drosophila*,” *Development*, vol. 140, no. 23, pp. 4818–4825, 2013.
- [112] W.-D. Heyer, K. T. Ehmsen, and J. Liu, “Regulation of homologous recombination in eukaryotes,” *Annual Review of Genetics*, vol. 44, pp. 113–139, 2010.
- [113] J. M. Daley and P. Sung, “53BP1, BRCA1, and the choice between recombination and end joining at DNA double-strand breaks,” *Molecular and Cellular Biology*, vol. 34, no. 8, pp. 1380–1388, 2014.
- [114] L. Ye, J. Wang, A. I. Beyer et al., “Seamless modification of wild-type induced pluripotent stem cells to the natural CCR5Delta32 mutation confers resistance to HIV infection,” *Proceedings of the National Academy of Sciences of the United States of America*, vol. 111, no. 26, pp. 9591–9596, 2014.
- [115] F. Xie, L. Ye, J. C. Chang et al., “Seamless gene correction of  $\beta$ -thalassemia mutations in patient-specific iPSCs using CRISPR/Cas9 and piggyBac,” *Genome Research*, vol. 24, no. 9, pp. 1526–1533, 2014.
- [116] S. Ramakrishna, “Surrogate reporter-based enrichment of cells containing RNA-guided Cas9 nuclease-induced mutations,” *Nature Communications*, vol. 5, article 3378, 2014.
- [117] J. Drost, R. H. van Jaarsveld, B. Ponsioen et al., “Sequential cancer mutations in cultured human intestinal stem cells,” *Nature*, vol. 521, no. 7550, pp. 43–47, 2015.
- [118] M. McCormick, “Sib selection,” in *Methods in Enzymology*, vol. 151, chapter 33, pp. 445–449, Elsevier, 1987.
- [119] C. Smith, A. Gore, W. Yan et al., “Whole-genome sequencing analysis reveals high specificity of CRISPR/Cas9 and TALEN-based genome editing in human iPSCs,” *Cell Stem Cell*, vol. 15, no. 1, pp. 12–13, 2014.
- [120] K. Suzuki, C. Yu, J. Qu et al., “Targeted gene correction minimally impacts whole-genome mutational load in human-disease-specific induced pluripotent stem cell clones,” *Cell Stem Cell*, vol. 15, no. 1, pp. 31–36, 2014.
- [121] A. Veres, B. S. Gosis, Q. Ding et al., “Low incidence of off-target mutations in individual CRISPR-Cas9 and TALEN targeted human stem cell clones detected by whole-genome sequencing,” *Cell Stem Cell*, vol. 15, no. 1, pp. 27–30, 2014.
- [122] H. O’Geen, I. M. Henry, M. S. Bhakta, J. F. Meckler, and D. J. Segal, “A genome-wide analysis of Cas9 binding specificity using ChIP-seq and targeted sequence capture,” *Nucleic Acids Research*, vol. 43, no. 6, pp. 3389–3404, 2015.
- [123] D. Kim, S. Bae, J. Park et al., “Digenome-seq: genome-wide profiling of CRISPR-Cas9 off-target effects in human cells,” *Nature Methods*, vol. 12, no. 3, pp. 237–243, 2015.
- [124] S. Q. Tsai, Z. Zheng, N. T. Nguyen et al., “GUIDE-seq enables genome-wide profiling of off-target cleavage by CRISPR-Cas nucleases,” *Nature Biotechnology*, vol. 33, no. 2, pp. 187–197, 2015.
- [125] R. L. Frock, J. Hu, R. M. Meyers, Y. Ho, E. Kii, and F. W. Alt, “Genome-wide detection of DNA double-stranded breaks induced by engineered nucleases,” *Nature Biotechnology*, vol. 33, no. 2, pp. 179–186, 2015.
- [126] L. Yang, D. Grishin, G. Wang et al., “Targeted and genome-wide sequencing reveal single nucleotide variations impacting specificity of Cas9 in human stem cells,” *Nature Communications*, vol. 5, article 5507, 2014.
- [127] Z. Zhu, N. Verma, F. González, Z. Shi, and D. Huangfu, “A CRISPR/Cas-mediated selection-free knockin strategy in human embryonic stem cells,” *Stem Cell Reports*, vol. 4, no. 6, pp. 1103–1111, 2015.
- [128] F. T. Merkle, W. Neuhausser, D. Santos et al., “Efficient CRISPR-Cas9-mediated generation of knockin human pluripotent stem cells lacking undesired mutations at the targeted locus,” *Cell Reports*, vol. 11, no. 6, pp. 875–883, 2015.
- [129] V. M. Bedell and S. C. Ekker, “Using engineered endonucleases to create knockout and knockin zebrafish models,” *Methods in Molecular Biology*, vol. 1239, pp. 291–305, 2015.
- [130] G. Schwank, B.-K. Koo, V. Sasselli et al., “Functional repair of CFTR by CRISPR/Cas9 in intestinal stem cell organoids of cystic fibrosis patients,” *Cell Stem Cell*, vol. 13, no. 6, pp. 653–658, 2013.
- [131] C. Y. Park, D. Kim, J. Son et al., “Functional correction of large factor VIII Gene chromosomal inversions in hemophilia a patient-derived iPSCs Using CRISPR-Cas9,” *Cell Stem Cell*, vol. 17, no. 2, pp. 213–220, 2015.
- [132] C. Y. Park, T. Halevy, D. Lee et al., “Reversion of *FMRI* methylation and silencing by editing the triplet repeats in fragile X iPSC-derived neurons,” *Cell Reports*, vol. 13, no. 2, pp. 234–241, 2015.
- [133] L. Xu, K. H. Park, L. Zhao et al., “CRISPR-mediated genome editing restores dystrophin expression and function in *mdx* mice,” *Molecular Therapy*, 2015.

- [134] R. Flynn, A. Grundmann, P. Renz et al., “CRISPR-mediated genotypic and phenotypic correction of a chronic granulomatous disease mutation in human iPSCs,” *Experimental Hematology*, vol. 43, no. 10, pp. 838–848.e3, 2015.
- [135] C. W. Chang, Y. Lai, E. Westin et al., “Modeling human severe combined immunodeficiency and correction by CRISPR/Cas9-enhanced gene targeting,” *Cell Reports*, vol. 12, no. 10, pp. 1668–1677, 2015.
- [136] A. L. Firth, T. Menon, G. Parker et al., “Functional gene correction for cystic fibrosis in lung epithelial cells generated from patient iPSCs,” *Cell Reports*, vol. 12, no. 9, pp. 1385–1390, 2015.
- [137] P. Xu, Y. Tong, X.-z. Liu et al., “Both TALENs and CRISPR/Cas9 directly target the HBB IVS2-654 (C > T) mutation in  $\beta$ -thalassemia-derived iPSCs,” *Scientific Reports*, vol. 5, Article ID 12065, 2015.
- [138] B. Song, Y. Fan, W. He et al., “Improved hematopoietic differentiation efficiency of gene-corrected beta-thalassemia induced pluripotent stem cells by CRISPR/Cas9 system,” *Stem Cells and Development*, vol. 24, no. 9, pp. 1053–1065, 2015.
- [139] D. G. Ousterout, A. M. Kabadi, P. I. Thakore, W. H. Majoros, T. E. Reddy, and C. A. Gersbach, “Multiplex CRISPR/Cas9-based genome editing for correction of dystrophin mutations that cause Duchenne muscular dystrophy,” *Nature Communications*, vol. 6, article 6244, 2015.
- [140] M. J. Osborn, R. Gabriel, B. R. Webber et al., “Fanconi anemia gene editing by the CRISPR/Cas9 system,” *Human Gene Therapy*, vol. 26, no. 2, pp. 114–126, 2015.
- [141] H. L. Li, N. Fujimoto, N. Sasakawa et al., “Precise correction of the dystrophin gene in duchenne muscular dystrophy patient induced pluripotent stem cells by TALEN and CRISPR-Cas9,” *Stem Cell Reports*, vol. 4, no. 1, pp. 143–154, 2015.
- [142] Y. Wu, H. Zhou, X. Fan et al., “Correction of a genetic disease by CRISPR-Cas9-mediated gene editing in mouse spermatogonial stem cells,” *Cell Research*, vol. 25, no. 1, pp. 67–79, 2015.
- [143] C. Long, J. R. McAnally, J. M. Shelton, A. A. Mireault, R. Bassel-Duby, and E. N. Olson, “Prevention of muscular dystrophy in mice by CRISPR/Cas9-mediated editing of germline DNA,” *Science*, no. 6201, pp. 1184–1188, 2014.
- [144] M. Claussnitzer, S. N. Dankel, K. Kim et al., “FTO obesity variant circuitry and adipocyte browning in humans,” *The New England Journal of Medicine*, vol. 373, no. 10, pp. 895–907, 2015.
- [145] R. M. Walsh and K. Hochedlinger, “A variant CRISPR-Cas9 system adds versatility to genome engineering,” *Proceedings of the National Academy of Sciences of the United States of America*, vol. 110, no. 39, pp. 15514–15515, 2013.

## Research Article

# Calcium/Cobalt Alginate Beads as Functional Scaffolds for Cartilage Tissue Engineering

Stefano Focaroli,<sup>1</sup> Gabriella Teti,<sup>1</sup> Viviana Salvatore,<sup>1</sup>  
Isabella Orienti,<sup>2</sup> and Mirella Falconi<sup>1</sup>

<sup>1</sup>Department of Biomedical and Neuromotor Sciences, University of Bologna, 40126 Bologna, Italy

<sup>2</sup>Department of Pharmacy and Biotechnology, University of Bologna, 40126 Bologna, Italy

Correspondence should be addressed to Mirella Falconi; mirella.falconi@unibo.it

Received 30 July 2015; Revised 6 October 2015; Accepted 18 October 2015

Academic Editor: Malin Jonsson

Copyright © 2016 Stefano Focaroli et al. This is an open access article distributed under the Creative Commons Attribution License, which permits unrestricted use, distribution, and reproduction in any medium, provided the original work is properly cited.

Articular cartilage is a highly organized tissue with complex biomechanical properties. However, injuries to the cartilage usually lead to numerous health concerns and often culminate in disabling symptoms, due to the poor intrinsic capacity of this tissue for self-healing. Although various approaches are proposed for the regeneration of cartilage, its repair still represents an enormous challenge for orthopedic surgeons. The field of tissue engineering currently offers some of the most promising strategies for cartilage restoration, in which assorted biomaterials and cell-based therapies are combined to develop new therapeutic regimens for tissue replacement. The current study describes the *in vitro* behavior of human adipose-derived mesenchymal stem cells (hADSCs) encapsulated within calcium/cobalt (Ca/Co) alginate beads. These novel chondrogenesis-promoting scaffolds take advantage of the synergy between the alginate matrix and  $\text{Co}^{+2}$  ions, without employing costly growth factors (e.g., transforming growth factor betas (TGF- $\beta$ s) or bone morphogenetic proteins (BMPs)) to direct hADSC differentiation into cartilage-producing chondrocytes.

## 1. Introduction

Articular cartilage covers the ends of bones in synovial joints and acts as a load-bearing material. Articular cartilage repair is one of the most challenging issues in the field of tissue regeneration because of the limited capacity of cartilage for self-regeneration once damaged [1–5]. Various surgical approaches are widely used to repair injured cartilage, including multiple drilling to encourage revascularization, abrasion arthroplasty, and perichondrial resurfacing. However, the efficacy of such strategies remains controversial, and these approaches are also unsatisfactory in terms of restoring the original structure and function of cartilage [6–10].

To overcome these drawbacks, cell-based therapy is currently under intense review for cartilage repair, and many different tactics and cell types have been explored for this purpose. Autologous chondrocyte implantation (ACI) was the first strategy employed in clinical practice, utilizing chondrocytes harvested from an area of the patient's own cartilage

with diminished weight-bearing function [11–13]. However, several problems were reported with this technique, such as limited proliferative potential of the obtained chondrocytes and loss of functional cell phenotypes in culture [6, 11, 14].

Mesenchymal stem cells (MSCs) are a promising alternative cell source for cartilage repair. When appropriately stimulated, MSCs can differentiate into a variety of cell types, including cartilage-producing chondrocytes [4, 15–19]. MSCs are frequently isolated from bone marrow. Nevertheless, cell harvesting and isolation from bone marrow are associated with distinct disadvantages. For example, bone marrow aspiration can be painful for the patient, and the aspirates must be concentrated by using techniques that involve relatively high-cost instrumentation. Furthermore, MSC yields from bone marrow are quite low. Additional tissues have thus been proposed as a source of MSCs, including adipose tissue, which is abundant in adult stem cells, relatively easy to obtain from patients, and less expensive to handle than bone marrow for MSC isolation [4, 20–22]. In any case, common strategies

to differentiate adult stem cells into chondrocytes still require the use of costly growth factors in the culture medium, such as transforming growth factor betas (TGF- $\beta$ s), insulin-like growth factors, and bone morphogenetic proteins (BMPs). Of note, these additives could potentially lead to unexpected side effects during use in clinical practice [15, 23].

Recently, a number of research groups demonstrated that chondrogenic differentiation of MSCs can be achieved by maintaining the cells under hypoxic conditions [23–26], with the aim of reproducing the native environment of articular cartilage. Articular cartilage is an avascular tissue, deriving its oxygen supply from synovial fluid and subchondral bone. For this reason, the oxygen tension in the deepest layers of articular cartilage is no more than 1–6% [25, 27, 28]. Moreover, during endochondral bone formation, MSCs differentiate into chondrocytes that form a hyaline cartilage-rich matrix, which serves as a template for epiphyseal growth plate formation. These events occur during an avascular period in a decidedly hypoxic environment [22, 29].

The molecular mechanism associated with cell survival in the low oxygen environment involves the activation of the hypoxia inducible factor 1 (HIF-1) transcriptional complex. HIF-1 is a major mediator of the hypoxic response that is essential for chondrocyte differentiation and survival *in vivo*. HIF-1 contains two subunits: HIF-1 $\alpha$  and HIF-1 $\beta$ . Under normoxic conditions, HIF-1 $\alpha$  is rapidly degraded by prolyl-hydroxylase domain enzymes (PHDs) and factor inhibiting HIF (FIH) hydroxylase. The PHDs and FIH are inhibited at low oxygen tension; hence, HIF-1 $\alpha$  escapes degradation and forms heterodimers with HIF-1 $\beta$ , permitting migration of the HIF-1 $\alpha$ /HIF-1 $\beta$  complex into the nucleus and activation of target gene transcription, including that of cartilage-specific genes [22, 24, 26, 30].

Hypoxic conditions and HIF-1 upregulation can also be evoked by chemical induction; for instance, cobalt is well-known as a hypoxia-mimicking agent. This characteristic stems from the ability of cobalt ions (Co<sup>+2</sup>) to inactivate FIH by substitution for Fe<sup>+2</sup> in the iron-binding center of the enzyme [31–33]. Regardless, the HIF-1-promoted differentiation of MSCs into chondrocytes is not sufficient for the ultimate purpose of restoring cartilage defects. Exogenously transplanted cells must also be supported by a biocompatible physical matrix (i.e., a scaffold), and selection of a suitable biomaterial for scaffolding is a critical factor in cartilage tissue engineering.

Alginate is widely used as a polymer for chondrogenic differentiation of MSCs [34–37]. This biomaterial is a naturally occurring heteropolysaccharide isolated from brown sea algae and is composed of  $\beta$ -D-mannuronic acid and  $\alpha$ -L-guluronic residues. In the presence of divalent cations (e.g., calcium (Ca<sup>+2</sup>), barium (Ba<sup>+2</sup>), Co<sup>+2</sup>, and strontium (Sr<sup>+2</sup>)), alginate can be transformed into a hydrogel by ionic interactions between the  $\alpha$ -L-guluronic residues of two distinct polymeric chains and the above-mentioned cations [35, 38–41]. Several tissue engineering studies have demonstrated that alginate provides an ideal environment to facilitate the spatial distribution of MSCs, resulting in a structural organization that resembles the native *in vivo* cartilage microenvironment [34–37]. Furthermore, alginate

exerts chondroinductive actions to promote the synthesis of cartilage-specific matrix components [42–44].

The current study describes a new strategy to stimulate chondrogenic differentiation of commercially available human adipose-derived mesenchymal stem cells (hADSCs) via their encapsulation into a Ca/Co alginate bead scaffold. This approach takes advantage of the synergic effect of the alginate matrix and Co<sup>+2</sup> ions on chondrogenesis and does not rely on TGF- $\beta$ s, BMPs, or other exogenous growth factors or additives. Therefore, Ca/Co alginate bead scaffolds might be beneficial for prospective applications in articular cartilage repair.

## 2. Materials and Methods

**2.1. hADSC Culture.** hADSCs were purchased from a commercial source (Cat. number PT-5006; Lonza, Basel, Switzerland) and cultured in Dulbecco's modified Eagle's medium (DMEM; Gibco, Life Technologies, Monza, Italy) supplemented with 10% fetal bovine serum (FBS; Gibco, Life Technologies) and 1% penicillin/streptomycin in a humidified atmosphere (5% CO<sub>2</sub>) at 37°C. When the cells reached ~90% confluence, they were detached from the culture surface with 0.25% trypsin and subcultured. The hADSCs from passages 3–7 were used for further study.

**2.2. Alginate Solution.** Alginic acid sodium salt derived from brown algae (Na-alg) and suitable for cell encapsulation was obtained from Sigma-Aldrich (St. Louis, MO, USA). To prepare the Na-alg solution, 1% (w/v) of the solid sodium salt was dissolved in sterile 10 mM HEPES buffer (pH 7.4), and the mixture was filtered through a 0.2 mm membrane under sterile conditions.

**2.3. Cell-Encapsulated Alginate Bead Production.** hADSCs were detached from plastic tissue culture flasks by using 0.25% trypsin, resuspended at a density of  $2 \times 10^6$  cells/mL in sterile Na-alg solution, and dripped by 25-gauge needle into various gelling baths, all containing 200 mM CaCl<sub>2</sub> and decreasing concentrations of CoCl<sub>2</sub> (10, 5, 2.5, and 1.25 mM). The gelling baths were buffered with 10 mM HEPES. A 200 mM CaCl<sub>2</sub> solution was used as the control gelling bath. The hADSC/Na-alg droplet suspension was maintained for 30 min at 37°C to form alginate beads. The resulting samples were designated Co10, Co5, Co2.5, Co1.25, and control based on the concentration of CoCl<sub>2</sub> in the initial gelling bath. After washing the beads with HEPES buffer, DMEM supplemented with 10% FBS and 1% penicillin/streptomycin was added to tissue culture wells containing alginate-encapsulated cells. The prepared beads were incubated in a humidified environment (5% CO<sub>2</sub>) at 37°C. Cells within the beads were cultured for 7, 14, and 21 days, and the medium was changed every 3–4 days.

**2.4. Morphology and Bead Size Distribution.** Measurements of bead particle size (mean microsphere diameter) were performed by using a Nikon Eclipse E800 optical microscope (Nikon, Tokyo, Japan).

**2.5. Assessment of Cell Viability and Cell Imaging.** Cell viability was assessed up until day 21 of culture by using a LIVE/DEAD Viability/Cytotoxicity Assay kit (Life Technologies, Carlsbad, CA, USA). Encapsulated hADSCs were incubated for 15 min in HEPES buffer containing  $0.1\ \mu\text{M}$  calcein AM, a cell-permeant fluorescent dye, and  $0.1\ \mu\text{M}$  ethidium homodimer-1, a DNA-binding fluorescent dye. The samples were washed with HEPES buffer, transferred to a glass-bottomed 24-well plate, and immediately imaged by using a Nikon Eclipse E800 microscope. Live cells (green) and dead cells (red) were counted by using ImageJ software (National Institutes of Health, Bethesda, MD, USA). Cell viability was obtained by dividing the number of live cells by the total number of cells (live + dead).

**2.6. Histological Analysis.** Encapsulated cells were fixed at each experimental time point with 4% paraformaldehyde in 10 mM HEPES buffer for 2 h at  $4^\circ\text{C}$ . They were then dehydrated in an ascending series of alcohol solutions (50%, 70%, 90%, and 100%) and embedded in LR white resin (Sigma-Aldrich). Thin sections were prepared, stained with 1% toluidine blue, and observed by using a Nikon Eclipse E800 microscope.

**2.7. Quantitative Real-Time Polymerase Chain Reaction (qRT-PCR).** To evaluate the differentiation capacity of the encapsulated hADSCs, samples were treated with 55 mM sodium citrate, 55 mM EDTA, and 0.9% NaCl in 10 mM HEPES-buffered saline (pH 6.8) with gentle shaking for 5 min. This resulted in formation of diluted Na-alg and the release of hADSCs from the alginate beads. At the end of each experimental time point, total RNA was extracted from the released cells by using a NucleoSpin RNA I kit (Macherey-Nagel, Duren, Germany). The RNA was then quantified by using a NanoDrop ND-1000 full-spectrum (ultraviolet/visible light) spectrophotometer (Thermo Scientific, Wilmington, DE, USA).

Next, cDNA was transcribed with reverse transcriptase SUPRII (Invitrogen, Carlsbad, CA, USA), and mRNA expression levels were analyzed via qRT-PCR by using a 7500 Real-Time PCR machine (Applied Biosystems, Life Technologies, Monza, Italy). The following TaqMan assays (Applied Biosystems, Life Technologies) were used for mRNA quantification: collagen type II (Col2A1; Hs00264051\_m1), collagen type I (Col1A1; Hs00164004\_m1), collagen type X (Col10A1; Hs00166657\_m1), Sox9 (Sox9; Hs01001343\_g1), versican (VCAN; Hs00171642\_m1), and HIF-1 $\alpha$  (HIF-1A; Hs00153153\_m1). Relative gene expression levels were normalized to that of glyceraldehyde 3-phosphate dehydrogenase (GAPDH; Hs99999905\_m1). Data are presented as fold changes relative to levels in control samples (cells encapsulated within alginate beads prepared with  $\text{CaCl}_2$  alone (Ca alginate beads) and cultured for the same amount of time) by using formula  $2^{-\Delta\Delta\text{CT}}$ , as recommended by the manufacturer (User Bulletin number 2 P/N 4303859; Applied Biosystems).

**2.8. Statistical Analysis.** Statistical analysis of quantifiable data was conducted by performing an analysis of variance

followed by Dunnett's multiple comparison test with GraphPad Prism 5.0 software (GraphPad Software, Inc., San Diego, CA, USA). Statistical differences between conditions were considered significant at  $P < 0.05$ .

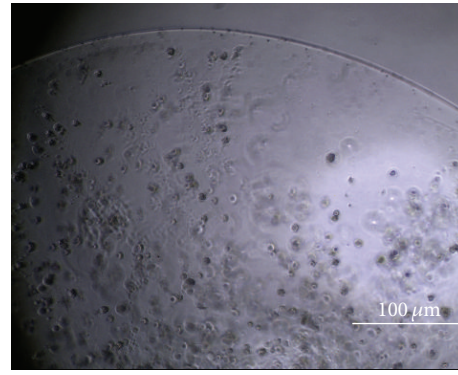
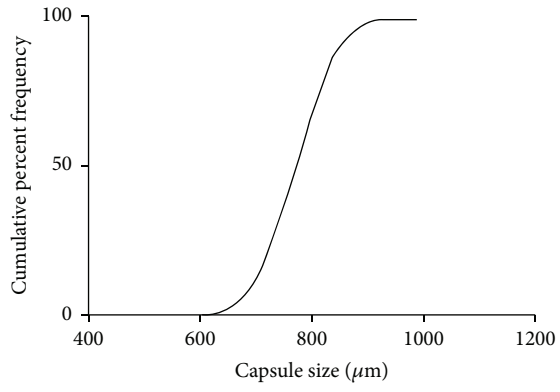
### 3. Results

**3.1. Size Distribution of hADSC-Loaded Capsules.** Alginate droplets containing encapsulated hADSCs were collected in gelling baths containing  $\text{CaCl}_2$  and varying amounts of  $\text{CoCl}_2$  so as to evaluate  $\text{Co}^{+2}$  concentration effects on the morphological characteristics of the particles. As a control, a gelling solution containing only  $\text{CaCl}_2$  was employed. First, the size distribution of the cell-encapsulated alginate beads was monitored, as shown in Figure 1. For all samples, the particle diameters were confined within a narrow size range, with a mean diameter ranging from  $789 \pm 52$  to  $826 \pm 74\ \mu\text{m}$ . By comparison, the mean diameter of the control beads was  $810 \pm 36\ \mu\text{m}$ . These findings suggest that  $\text{Co}^{+2}$  concentration did not significantly affect capsule size.

Light microscopic images showed a uniform cell distribution at 2 h after production of the hADSC-encapsulated alginate beads (Figures 1(a')–1(e')). Macroscopically (Figure 2), the particles maintained their spherical shape and exhibited a smooth surface. These properties were maintained during the 21 days in culture, and no macroscopic evidence of particle degradation or deformation was noted.

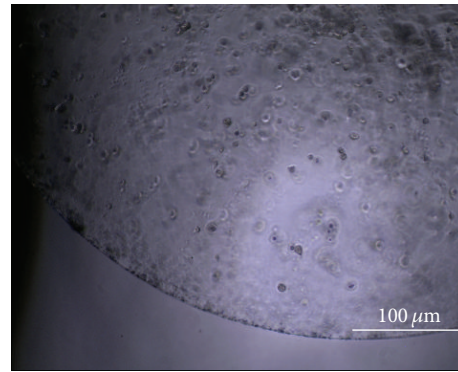
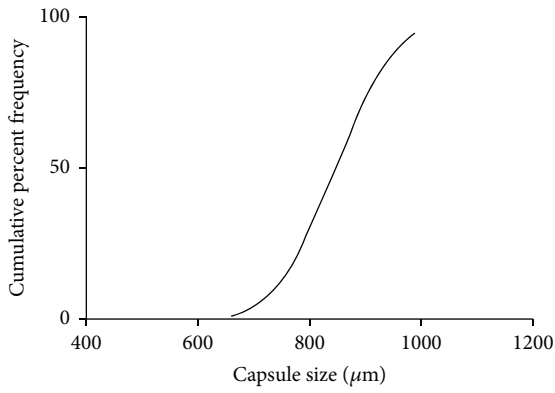
**3.2. Cell Viability.** To evaluate the potential toxicity of  $\text{Co}^{+2}$  ions against encapsulated hADSCs, a calcein AM/ethidium homodimer-1 assay was performed. Images of the stained cells within the alginate beads are shown in Figure 3, where live cells are green and dead cells are red. The images were employed to measure cell viability at 7, 14, and 21 days in culture (Figure 3(f)). The live/dead cell ratios for hADSCs encapsulated within the Co1.25 and Co2.5 beads did not differ significantly from that in the corresponding controls, although the ratio appeared to be slightly less than the control ratio in the Co2.5 group at all the time points examined. Cell viability in the Co5 sample was comparable to that in the control at 7 days in culture, but the number of live cells decreased at 14 and 21 days, with a significant difference from the control at 21 days. Cells in the Co10 sample showed a relative cell viability of 40.13%, 12.36%, and 7.24% on days 7, 14, and 21, respectively, which was significantly lower than the control at each time point, indicating the potential toxicity of  $\text{Co}^{+2}$  contained within the alginate beads (Figure 3).

**3.3. Histological Observations.** The round shape of the hADSCs within the alginate beads and the unfilled spaces, or lacunae, associated with cartilage tissue-like structures were both illustrated by toluidine blue staining (Figure 4). After 21 days in culture, lacunae and matrix deposition were clearly revealed in the Co2.5 sample. The Co5 beads demonstrated similar cell behavior as the Co2.5 beads, even though the number of lacunae in the encapsulated cells was lower than that observed for the Co2.5 sample. The numbers of encapsulated cells within the Co1.25 and Co10 beads were



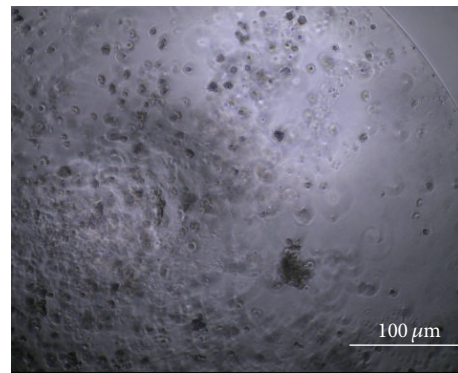
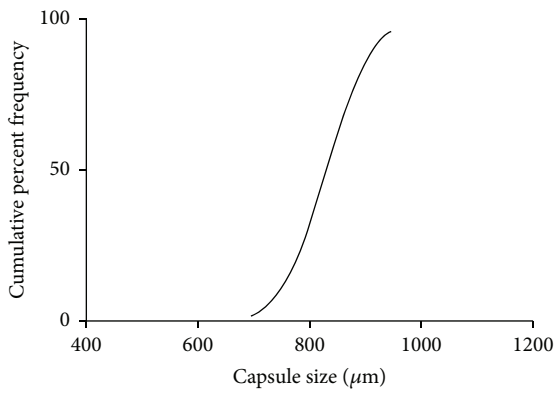
(a)

(a')



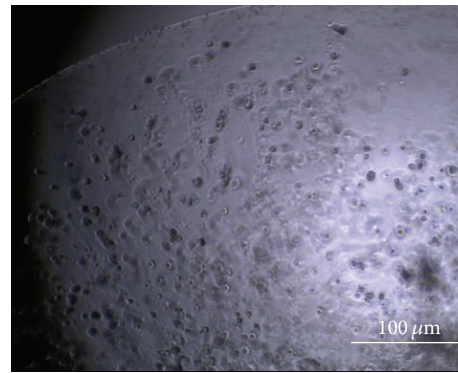
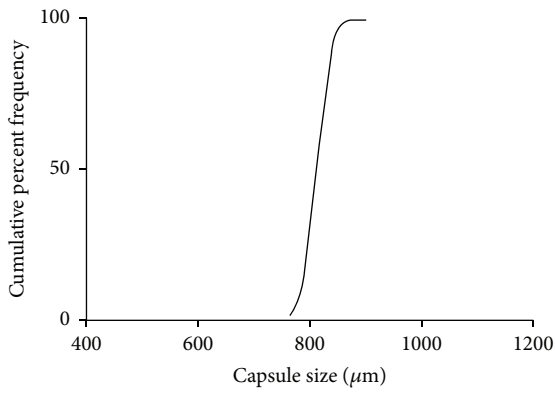
(b)

(b')



(c)

(c')



(d)

(d')

FIGURE 1: Continued.

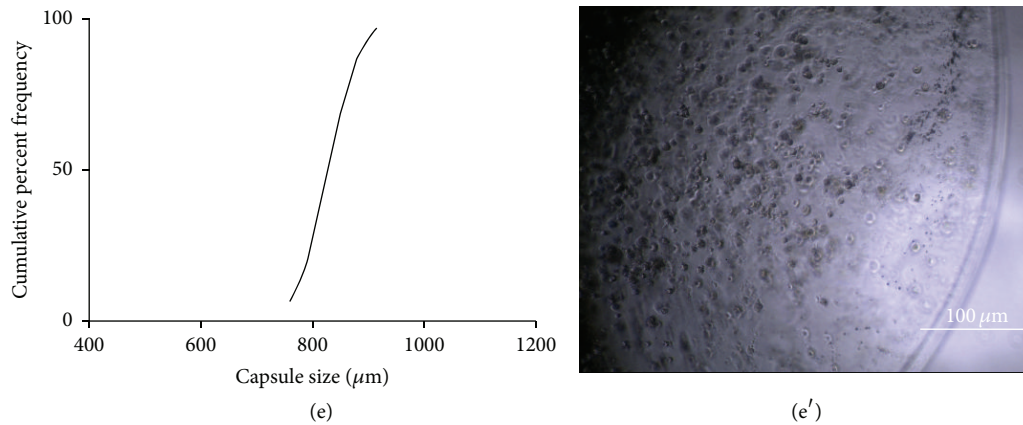


FIGURE 1: Cumulative size distribution (a–d) and microscopic images (a'–d') of Ca/Co alginate beads with encapsulated hADSCs at 2 h after preparation. ((a), (a')) Control sample; ((b), (b')) Co1.25 sample; ((c), (c')) Co2.5 sample; ((d), (d')) Co5 sample; and ((e), (e')) Co10 sample. The mean bead diameters were as follows: control,  $810 \pm 36 \mu\text{m}$ ; Co1.25,  $821 \pm 98$ ; Co2.5,  $789 \pm 52$ ; Co5,  $826 \pm 74 \mu\text{m}$ ; and Co10,  $804 \pm 16 \mu\text{m}$ .

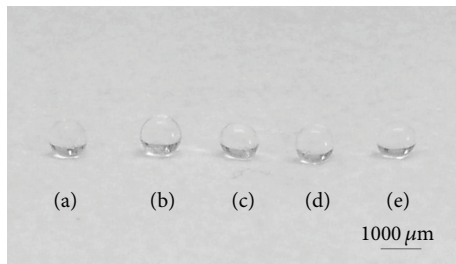


FIGURE 2: Images of Ca/Co alginate beads with encapsulated hADSCs on day 21 in culture. (a) Control sample; (b) Co1.25 sample; (c) Co2.5 sample; (d), Co5 sample; and (e) Co10 sample.

quite limited, and the lacunae had an irregular appearance in the Co10 sample and were not well defined.

**3.4. qRT-PCR Analysis of mRNA Expression Levels of Chondrogenic Markers in hADSCs.** To verify hADSC differentiation into chondrocytes, mRNA expression levels of HIF-1, chondrogenic markers (collagen type II, Sox9, and versican), and chondrogenic hypertrophic marker (collagen type 10) were quantified in the cells by qRT-PCR. The Sox9 mRNA expression profile in the control samples showed a peak at 14 days in culture, followed by downregulation at 21 days. Gene expression of collagen type II and HIF-1 decreased at 14 and 21 days, while that of versican remained unaltered over the 21-day culture period (Figure 5). The Co1.25 sample exhibited strong upregulation of Sox9 and versican gene expression at 14 days, yielding mRNA levels that were 30- and 18-fold higher than control levels, respectively. However, Sox9 and versican mRNA expression levels were similar to control levels at day 21, and HIF-1 and collagen type II gene expression did not vary significantly over the course of the experiment (Figure 5(a)). Sox9 gene expression in the Co2.5 sample continuously increased from day 7 to day 21, while the control expression levels decreased from day 14 to day 21. HIF-1 mRNA levels showed upregulation at 7 days, but

the expression levels decreased at 14 and 21 days, and were similar to control levels (Figure 5(b)). Sox9 and versican mRNA levels both showed continuous increases in the Co5 sample (Figure 5(c)), and versican mRNA levels showed the same trend in the Co10 sample (Figure 5(d)). In the Co5 sample (Figure 5(c)), versican mRNA expression levels were ~3-fold higher than the control level at 21 days in culture. Meanwhile, HIF-1 showed a similar trend as in the Co2.5 sample, with a ~2-fold increase at 7 days in culture, followed by downregulation on days 14 and 21. The Col2A1/Col1A1 ratio showed no significant differences in Co1.25 at 7 and 14 days of culture with respect to control and it increased after 21 days of culture; differently the ratio in Co2.5 and Co5 resulted in being higher than control in all experimental times whereas the Co10 values were similar to control, except for day 21 where a decrease was shown (Figure 6(a)). Concerning the Col10A1, its expression resulted similar in all experimental conditions (Figure 6(b)).

## 4. Discussion

The main goal of the present work was to induce chondrogenic differentiation of hADSCs by employing low-cost alginate materials and straightforward techniques. Alginate hydrogels are widely used as scaffolds in tissue engineering applications because they provide a three-dimensional structure reminiscent of the native extracellular matrix of cells within tissues. Alginate also has the ability to promote and stabilize the chondrogenic phenotype [14, 35, 43, 44]. Here, we exploited the synergic effect of alginate in combination with  $\text{Co}^{+2}$  ions to mimic the natural environment and biophysical properties of cartilage tissue *in vivo*. Due to its negative charge and abundance of hydroxyl functional groups, alginate shows a high affinity toward bivalent ions, which then trigger gel formation by generation of interchain bridges after contact with the polysaccharide [35, 38–41].

Divalent ions not only are adsorbed onto the surface of the biomaterial in contact with the gelling bath solution, but

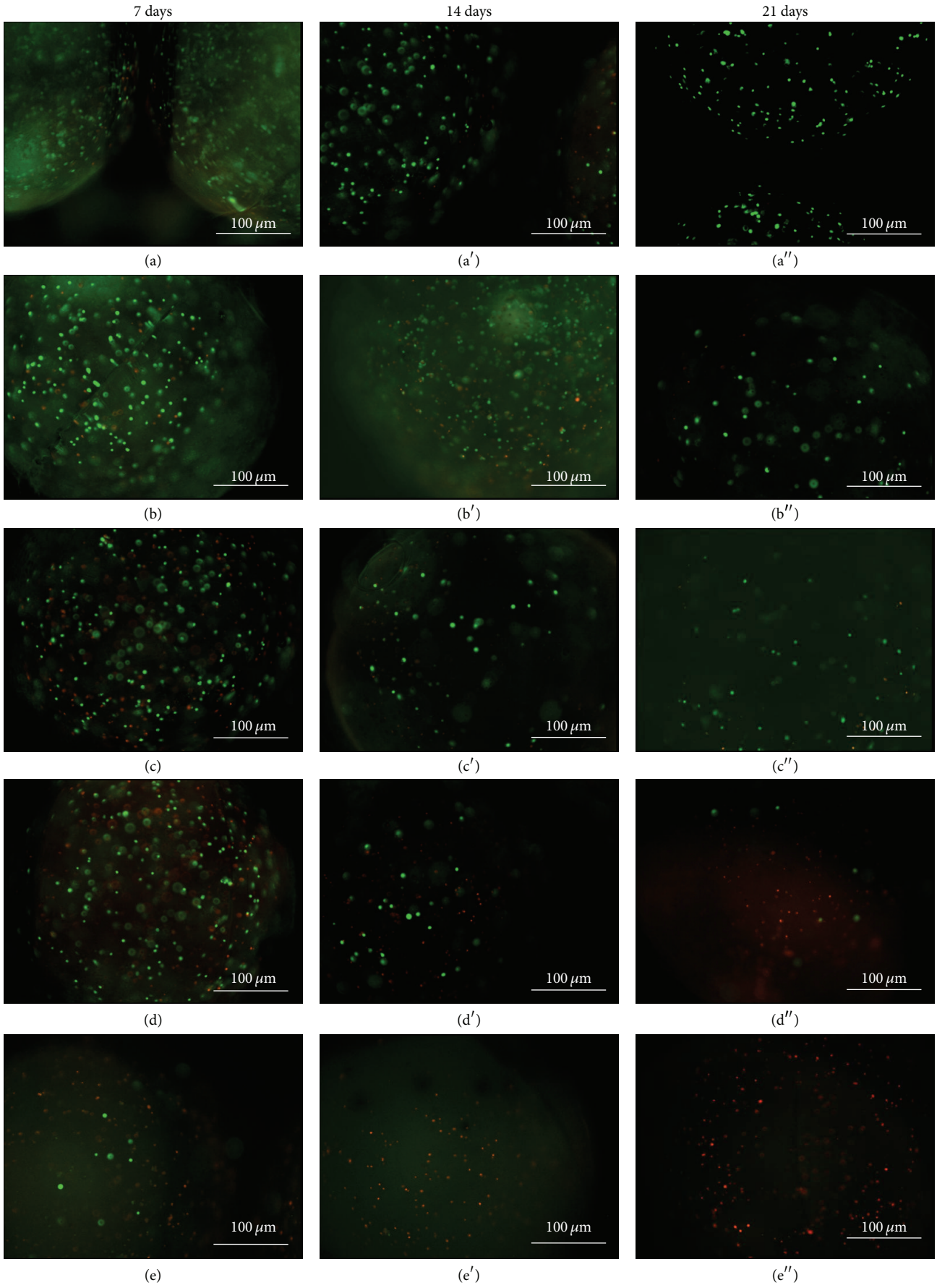


FIGURE 3: Continued.

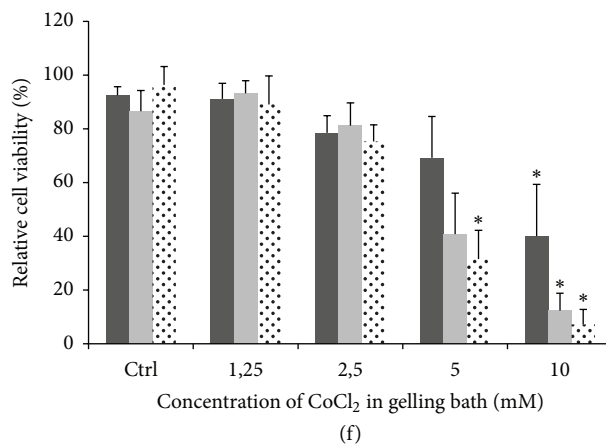


FIGURE 3: Live/dead (green/red) staining of hADSCs encapsulated within alginate Ca/Co beads. ((a), (a'), (a'')) Control sample; ((b), (b'), (b'')) Co1.25 sample; ((c), (c'), (c'')) Co2.5 sample; ((d), (d'), (d'')) Co5 sample; and ((e), (e'), (e'')) Co10 sample. (f) Cell viability of hADSCs (live cells/live + dead cells) encapsulated within Ca/Co alginate beads. Black bar: 7 days; dark grey bar: 14 days; light grey bar: 21 days. Data are given as the means  $\pm$  the standard deviation (SD) ( $n = 3$  independent experiments); \* indicates statistical differences compared to control samples at the same time point ( $P < 0.05$ ).

also diffuse into the gel through microscopic channels. In this manner, the ions can interact with functional groups inside the gel [45]. This process permits the formation of a uniform gel structure, where the ions are homogeneously distributed. In this study, the alginate gel was obtained by using CaCl<sub>2</sub> and varying concentrations of CoCl<sub>2</sub>. Co<sup>+2</sup> ions, like Ca<sup>+2</sup> ions, participate in the gelation process by producing an *in situ* Co<sup>+2</sup> reservoir directly available to the encapsulated cells.

Keeping our low-cost philosophy in mind, we produced cell-encapsulated alginate beads via a dripping technique. This method is widely used in cell encapsulation because it is easy to set up and requires no expensive instrumentation [46, 47]. Although some researchers prefer other approaches to generate alginate particles (e.g., emulsification or electrostatic droplet generation techniques [48–50]), our experimental conditions yielded alginate beads with a narrow size distribution and a smooth spherical shape, two critical parameters for quality control of three-dimensional cell culture scaffolds [46, 51, 52] (Figures 1 and 2). Therefore, the dripping method is reproducible and suitable for our aims.

The ideal conditions for survival of encapsulated cells were empirically determined by assessing relative cell viability within alginate beads collected in gelling baths containing varying amounts of Co<sup>+2</sup>. Consequently, the live/dead cell assay showed a dose-response relationship with Co<sup>+2</sup> concentration, with enhanced viability of hADSCs in Co1.25 and Co2.5 alginate spheres after 21 days in culture. These findings suggest that initial Co<sup>+2</sup> concentrations of 1.25 and 2.5 mM in the gelling bath are well tolerated by the cells. However, cell viability was reduced in the Co5 and Co10 samples, indicating that high Co<sup>+2</sup> concentrations are not ideal for long-term study of chondrogenic differentiation. For example, the live/dead cell ratio in the Co10 sample was ~45% at 7 days and decreased thereafter, ascribable to an acute cytotoxic effect of Co<sup>+2</sup> at elevated concentrations.

Importantly, an equilibrium exists between the concentration of Co<sup>+2</sup> in the gelling bath and that inside the alginate bead. We assumed that the Co<sup>+2</sup> concentration within the particle would be less than that in the gelling bath, allowing cell survival and differentiation. Regardless, future studies will be required to investigate the optimal Co<sup>+2</sup> concentration within the beads for chondrocytic differentiation of encapsulated stem cells.

Chondrogenic differentiation was monitored herein by qRT-PCR. HIF-1 gene expression was of particular interest because HIF-1 is a predominant mediator of the hypoxic response. As noted above, the HIF-1 $\alpha$  subunit is rapidly degraded under normoxic conditions by PHDs and FIH. Under hypoxic conditions, PHDs and FIH are inactivated and HIF-1 $\alpha$  is spared; hence, HIF-1 $\alpha$  can interact with HIF-1 $\beta$  and translocate into the nucleus. The HIF-1 $\alpha$ /HIF-1 $\beta$  complex then binds to hypoxia-responsive elements in cartilage marker genes, enhancing their transcription [19, 22, 26, 30].

Intriguingly, Co<sup>+2</sup> ions can reportedly increase HIF-1 mRNA synthesis [31]. In our experiments, HIF-1 mRNA expression levels were increased at 7 days in culture in the Co2.5 and Co5 samples and decreased thereafter. These results are suggestive of a negative HIF-1 feedback mechanism with prolonged hypoxic exposure. On the other hand, Sox9 mRNA expression levels were continuously upregulated in the Co2.5 and Co5 samples over the 21 days of the experiment, while the same trend was observed for versican mRNA levels in the Co5 sample. These two markers have pivotal functions during the early stages of chondrogenic differentiation: Sox9 is a transcription factor that regulates cell condensation and the production of other chondrogenic markers, such as collagen type II [53, 54], while versican is a hyaluronan-binding proteoglycan that plays specific roles at the articular cartilage surface and is involved in regulation of the cartilage cell phenotype [54–56].

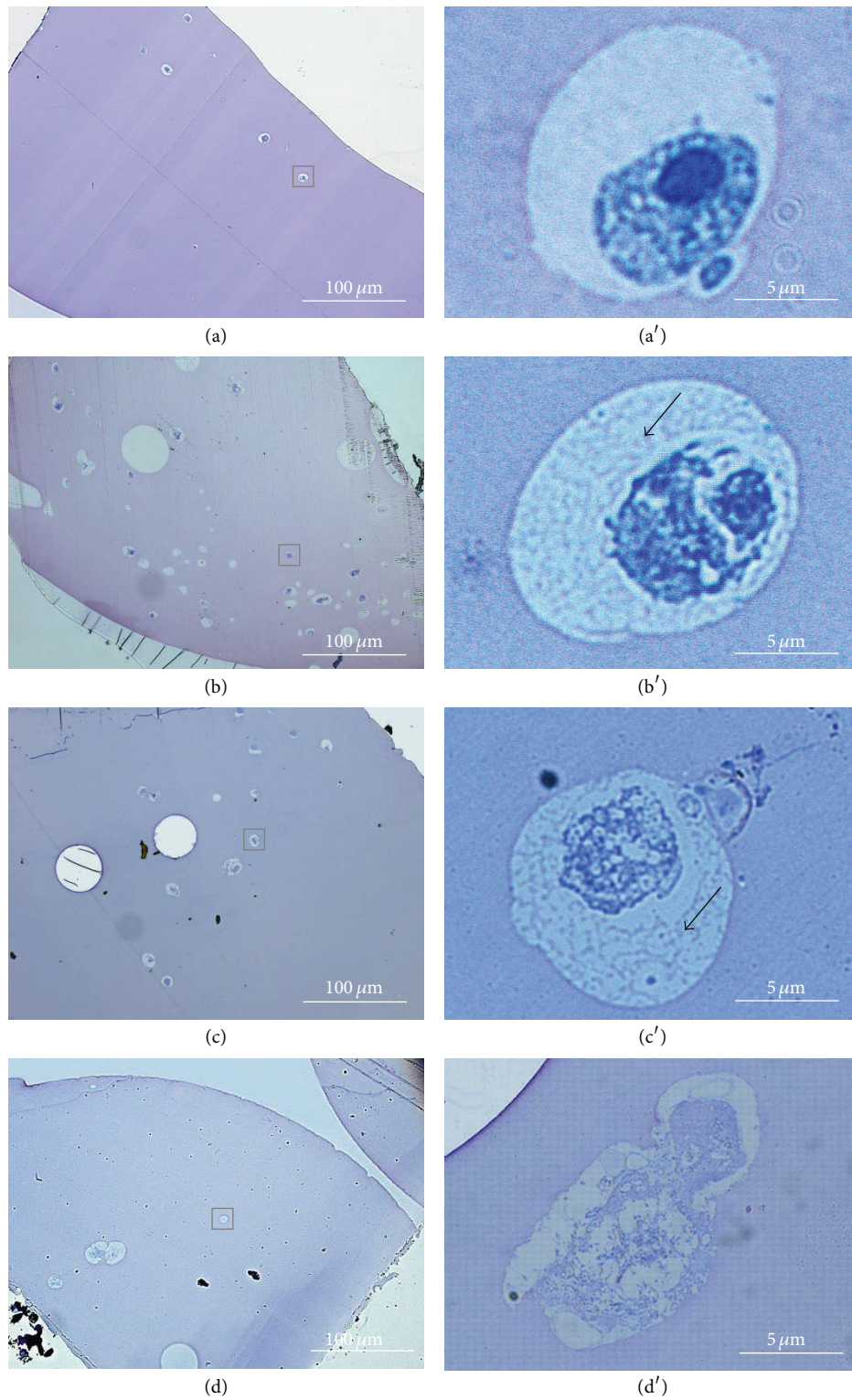


FIGURE 4: Microscopic images of hADSCs encapsulated within Ca/Co alginate beads at 21 days in culture and stained with toluidine blue. ((a), (a')) Co1.25 sample; ((b), (b')) Co2.5 sample; ((c), (c')) Co5 sample; and ((d), (d')) Co10 sample. Black arrows indicate proteoglycan matrix deposition. Black squares indicate lacunae.

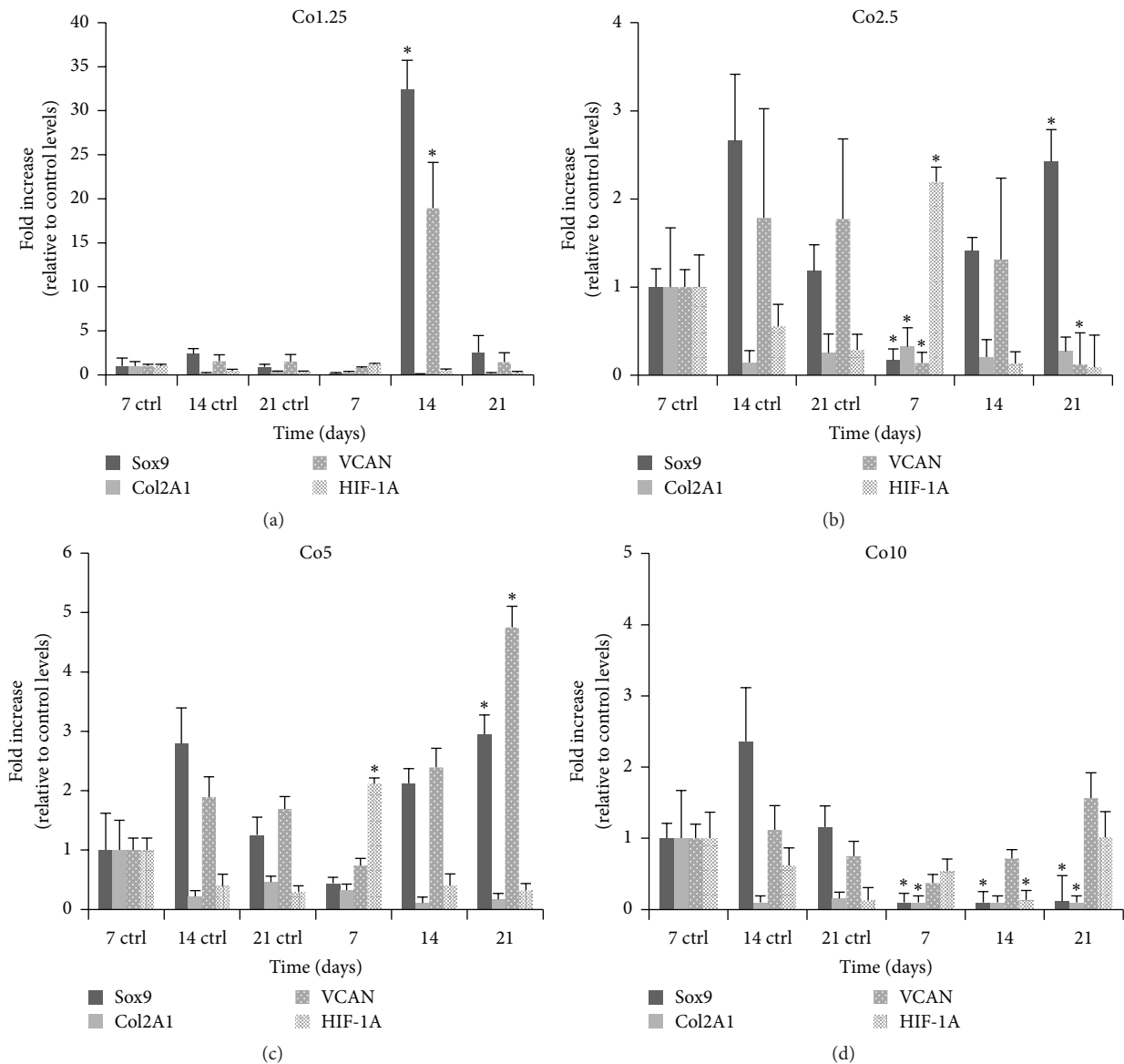


FIGURE 5: qRT-PCR analysis of hADSCs encapsulated within Ca/Co alginate beads. Expression levels of marker genes were normalized to that of GAPDH and calculated as fold changes relative to expression levels of hADSCs encapsulated within control Ca alginate beads at 7 days. Data are given as means  $\pm$  the SD ( $n = 3$  independent experiments; \*  $P < 0.05$ ). VCAN: versican.

Although the Co1.25 sample showed strong upregulation of Sox9 mRNA and versican mRNA at 14 days, no significant change in HIF-1 mRNA expression was observed at any time point. We surmise that the  $\text{Co}^{+2}$  concentration in the Co1.25 capsule was insufficient to promote chondrogenic differentiation and that the increased gene expression of chondrogenic markers in hADSCs resulted from induction by alginate alone.

Toluidine blue staining and histological observations confirmed the impact of the Co2.5 and Co5 samples on the early stages of chondrogenic differentiation. Both samples promoted the formation of numerous lacunae associated with cartilage tissue-like structures at day 21 in culture, as well as proteoglycan matrix deposition (Figures 4(b), 4(b') and

4(c), 4(c')). However, in agreement with the qRT-PCR results, no proteoglycan deposition into the lacunae was observed for the Co1.25 sample. Moreover, the irregular morphology of the cells in the Co10 sample again suggests that the conditions in this scaffold were inappropriate for optimal hADSC differentiation.

Collagen type II mRNA was only detected at low levels in all of the samples, even though collagen type II is a fundamental component of the cartilage extracellular matrix. Possibly, optimal collagen type II synthesis requires more time than the 21-day observation period of our study, depending on the culture system [37]. However, the Col1A1/Col2A1 ratio suggests that Co2.5 and Co5 samples may be more suitable for chondrogenic differentiation; in fact, a ~50-fold increase

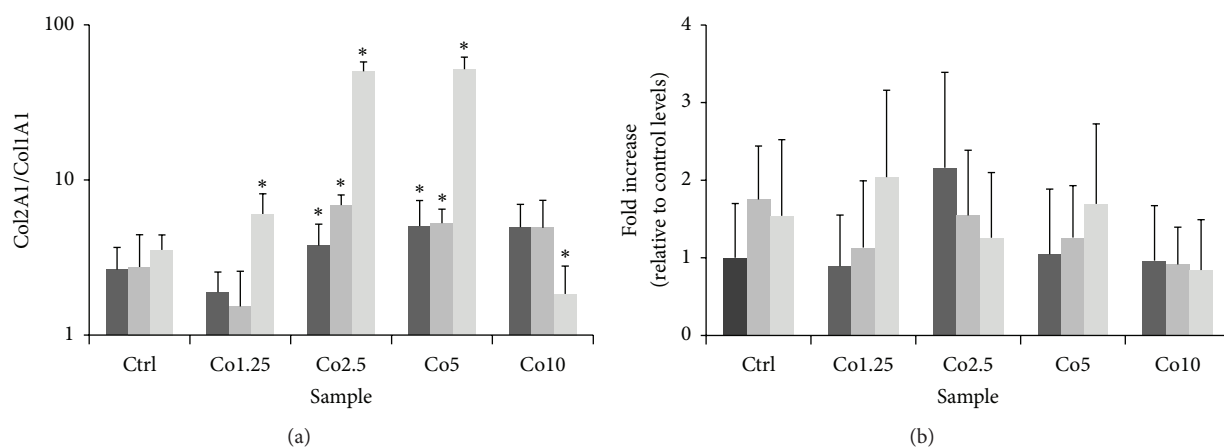


FIGURE 6: (a) Col1A1/Col1A2 mRNA ratio synthesized by hADSCs encapsulated within Ca/Co alginate beads. (b) qRT-PCR analysis of Col10A1. Expression levels of marker genes were normalized to that of GAPDH and calculated as fold changes relative to expression levels of hADSCs encapsulated within control Ca alginate beads at 7 days. Black bar: 7 days; dark grey bar: 14 days; light grey bar: 21 days. Data are given as means  $\pm$  the SD ( $n = 3$  independent experiments; \*  $P < 0.05$ ).

of Col2A1 in comparison with Col1A1 after 21 days could reveal a tendency of hADSCs to evolve in chondrocytes. Nevertheless, further investigations will be focused on the long-term maintenance of hADSCs within Co/Ca alginate beads to evaluate Col2A1 synthesis.

Finally, the expression of collagen type X was detected. This protein is expressed when chondrocytes hypertrophy. Generally, collagen type X is restricted to the deep cartilage zone and the adjacent calcified cartilage in adult articular cartilage. A hypertrophic chondrocyte is a cell that has gradually differentiated toward osteogenesis [57, 58]. In our experiments, the collagen type 10 expression is very low and similar to the control in all experimental conditions. The results reveal the beads have the advantage of keeping the differentiated cells in a chondrocyte or chondroprogenitor phenotypes without differentiating toward osteogenesis. However, as stated above, long-term studies are necessary.

## 5. Conclusions

This study shows a novel and low-cost approach to induce *in vitro* chondrogenic differentiation of MSCs encapsulated within alginate beads. This strategy exploits the synergic actions of  $\text{Co}^{+2}$  and alginate and does not include traditional differentiation-promoting growth factors. The alginate beads produced herein provide a cartilage tissue-mimetic environment and are promising for use in cartilage tissue engineering applications. In addition, the dripping technique used for bead production is straightforward, reproducible and permits gentle encapsulation of hADSCs without reducing cell viability. However, this work only represents an initial phase of our study of alginate beads for cartilage tissue engineering; the results suggest a chondroprogenitor phenotype of cells and the complete differentiation requires long-term experiments. Optimization of the  $\text{Co}^{+2}$  molar concentration in the beads and long-duration culturing are already underway in a continuation of the current investigation.

## Conflict of Interests

The authors declare that there is no conflict of interests regarding the publication of this paper.

## References

- [1] S. Dinescu, B. Galateanu, E. Radu et al., "A 3D porous gelatin-alginate-based-*ipn* acts as an efficient promoter of chondrogenesis from human adipose-derived stem cells," *Stem Cells International*, vol. 2015, Article ID 252909, 17 pages, 2015.
- [2] Y. Jang, Y. G. Koh, Y.-J. Choi et al., "Characterization of adipose tissue-derived stromal vascular fraction for clinical application to cartilage regeneration," *In Vitro Cellular & Developmental Biology—Animal*, vol. 51, no. 2, pp. 142–150, 2015.
- [3] J.-Y. Ko, K.-I. Kim, S. Park, and G.-I. Im, "In vitro chondrogenesis and in vivo repair of osteochondral defect with human induced pluripotent stem cells," *Biomaterials*, vol. 35, no. 11, pp. 3571–3581, 2014.
- [4] Y. Lin, E. Luo, X. Chen et al., "Molecular and cellular characterization during chondrogenic differentiation of adipose tissue-derived stromal cells in vitro and cartilage formation in vivo," *Journal of Cellular and Molecular Medicine*, vol. 9, no. 4, pp. 929–939, 2005.
- [5] E. Sivayoham and T. J. Woolford, "Current opinion on auricular reconstruction," *Current Opinion in Otolaryngology & Head and Neck Surgery*, vol. 20, no. 4, pp. 287–290, 2012.
- [6] R. Abdul Rahman, N. Mohamad Sukri, N. Md Nazir et al., "The potential of 3-dimensional construct engineered from poly(lactic-co-glycolic acid)/fibrin hybrid scaffold seeded with bone marrow mesenchymal stem cells for *in vitro* cartilage tissue engineering," *Tissue and Cell*, vol. 47, no. 4, pp. 420–430, 2015.
- [7] G. Bentley, L. C. Biant, R. W. J. Carrington et al., "A prospective, randomised comparison of autologous chondrocyte implantation versus mosaicplasty for osteochondral defects in the knee," *The Journal of Bone & Joint Surgery—British Volume*, vol. 85, no. 2, pp. 223–230, 2003.

- [8] S. Chen, P. Fu, R. Cong, H. Wu, and M. Pei, "Strategies to minimize hypertrophy in cartilage engineering and regeneration," *Genes & Diseases*, vol. 2, no. 1, pp. 76–95, 2015.
- [9] E. B. Hunziker, "Articular cartilage repair: basic science and clinical progress. A review of the current status and prospects," *Osteoarthritis and Cartilage*, vol. 10, no. 6, pp. 432–463, 2002.
- [10] D. Nestic, R. Whiteside, M. Brittberg, D. Wendt, I. Martin, and P. Mainil-Varlet, "Cartilage tissue engineering for degenerative joint disease," *Advanced Drug Delivery Reviews*, vol. 58, no. 2, pp. 300–322, 2006.
- [11] Á. Berta, Z. Duska, F. Tóth, and L. Hangody, "Clinical experiences with cartilage repair techniques: outcomes, indications, contraindications and rehabilitation," *Eklemler Hastalıkları ve Cerrahisi*, vol. 26, no. 2, pp. 84–96, 2015.
- [12] M. Brittberg, T. Tallheden, E. Sjögren-Jansson, A. Lindahl, and L. Peterson, "Autologous chondrocytes used for articular cartilage repair: an update," *Clinical Orthopaedics and Related Research*, vol. 391, supplement, pp. S337–S348, 2001.
- [13] S. N. Redman, S. F. Oldfield, C. W. Archer, P. J. Roughley, and C. Lee, "Current strategies for articular cartilage repair," *European Cells and Materials*, vol. 9, pp. 23–32, 2005.
- [14] F. Xu, L. Xu, Q. Wang, Z. Ye, Y. Zhou, and W.-S. Tan, "3D dynamic culture of rabbit articular chondrocytes encapsulated in alginate gel beads using spinner flasks for cartilage tissue regeneration," *BioMed Research International*, vol. 2014, Article ID 539789, 10 pages, 2014.
- [15] Z. Cai, B. Pan, H. Jiang, and L. Zhang, "Chondrogenesis of human adipose-derived stem cells by in vivo co-graft with auricular chondrocytes from microtia," *Aesthetic Plastic Surgery*, vol. 39, no. 3, pp. 431–439, 2015.
- [16] S. Focaroli, G. Teti, V. Salvatore et al., "Chondrogenic differentiation of human adipose mesenchymal stem cells: influence of a biomimetic gelatin genipin crosslinked porous scaffold," *Microscopy Research and Technique*, vol. 77, no. 11, pp. 928–934, 2014.
- [17] W. S. Toh, T. C. Lim, M. Kurisawa, and M. Spector, "Modulation of mesenchymal stem cell chondrogenesis in a tunable hyaluronic acid hydrogel microenvironment," *Biomaterials*, vol. 33, no. 15, pp. 3835–3845, 2012.
- [18] T. Vinardell, E. J. Sheehy, C. T. Buckley, and D. J. Kelly, "A comparison of the functionality and in vivo phenotypic stability of cartilaginous tissues engineered from different stem cell sources," *Tissue Engineering—Part A*, vol. 18, no. 11–12, pp. 1161–1170, 2012.
- [19] W. Wang, N. He, C. Feng et al., "Human adipose-derived mesenchymal progenitor cells engraft into rabbit articular cartilage," *International Journal of Molecular Sciences*, vol. 16, no. 6, pp. 12076–12091, 2015.
- [20] G. Bassi, L. Pacelli, R. Carusone, J. Zanoncello, and M. Kramer, "Adipose-derived stromal cells (ASCs)," *Transfusion and Apheresis Science*, vol. 47, no. 2, pp. 193–198, 2012.
- [21] M. H. Lim, W. K. Ong, and S. Sugii, "The current landscape of adipose-derived stem cells in clinical applications," *Expert Reviews in Molecular Medicine*, vol. 16, article e8, 2014.
- [22] A. B. Adesida, A. Mulet-Sierra, and N. M. Jomha, "Hypoxia mediated isolation and expansion enhances the chondrogenic capacity of bone marrow mesenchymal stromal cells," *Stem Cell Research & Therapy*, vol. 3, article 9, 2012.
- [23] E. Duval, C. Baugé, R. Andriamanalijaona et al., "Molecular mechanism of hypoxia-induced chondrogenesis and its application in in vivo cartilage tissue engineering," *Biomaterials*, vol. 33, no. 26, pp. 6042–6051, 2012.
- [24] T. D. Bornes, N. M. Jomha, A. Mulet-Sierra, and A. B. Adesida, "Hypoxic culture of bone marrow-derived mesenchymal stromal stem cells differentially enhances in vitro chondrogenesis within cell-seeded collagen and hyaluronic acid porous scaffolds," *Stem Cell Research & Therapy*, vol. 6, article 84, 2015.
- [25] E. Duval, S. Leclercq, J.-M. Elissalde, M. Demoor, P. Galéra, and K. Boumédiène, "Hypoxia-inducible factor  $1\alpha$  inhibits the fibroblast-like markers type I and type III collagen during hypoxia-induced chondrocyte redifferentiation: hypoxia not only induces type II collagen and aggrecan, but it also inhibits type I and type III collagen in the hypoxia-inducible factor  $1\alpha$ -dependent redifferentiation of chondrocytes," *Arthritis & Rheumatism*, vol. 60, no. 10, pp. 3038–3048, 2009.
- [26] C. L. Murphy, B. L. Thoms, R. J. Vaghjiani, and J. E. Lafont, "Hypoxia. HIF-mediated articular chondrocyte function: prospects for cartilage repair," *Arthritis Research & Therapy*, vol. 11, no. 1, p. 213, 2009.
- [27] K. H. Falchuk, E. J. Goetzl, and J. P. Kulka, "Respiratory gases of synovial fluids. An approach to synovial tissue circulatory-metabolic imbalance in rheumatoid arthritis," *The American Journal of Medicine*, vol. 49, no. 2, pp. 223–231, 1970.
- [28] T. Kiaer, J. Gronlund, and K. H. Sorensen, "Subchondral pO<sub>2</sub>, pCO<sub>2</sub>, pressure, pH, and lactate in human osteoarthritis of the hip," *Clinical Orthopaedics and Related Research*, vol. 229, pp. 149–155, 1988.
- [29] E. Mariani, L. Pulsatelli, and A. Facchini, "Signaling pathways in cartilage repair," *International Journal of Molecular Sciences*, vol. 15, no. 5, pp. 8667–8698, 2014.
- [30] B. L. Thoms, K. A. Dudek, J. E. Lafont, and C. L. Murphy, "Hypoxia promotes the production and inhibits the destruction of human articular cartilage," *Arthritis and Rheumatism*, vol. 65, no. 5, pp. 1302–1312, 2013.
- [31] S. Gao, J. Zhou, Y. Zhao, P. Toselli, and W. Li, "Hypoxia-response element (HRE)-directed transcriptional regulation of the rat lysyl oxidase gene in response to cobalt and cadmium," *Toxicological Sciences*, vol. 132, no. 2, pp. 379–389, 2013.
- [32] H. Huang, J. Yu, D. Yu, Y. Li, and S. Lu, "Effects of chemically induced hypoxia on in vitro expression of hypoxia inducible factor- $1\alpha$ , vascular endothelial growth factor, aggrecanase-1, and tissue inhibitor of metalloproteinase-3 in rat mandibular condylar chondrocytes," *Journal of Oral & Facial Pain and Headache*, vol. 28, no. 3, pp. 269–276, 2014.
- [33] J. Li and H.-M. Wang, "Effects of cobalt chloride on phenotypes of normal human saphenous vein smooth muscle cells," *International Journal of Clinical and Experimental Medicine*, vol. 7, no. 12, pp. 4933–4941, 2014.
- [34] T. Kurth, E. Hedbom, N. Shintani et al., "Chondrogenic potential of human synovial mesenchymal stem cells in alginate," *Osteoarthritis and Cartilage*, vol. 15, no. 10, pp. 1178–1189, 2007.
- [35] K. Y. Lee and D. J. Mooney, "Alginate: properties and biomedical applications," *Progress in Polymer Science*, vol. 37, no. 1, pp. 106–126, 2012.
- [36] K. Nakashima, K. Nakatsuka, K. Yamashita, K. Kurita, and T. Hayakawa, "An in vitro model of cartilage degradation by chondrocytes in a three-dimensional culture system," *International Journal of Biomedical Science*, vol. 8, no. 4, pp. 249–257, 2012.
- [37] K. Stölzel, G. Schulze-Tanzil, H. Olze, S. Schwarz, E. M. Feldmann, and N. Rotter, "Immortalised human mesenchymal stem cells undergo chondrogenic differentiation in alginate and PGA/PLLA scaffolds," *Cell and Tissue Banking*, vol. 16, no. 1, pp. 159–170, 2015.

- [38] X. Huang, X. Zhang, X. Wang, C. Wang, and B. Tang, "Microenvironment of alginate-based microcapsules for cell culture and tissue engineering," *Journal of Bioscience and Bioengineering*, vol. 114, no. 1, pp. 1–8, 2012.
- [39] S. Mazzitelli, M. Borgatti, G. Breveglieri, R. Gambari, and C. Nastruzzi, "Encapsulation of eukaryotic cells in alginate microparticles: cell signaling by TNF-alpha through capsular structure of cystic fibrosis cells," *Journal of Cell Communication and Signaling*, vol. 5, no. 2, pp. 157–165, 2011.
- [40] S. Mazzitelli, L. Capretto, X. L. Zhang et al., "Process optimization for the production of alginate microparticles containing WJMSCs by a design of experiments (doe) approach," *Journal of Controlled Release*, vol. 148, no. 1, pp. e76–e77, 2010.
- [41] Y. A. Mørch, M. Qi, P. O. M. Gundersen et al., "Binding and leakage of barium in alginate microbeads," *Journal of Biomedical Materials Research Part A*, vol. 100, no. 11, pp. 2939–2947, 2012.
- [42] S. C. N. Chang, J. A. Rowley, G. Tobias et al., "Injection molding of chondrocyte/alginate constructs in the shape of facial implants," *Journal of Biomedical Materials Research*, vol. 55, no. 4, pp. 503–511, 2001.
- [43] S. C. N. Chang, G. Tobias, A. K. Roy, C. A. Vacanti, and L. J. Bonassar, "Tissue engineering of autologous cartilage for craniofacial reconstruction by injection molding," *Plastic and Reconstructive Surgery*, vol. 112, no. 3, pp. 793–799, 2003.
- [44] M. M. Pleumeekers, L. Nimeskern, W. L. M. Koevoet et al., "The in vitro and in vivo capacity of culture-expanded human cells from several sources encapsulated in alginate to form cartilage," *European Cells and Materials*, vol. 27, pp. 264–280, 2014.
- [45] A. E. Navarro, H. Musaev, K. Serrano et al., "Adsorption kinetics of cobalt (II) ions onto alginate beads from aqueous solutions," *Earth Science & Climatic Change*, vol. 5, no. 8, pp. 223–228, 2014.
- [46] E.-S. Chan, B.-B. Lee, P. Ravindra, and D. Poncelet, "Prediction models for shape and size of ca-alginate macrobeads produced through extrusion-dripping method," *Journal of Colloid and Interface Science*, vol. 338, no. 1, pp. 63–72, 2009.
- [47] J. M. C. Puguán, X. Yu, and H. Kim, "Characterization of structure, physico-chemical properties and diffusion behavior of Ca-Alginate gel beads prepared by different gelation methods," *Journal of Colloid and Interface Science*, vol. 432, pp. 109–116, 2014.
- [48] C. A. Hoesli, R. L. Kiang, D. Mocinecová et al., "Reversal of diabetes by betaTC3 cells encapsulated in alginate beads generated by emulsion and internal gelation," *Journal of Biomedical Materials Research Part B: Applied Biomaterials*, vol. 100, no. 4, pp. 1017–1028, 2012.
- [49] C. J. Martinez, J. W. Kim, C. Ye et al., "A microfluidic approach to encapsulate living cells in uniform alginate hydrogel microparticles," *Macromolecular Bioscience*, vol. 12, no. 7, pp. 946–951, 2012.
- [50] S. Tendulkar, S.-H. Mirmalek-Sani, C. Childers, J. Saul, E. C. Opara, and M. K. Ramasubramanian, "A three-dimensional microfluidic approach to scaling up microencapsulation of cells," *Biomedical Microdevices*, vol. 14, no. 3, pp. 461–469, 2012.
- [51] S. Haeberle, L. Naegele, R. Burger, F. V. Stetten, R. Zengerle, and J. Ducre, "Alginate bead fabrication and encapsulation of living cells under centrifugally induced artificial gravity conditions," *Journal of Microencapsulation*, vol. 25, no. 4, pp. 267–274, 2008.
- [52] H. Keshaw, A. Forbes, and R. M. Day, "Release of angiogenic growth factors from cells encapsulated in alginate beads with bioactive glass," *Biomaterials*, vol. 26, no. 19, pp. 4171–4179, 2005.
- [53] V. Lefebvre, P. Li, and B. De Crombrughe, "A new long form of Sox5 (L-Sox5), Sox6 and Sox9 are coexpressed in chondrogenesis and cooperatively activate the type II collagen gene," *The EMBO Journal*, vol. 17, no. 19, pp. 5718–5733, 1998.
- [54] B. Rocha, V. Calamia, V. Casas, M. Carrascal, F. J. Blanco, and C. Ruiz-Romero, "Secretome analysis of human mesenchymal stem cells undergoing chondrogenic differentiation," *Journal of Proteome Research*, vol. 13, no. 2, pp. 1045–1054, 2014.
- [55] T. N. Wight, "Versican: a versatile extracellular matrix proteoglycan in cell biology," *Current Opinion in Cell Biology*, vol. 14, no. 5, pp. 617–623, 2002.
- [56] Y. Zhang, Y. Wu, L. Cao et al., "Versican modulates embryonic chondrocyte morphology via the epidermal growth factor-like motifs in G3," *Experimental Cell Research*, vol. 263, no. 1, pp. 33–42, 2001.
- [57] C.-C. Wang, K.-C. Yang, K.-H. Lin, H.-C. Liu, and F.-H. Lin, "A highly organized three-dimensional alginate scaffold for cartilage tissue engineering prepared by microfluidic technology," *Biomaterials*, vol. 32, no. 29, pp. 7118–7126, 2011.
- [58] M. B. Goldring, K. Tsuchimochi, and K. Ijiri, "The control of chondrogenesis," *Journal of Cellular Biochemistry*, vol. 97, no. 1, pp. 33–44, 2006.

## Research Article

# High Content Analysis of Human Pluripotent Stem Cell Derived Hepatocytes Reveals Drug Induced Steatosis and Phospholipidosis

Arvind Pradip,<sup>1,2</sup> Daniella Steel,<sup>1,3</sup> Susanna Jacobsson,<sup>1</sup>  
Gustav Holmgren,<sup>1,4</sup> Magnus Ingelman-Sundberg,<sup>5</sup> Peter Sartipy,<sup>1,4,6</sup>  
Petter Björquist,<sup>1,7</sup> Inger Johansson,<sup>5</sup> and Josefina Edsbacke<sup>1</sup>

<sup>1</sup>Takara Bio Europe AB (Former Cellectis AB/Cellartis AB), Arvid Wallgrens Backe 20, 413 46 Göteborg, Sweden

<sup>2</sup>Novo Nordisk A/S, Stem Cell Development, 2880 Bagsværd, Denmark

<sup>3</sup>Horizon Discovery Ltd, 7100 Cambridge Research Park, Waterbeach, Cambridge CB25 9TL, UK

<sup>4</sup>Systems Biology Research Center, School of Bioscience, University of Skövde, 541 28 Skövde, Sweden

<sup>5</sup>Department of Physiology and Pharmacology, Section of Pharmacogenetics, Karolinska Institutet, 171 77 Stockholm, Sweden

<sup>6</sup>AstraZeneca R&D, GMD CVMD GMed, 431 83 Mölndal, Sweden

<sup>7</sup>NovaHep AB, Arvid Wallgrens Backe 20, 413 46 Göteborg, Sweden

Correspondence should be addressed to Josefina Edsbacke; [josefina.edsbacke@takara-clontech.eu](mailto:josefina.edsbacke@takara-clontech.eu)

Received 30 July 2015; Revised 7 October 2015; Accepted 13 October 2015

Academic Editor: Toon van Veen

Copyright © 2016 Arvind Pradip et al. This is an open access article distributed under the Creative Commons Attribution License, which permits unrestricted use, distribution, and reproduction in any medium, provided the original work is properly cited.

Hepatotoxicity is one of the most cited reasons for withdrawal of approved drugs from the market. The use of nonclinically relevant *in vitro* and *in vivo* testing systems contributes to the high attrition rates. Recent advances in differentiating human induced pluripotent stem cells (hiPSCs) into pure cultures of hepatocyte-like cells expressing functional drug metabolizing enzymes open up possibilities for novel, more relevant human cell based toxicity models. The present study aimed to investigate the use of hiPSC derived hepatocytes for conducting mechanistic toxicity testing by image based high content analysis (HCA). The hiPSC derived hepatocytes were exposed to drugs known to cause hepatotoxicity through steatosis and phospholipidosis, measuring several endpoints representing different mechanisms involved in drug induced hepatotoxicity. The hiPSC derived hepatocytes were benchmarked to the HepG2 cell line and generated robust HCA data with low imprecision between plates and batches. The different parameters measured were detected at subcytotoxic concentrations and the order of which the compounds were categorized (as severe, moderate, mild, or nontoxic) based on the degree of injury at isomolar concentration corresponded to previously published data. Taken together, the present study shows how hiPSC derived hepatocytes can be used as a platform for screening drug induced hepatotoxicity by HCA.

## 1. Introduction

The liver is the most important and susceptible organ in drug toxicity being functionally interposed between site of absorption and systemic circulation [1]. Drug induced liver injury (DILI) is broadly classified into intrinsic (dose dependent and usually predictable) and idiosyncratic (does not depend on dose and unpredictable). DILI has been reported as the major reason for withdrawal of approved

drugs from the market [2]. Nearly 90% of the lead candidates identified by current *in vitro* screens fail to become drugs and about 50–60% of drugs progressing to clinical trials fail in the late stages of drug development [3, 4]. This raises a need for devising more relevant and effective screening strategies for identifying new candidate drugs (CDs), with low risk to cause DILI [5]. DILI in particular makes it more difficult owing to several mechanisms of toxicity being involved. In addition, complex interactions with the immune system, exposure

to viral infections, and genetic background of individuals affect the sensitivity of DILI [6]. Different compounds have their own sequential pattern through which they manifest an injury. Also a single drug can have multiple effects with several mechanisms of toxicity [1]. Despite the numerous animal and *in vitro* models available, currently used assays have low concordance with human liver toxicity [7, 8]. The cells need to be of human origin with functional drug metabolic competence due to substantial species differences.

High content analysis (HCA) is a powerful cell based screening method showing high sensitivity and specificity in combination with an appropriate cell source. This technology employs simultaneous measurement of multiple endpoints which are relevant to the mechanisms involved in toxicity [9]. Several cellular models are being used to study drug metabolism and toxicity. Some of the more well-established models are primary cell cultures, immortalized cell lines, intracellular fractions, precision cut liver slices, and whole perfused livers [10]. However, due to different limitations of these models, there is currently no ideal *in vitro* assay for testing hepatotoxicity.

Human pluripotent stem cells (hPSC) possess two very important capabilities, infinite self-renewal and the ability to differentiate into any cell type in the human body. Hence, they are being explored as a promising source of functional human hepatocytes. Hepatocytes can be derived from both human *embryonic* stem cells (hESCs) and human *induced pluripotent* stem cells (hiPSCs) [11, 12]. These cells have several significant advantages over existing systems, such as the fact that they are of human origin, the fact that they allow cell manufacturing with consistency between batches with an endless supply of cell material, and the opportunity to select genetic background of the starting material [13, 14]. Recently, advances in differentiating hESC and hiPSC to hepatocytes have been made generating highly pure cultures of hiPS derived hepatocyte like cells expressing hepatic markers and functional drug metabolizing cytochrome P450 enzymes. The hiPSC derived hepatocytes used in this study were differentiated from Cellartis human iPSC line, ChiPS4, using Cellartis DE Diff Kit and Hepatocyte Diff Kits (referred to as hiPS-HEP in previous publications) [15, 16]. The hiPS-hepatocytes exhibit typical hepatic morphology, expressing many hepatic markers (Figure 1), and are capable of metabolizing drugs via the cytochrome P450 (CYP) families 1A and 3A [15].

In the present study, we show that the hiPSC derived hepatocyte can serve as a platform for monitoring drug induced steatosis and phospholipidosis by HCA following mechanistic endpoints such as viability, nuclear changes, mitochondrial membrane potential (MMP), reactive oxygen species (ROS), and plasma membrane permeability (PMP). The hiPS-hepatocyte platform was benchmarked against the well-established HepG2 cells. Based on the toxic mechanisms involved, the chemicals amiodarone, doxycycline, tetracycline, and sodium citrate were categorized as severe, moderate, mild, and nontoxic. The assays for various parameters were robust and reproducible between wells, plates, and batches and thus hiPSC derived hepatocytes are a promising *in vitro* cell system for toxicity assessment by HCA.

## 2. Materials and Methods

**2.1. Human Induced Pluripotent Stem Cells and Hepatic Differentiation.** The hiPSC line ChiPSC4 (Takara Bio Europe AB) was derived as described before using human dermal fibroblasts [15]. ChiPSC4 was maintained and cultured under standard conditions in the Cellartis DEF-CS with continuous passaging twice a week according to manufacturer manual (Takara Bio Europe AB).

For hepatic differentiation, a serum- and feeder-free procedure recapitulating liver development was applied. First, ChiPSC4 was guided to differentiate into definitive endoderm using the Cellartis DE Diff Kit (Takara Bio Europe AB; Y30030), containing complete media and coating solution for differentiation of hPSC to DE cells in 2D culture. On day 7 of differentiation, the DE cells were enzymatically dissociated and reseeded into fibronectin coated 96-well plates. Briefly, fibronectin solution was prepared by diluting fibronectin (Sigma; F0895) 1:20 to 50  $\mu\text{g}/\text{mL}$  in D-PBS<sup>+/+</sup> (Life Tech; 14200-067). Wells of 96-well plates were coated by adding fibronectin solution 0.15 mL per  $\text{cm}^2$  to the wells and let to incubate for >60 min at RT. DE cells were enzymatically detached using TrypLE Select (Life Tech; 12563-011) 0.1 mL/ $\text{cm}^2$  and incubated for 3–5 min at 37°C. The enzymatic reaction was stopped by adding 10% KO-SR (Life Tech; 10828-028) in D-PBS<sup>-/-</sup> to achieve a 1:1 dilution of the cell suspension. Next, the cell suspension was centrifuged for 5 min at 300 g at RT, the supernatant was removed, and the cell pellet was resuspended in warm Hepatocyte Thawing and Seeding medium (Cellartis Hepatocyte Diff Kit; Takara Bio Europe AB; Y30050). Prior to seeding of cells, excess coating was removed and 150 K DE cells/ $\text{cm}^2$  were seeded in the 96-well plates. On days 9 and 11 (counted from the start of ChiPSC4 differentiation), medium was changed using Hepatocyte Progenitor Medium (Cellartis Hepatocyte Diff Kit). On day 14 and onwards, medium changes were performed every second or third days using warm Williams Medium E (Life Tech; 32551-087) supplemented with 0.1% PEST, HCM Single Quots (Lonza; CC-4182; GA-1000 was omitted), 10 ng/mL Oncostatin M (PromoKine; C-65020), 40 ng/mL Hepatocyte Growth Factor (PromoKine; C-64530), 0.1  $\mu\text{M}$  dexamethasone (Sigma; D8893), and 1.4  $\mu\text{M}$  BIO (Sigma; B1686).

The differentiation procedure described above corresponds to Cellartis hiPS-HEP by Takara Bio Europe AB (Göteborg, Sweden).

**2.2. Immunocytochemistry.** Human iPSC derived hepatocytes were stained as previously described in Ulvestad et al. [15]. The primary antibodies used in this study were rabbit anti- $\alpha$ 1-antitrypsin (1:200, A0012, DAKO), mouse anti-CK18 (1:100, M7010, DAKO), and rabbit anti-HNF4 $\alpha$  (1:300, sc-8987, SantaCruz Biotechnology). The following secondary antibodies were used and purchased from Life Technologies: donkey anti-rabbit Alexa Fluor 488 IgG (1:1000, A21206), donkey anti-rabbit Alexa Fluor 594 IgG (1:1000, A21207), and goat-anti-mouse Alexa Fluor 488 (1:500, A11029).

TABLE 1: Compounds studied according to their documented mechanism of action.

Compounds	MW	CAS number	Therapeutic group/chemical class	Mechanism of toxicity
Amiodarone HCl	681.8	19774-82-4	Antiarrhythmic agent	ST, PL, MI
Doxycycline	512.94	24390-14-5	Antibiotic	MI, AP, ST
Tetracycline hydrochloride	480.9	64-75-5	Antibiotic	ST, MI

AP: apoptosis; CAS: chemical abstracts service; MI: mitochondrial impairment; MW: molecular weight; PL: phospholipidosis; ST: steatosis.

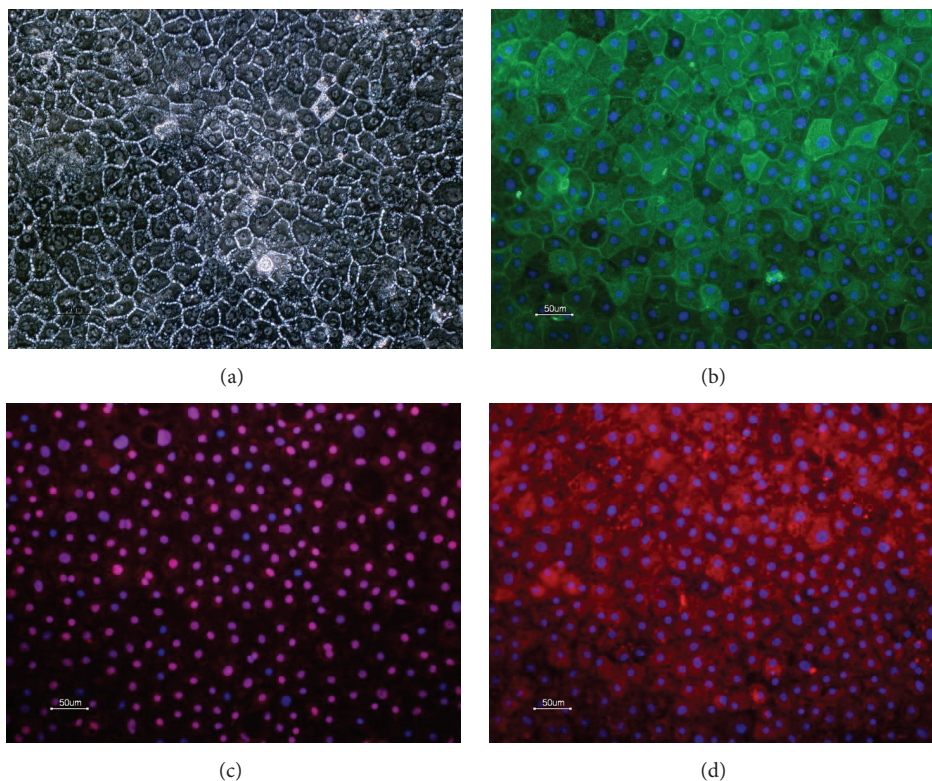


FIGURE 1: Morphology of hiPSC derived hepatocytes (a) and expression of hepatic markers cytokeratin 18 (b), HNF4 $\alpha$  (c), and alpha-1-antitrypsin (d). Scale bars equal 50  $\mu$ m.

**2.3. Materials for HCA.** The fluorescent dyes (Hoechst 33342, HCS LipidTOX Green neutral lipids (H34475), HCS LipidTOX Red phospholipidosis (H34351), MitoTracker orange CMTMRos (M7510), carboxy-H2DCFDA (C400), and TOTO-3 Iodide (T3604)) were from Life Technologies, Invitrogen. The CellBIND 96 Well Flat Clear Bottom Black Polystyrene Microplates were purchased from Corning.

**2.4. Selection of Compounds.** Three compounds (amiodarone hydrochloride, doxycycline, and tetracycline hydrochloride) known to induce hepatotoxicity through steatosis and phospholipidosis were studied (Table 1) [17]. As a negative control, sodium citrate, a nontoxic agent, was included. Positive controls were included to assess the quality of testing in each plate. Compounds with known responses were added in triplicate for each endpoint being measured. The following drugs/agents were used as positive controls for different toxic read-outs: Cyclosporin A (30  $\mu$ M) for neutral lipids, propranolol (30  $\mu$ M) for phospholipids, mitochondrial uncoupler FCCP (100  $\mu$ M) for mitochondrial membrane potential, and

tert-Butyl hydroperoxide (TBHP) luperox (100  $\mu$ M) for reactive oxygen species. When the control treated values deviated more than three standard deviations away from the mean of the other two wells, they were considered as outliers. If more than three outliers occurred in a plate, the experiment was discarded and repeated.

**2.5. HepG2 Cell Culture.** HepG2 cells (HB-8065, ATCC) were cultured according to the provider's instructions and as previously described [15]. Briefly, the cells were grown in DMEM supplemented with 10% heat inactivated FBS, 1% penicillin-streptomycin (PEST), 1% sodium pyruvate, and 1% nonessential amino acids. Cells were passaged at 1:8 or 1:6 every 3-4 days when they reach 75–80% confluence. Seeding density was optimized for HCA application to ensure that the cells were in a monolayer (5000 cells per well in 96-well plates) for precise imaging. The cells were grown for 48 h to attach and stabilize. The experiments performed with HepG2 cells were designed to ensure that each assay was performed with cells in a similar growth phase.

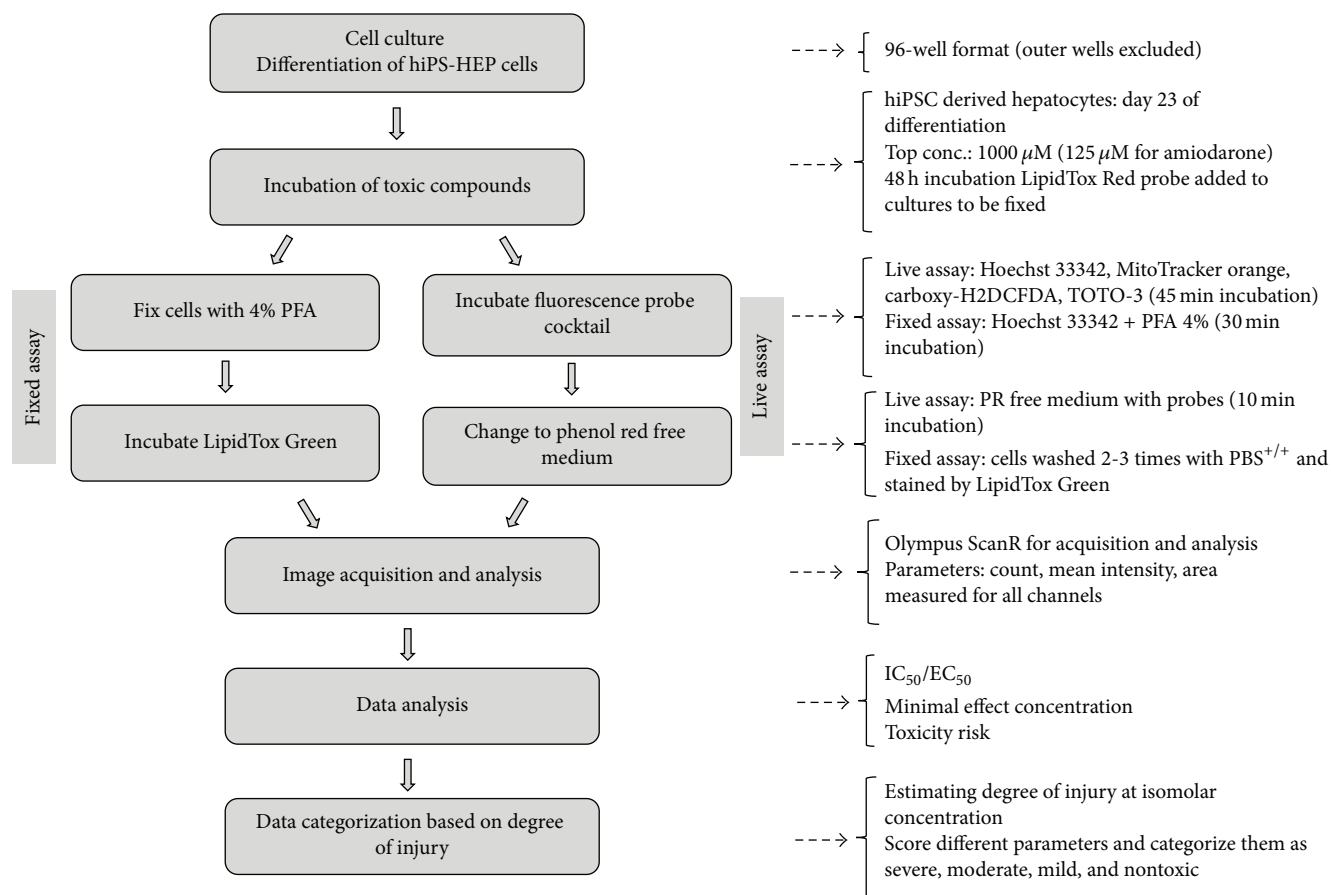


FIGURE 2: HCA assay scheme for screening drug induced steatosis and phospholipidosis.

**2.6. Assay Procedure.** The cells were treated for 48 h with compounds at varying concentrations (half log dilution from the top concentration). The highest concentrations were fixed approximately 100-fold their  $C_{\text{max}}$ , 1000  $\mu\text{M}$  for doxycycline, tetracycline, and sodium citrate, and 125  $\mu\text{M}$  for amiodarone. The stock solutions were prepared in DMSO or water and were diluted in culture medium to obtain the final concentration. Each concentration was assayed in triplicate wells. Vehicle control wells were included and the final DMSO concentration in the medium never exceeded 0.5% (v/v). Each batch had two plates each for fixed and live assays. The experimental process is illustrated in Figure 2.

**2.7. Probes.** Hoechst 33342, a cell-permeant nuclear dye, was used for measuring nuclei changes and cell number. LipidTOX Green neutral lipids and LipidTox Red phospholipidosis were used for identifying neutral lipid and phospholipid formation within the cells. MMP changes ( $\Delta\psi\text{m}$ ) within the cell were measured using MitoTracker orange. Carboxy-H2DCFDA (6-carboxy-2',7'-dichlorodihydrofluorescein diacetate) an acetylated fluorescent was used for measuring ROS. And finally, TOTO-3 was used for assessing PMP.

The fluorescence probes were grouped into two sets according to their optical compatibility and requirement of

fixed or live material. The probe concentrations were optimized and were grouped in such a way that their absorption and emission spectrum did not overlap to avoid spectral bleed-through while taking the spectral range of quadruple filter being used into consideration. The fluorescent probes for neutral lipids and phospholipids required the cells to be fixed and were assigned to the fixed assay. The probes MitoTracker orange, carboxy-H2DCFDA, and TOTO-3 were assigned to the live assay. Hoechst 33342 was included in both the fixed and live assays.

**2.8. Administration of Probes.** Following compound incubation, probes were administered to the cultures of the live assay. 50  $\mu\text{L}$  medium containing MitoTracker orange, carboxy-H2DCFDA, TOTO-3, and Hoechst probes was loaded to the cells with 100  $\mu\text{L}$  medium to a final concentration of 300 nM, 25  $\mu\text{M}$ , 1  $\mu\text{M}$ , and 1X, respectively. After incubation for 45 min at optimal cell culture conditions, the cells were changed to phenol red (PR) free medium for live cell imaging. For fixed assay, LipidTox Red probe was added with the compounds, and after 48 h the cells were fixed in 4% PFA supplemented with 1X Hoechst stain for 30 min at room temperature. Subsequently, cells were washed with PBS<sup>+/+</sup> and 1X LipidTOX Green stain diluted in PBS<sup>+/+</sup> was

incubated with the cells for 30 min at room temperature. The plates were imaged without removing the buffer with probe.

**2.9. Image Acquisition.** The cells were imaged using an Olympus ScanR system. Prior to image acquisition, the heating system and CO<sub>2</sub> gas flow were started to ensure optimal conditions in the ScanR chamber for live cell analysis. The incubator was set to 37°C with 5% CO<sub>2</sub> and relative humidity of 90%. The LUCPLFLN 20X long distance objective with NA 0.45 was used to image distinct fluorescence channels. In order to cover the entire well and also to capture maximum cell events sixteen fields per well (4×4 tile grid spread equally) were imaged. The channel exposure time for LipidTOX Green, LipidTOX Red, MitoTracker orange, and carboxy-H2DCFHDA were set based on the fluorescence of the negative control wells and were set constant within each plate. Exposure time for Hoechst and TOTO-3 was set in the range of 1–10 ms depending on cellular fluorescence intensity.

**2.10. Image Analysis.** The acquired images were analyzed using ScanR analysis program from Olympus. Background correction was applied for all images with a constant filter size value before quantification. During analysis, out-of-focus images were discarded to avoid deluding intensity values. Hoechst fluorescence signal identifying nuclei was used as the main object for cell count and other parameters measuring nuclear changes. To define main object, intensity threshold was used as object finding module. Watershed algorithm was applied to separate clusters along the indentations along the contours of the clusters to get individual cells. All other fluorescence signals were considered as subobjects. A ring area was applied around the main objects/nuclei with a set distance marking cytosolic region around the nucleus. This area is assigned *mask* and all other parameters besides the nucleus (the main object)-related parameters were measured within the mask area. Selected parameters such as count, total intensity, mean intensity, and area were estimated for each fluorescence channel. LipidTox Green and LipidTOX Red fluorescence defined for neutral lipids and phospholipids, respectively, were measured as spots for estimating number of lipid/phospholipid droplets per cell. MMP, ROS, and PMP parameters were estimated using intensity module. The analyzed parameters were exported to Microsoft excel for further calculations. The values for each parameter were normalized to the vehicle control and are presented as percentage of vehicle control.

**2.11. Data Analysis.** For each parameter analyzed, the dose response curves were plotted and IC<sub>50</sub>/EC<sub>50</sub> values were generated when possible with GraphPad Prism 5 using nonlinear four-parameter logistic curve fit (least squares). The minimal effect concentration (MEC) was defined as the lowest concentration that produced significant difference ( $p \leq 0.05$ ) when compared to the vehicle control. The toxicity risk (TR) for each compound was defined as ratio of minimal effective concentration to the maximum plasma concentration of the drug ( $C_{max}$ ). Steatotic risk index (SRI) was calculated as the ratio of the MEC for neutral lipid accumulation or for ROS generation to  $C_{max}$ .

In order to classify compounds according to their toxicity potential, the level of change was calculated for each parameter at isomolar concentration of 100 μM (except for amiodarone HCl at 125 μM). The scoring sheet used for estimating the degree of injury was adapted from Tolosa et al. [18]. Four different scores were assigned according to the level of variation when compared to the vehicle control; 0 (variation lower than 20%), 1 (variation ±20–40%), 2 (variation ±40–60%), and 3 (variation ±60–100%). The percentage change for steatosis and phospholipidosis was in a different range, so different levels were established. The scores were assigned as 0 (variation lower than 25%), 1 (variation between 25 and 150%), 2 (variation between 150 and 300%), and 3 (variation >300%). The individual scores for each parameter were summed up to estimate the severity or the degree of injury of the compound. The compounds were classified based on the degree of injury as severely toxic (≥15), moderately toxic (6–15), mildly toxic (1–5), and nontoxic (0). The order in which the compounds were classified was compared between hiPS-HEP and HepG2 cells.

**2.12. Assessment of Predictivity.** Sensitivity was measured as the proportion of toxic drugs testing positive, TP/(TP + FN), where TP is the number of toxic compounds testing positive and FN is the number of toxic drugs testing negative. Specificity was measured as proportion of nontoxic drugs testing negative, TN/(TN + FN), where TN is the number of nontoxic drugs testing negative and FN is the number of nontoxic drugs testing positive. For predicting overall toxicity producing a positive response, a compound should have a clear dose response relationship and the magnitude of effect had to be biologically relevant. The compound was not considered positive if the effects were seen only at the highest concentration unless subsequent effect was measured for either of the parameters at lower concentration. An effect was considered positive when the parameter analyzed showed significant difference of  $p \leq 0.05$  when compared to the control.

**2.13. Assay Imprecision.** To estimate the degree of random variation and artifacts in the assay, imprecision in different parameters was determined. The variations were estimated between the following: (1) well-to-well within a plate, (2) plate-to-plate within a batch, and (3) batch-to-batch for every parameter measured. Negative control wells were used to assess imprecision in cell count, nuclear changes, and plasma membrane permeability. Positive control wells were used for assessing imprecision in MMP, steatosis, phospholipidosis, and ROS. Values were considered as outliers and excluded, when they were more than three standard deviations away from the corresponding mean values for each parameter.

To estimate well-to-well coefficient of variance, mean, standard deviation, and CV% were calculated for every control well ( $N = 3$ ) and an average CV% of all the eight plates was reported for well-to-well variation. The well-to-well mean values for each parameter within a plate ( $N = 2$ ) were then averaged and its CV% was calculated for plate-to-plate variation. For batch-to-batch variance, the mean values from each plate were averaged and its CV% was reported ( $N = 4$ ).

**2.14. Statistical Analysis.** Test compounds and controls were measured in triplicate with at least three independent experiments for both hiPS-HEP and HepG2 cells. The statistical analysis was performed using one-way ANOVA, with Dunnett's test as the post hoc method. A *p* value equal to or below 0.05 was considered statistically significant.

### 3. Results

**3.1. Characterization of Human iPS Derived Hepatocytes.** The morphological characteristics of hiPSC derived hepatocytes were monitored at the start of the experiment and during toxicity dosing. The hiPSC derived hepatocytes displayed distinct morphology closely resembling human primary hepatocytes *in vitro* (Figure 1). They formed a monolayer of flat polygonal shaped cells and were often binucleated. The hiPSC derived hepatocytes expressed typical hepatic markers, for example, cytokeratin 18, HNF4 $\alpha$ , and alpha-1-antitrypsin, uniformly in the cultures (Figure 1). It was previously described and shown that the hiPS derived hepatocytes (denoted Cellartis hiPS-HEP) express functional cytochrome P450 activity of CYP1A and 3A [15].

**3.2. HCA Assessment of Drug Induced Steatosis and Phospholipidosis.** Multiplexing different probes gave an overview of the mechanisms being affected by a compound. Different parameters were measured within a specific cytoplasmic mask around single- or binuclei of the cells. Dose response curves of parameters measured for amiodarone, doxycycline, tetracycline, and sodium citrate in hiPSC derived hepatocytes and HepG2 cultures were quite consistent between the two cell systems. However, the sequence of parametric changes varied between compounds and the two cell sources.

The dose response effects of amiodarone, doxycycline, tetracycline hydrochloride, and sodium citrate in hiPSC derived hepatocytes are shown in Figure 3. Amiodarone induced both steatosis and phospholipidosis and displayed no cytotoxic effects below 12.5  $\mu$ M, while the cell count decreased by 76% at 39.5  $\mu$ M. Sequential events were observed as follows: phospholipid accumulation started at 4  $\mu$ M, followed by an increase in ROS and subsequent increase in MMP. Hyperpolarization of mitochondrial membrane was detected in doses up to 40  $\mu$ M where at higher doses the mitochondrial membrane potential dropped. Phospholipids were not detected at concentrations higher than 40  $\mu$ M. Pronounced steatogenic effects were apparent with 18-fold increase in number of lipid droplets compared to control and in a dose dependent increase of intensity and mean lipid area. Figure 4 shows high magnification images of lipid droplet formation in hiPSC derived hepatocytes induced by the steatogenic drugs amiodarone, doxycycline, tetracycline, and cyclosporine A and phospholipid accumulation induced by amiodarone and propranolol.

Doxycycline had effects on plasma membrane permeability (PMP) at low concentrations starting from 32  $\mu$ M. The cell count was reduced by 50% at 100  $\mu$ M and significant increase in lipid accumulation was observed at 320  $\mu$ M. In parallel to lipid accumulation, doxycycline induced a concentration

dependent depolarization of the mitochondrial membrane, while ROS levels were unaffected. As expected, no changes were detected for phospholipid parameters.

Tetracycline hydrochloride had minimal cytotoxic effects. The mean nuclear intensity and area were similar to the control up to 100  $\mu$ M, and at higher concentrations small increases by 12% and 14%, respectively, were observed. The sequence of effects was as follows: at 32  $\mu$ M the mitochondrial membrane potential (MMP) and the accumulation of lipid droplets increased, at 100  $\mu$ M the oxidative stress increased, and at 320  $\mu$ M the nuclear changes were evident for both nuclear intensity and area. Finally, at the highest concentration, PMP was slightly affected by an increase of 8% compared to the control. Accumulation of phospholipids was not detected.

No significant effects were caused by the negative control substance sodium citrate. The parameters measured were consistent over the whole dose range.

**3.3. Determination of IC<sub>50</sub>/EC<sub>50</sub>.** The IC<sub>50</sub> and EC<sub>50</sub> values were calculated for each parameter which had a complete range of dose response (Table 2). For dose response curves which had a wide confidence interval the values were treated as ambiguous, thus a direct correlation or comparison between hiPSC derived hepatocytes and HepG2 cell lines could not be established. The values were highly correlated with the concentration at which evident effects were seen. The IC<sub>50</sub> and EC<sub>50</sub> values in relation to the parameters investigated aid at determining the likely mechanisms through which the compounds cause toxicity.

From Table 1, it can overall be inferred that the most sensitive parameters were ROS and nuclear area for both the hiPSC derived hepatocytes and HepG2 cells. In general, hiPSC derived hepatocytes had a more complete dose response than HepG2 for the concentrations measured. The most sensitive parameter for amiodarone was nuclear area followed by phospholipid area in hiPSC derived hepatocytes and ROS and cell count for HepG2.

**3.4. Classifying Compounds by Their Mechanism of Action Using MEC.** The minimal effective concentration (MEC) was calculated as the lowest concentration with a significant change (*p* < 0.05) when compared to the control for all parameters (Table 3). The mechanism affected at the lowest concentration was considered as the main mechanism for toxicity (denoted in bold). The significance of cytotoxic signals was estimated by calculating TR and SRI as mentioned under methods [7].

The ranking of sensitivities of the different parameters was different when assessed based on MEC in comparison to IC<sub>50</sub> or EC<sub>50</sub> values. This difference likely reflects that the point of first clear significant effect (measured as MEC) measures a low dose enhancement while to reach half maximal mark (which is measured as IC<sub>50</sub>/EC<sub>50</sub>) was prolonged for some parameters.

**3.5. Predictivity of the Assay: Specificity and Sensitivity.** The specificity of the assay in hiPSC derived hepatocytes and

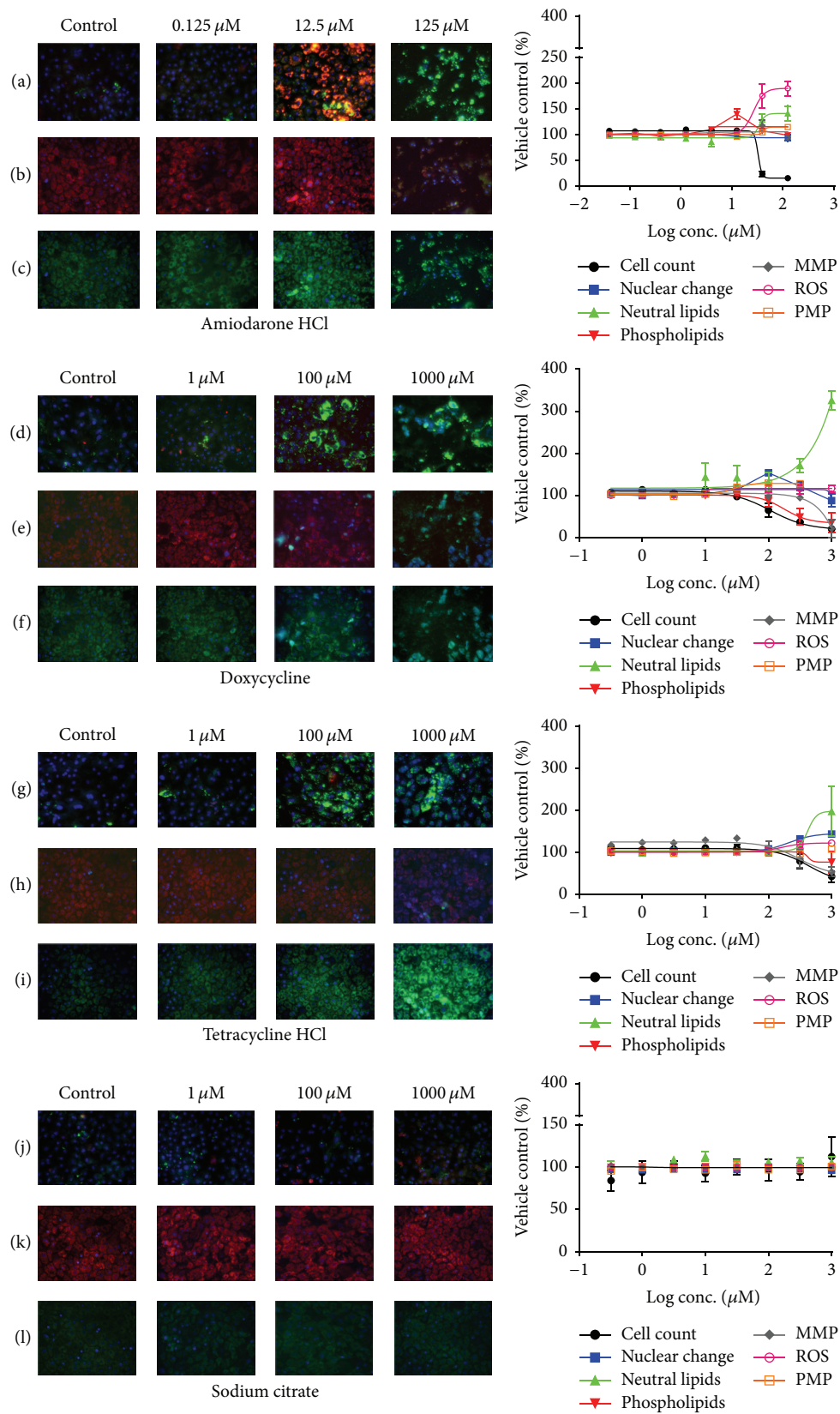


FIGURE 3: Representative images of dose response effects of amiodarone HCl (a–c), doxycycline (d–f), tetracycline hydrochloride (g–i), and sodium citrate (j–l) at three different concentrations in hiPSC derived hepatocytes. Nuclei were detected by Hoechst 33342 (blue) staining in all images. Fluorescence of LipidTOX neutral lipids (green) and LipidTOX phospholipids (red) in rows (a), (d), (g), and (j) and MMP (red) and PMP (green) in (b), (e), (h), and (k). ROS (green) in (c), (f), (i), and (l), respectively. Values denoted are mean  $\pm$  SEM ( $N = 3$ ).

TABLE 2: IC<sub>50</sub>/EC<sub>50</sub> values for drug induced effects on different parameters measured in hiPSC derived hepatocytes (hiPS-HEP) and HepG2.

Compound Cell line	Amiodarone			Doxycycline			Tetracycline		
	hiPS-HEP	HepG2		hiPS-HEP	HepG2		hiPS-HEP	HepG2	
Fixed									
Nucleus									
Cell count	31.0	7.6		107	165		432	558	
MI	95.7	140		47.2	892		<b>211</b>	348	
Area	<b>2.2</b>	39.5		96.1	OR		<b>105</b>	464	
Steatosis									
Count	21.0	19.5		115	260		184	<b>36.3</b>	
MI	34.1	23.6		441	OR		418	361	
Area	25.5	30.6		—	398		213	287	
Phospholipidosis									
Count	6.1	8.9		NA	NA		NA	NA	
MI	6.0	35.6		NA	NA		NA	NA	
Area	<b>4.5</b>	7.3		NA	NA		NA	NA	
Live									
Nucleus									
Cell count	21.9	<b>7.2</b>		69.4	<b>120.3</b>		243	836	
MI	22.4	25.0		120	153		380	959	
Area	10.4	29.1		204.3	—		211	336	
MMP									
MI	20.8	345		644	622		—	<b>265</b>	
ROS									
MI	26.5	<b>4.6</b>		<b>10.5</b>	<b>115</b>		160	1149	
PMP									
MI	42.2	147		<b>26.9</b>	OR		OR	OR	

Four-parameter variable slope curve fit using the least squares method was applied for generating dose response curves in GraphPad Prism software. Parameters with the lowest and second lowest IC<sub>50</sub>/EC<sub>50</sub> values are denoted in bold; values in italics had an ambiguous near complete dose response curve fit; [OR], curves which were out of range. Values denoted are mean values from three different experimental batches ( $N = 3$ ). All values are represented as  $\mu\text{M}$ .

TABLE 3: Cytotoxic effects of the tested compounds in hiPSC derived hepatocytes (hiPS-HEP) and HepG2: minimal effective concentration and toxicity risk steatotic risk index.

Cell system	Compound	Fixed assay									Live assay						SRI <sup>c</sup>			
		V	NC			S			PL			V	NC	MMP	ROS	PMP	C <sub>max</sub> <sup>a</sup>	TR <sup>b</sup>	Lipid	ROS
		CC	MI	A	C	MI	A	C	MI	A	CC	MI	A	MI	MI	MI				
hiPS-HEP	AMD	39.5	39.5	—	39.5	125	39.5	<b>12.5</b>	<b>12.5</b>	<b>12.5</b>	39.5	39.5	—	39.5	39.5	125	2.2	5.7	18	18
	DOX	100	—	316	316	1000	—	—	—	—	1000	100	100	1000	—	<b>31.6</b>	8.8	3.6	36	>114
	TET	1000	—	<b>316</b>	<b>316</b>	1000	—	—	—	—	1000	—	<b>316</b>	—	<b>316</b>	—	14.2	22.3	22	22
	SC	—	—	—	—	—	—	—	—	—	—	—	—	—	—	—	NA	NA	NA	NA
HepG2	AMD	<b>4</b>	39.5	125	39.5	39.5	125	—	—	—	12.5	39.5	39.5	12.5	12.5	125	2.2	1.8	18	6
	DOX	<b>100</b>	1000	1000	316	1000	—	—	—	—	316	—	—	1000	316	1000	8.8	11.4	36	36
	TET	316	<b>100</b>	316	<b>100</b>	<b>100</b>	—	—	<b>100</b>	—	—	1000	316	—	1000	1000	14.2	7.0	7	70
	SC	—	—	—	—	—	—	—	—	—	—	—	—	—	—	—	NA	NA	NA	NA

Mechanism affected at the lowest concentration is denoted in bold. Statistical significance was performed using one-way ANOVA followed by Dunnett's test. AMD: amiodarone HCl; DOX: doxycycline; TET: tetracycline; V: viability; NC: nuclear changes; S: steatosis; PL: phospholipidosis; MMP: mitochondrial membrane potential; ROS: reactive oxygen species; PMP: plasma membrane permeability; CC: cell count; MI: mean intensity; A: area; C: droplet count.

<sup>a</sup>Maximum plasma concentration of the drug (C<sub>max</sub>). <sup>b</sup>The toxicity risk (TR) for each compound was defined as ratio of minimal effective concentration to the maximum plasma concentration of the drug (C<sub>max</sub>). <sup>c</sup>Steatotic risk index (SRI) was calculated as the ratio of the MEC for neutral lipid accumulation or for ROS generation to the C<sub>max</sub>.

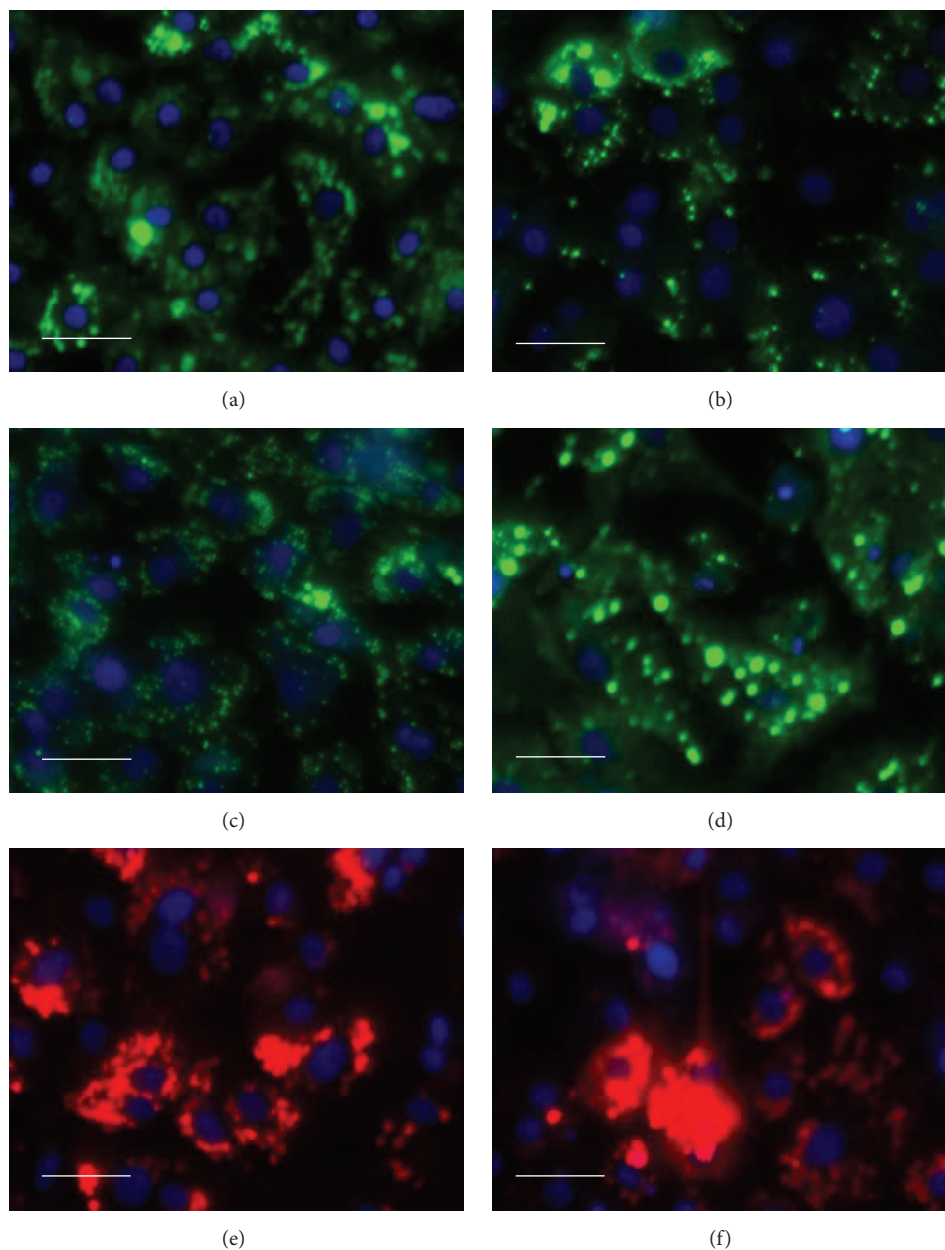


FIGURE 4: High magnification images of drug induced neutral lipid accumulation in droplets of hiPS derived hepatocytes (LipidTox Green) by amiodarone 12,5 μM (a), doxycycline 32 μM (b), tetracycline 100 μM (c), and cyclosporine A 30 μM (positive control, d) and drug induced phospholipidosis (LipidTox Red) by amiodarone 12,5 μM (e) and propranolol 30 μM (positive control, f). Nuclei are stained blue by DAPI. Scale bar 50 μM.

HepG2 cells for the three compounds tested was 100%. The number of compounds screened to present a tangible predictivity value is too low in this study to be able to fully address specificity of the two *in vitro* systems. Overall the sensitivity was 100% for nuclear changes, ROS, and steatosis in both hiPSC derived hepatocytes and HepG2. Human iPSC derived hepatocytes appear less sensitive to PMP since one of the three compounds (tetracycline hydrochloride) did not generate any significant changes. However, it is uncertain whether a cytotoxic effect is expected with tetracycline hydrochloride for the concentrations measured. Notably, HepG2 cells that

previously have been documented for detecting phospholipidosis were less sensitive than hiPSC derived hepatocytes and failed to detect phospholipid accumulation by amiodarone.

### 3.6. Categorizing Compounds Based on Their Degree of Injury.

The degree of injury was estimated at isomolar concentration of 125 μM for amiodarone and 100 μM for doxycycline, tetracycline, and sodium citrate. The scores were assigned for each parameter according to the level of variation in comparison to the control value. The compounds were categorized based on the total scores according to Tolosa et al. [18] and as

TABLE 4: Categorizing compounds based on their degree of injury at isomolar concentration of 100  $\mu\text{M}$  for each parameter measured.

Degree of injury	hiPSC derived hepatocytes	HepG2
Severe hepatotoxicity	Amiodarone HCl*	Amiodarone HCl*
Moderate hepatotoxicity	Doxycycline	
Mild hepatotoxicity	Tetracycline HCl	Doxycycline, tetracycline HCl, sodium citrate
Nontoxic	Sodium citrate	

Refer supplementary-I Table 1 for the scoring sheet on degree of injury calculation (see Supplementary Material available online at <http://dx.doi.org/10.1155/2016/2475631>). \*Degree of injury measured at 125  $\mu\text{M}$  for amiodarone.

described in methods (Table 4). Amiodarone and tetracycline were categorized as severely and mildly toxic, respectively, in both cell types. Doxycycline which was moderately toxic in hiPSC derived hepatocytes was categorized as mildly toxic in HepG2. Sodium citrate, a nontoxicant, was mildly toxic in HepG2 and nontoxic in hiPSC derived hepatocytes.

**3.7. Assay Imprecision.** The variance measurement between well-to-well, plate-to-plate, and batch-to-batch variation for each parameter in hiPSC derived hepatocytes and HepG2 is shown in Table 5. Overall, well-to-well variations within a plate had the most precise measurements for both hiPSC derived hepatocytes and HepG2. The variation of cell count between plates and batches, respectively, was high compared to other parameters measured. The higher variances for cell count in live assays could be due to the conditions maintained during imaging.

When comparing the cell sources for preciseness, hiPSC derived hepatocytes were clearly more consistent for live cell analysis. Key parameters like MMP, ROS, PMP, neutral lipid area, nuclear area, and nuclear mean intensity between plates and batches are more precise in hiPSC derived hepatocytes than HepG2 cells. The average variations ( $\text{CV}\% \pm \text{SD}$ ) for the selected parameters were  $5.3 \pm 3$  for hiPSC derived hepatocytes compared to  $13.6 \pm 7.3$  for HepG2. However, intensity values for neutral lipids and phospholipids in fixed assay displayed lower variance in HepG2 cells.

#### 4. Discussion

In the present study, we show that hiPSC derived hepatocytes might be highly sensitive and specific as an *in vitro* model for detecting drug induced steatosis and phospholipidosis, as here monitored by HCA for three different compounds. Three test drugs known to induce steatosis and/or phospholipidosis were applied to the hiPSC derived hepatocytes based model system and to a well-established model system, HepG2 cells, for benchmarking. The aim was to investigate the potential of hiPSC derived hepatocytes to serve as a platform for mechanism-based toxicity testing by HCA and its ability to correlate to known clinical toxicity patterns in humans. Since

the selected drugs are known to affect cell-health at varying concentrations and through multiple mechanisms, the assay was multiplexed with different fluorescent probes to detect several endpoints.

DILI or drug induced hepatotoxicity is known to have an intrinsic and idiosyncratic mechanism of which the most common effects are mitochondrial impairment, oxidative stress, steatosis, cholestasis, phospholipidosis, and immune mediated and apoptotic or necrotic cell death [1, 17]. Most studies on drug induced steatosis are from clinical studies in humans and as a consequence costly failures of candidate drugs due to toxicity are discovered late in the drug discovery process [8, 19]. There is therefore an urgent need for more relevant and predictive cell based model systems to screen for compounds inducing steatosis and phospholipidosis at an early stage in the drug discovery process.

Phospholipidosis, characterized by excessive intracellular accumulation of phospholipids in lysosomes and subsequent formation of lamellar bodies, is multifactorial through several mechanisms [20]. While the biochemical conditions have been well characterized, it is unclear whether drug induced phospholipidosis per se is detrimental to humans. However, many researchers consider it as an indicator for the accumulation of drugs and their metabolites accumulating within the cell, which can have severe implications during chronic exposure [21]. Drug induced liver steatosis has been reported to be caused by multiple mechanism, for example, direct inhibition of  $\beta$ -oxidation, impairment of mitochondrial respiratory chain (MRC) giving rise to enhanced ROS formation, mitochondrial dysfunction, and increased triglyceride (TG) synthesis [19, 21]. These different mechanisms are highly related and consequently an early alteration in homeostasis of one or more mechanisms leads to subsequent detrimental effects in the hepatocytes which account for the histopathological findings in drug induced steatosis and phospholipidosis [18, 22, 23]. Compounds are known to undergo repeated oxidation or reduction cycles which produce free radicals exceeding antioxidative threshold, thereby imposing oxidative stress [24]. A subsequent increase in ROS can damage proteins, lipids, or DNA which would in turn cause altered  $\text{Ca}^{2+}$  homeostasis, lipid peroxidation, or mitochondrial dysfunction [19, 25]. Altered  $\text{Ca}^{2+}$  can disrupt membrane permeability, influence mitochondrial respiratory chain [26], and also activate proteases and endonucleases leading to necrosis or apoptosis [27]. Alternatively, compounds which directly cause an imbalance in MMP would induce ROS formation causing subsequent cell death [27]. This current study demonstrates that hiPSC derived hepatocytes exposed to well-known drugs reflect the sequential mechanistic effects reported in the literature (Table 1 and Figure 3).

Cell viability in response to 48 h amiodarone treatment has previously been reported for hiPSC derived hepatocytes (hiPS-HEP) and HepG2 in Holmgren et al. 2014 [16] with slightly different outcome compared to what was shown in the current data set. The two cell types showed similar dose response curves for viability measured by the proliferation and viability assay EZ4U in Holmgren et al. study [16], while HCA measurement of viability by cell count revealed that

TABLE 5: Comparison of assay imprecision for each parameter measured in hiPSC derived hepatocytes (hiPS-HEP) and HepG2.

Assay parameter	Variation between wells in a plate		Variation between plates in a batch		Variation between batches	
	hiPS-HEP	HepG2	hiPS-HEP	HepG2	hiPS-HEP	HepG2
	CV% $\pm$ SD	CV% $\pm$ SD	CV%	CV%	CV%	CV%
CC (fixed)	6.8 $\pm$ 4.8	8.9 $\pm$ 2.6	13.0	4.1	26.7	22.6
CC (live)	15.3 $\pm$ 12.3	18.9 $\pm$ 17.3	25.8	25.5	35.3	35.0
NC						
MI	2.4 $\pm$ 1.3	1.0 $\pm$ 0.6	6.0	22.3	4.1	12.9
Area	2.3 $\pm$ 1.1	2.2 $\pm$ 0.9	6.4	6.7	5.5	6.9
ST						
MI	6.3 $\pm$ 2.7	5.0 $\pm$ 4.6	9.9	5.7	21.4	8.6
Area	3.9 $\pm$ 3.1	3.5 $\pm$ 4.5	1.1	10.7	6.6	9.5
PH						
MI	3.2 $\pm$ 1.5	1.8 $\pm$ 1.4	7.9	4.5	8.1	4.0
Area	2.4 $\pm$ 1.0	10.2 $\pm$ 10.5	18.1	37.0	13.3	2.8
MMP						
MI	4.7 $\pm$ 6.2	3.4 $\pm$ 2.7	12.3	22.1	6.8	22.4
ROS						
MI	0.9 $\pm$ 0.84	4.1 $\pm$ 2.8	4.0	7.3	5.8	5.2
PMP						
MI	4.8 $\pm$ 3.02	2.6 $\pm$ 2.0	3.9	14.7	0.6	23.0

Imprecisions of cell-to-cell within a well, well-to-well within a plate, plate-to-plate within a batch, and batch-to-batch are compared for all parameters measured. For calculating well-to-well variance, a mean, SD, and CV% were calculated for every control well ( $N = 3$ ) and an average CV% of all the eight plates was reported for well-to-well variation. The well-to-well mean values for each parameter within a batch ( $N = 2$ ) were then averaged and its CV% was calculated. The average CV% from the four batches was used to show plate-to-plate variation. For batch-to-batch variance, the mean values from each plate were averaged and its CV% was reported ( $N = 4$ ).

HepG2 cells were more sensitive to amiodarone than the hiPSC derived hepatocytes (Tables 2 and 3). Data suggests that cell count by HCA is a more sensitive method to measure viability.

In the present study, several insights were gained by estimating the  $IC_{50}/EC_{50}$  values for each parameter measured (Table 2) (excluding values higher than cell counts  $IC_{50}$  value, i.e., effects seen after 50% loss of cells). Notably, HepG2 cells depict a poorer predictivity for the different mechanistic parameters at subcytotoxic concentrations compared to hiPSC derived hepatocytes. Most of the parameters measured for amiodarone and doxycycline had  $IC_{50}/EC_{50}$  values higher than  $IC_{50}$  value for cell count in HepG2 cells.

Since  $IC_{50}/EC_{50}$  for a few parameters had ambiguous values due to the wide dose range tested, MEC, a system created for estimating the toxicity potential to screen compounds, was calculated for the two cell sources [18]. The toxicity risk of a compound, calculated as the ratio of MEC to  $C_{max}$ , gives an indication of the significance of the cytotoxic signals. These ratios provide an estimate of minimal safety margin [7]. Notably, both hiPSC derived hepatocytes and HepG2 had 100% sensitivity with a cutoff TR of 30.

The sensitivity in predicting various mechanisms was quite similar for hiPSC derived hepatocytes and HepG2 cells. The drug induced effects observed were comparable to those previously reported in HepG2 and primary hepatocytes (freshly isolated and cryopreserved) [9, 19]. For compounds

inducing steatosis and phospholipidosis, accumulation of neutral lipids and phospholipids were observed at subcytotoxic concentrations. The simultaneous incorporation of multiple probes to the assay resulted in different mechanistic read-outs and gave a good predictivity of human toxicity.

Human iPSC derived hepatocytes failed to predict the effect on PMP when treated with tetracycline hydrochloride. However, whether this compound has an effect on PMP in intact liver is unclear. Significant changes on tetracycline induced MMP were not detected in any of the two model systems tested. Amiodarone, a cationic amphiphilic compound, interferes with both mitochondrial and lysosomal function, causing steatosis and phospholipidosis [28]. HepG2 had a false negative prediction of amiodarone induced phospholipidosis. In hiPSC derived hepatocytes there was an induction of phospholipids at lower concentrations but not at higher concentrations followed by steatogenic lipid accumulation in droplets of the cells (Figures 3 and 4).

To understand the significance/relevance of HCA results, a scoring system was applied to estimate the degree of injury induced by a compound at a fixed concentration. Based on the degree of injury, the compounds were categorized as severe, moderate, mild, or nontoxic. The compounds identified with DILI potential and the order by which the compounds were categorized were in accordance with previously published data on primary human hepatocytes and HepG2 cells [7, 9, 19]. By ranking these compounds individually based on

their severity, we found that the results for hiPSC derived hepatocytes were in line with FDA-approved drug labeling for the study of DILI [29]. In HepG2 cultures, the negative control sodium citrate generated a false positive score for phospholipidosis at 100  $\mu$ M and was thereby falsely categorized as mildly toxic. Based on the MEC and degree of injury scoring detected in this study, hiPSC derived hepatocytes are superior to HepG2 as a model for predicting phospholipidosis. Although an interesting and promising result, the present evaluation is based on only four compounds/chemicals, while a larger set of compounds with a wide range of toxicity potential has to be screened in order to validate the sensitivity and specificity of hiPSC derived hepatocytes as a predictive model system.

Presently, primary human hepatocytes (PHH) are the gold standard for liver toxicity testing and in sandwich cultures PHH can be maintained for long term up to 14 days. Chlorpromazine exposure for short and long term induces different types of hepatotoxicity in PHH sandwich cultures including steatosis revealed by transcriptomic analysis [30]. However, the interindividual variability, complications in culturing, and rapidly decreasing functionality associated with these cells have led to a wide use of immortalized cell lines [31]. HepG2 cells which are derived from a human adenocarcinoma of the liver are being preferred over HeLa, ECC-1, and CHO-K1 cell lines for hepatotoxicity studies [32, 33]. However, their biotransformation capacity via cytochrome P450 enzymes is less than 1% of normal hepatocytes [33, 34]. For many compounds, the reactive metabolite is more toxic than the parent compound [18]. To screen such compounds, improved *in vitro* model systems need to be developed. HepaRG cells, a highly differentiated hepatic cell line derived from human liver carcinoma, have been reported to have high cytochrome P450 activity, functional drug transporters, and nuclear receptors making them a promising model for bioactivation and uptake studies [35, 36]. In addition, HepaRG has been shown to be a well-suited model for studying mechanistic hepatotoxicity such as steatosis, phospholipidosis, and cholestasis [37]. Moreover, amiodarone and tetracycline induce lipid droplets in HepaRG cells as well as phospholipidosis by amiodarone [37, 38]. However, the sensitivity and predictivity of these cells in detecting hepatotoxic drugs have been shown to be much lower than cryopreserved hepatocytes [39]. Importantly, these progenitor cells originate from one individual having a specific genotype. This limitation needs also to be taken into account for assessing metabolic and toxicity studies [40]. Hepatocytes derived from hESCs and hiPSCs may bridge today's gaps in safety pharmacology and toxicology by providing more stable metabolically competent cells with a functionality comparable to freshly isolated hepatocytes [11]. The two essential bottlenecks of limited supply and batch-to-batch variability can be efficiently surpassed with hiPSC derived material. In addition, hiPSC derived hepatocytes will offer a unique possibility to design/choose a desired genetic background and phenotype of the model cells. For hiPSC derived hepatocytes to replace the existing model systems, a large compound set has to be screened and the cells must recapitulate previously established results. The possibility to

correlate observed effects and pathways with an *in vivo* effect would be the most desirable form of validation. Interestingly, in our assay using hiPS derived hepatocytes, the order in which the different mechanistic effects were observed for amiodarone was similar to the clinical findings in humans reported in a case study [41].

It has been reported that conventional assays which measure late lethal events (*e.g.*, cell membrane rupture and LDH release) have poor concordance with human toxicity. A greater predictive power could be achieved when an assay can detect effects at subcytotoxic concentrations prior to the onset of general degeneration and cell death [7]. Mitochondrial potential and cellular redox states are the most important mechanisms of drug induced hepatotoxicity [9] and these two parameters had the highest sensitivity in hiPSC derived hepatocytes based on  $IC_{50}/EC_{50}$  values (Table 2). The current assay using hiPSC derived hepatocytes displayed very low variance between wells, plates, and batches. The imprecision values measured for all the parameters were quite comparable between HepG2 and hiPSC derived hepatocytes and were of the same range with previous work in HepG2 cells [7]. Overall, hiPSC derived hepatocytes are as robust for live cell analysis as the well-established and very user-friendly cell line HepG2 cells (Table 5). The robustness of the hiPSC derived hepatocyte model in combination with the reported stability of important functionalities [15] also allows for long term chronic toxicity testing [16].

## 5. Conclusions

The present study shows that homogenous cultures of hiPSC derived hepatocytes can be used as a platform to assess mechanistic toxicity and reveal drug induced steatosis and phospholipidosis by image based HCA. Importantly, the hiPSC derived hepatocytes generated reproducible and consistent HCA data with low imprecision between wells, plates, and batches; thus hiPSC derived hepatocytes can serve as a robust platform for image based HCA. In addition, the hiPSC derived hepatocytes could categorize test compounds as severe, moderate, mild, or nontoxic based on the degree of injury at isomolar concentration in concordance with previously published data. Moreover, the hiPSC technology opens up further possibilities to generate infinite numbers of hepatocytes from, for example, DILI patients and individuals representing different phenotypic and genotypic variations. In addition, the development of more sensitive and complex *in vitro* toxicity models for drug screening, based on hiPSC derived hepatocytes in combination with coculturing systems with nonparenchymal liver cells or T cells, is anticipated. The present study clearly reveals the potential of the use of hiPSC derived hepatocytes in assessing hepatotoxicity *in vitro* by the use of HCA.

## Conflict of Interests

The authors are (Josefina Edsbacke) or were, during the course of this work (Arvind Pradip, Daniella Steel, Petter

Björquist, and Peter Sartipy), employees of former Collectis AB/Cellartis AB, now Takara Bio Europe AB.

## Authors' Contribution

Arvind Pradip, Inger Johansson, and Josefina Edsbagge conceived and designed the experiments. Arvind Pradip and Susanna Jacobsson performed and analyzed them. Peter Sartipy, Arvind Pradip, Petter Björquist, and Josefina Edsbagge wrote the paper. Inger Johansson, Daniella Steel, Magnus Ingelman-Sundberg, and Gustav Holmgren did the review of paper and project.

## Acknowledgments

The authors acknowledge the Centre for Cellular Imaging at Göteborg University, for the support and use of imaging equipment. This study was supported by IMI-JU Project MIP-DILI (Grant Agreement 115336) and the Systems Biology Research Centre (University of Skövde, Sweden) under grants from the Knowledge Foundation [2011/0295 and 2013/89].

## References

- [1] S. Russmann, G. A. Kullak-Ublick, and I. Grattagliano, "Current concepts of mechanisms in drug-induced hepatotoxicity," *Current Medicinal Chemistry*, vol. 16, no. 23, pp. 3041–3053, 2009.
- [2] A. Pandit, T. Sachdeva, and P. Bafna, "Drug-induced hepatotoxicity: a review," *Journal of Applied Pharmaceutical Science*, vol. 2, no. 5, pp. 233–243, 2012.
- [3] C. Smith, "Tools for drug discovery: tools of the trade," *Nature*, vol. 446, no. 7132, pp. 219–222, 2007.
- [4] A. Sivaraman, J. K. Leach, S. Townsend et al., "A microscale in vitro physiological model of the liver: predictive screens for drug metabolism and enzyme induction," *Current Drug Metabolism*, vol. 6, no. 6, pp. 569–591, 2005.
- [5] A. Hill, N. Mesens, M. Steemans, J. J. Xu, and M. D. Aleo, "Comparisons between in vitro whole cell imaging and in vivo zebrafish-based approaches for identifying potential human hepatotoxicants earlier in pharmaceutical development," *Drug Metabolism Reviews*, vol. 44, no. 1, pp. 127–140, 2012.
- [6] N. Chalasani and E. Björnsson, "Risk factors for idiosyncratic drug-induced liver injury," *Gastroenterology*, vol. 138, no. 7, pp. 2246–2259, 2010.
- [7] P. J. O'Brien, W. Irwin, D. Diaz et al., "High concordance of drug-induced human hepatotoxicity with in vitro cytotoxicity measured in a novel cell-based model using high content screening," *Archives of Toxicology*, vol. 80, no. 9, pp. 580–604, 2006.
- [8] J. J. Xu, D. Diaz, and P. J. O'Brien, "Applications of cytotoxicity assays and pre-lethal mechanistic assays for assessment of human hepatotoxicity potential," *Chemico-Biological Interactions*, vol. 150, no. 1, pp. 115–128, 2004.
- [9] J. J. Xu, P. V. Henstock, M. C. Dunn, A. R. Smith, J. R. Chabot, and D. de Graaf, "Cellular imaging predictions of clinical drug-induced liver injury," *Toxicological Sciences*, vol. 105, no. 1, pp. 97–105, 2008.
- [10] E. F. A. Brandon, C. D. Raap, I. Meijerman, J. H. Beijnen, and J. H. M. Schellens, "An update on in vitro test methods in human hepatic drug biotransformation research: pros and cons," *Toxicology and Applied Pharmacology*, vol. 189, no. 3, pp. 233–246, 2003.
- [11] R. Kia, R. L. C. Sison, J. Heslop et al., "Stem cell-derived hepatocytes as a predictive model for drug-induced liver injury: are we there yet?" *British Journal of Clinical Pharmacology*, vol. 75, no. 4, pp. 885–896, 2013.
- [12] J. Jensen, J. Hyllner, and P. Björquist, "Human embryonic stem cell technologies and drug discovery," *Journal of Cellular Physiology*, vol. 219, no. 3, pp. 513–519, 2009.
- [13] J. Czyz, C. Wiese, A. Rolletschek, P. Blyszczuk, M. Cross, and A. M. Wobus, "Potential of embryonic and adult stem cells in vitro," *Biological Chemistry*, vol. 384, no. 10–11, pp. 1391–1409, 2003.
- [14] K. Takahashi, K. Tanabe, M. Ohnuki et al., "Induction of pluripotent stem cells from adult human fibroblasts by defined factors," *Cell*, vol. 131, no. 5, pp. 861–872, 2007.
- [15] M. Ulvestad, P. Nordell, A. Asplund et al., "Drug metabolizing enzyme and transporter protein profiles of hepatocytes derived from human embryonic and induced pluripotent stem cells," *Biochemical Pharmacology*, vol. 86, no. 5, pp. 691–702, 2013.
- [16] G. Holmgren, A.-K. Sjögren, I. Barragan et al., "Long-term chronic toxicity testing using human pluripotent stem cell-derived hepatocytes," *Drug Metabolism and Disposition*, vol. 42, no. 9, pp. 1401–1406, 2014.
- [17] M. J. Gómez-Lechón, L. Tolosa, J. V. Castell, and M. T. Donato, "Mechanism-based selection of compounds for the development of innovative in vitro approaches to hepatotoxicity studies in the LIINTOP project," *Toxicology in Vitro*, vol. 24, no. 7, pp. 1879–1889, 2010.
- [18] L. Tolosa, S. Pinto, M. T. Donato et al., "Development of a multiparametric cell-based protocol to screen and classify the hepatotoxicity potential of drugs," *Toxicological Sciences*, vol. 127, no. 1, pp. 187–198, 2012.
- [19] M. T. Donato, A. Martínez-Romero, N. Jiménez et al., "Cytometric analysis for drug-induced steatosis in HepG2 cells," *Chemico-Biological Interactions*, vol. 181, no. 3, pp. 417–423, 2009.
- [20] L. A. Chatman, D. Morton, T. O. Johnson, and S. D. Anway, "A strategy for risk management of drug-induced phospholipidosis," *Toxicologic Pathology*, vol. 37, no. 7, pp. 997–1005, 2009.
- [21] M. T. Donato, L. Tolosa, N. Jiménez, J. V. Castell, and M. J. Gómez-Lechón, "High-content imaging technology for the evaluation of drug-induced steatosis using a multiparametric cell-based assay," *Journal of Biomolecular Screening*, vol. 17, no. 3, pp. 394–400, 2012.
- [22] M. J. Reasor, K. L. Hastings, and R. G. Ulrich, "Drug-induced phospholipidosis: issues and future directions," *Expert Opinion on Drug Safety*, vol. 5, no. 4, pp. 567–583, 2006.
- [23] P. Lettéron, A. Sutton, A. Mansouri, B. Fromenty, and D. Pessayre, "Inhibition of microsomal triglyceride transfer protein: another mechanism for drug-induced steatosis in mice," *Hepatology*, vol. 38, no. 1, pp. 133–140, 2003.
- [24] H. Jaeschke, G. J. Gores, A. I. Cederbaum, J. A. Hinson, D. Pessayre, and J. J. Lemasters, "Mechanisms of hepatotoxicity," *Toxicological Sciences*, vol. 65, no. 2, pp. 166–176, 2002.
- [25] G. Labbe, D. Pessayre, and B. Fromenty, "Drug-induced liver injury through mitochondrial dysfunction: mechanisms and detection during preclinical safety studies," *Fundamental & Clinical Pharmacology*, vol. 22, no. 4, pp. 335–353, 2008.
- [26] Z. Dong, P. Saikumar, J. M. Weinberg, and M. A. Venkatchalam, "Calcium in cell injury and death," *Annual Review of Pathology*, vol. 1, pp. 405–434, 2006.

- [27] I. Grattagliano, L. Bonfrate, C. V. Diogo, H. H. Wang, D. Q. H. Wang, and P. Portincasa, "Biochemical mechanisms in drug-induced liver injury: certainties and doubts," *World Journal of Gastroenterology*, vol. 15, no. 39, pp. 4865–4876, 2009.
- [28] D. Pessayre, B. Fromenty, A. Berson et al., "Central role of mitochondria in drug-induced liver injury," *Drug Metabolism Reviews*, vol. 44, no. 1, pp. 34–87, 2012.
- [29] M. Chen, V. Vijay, Q. Shi, Z. Liu, H. Fang, and W. Tong, "FDA-approved drug labeling for the study of drug-induced liver injury," *Drug Discovery Today*, vol. 16, no. 15-16, pp. 697–703, 2011.
- [30] C. Parmentier, G. L. Truisci, K. Moenks et al., "Transcriptomic hepatotoxicity signature of chlorpromazine after short- and long-term exposure in primary human sandwich cultures," *Drug Metabolism and Disposition*, vol. 41, no. 10, pp. 1835–1842, 2013.
- [31] J. A. Lewis, W. E. Dennis, J. Hadix, and D. A. Jackson, "Analysis of secreted proteins as an in vitro model for discovery of liver toxicity markers," *Journal of Proteome Research*, vol. 9, no. 11, pp. 5794–5802, 2010.
- [32] W. G. E. J. Schoonen, J. A. D. M. de Roos, W. M. A. Westerink, and E. Débiton, "Cytotoxic effects of 110 reference compounds on HepG2 cells and for 60 compounds on HeLa, ECC-1 and CHO cells. II Mechanistic assays on NAD(P)H, ATP and DNA contents," *Toxicology in Vitro*, vol. 19, no. 4, pp. 491–503, 2005.
- [33] W. M. A. Westerink and W. G. E. J. Schoonen, "Cytochrome P450 enzyme levels in HepG2 cells and cryopreserved primary human hepatocytes and their induction in HepG2 cells," *Toxicology in Vitro*, vol. 21, no. 8, pp. 1581–1591, 2007.
- [34] S. Wilkening, F. Stahl, and A. Bader, "Comparison of primary human hepatocytes and hepatoma cell line HepG2 with regard to their biotransformation properties," *Drug Metabolism and Disposition*, vol. 31, no. 8, pp. 1035–1042, 2003.
- [35] A. Guillouzo, A. Corlu, C. Aninat, D. Glaize, F. Morel, and C. Guguen-Guillouzo, "The human hepatoma HepaRG cells: a highly differentiated model for studies of liver metabolism and toxicity of xenobiotics," *Chemico-Biological Interactions*, vol. 168, no. 1, pp. 66–73, 2007.
- [36] M. Szabo, Z. Veres, Z. Baranyai, F. Jakab, and K. Jemnitz, "Comparison of human hepatoma HepaRG cells with human and rat hepatocytes in uptake transport assays in order to predict a risk of drug induced hepatotoxicity," *PLoS ONE*, vol. 8, no. 3, Article ID e59432, 2013.
- [37] S. Anthérieu, C. Chesné, R. Li, C. Guguen-Guillouzo, and A. Guillouzo, "Optimization of the HepaRG cell model for drug metabolism and toxicity studies," *Toxicology in Vitro*, vol. 26, no. 8, pp. 1278–1285, 2012.
- [38] S. Anthérieu, A. Rogue, B. Fromenty, A. Guillouzo, and M.-A. Robin, "Induction of vesicular steatosis by amiodarone and tetracycline is associated with up-regulation of lipogenic genes in heparg cells," *Hepatology*, vol. 53, no. 6, pp. 1895–1905, 2011.
- [39] H. H. J. Gerets, K. Tilmant, B. Gerin et al., "Characterization of primary human hepatocytes, HepG2 cells, and HepaRG cells at the mRNA level and CYP activity in response to inducers and their predictivity for the detection of human hepatotoxins," *Cell Biology and Toxicology*, vol. 28, no. 2, pp. 69–87, 2012.
- [40] T. B. Andersson, K. P. Kanebratt, and J. G. Kenna, "The HepaRG cell line: a unique in vitro tool for understanding drug metabolism and toxicology in human," *Expert Opinion on Drug Metabolism & Toxicology*, vol. 8, no. 7, pp. 909–920, 2012.
- [41] M. Atiq, J. C. Davis, L. W. Lamps, S. S. Beland, and J. E. Rose, "Amiodarone induced liver cirrhosis. Report of two cases," *Journal of Gastrointestinal and Liver Diseases*, vol. 18, no. 2, pp. 233–235, 2009.

## Research Article

# Hematopoietic Stem and Progenitor Cell Expansion in Contact with Mesenchymal Stromal Cells in a Hanging Drop Model Uncovers Disadvantages of 3D Culture

Olga Schmal,<sup>1</sup> Jan Seifert,<sup>2</sup> Tilman E. Schäffer,<sup>2</sup> Christina B. Walter,<sup>3</sup> Wilhelm K. Aicher,<sup>4</sup> and Gerd Klein<sup>1</sup>

<sup>1</sup>Center for Medical Research, Department of Medicine II, University of Tübingen, 72072 Tübingen, Germany

<sup>2</sup>Institute of Applied Physics, University of Tübingen, 72076 Tübingen, Germany

<sup>3</sup>Department of Obstetrics and Gynecology, University of Tübingen, 72076 Tübingen, Germany

<sup>4</sup>Department of Urology, University of Tübingen, 72076 Tübingen, Germany

Correspondence should be addressed to Gerd Klein; [gerd.klein@uni-tuebingen.de](mailto:gerd.klein@uni-tuebingen.de)

Received 6 August 2015; Accepted 12 October 2015

Academic Editor: Toon van Veen

Copyright © 2016 Olga Schmal et al. This is an open access article distributed under the Creative Commons Attribution License, which permits unrestricted use, distribution, and reproduction in any medium, provided the original work is properly cited.

Efficient *ex vivo* expansion of hematopoietic stem cells with a concomitant preservation of stemness and self-renewal potential is still an unresolved ambition. Increased numbers of methods approaching this issue using three-dimensional (3D) cultures were reported. Here, we describe a simplified 3D hanging drop model for the coculture of cord blood-derived CD34<sup>+</sup> hematopoietic stem and progenitor cells (HSPCs) with bone marrow-derived mesenchymal stromal cells (MSCs). When seeded as a mixed cell suspension, MSCs segregated into tight spheroids. Despite the high expression of niche-specific extracellular matrix components by spheroid-forming MSCs, HSPCs did not migrate into the spheroids in the initial phase of coculture, indicating strong homotypic interactions of MSCs. After one week, however, HSPC attachment increased considerably, leading to spheroid collapse as demonstrated by electron microscopy and immunofluorescence staining. In terms of HSPC proliferation, the conventional 2D coculture system was superior to the hanging drop model. Furthermore, expansion of primitive hematopoietic progenitors was more favored in 2D than in 3D, as analyzed in colony-forming assays. Conclusively, our data demonstrate that MSCs, when arranged with a spread (monolayer) shape, exhibit better HSPC supportive qualities than spheroid-forming MSCs. Therefore, 3D systems are not necessarily superior to traditional 2D culture in this regard.

## 1. Introduction

Hematopoietic stem cell (HSC) transplantation is a common treatment procedure for patients suffering from hematopoietic disorders or blood cell cancer [1]. Hematopoietic stem and progenitor cells (HSPCs) derived from umbilical cord blood (UCB) proved to be an effective source for transplantation, combined with the benefit of a minimally invasive recovery method and the possibility of UCB cryopreservation [2–4]. But the small number of available donor cells is often the limiting factor for treatment outcome. Hence, for an efficient *ex vivo* expansion of HSPCs an effective culture method is required which ensures the maintenance of their stemness including the high self-renewal potential.

Hematopoiesis takes place in multiple anatomical regions during embryogenesis. Primitive blood formation starts in the yolk sac and moves to the aorta-gonad-mesonephros region, and definitive hematopoiesis first occurs in the fetal liver [5–7]. During the last trimester of pregnancy, HSPCs migrate from the fetal liver to the circulating blood as hematopoiesis shifts to the bone marrow postnatally. This phenomenon enables the isolation of increased numbers of CD34<sup>+</sup> HSPCs from UCB.

Endosteal and vascular niches are unique microenvironments in the adult bone marrow that ensure lifelong maintenance and regulation of HSCs through a specialized combination of cellular and molecular components [8, 9]. Bone-forming osteoblasts, bone-resorbing osteoclasts,

pericytes surrounding endothelial cells, and mesenchymal stromal cells (MSCs) create a particular extracellular matrix (ECM) and express a variety of cytokines, chemokines, and adhesion receptors regulating HSC quiescence, self-renewal, and differentiation [10–14]. Early long-term culture experiments showed that marrow stromal cells are able to maintain HSC self-renewal and proliferation *in vitro* [15, 16]. More recent studies identified MSCs as key players in the niche in view of the growing number of MSC subpopulations detected in the bone marrow based on their individual expression pattern of CD146, CD140a, CD51, leptin receptor, or nestin [11, 13, 17, 18]. These subpopulations show high potential for HSC maintenance, an ability that designates MSCs as the most frequently used cell type for supporting HSC expansion *ex vivo*.

There are increasing efforts to switch from two-dimensional (2D) to three-dimensional (3D) systems because 3D culture conditions are thought to reflect the *in vivo* situation more accurately, compared with the culture of cells as monolayers. A large diversity of approaches has been reported which have attempted to mimic the inherent HSC environment in a 3D manner via cell encapsulation with hydrogels of natural or artificial origin or self-assembling peptides and polyacrylates [19–22]. Culture devices with low adhesion potential and microwell arrays were tested as 3D models, but some of these should be considered as “quasi-3D models” only [23–25]. Biocompatible macroporous scaffolds which resemble the physiological architecture of trabecular bone seem to more closely represent the natural stem cell habitats [26–28]. However, many of these culture methods are afflicted with disadvantages due to the requirement for complex surface modifications, the use of components of animal origin, or technically demanding and time consuming production processes, making their establishment in routine stem cell laboratories nearly impossible.

In the present study, we sought to evolve an easy-to-use 3D model for the expansion of cord blood-derived HSPCs in coculture with bone marrow-derived MSCs, two cell types which are easily available to most clinical laboratories. Here, we describe a procedure of hanging drop cultures that leads to compact spheroid formation. Cell-cell interactions in the spheroids were visualized by electron microscopy, and synthesis of niche-specific ECM substrates was analyzed using immunofluorescence staining. HSPC proliferation in hanging drops was compared to the coculture in 2D plastic dishes. Finally, colony-forming assays were performed in order to investigate the differentiation potential of HSPCs expanded in the 3D model.

## 2. Materials and Methods

**2.1. Human Primary Cells and Cell Culture.** Umbilical cord blood and bone marrow aspirates were obtained from healthy donors with written informed consent from the Department of Gynecology and Obstetrics or from the BG Trauma Clinic, University of Tübingen, respectively, in accordance with the guidelines of the local ethics committee (reference numbers 005/2012BO2 and 453/2011/BO). Mononuclear cells (MNCs) from cord blood were isolated

by Histopaque (1.077 g/mL) density-gradient centrifugation (Sigma-Aldrich, Taufkirchen, Germany) and washed with Dulbecco's phosphate-buffered saline (DPBS; Invitrogen, Life Technologies, Darmstadt, Germany) supplemented with 2 mM EDTA (Biochrom, Berlin, Germany). The MNC population was labeled with anti-CD34-conjugated microbeads according to the instructions of the manufacturer (Miltenyi Biotec, Bergisch Gladbach, Germany). CD34<sup>+</sup> HSPCs were enriched by magnetic cell separation using MACS columns (Miltenyi Biotec) and used immediately for coculture experiments. MNCs from bone marrow aspirates, enriched by Histopaque (1.077 g/mL) density-gradient centrifugation, were seeded in T75 cell culture flasks in MSC expansion medium compliant with the current good medical procedure regulations (GMP). The GMP medium consisted of DMEM low glucose (Lonza, Basel, Switzerland) supplemented with 5% fresh frozen plasma (TCS Bioscience, Buckingham, United Kingdom), 5% human thrombocyte lysate (Blood Cell Donation Center, University of Tübingen), 2 mM L-glutamine (Lonza), 1000 IE heparin sodium salt (Roth, Karlsruhe, Germany), and 25 mM HEPES sodium salt solution (Sigma-Aldrich). Nonattached cells were removed after 24 hours. Adherent cells were routinely characterized according to the minimum criteria for multipotent MSCs recommended by a consensus conference of the International Society for Cellular Therapy [29]. In the present study, MSCs of passage 2 to passage 4 were used.

**2.2. 3D Hanging Drop Cultures.** After detachment from culture flasks,  $5 \times 10^3$  MSCs were seeded in 40  $\mu$ L medium per well of a Perfecta3D 96-well hanging drop plate (3D Biomatix, Biotrend, Cologne, Germany). The developed spheroids were harvested and analyzed at different time points.

Coculture experiments were performed with a mixture of  $5 \times 10^3$  MSCs and  $5 \times 10^2$  CD34<sup>+</sup> HSPCs per well in 40  $\mu$ L medium consisting of GMP and serum-free expansion medium (SFEM; Stem Cell Technologies, Grenoble, France) at a 1:4 ratio supplemented with the recombinant human cytokines Flt-3 ligand, stem cell factor (100 ng/mL each), interleukin-3, and interleukin-6 (20 ng/mL each) (CC100; Stem Cell Technologies), from here on referred to as “GMP-SFEM-CC100 medium.” Cells were kept in a fully humidified atmosphere with 5% CO<sub>2</sub> at 37°C. A partial medium exchange was performed every 2 to 3 days.

**2.3. Inhibition of Spheroid Formation.** In a hanging drop plate,  $5 \times 10^3$  MSCs suspended in 40  $\mu$ L GMP medium were seeded per well. Cells were treated overnight with the function-blocking monoclonal antibody against the extracellular domain of N-cadherin (clone 8C11; BioLegend, London, United Kingdom) or with the monoclonal anti-cadherin-11 antibody (clone 283416; R&D Systems, Wiesbaden, Germany). Spheroid formation was examined under a light microscope and representative pictures were taken.

**2.4. Spheroid Harvesting and Cryosectioning.** Cryosections of spheroids were used for immunostaining. MSCs alone or in coculture with CD34<sup>+</sup> HSPCs were incubated in hanging

drop plates for up to two weeks. Pictures of MSC spheroids were taken at regular intervals and spheroid diameters were determined using the AxioVision Rel. 4.8 software from Zeiss (Göttingen, Germany). On different days of co- or monoculture, spheroids were washed with PBS supplemented with  $\text{Ca}^{2+}$  and  $\text{Mg}^{2+}$  ( $\text{PBS}^{++}$ ) in hanging drop plates and fixed with 4% paraformaldehyde (PFA; Electron Microscopy Sciences, Hatfield, USA) for 30 min at room temperature in the dark and stained with Trypan blue (0.5% solution; PAA Laboratories, Cölbe, Germany) for 3 to 5 min, embedded in Tissue-Tek O.C.T. compound (Sakura Finetek Europe, Staufen, Germany), and frozen at  $-20^{\circ}\text{C}$ . Cryosections of 5 or 8  $\mu\text{m}$  thickness were air dried for 1 h and stored at  $-20^{\circ}\text{C}$ .

**2.5. Immunofluorescence Staining.** Spheroid cryosections were thawed and fixed with 4% PFA for 15 min at room temperature. Samples were incubated for 1 h with primary antibodies diluted in  $\text{PBS}^{++}$  containing 0.1% bovine serum albumin (BSA; Sigma-Aldrich). In this study, we used the mouse anti-N-cadherin antibody (clone 8C11), the mouse anti-cadherin-11 antibody (clone 283416), and the mouse anti-CD45 (clone HI30; BioLegend) and mouse anti-CD90 (clone 5E10; BioLegend) antibodies. Different laminin chains were detected with the polyclonal rabbit anti-alpha2 chain antiserum (Bioss, Freiburg, Germany) and the mouse anti-alpha4 (clone 3H2) and anti-alpha5 chain (clone 4B12) antibodies (both kindly provided by Dr. Sulev Ingerpuu, IMCB, University of Tartu, Estonia). ECM components were stained with the rabbit anti-collagen type IV (kind gift of Dr. Johannes Eble, University of Münster, Germany) and rabbit anti-collagen type VI [30] antibodies. The mouse anti-fibronectin (clone PIH11) and the mouse anti-tenascin-C (clone T2H5) antibodies were obtained from R&D Systems and Abcam (Cambridge, United Kingdom), respectively. For apoptosis analysis, sections were permeabilized using 0.1% Triton X-100 (AppliChem; Schubert & Weiss, Munich, Germany), incubated for 1 h in blocking buffer (5% normal goat serum, 0.3% Triton X-100 in PBS), and stained overnight with the rabbit antibody against cleaved caspase-3 (clone 5A1E) or the antibody detecting cleaved PARP (clone D64E10; both from Cell Signaling Technology; New England Biolabs, Frankfurt, Germany) at  $+4^{\circ}\text{C}$ . After washing with  $\text{PBS}^{++}$ , bound primary antibodies were detected by Cy3-conjugated goat anti-mouse, Cy3-conjugated goat anti-rabbit, and Alexa Fluor 488-conjugated goat anti-rabbit antibodies (Jackson ImmunoResearch; Dianova, Hamburg, Germany). Cell nuclei were identified by counterstaining with 4',6-diamino-2-phenylindole-dihydrochloride (DAPI, 1  $\mu\text{g}/\text{mL}$ ; Roche, Mannheim, Germany). Primary antibodies were omitted for control staining. Photographs were taken using the AxioPhot microscope (Zeiss).

**2.6. Scanning Electron Microscopy (SEM).**  $\text{CD34}^{+}$  HSPCs were incubated with MSCs in hanging drop plates at a ratio of 0.5 :  $5 \times 10^3$  for up to 7 days. At different time points, coculture samples were prepared for SEM analysis. Cells in hanging drops were washed with  $\text{PBS}^{++}$ , fixed with Karnovsky's fixative (2% paraformaldehyde (Electron Microscopy Sciences), 2.5% glutaraldehyde (Serva, Heidelberg, Germany))

for 30 min at room temperature in the dark, washed with  $\text{PBS}^{++}$ , and stored in 70% ethanol at  $+4^{\circ}\text{C}$  until all samples were collected. Dehydration was performed with an increasing graded ethanol series. The samples were dried at room temperature, immobilized to coverslips via a one-component cyanoacrylate adhesive (Wevo-Cyamet 75; Wevo-Chemie, Ostfildern, Germany), and mounted onto aluminum holders using conductive tabs (G3347, Plano, Wetzlar, Germany) and then sputter coated with a 20 nm gold layer. Analysis was performed using a scanning electron microscope (XL30, Philips, Amsterdam, Netherlands). SEM images were recorded with an acceleration voltage of 10 kV.

**2.7. MSC Proliferation Analysis.**  $5 \times 10^3$  MSCs suspended in 40  $\mu\text{L}$  GMP-SFEM-CC100 medium were seeded in parallel in a hanging drop plate and in a conventional 96-well flat-bottom plate and cultivated in a humidified environment with 5%  $\text{CO}_2$  at  $37^{\circ}\text{C}$ . Partial medium changes were performed as required. On day 3 and day 7, spheroids were harvested by pipetting into a 96-well plate. Medium was removed from the 2D and 3D cultures and plates were directly transferred to  $-80^{\circ}\text{C}$ . The MSC proliferation rate was determined by analysis of DNA content (performed in triplicate) using the CyQUANT kit from Invitrogen following the manufacturer's instructions. A calibration curve was generated by seeding different MSC numbers in a 96-well plate.

**2.8. HSPC Expansion Analysis.**  $5 \times 10^2$   $\text{CD34}^{+}$  HSPCs were seeded in 40  $\mu\text{L}$  GMP-SFEM-CC100 medium per well either alone (monoculture) or together with  $5 \times 10^3$  MSCs (coculture) in a flat-bottom or a hanging drop 96-well plate (2D or 3D, resp.). On days 4, 7, 10, and 14, the HSPC proliferation rate was determined by manually counting the number of cells under a light microscope (performed in triplicate). Cell aggregations in the 3D culture were separated by pipette mixing, and cells in the 2D culture were detached by incubation with Accutase solution (Sigma-Aldrich) for 3 to 5 min. HSPCs were clearly distinguishable from MSCs based on cell size, shape, and granularity.

**2.9. Colony-Forming Assay.** In order to analyze the influence of 2D and 3D culture conditions on the differentiation potential of hematopoietic progenitors, colony-forming assays were performed with HSPCs expanded in triplicate in coculture with MSCs for one week.  $10^3$  HSPCs per replicate were diluted in 100  $\mu\text{L}$  Iscove's modified Dulbecco's medium plus 2% fetal bovine serum (Stem Cell Technologies) and added to 1 mL methylcellulose medium containing recombinant human stem cell factor, granulocyte-macrophage colony-stimulating factor, interleukin-3, and erythropoietin (MethoCult H4434, Stem Cell Technologies). Cells plated in 35 mm petri dishes were cultured in a fully humidified environment with 5%  $\text{CO}_2$  at  $37^{\circ}\text{C}$  for 14 days. Cell aggregates containing more than 50 cells were identified as single colonies using an inverted microscope (Axiovert 135; Zeiss). Burst-forming unit erythrocyte (BFU-E) and colony-forming unit-granulocyte/macrophage (CFU-GM) colonies as well as colonies arising from multipotent granulocyte, erythrocyte,

macrophage, and megakaryocyte progenitors (CFU-GEMM) were counted independently by two investigators on the basis of morphological criteria. The differentiation potential of cells

expanded in 2D or 3D was compared to freshly isolated, nonexpanded CD34<sup>+</sup> HSPCs. The CFU fold increase for the different progenitors was calculated as follows:

$$\frac{\text{CFU number of expanded HSPCs} \times \text{proliferation factor in 2D or 3D after one week}}{\text{CFU number of nonexpanded HSPCs}} = \text{CFU fold increase.} \quad (1)$$

**2.10. Immunoblotting.** Total protein extracts were obtained by incubating confluent MSC cultures with extraction buffer containing 1% NP-40, 150 mM NaCl, 40 mM Tris, 2 mM EDTA, 0.5% sodium deoxycholate, 0.1% SDS (pH 8), and a proteinase inhibitor cocktail (Roche). Cell lysates were diluted in a DTT-containing sample buffer and run on 6% SDS polyacrylamide gels. PVDF membranes (Merck Millipore, Schwalbach, Germany) were used for blotting. Unspecific binding sites were blocked with Tris-buffered saline containing 0.1% Tween-20 and 5% skimmed milk powder (Roth). Blot membranes were incubated with the mouse antibodies against N-cadherin and cadherin-11 overnight at +4°C. Bound primary antibodies were detected with HRP-conjugated or AP-conjugated anti-mouse antibodies (Dako, Hamburg, Germany) and the chemiluminescence reagent Immobilon Western (Merck Millipore) or the BCIP/NBT substrate (Sigma), respectively.

**2.11. Statistical Analysis.** Values are expressed as mean ± standard deviation (SD). Statistical significance was determined by two-tailed parametric *t*-tests or one-way ANOVA using GraphPad Prism 5 software (Version 5.01). Differences were considered to be significant for \**p* < 0.05, \*\**p* < 0.01, and \*\*\**p* < 0.001 with increasing degrees of significance.

### 3. Results

**3.1. Hanging Drop Culture of MSCs Leads to Spheroid Formation and Proliferation Arrest.** Prior to the 3D coculture, the behavior of MSCs in the hanging drop model was examined.  $5 \times 10^3$  cells were seeded in 40  $\mu$ L medium per well of a 96-well hanging drop plate. Within one day, the MSCs readily aggregated into a single compact spheroid of approximately 380–400  $\mu$ m in diameter. Hematoxylin/eosin staining of cryosections revealed a spongy core of the spheroid with bulky intercellular spaces surrounded by a tight ring of MSCs (Figure 1(a)). The cell adhesion molecules N-cadherin and cadherin-11, earlier shown to mediate the interaction of human HPCs and MSCs [31], were both expressed by bone marrow-derived MSCs as confirmed by Western blotting (Figure 1(b)). Immunofluorescence staining of cryosections showed an even distribution of cadherin-11 throughout the spheroid, whereas the N-cadherin signal was more prominent in the periphery and rather faint in the spongy core (Figure 1(b)). Nevertheless, MSC spheroid formation was impaired to a higher extent by a function-blocking anti-N-cadherin antibody than after addition of an anti-cadherin-11 antibody, leading to the formation of additional small

aggregates (Figure 1(c)). This inhibitory effect, however, was short-lived because no differences were detectable on day 2 compared to the untreated spheroids. These findings show that MSCs devoid of any substrate give rise to compact aggregates with tight homotypic interactions. N-cadherin and cadherin-11 are at least partly responsible for the observed cell-cell contact formation, but it is likely that additional cell adhesion molecules are also involved.

After spheroid formation was completed, the diameter of the cell aggregate decreased gradually during the following two weeks of culture to almost half of the original size (Figure 1(d)), indicating that, in contrast to their high expansion rate under 2D culture conditions, MSCs do not proliferate in this 3D model. Indeed, quantification of DNA content after 3 and 7 days revealed considerably lower cell numbers per spheroid compared with the MSC numbers in the starting culture (Figure 1(e)). This assay was performed in GMP-SFEM-CC100 medium at a 1:4 ratio because this mixture was identified as the optimum for HSPC expansion in the coculture studies (Supplementary Figure S3 (see Supplementary Material available online at <http://dx.doi.org/10.1155/2016/4148093>)). The MSC growth cessation in spheroids was only partly due to the medium composition and was mainly a consequence of the 3D culture conditions because spheroids incubated in the MSC expansion medium GMP exhibited the same growth behaviour (Supplementary Figure S1). The proliferation arrest in spheroids was accompanied by an onset of apoptotic events. The nuclear protein PARP1 can be processed by proteolytic activation of caspase-3, a key step during apoptosis induction. Caspase-3 and cleaved PARP1-positive cells could be detected in the central region of 3-day-old spheroids (Figure 1(f)). The number of apoptotic cells was clearly increased after one week. In summary, MSC spheroids were characterized by a continually shrinking diameter due to aggregate compaction (comparing days 3 and 6 in Figure 1(f)), lack of proliferation, and the onset of apoptosis.

**3.2. Cord Blood HSPCs Disrupt MSC Spheroids in the Hanging Drop Coculture.** CD34<sup>+</sup> HSPCs isolated from umbilical cord blood were seeded together with bone marrow-derived MSCs at a ratio of  $5 \times 10^2 : 5 \times 10^3$  per well in a 96-well hanging drop plate and cultured in GMP-SFEM-CC100 for 2 weeks (Figure 2(a)). As described for MSCs alone, the MSCs in the coculture similarly aggregated into compact spheroids which were surrounded by rapidly expanding HSPCs (Figure 2(b)). Scanning electron microscopy (SEM) revealed that, at the beginning (day 3), MSC spheroids exhibited a smooth surface with only a few HSPCs attached to it (Figure 2(c)). With

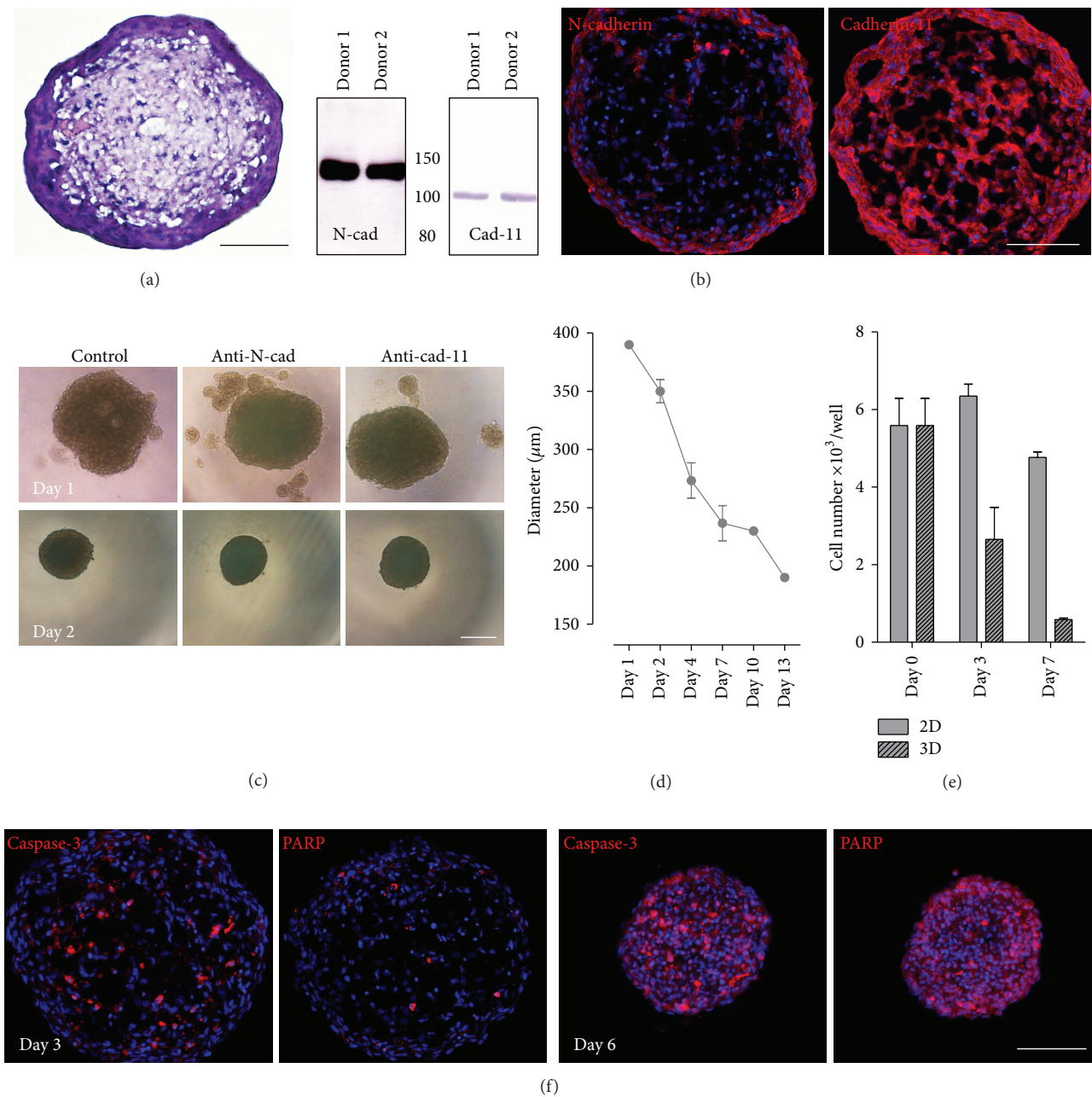


**FIGURE 1:** MSCs cultured in hanging drop plates form stable spheroids and do not proliferate.  $5 \times 10^3$  mesenchymal stromal cells seeded in a hanging drop plate aggregate into a spheroid. (a) Hematoxylin/eosin staining of a spheroid cryosection shows a typical morphology with vast intercellular spaces in the central region and a tight peripheral MSC ring after 3 days of culture. (b) Human bone marrow MSCs express the cell adhesion molecules N-cadherin and cadherin-11 as shown by immunoblotting of lysates from confluent cell layers of two different donors. Using immunofluorescence staining, both cadherins were clearly detectable in MSC spheroids. (c) Aggregation of MSCs into spheroids was investigated in the presence of antibodies against N-cadherin and cadherin-11. On day 1, additional smaller aggregates were detectable as compared to the untreated cells, while all spheroids showed a similar morphology on the second culture day. (d) Determination of the diameter of the formed MSC spheroids with the AxioVision software revealed a continual decrease over two weeks. Spheroid sizes of four different donors were analyzed. Data are means  $\pm$  SD. (e) Cell numbers of MSCs cultured in GMP-SFEM-CC100 medium as hanging drops (3D) or in conventional 2D plates were quantified in triplicate and are shown as means  $\pm$  SD. The data are representative of three donors with comparable results. (f) Apoptotic cells in 3- and 6-day-old spheroids were detected by staining with specific anti-caspase-3 and anti-PARP antibodies. Cell nuclei were counterstained with DAPI. The immunofluorescence and light microscopy pictures are representative for MSC spheroids of at least three different donors. Scale bars: 100  $\mu\text{m}$  (a, b, and f) and 250  $\mu\text{m}$  (c).

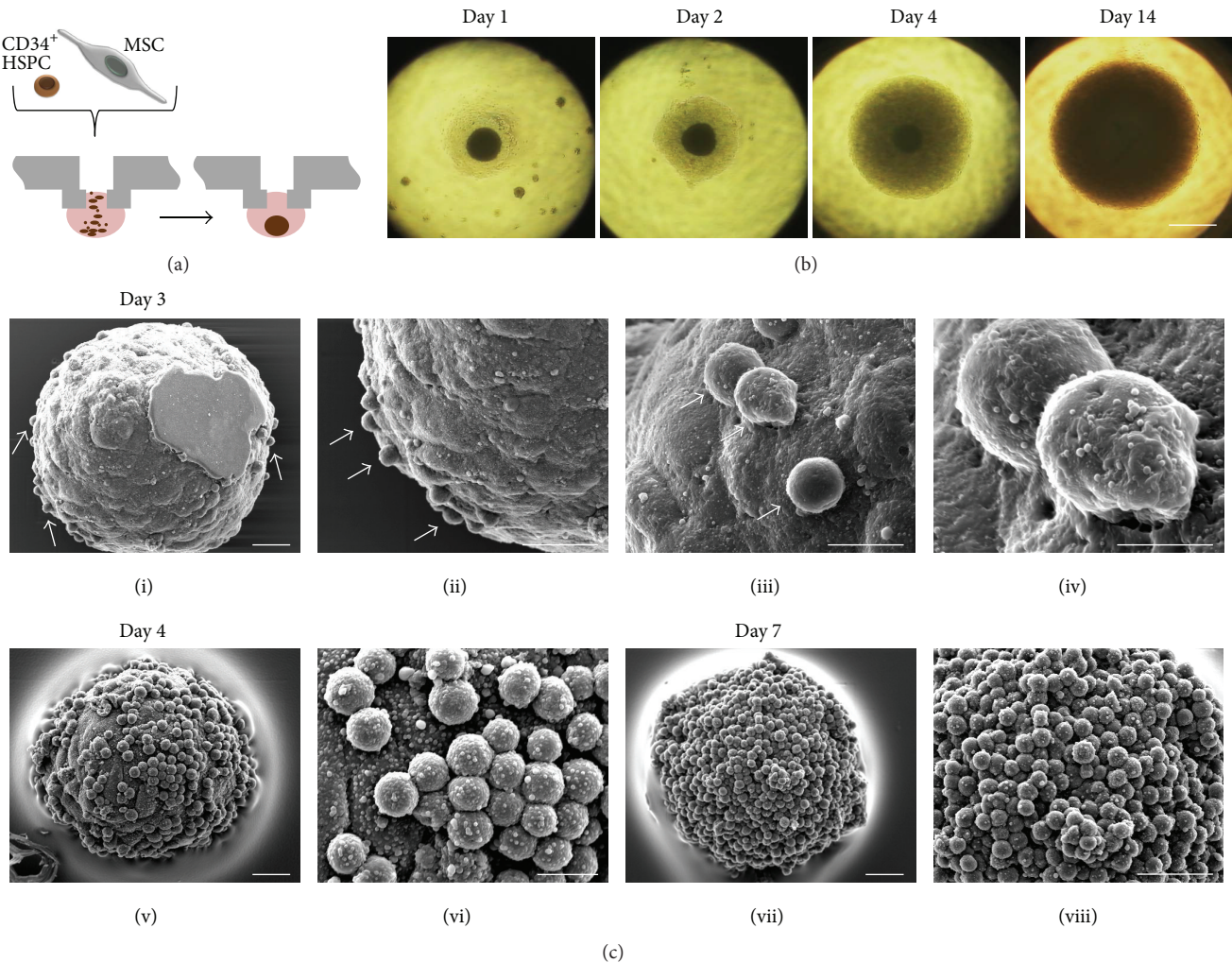


**FIGURE 2:** Attachment of CD34<sup>+</sup> HSPCs to newly formed spheroids increases with time. (a) For coculture experiments,  $5 \times 10^2$  CD34<sup>+</sup> HSPCs were seeded together with  $5 \times 10^3$  bone marrow MSCs per hanging drop and incubated for up to two weeks in GMP-SFEM-CC100 medium. (b) Light microscopy images depict the aggregation of MSCs into spheroids in the coculture as soon as one day after culture. Surrounding HSPCs expanded greatly over time. After 14 days, the cell density in the hanging drop was very high and the spheroid in the center became invisible. Scale bar: 500  $\mu\text{m}$ . (c) Spheroids formed in cocultures were examined by scanning electron microscopy (SEM). A series of images from day 3 with increasing magnification (i–iv) shows a spheroid with only a few adhering HSPCs, identified as small round cells (arrows) attaching to the surface of the relatively smooth spheroid. On day 4, significantly more HSPCs attached to the spheroid (v, vi). After 7 days, the whole surface of the spheroid was covered by HSPCs, which also seem to attach to each other (vii, viii). Scale bars: 25  $\mu\text{m}$  (i, ii, v, vii, and viii); 10  $\mu\text{m}$  (iii, vi); and 5  $\mu\text{m}$  (iv).

increasing time, HSPC adhesion increased (day 4) until after one week of coculture when the entire spheroid surface was covered with HSPCs. Here, the hematopoietic cells attached not only to the MSCs but also to one another (Figure 2(c)).

For the analysis of spheroid composition and for determination of the localization of both cell types inside of the aggregate, cryosections were immunostained with antibodies against CD90, a MSC-specific surface marker, and against CD45, a pan-hematopoietic marker, for which MSCs are known to be negative. During the initial phase of coculture, there was no evidence of HSPC occurrence inside MSC spheroids because no CD45 signal was detectable at day 3 (Figure 3). Instead, all cells were positive for CD90. The spheroid morphology already described in the previous

section was evident with a dense peripheral MSC ring which presumably prevented HSPC invasion. This morphology turned steadily into a more compact MSC aggregation resulting in smaller spheroid diameters. On day 6, CD45<sup>+</sup> HSPCs occurred at the spheroid surface (Figure 3). After two weeks of cocultivation, the vast majority of cells in the aggregate were CD45<sup>+</sup>, whereas CD90 showed a faint patchy staining intensity, indicating a collapse of the MSC core (Figure 3). In conclusion, the HSPC adhesion strength in this 3D hanging drop model is rather weak because they could easily be dissociated from the MSC spheroid by extensive pipetting and without the addition of digesting enzymes. In spite of a mixed MSC-HSPC suspension at the seeding time point, the two cell types segregated and rearranged reproducibly,

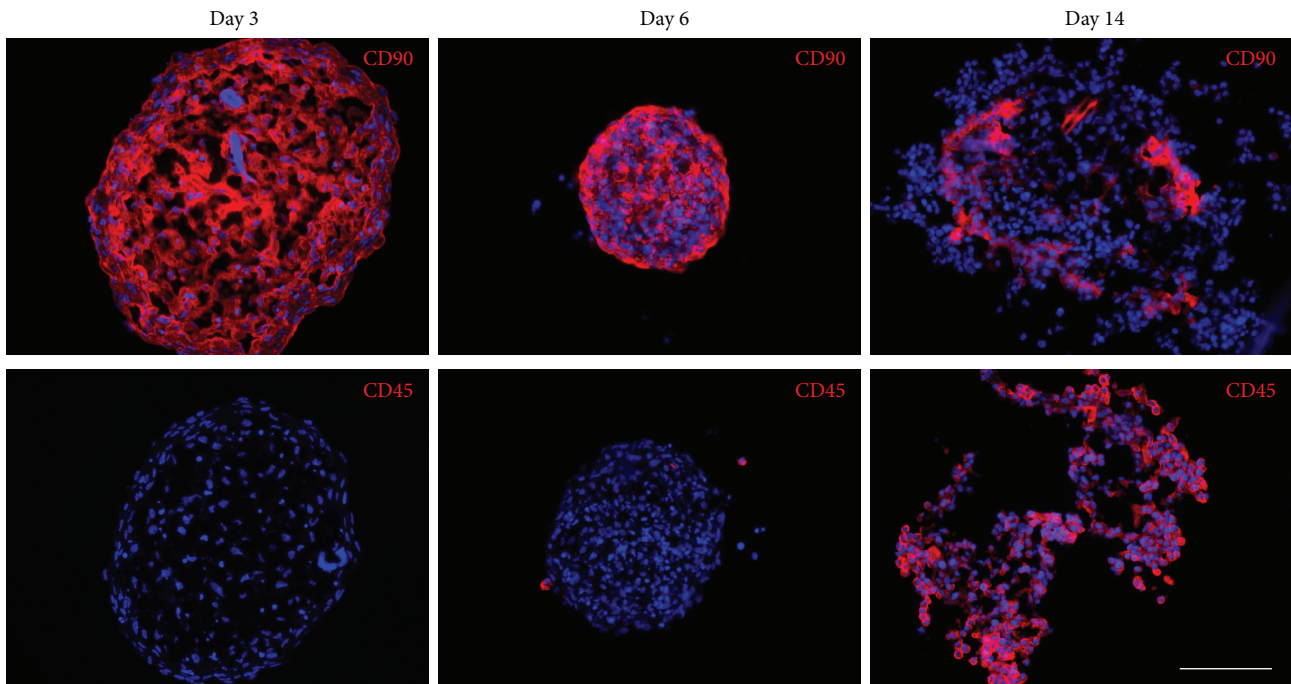


FIGURE 3: HSPCs, initially excluded by spheroid-forming MSCs, penetrate the spheroids after one week of coculture. Immunofluorescence staining of spheroid cryosections with antibodies against CD90 detecting MSCs and CD45 detecting hematopoietic cells revealed that on day 3 of coculture the spheroids were exclusively made up of MSCs. After 6 days of coculture, compaction of the spheroid occurred and CD90 staining was still present throughout the spheroid. Only a few CD45<sup>+</sup> cells were attached to the spheroid surface. On day 14 of coculture, most cells were stained with the anti-CD45 antibody, while the CD90<sup>+</sup> cells of the core seemed to be collapsed. Cell nuclei were counterstained with DAPI. Scale bar: 100  $\mu$ m.

indicating that the homotypic interactions of MSCs outweigh their contact to hematopoietic cells.

**3.3. MSC Spheroids Synthesize Niche-Specific ECM.** The expression pattern of bone marrow ECM components inside the spheroids was investigated by immunofluorescence staining. In adult human bone marrow, the laminin isoform LM511 was identified as an essential constituent of the ECM [32, 33]. Immunofluorescence staining of spheroid cryosections with laminin chain-specific antibodies revealed strong signals for the alpha5, beta1, and gamma1 chains (Figure 4(a)). The laminin alpha4 chain, also expressed by bone marrow cells [33], has been implicated in adhesion and migration of hematopoietic progenitors [32]. The laminin alpha4 chain was observed to be present to a high degree in MSC spheroids (Figure 4(a)). The laminin alpha2, beta2, and gamma2 chains, also described in the bone marrow [34, 35], were absent in the spheroids (Supplementary Figure S2). In summary, MSCs cultured as spheroids vigorously express LM411 and LM511.

The basement membrane component collagen type IV was detectable throughout the early MSC spheroid and was expressed to a similarly high degree as fibronectin, a basic constituent of the bone marrow extracellular matrix (Figure 4(b)). In addition, 3-day-old spheroids synthesized considerable amounts of the large glycoprotein tenascin-C and the microfibrillar collagen type VI. Both ECM proteins display strong cytoadhesive properties for hematopoietic

progenitor cells [30, 36]. MSC spheroids were also positive for the fibrillar collagen type I and for the proteoglycan perlecan (Supplementary Figure S2B), an integral part of basement membranes, which is an antiadhesive bone marrow substrate [37]. After 10 days in culture, expression of most ECM molecules was clearly reduced except for tenascin-C and collagen type VI (Figure 4(b)). Both components still produced a scaffold-like structure, thus probably allowing HSPC aggregation even after breakdown of the MSC core. These results demonstrate that various principal bone marrow ECM constituents involved in HSPC adhesion and regulation are synthesized by early MSC spheroids during hanging drop culture.

**3.4. HSPC Expansion in 2D Coculture Exceeds the Proliferation Rate in Hanging Drops.** A primary goal of the 3D coculture model was fast and efficient expansion of cord blood-derived CD34<sup>+</sup> HSPCs. In initial studies, a mixture of one volume MSC expansion medium GMP with four volumes HSPC expansion medium SFEM, supplemented with 100 ng/mL Flt-3L and SCF, and 20 ng/mL IL-3 and IL-6 (GMP-SFEM-CC100) yielded the highest proliferation rate (Supplementary Figure S3B). For comparison with 2D cultures, the MSC-HSPC suspension was seeded in the same volume with the same cell numbers in a conventional flat-bottom 96-well plate, in which MSCs readily adhered to the well bottom and HSPCs evenly attached to the MSC

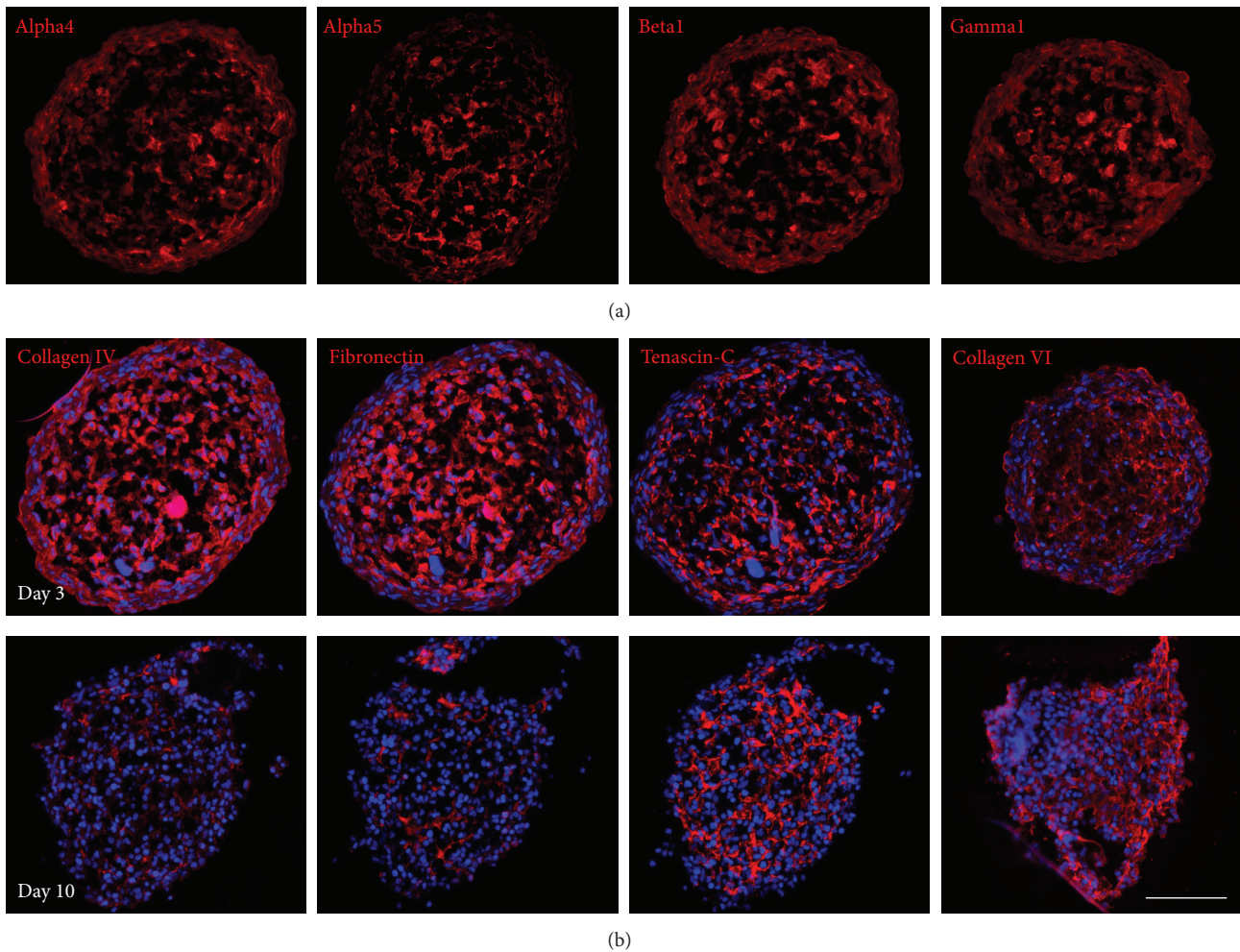
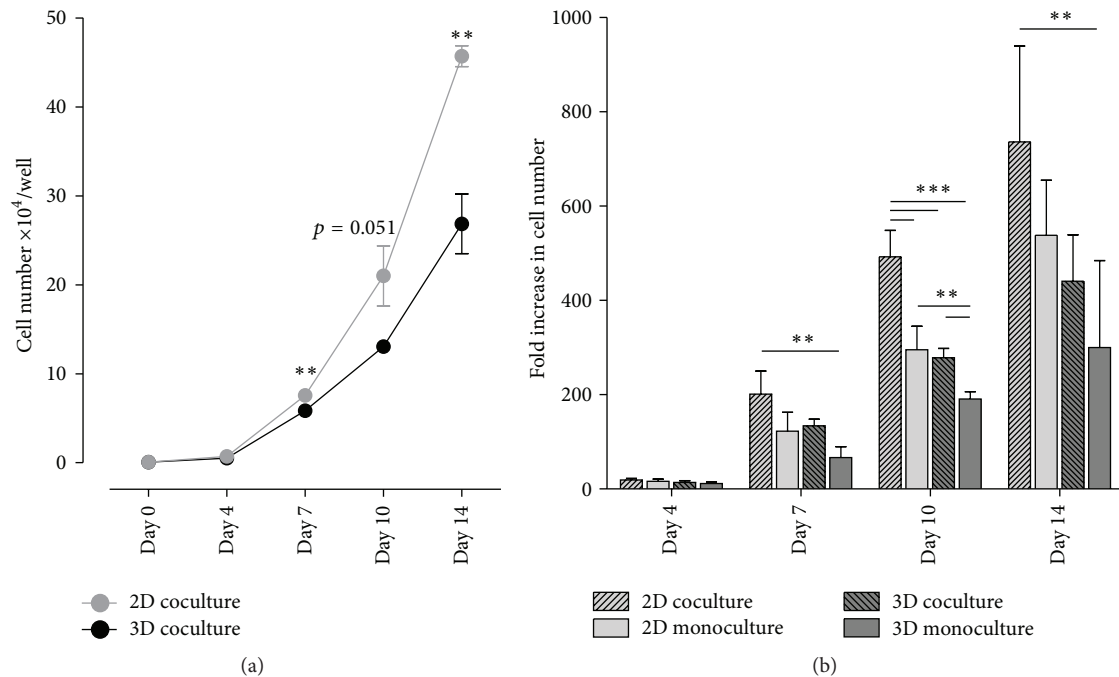


FIGURE 4: MSC spheroids express ECM components of the bone marrow. (a) The micrographs show immunofluorescence staining of 3-day-old MSC spheroid cryosections labeled with laminin chain-specific antibodies. Strong signals for the laminin alpha4, alpha5, beta1, and gamma1 chain were detected throughout the spheroids. (b) Sections from coculture spheroids harvested on days 3 and 10 were stained with antibodies against collagen type IV, fibronectin, tenascin-C, and collagen type VI. While all four matrix components were strongly expressed in early spheroids (upper panel), prominent expression was only detected for tenascin-C and collagen type VI in later stages of coculture (lower panel). Cell nuclei were counterstained with DAPI. Scale bar: 100  $\mu\text{m}$ .

monolayer (Supplementary Figure S3C). After one week of coincubation, numbers of expanded HSPCs per hanging drop were already significantly lower than in a comparable 2D well (Figure 5(a)). This difference became even more prominent after 14 days of culture ( $(26.9 \pm 3.4) \times 10^4$  cells under 3D and  $(45.7 \pm 1.2) \times 10^4$  cells under 2D conditions, resp.). Coculture of HSPCs with MSCs was beneficial compared with HSPCs as a monoculture in the corresponding system (Figure 5(b)). The positive effect on proliferation was more prominent when  $\text{CD}34^+$  HSPCs were coincubated with a MSC monolayer ( $736 \pm 204$  fold increase) than with a MSC spheroid ( $440 \pm 98$  fold increase). In the 2D monoculture system, the expanding HSPCs accumulate in one half of the well whereas in the 2D coculture an even HSPC distribution over the entire well area could be observed (Supplementary Figure S3C) indicating that direct cell-cell contact between HSPCs and MSCs was essential for an effective proliferation of the former.

**3.5. 3D Coculture Does Not Favor Expansion of Primitive Progenitors.** Multilineage differentiation potential of expanded HSPCs can be analyzed by colony-forming unit (CFU) assays. After 14 days of incubation, colonies deriving from erythroid progenitors (BFU-E), granulocyte/macrophage progenitors (CFU-GM), or multilineage granulocyte/erythrocyte/macrophage/megakaryocyte progenitors (CFU-GEMM) can be identified based on their morphological appearance and hemoglobin production. CFU assays with HSPCs expanded either as co- or monoculture under 2D and 3D conditions for 7-8 days were performed because differences in proliferation between the respective methods were already significant at this time point. Figure 6(a) depicts the distribution of the particular CFUs arising from unexpanded cells or from cells expanded in 2D or 3D, expressed as percentage of total colony counts. A general trend was observed for increasing BFU-E after expansion



**FIGURE 5:** HSPCs proliferate more extensively in coculture with MSC monolayers than with MSC spheroids. Expansion of HSPCs under 2D or 3D conditions was compared by seeding 500 HSPCs in combination with 5000 MSCs in conventional 96-well culture plates or in hanging drop plates, respectively, followed by determination of HSPC numbers at different time points. (a) Representative data from one donor show a significantly lower proliferation rate already after one week of coculture in 3D when compared with 2D. Samples were analyzed in triplicate. Statistical analysis was performed using a two-tailed parametric *t*-test. (b) The fold increase in HSPC numbers was obtained after expansion of 500 HSPCs in coculture or in monoculture. The highest proliferation rates were detected for the 2D coculture, whereas HSPCs incubated with MSC spheroids in 3D did not exceed the expansion level of the 2D monoculture. Statistical significance was assessed using one-way ANOVA. Data are shown as mean  $\pm$  standard deviation of four independent experiments with four donors (\*\*  $p < 0.01$ ; \*\*\*  $p < 0.001$ ).

at the expense of CFU-GEMM. This coincides with the high proliferative capacity of erythroid progenitors from cord blood when compared to stem cells originating from other sources [38]. HSPCs expanded on a MSC monolayer produced significantly more CFU-GM than those incubated in hanging drops. When the proliferation rate of HSPCs after one week in the respective system was taken into account and the CFU profile was expressed as a fold increase of colony numbers developed from  $10^3$  freshly isolated, unexpanded HSPCs (Figure 6(b)), the difference in CFU-GM was even more pronounced ( $225 \pm 21$  fold increase in 2D coculture;  $116 \pm 15$  in 2D monoculture;  $99 \pm 34$  in 3D coculture;  $50 \pm 27$  in 3D monoculture). The fold increase of BFU-E and CFU-GEMM tended to be higher after expansion in the 3D coincubation system but failed to reach statistical significance. In contrast, the total colony number for HSPCs deriving from the 2D coculture was significantly elevated in comparison to all other culture methods. According to these results, HSPC expansion with MSC spheroids in hanging drops has no significantly beneficial effect on their colony-forming potential over cells grown with MSC monolayers.

#### 4. Discussion

Fast and efficient *ex vivo* expansion of hematopoietic stem cells prior to transplantation is still a challenge which many

research groups have attempted to overcome by placing more and more emphasis on 3D techniques. In the present study, we analyzed a simplified 3D coincubation model of cord blood-derived  $CD34^+$  HSPCs together with bone marrow-derived MSCs in a hanging drop culture which led to an aggregation of MSCs into spheroids surrounded by HSPCs. Surprisingly, HSPC expansion in a conventional 2D culture system was higher than the proliferation rate in the 3D model, although the expression of many essential bone marrow ECM components was detected in the spheroids. Furthermore, HSPCs expanded in hanging drop plates were inferior to those from 2D culture with respect to their differentiation potential. Accordingly, in contrast to the widely accepted dogma, our study displayed that traditional 2D culture might, in some aspects, be advantageous over certain 3D systems.

The hanging drop culture method has been greatly improved by creating well plates with perforated arrays in which hanging drops are formed by gravity forces. These plates are currently a widely used culture system in tumor biology and drug testing studies and allow the application of automated liquid handling systems for high-throughput analyses [39–41]. Furthermore, this system is advantageous over other spheroid-based methods like low-adhesion culture devices or specific surface coatings due to its outstanding reproducibility by formation of uniquely sized aggregates. To the best of our knowledge, our study is the first that uses

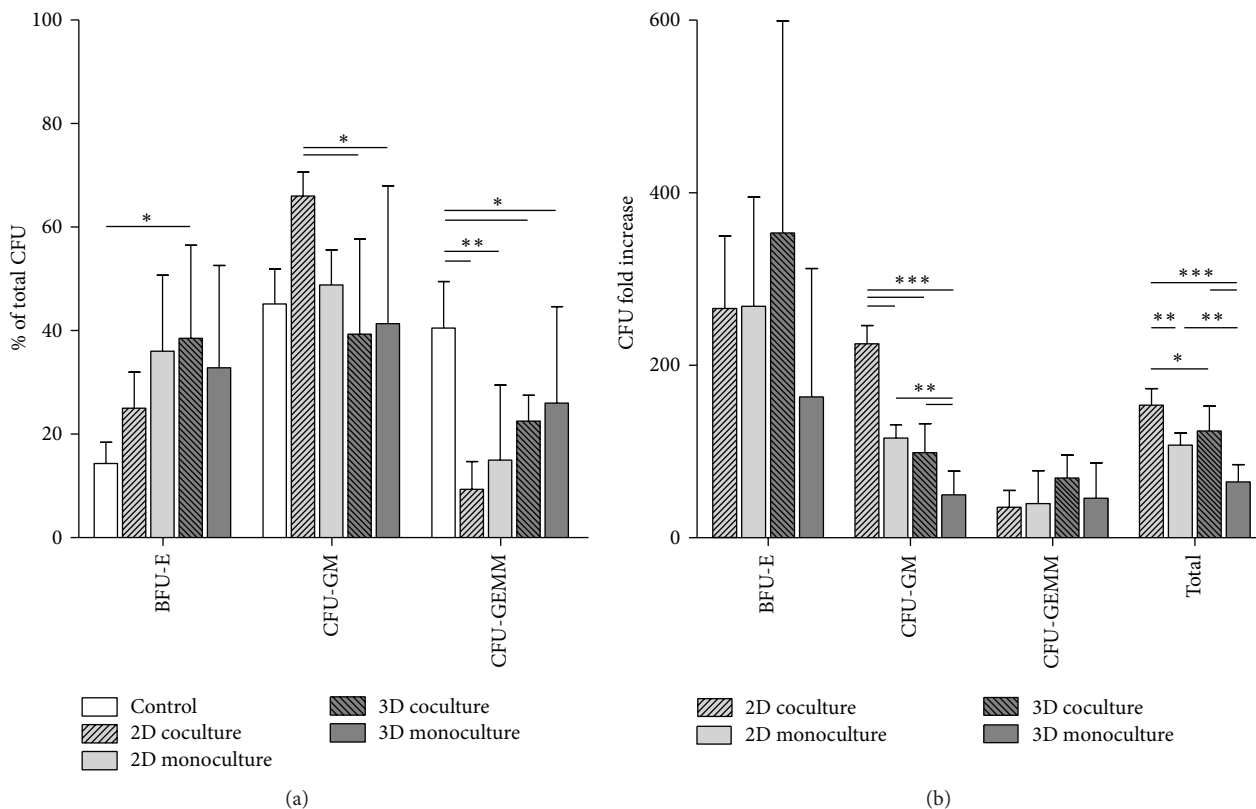


FIGURE 6: The 3D model is not favorable for the enhancement of primitive progenitors. Multilineage differentiation capacity of  $10^3$  HSPCs expanded in the hanging drop model or in a 2D culture plate was investigated after one week of culture with or without MSCs (coculture and monoculture, resp.) in a CFU assay. Results were compared to the CFU forming potential of  $10^3$  freshly isolated cord blood-derived HSPCs (control). (a) The BFU-E percentage of the total CFU number increased after *ex vivo* expansion at the expense of CFU-GEMM for all culture conditions. The CFU-GM percentage of the total CFU number was considerably augmented only for HSPCs in 2D coculture. (b) The CFU fold increase was obtained by comparison with colony numbers of nonexpanded cells and was calculated using the proliferation rate of HSPCs under the respective culture conditions. HSPCs expanded on an adherent MSC layer produced the largest number of total colonies. Values are expressed as mean  $\pm$  standard deviation of three independent experiments from three donors. One-way ANOVA was applied for statistical analysis (\* $p < 0.05$ ; \*\* $p < 0.01$ ; \*\*\* $p < 0.001$ ).

the hanging drop method for mimicking the HSC niche *in vitro*.

A recent study reported elevated expression levels of anti-inflammatory and anticancer factors by 3-day-old MSC spheroids [42]. Comparable to our findings, Bartosh and coworkers also observed spheroid compaction and the appearance of an epithelial-like layer on the surface [43]. Enhanced differentiation potential of MSCs into the adipogenic and osteogenic lineages or into epithelial and neuronal progenitors was also demonstrated with the spheroid incubation method [44, 45]. These reports emphasize that when MSCs are grown as monolayers or in 3D systems, changes occur not only in cell morphology and structure but also in transcriptome and proteome profiles and consequently in cell behavior. Cell growth most likely decreases in a 3D environment due to contact inhibition because most cells experience close interactions with several adjacent neighbors, which might explain the absence of MSC proliferation in the hanging drop spheroids. Plastic/substrate adherence is one of the characteristic criteria for highly expanding MSCs.

Hence, reduced or a lack of opportunities to firmly attach to a substrate might additionally impair their expansion potential.

The ECM is an essential constituent of the hematopoietic stem cell niches. Therefore the question arose whether exogenous ECM components should be added to the hanging drop culture. Matrigel is a widely used tool to create a 3D environment [46]. But due to its varying compositions of diverse ECM molecules, the use of Matrigel might hinder reproducibility [47]. Our 3D model shows that, within the spheroids, MSCs produce considerable amounts of ECM components also found in the hematopoietic niches *in vivo*. Notably the laminin isoforms LM411 and LM511, which are implicated in HSPC adhesion and migration [32, 33], were already detected in 3-day-old spheroids. Tenascin-C and fibronectin were also strongly expressed in the newly formed spheroids. Adhesion of HSPCs to these matrix components is mediated via the integrins  $\alpha4\beta1$  and  $\alpha9\beta1$ , respectively, which also regulate the proliferation of HSPCs [48, 49]. The bone-specific collagen type I and the microfibrillar collagen type VI, which both show cytoadhesive properties for HSPCs

[30, 50], as well as the antiadhesive proteoglycan perlecan [37] were also expressed in the spheroids.

Nevertheless, HSPCs did not migrate into the early spheroids and showed only low adhesive affinity for the MSCs at the beginning of the coculture. In the following time points, HSPC attachment increased considerably, which coincided with distinct spheroid compaction. Therefore, another important factor for HSPCs, substrate elasticity, should be considered in the comparison between 2D and 3D models. HSPCs have been shown to sense the biomechanical properties of their microenvironment and to transduce these signals into cellular responses [51]. Alterations in substrate elasticity can change adhesive interactions and migration of human HSPCs [52]. On the other hand, MSCs also decide upon their cell fate according to matrix elasticity and cell geometry [53, 54] which in turn may influence their HSPC-regulating capabilities. It is tempting to speculate that HSPCs sense a higher stiffness of the compact MSC spheroids and show increased attachment. This would be in line with the observation made in the 2D culture where almost all HSPCs adhered to the MSC monolayer from the beginning of the coculture, because cells spread on plastic are certainly less elastic than cells aggregated into a sphere with large intercellular spaces. Future studies using atomic force microscopy are required to test the correctness of these speculations.

Distinct MSC subpopulations of the human bone marrow were recently described to form differentially sized mesospheres during *in vitro* culture and to promote HSPC expansion [18, 55]. The proliferation-promoting ability of these aggregates was not dependent on cell-cell contacts. In contrast, our results support the need for a direct MSC-HSPC interaction, in line with reports from other groups [56, 57]. HSPCs expanded to a higher extent when grown on a MSC monolayer, thereby experiencing a larger contact area than their counterparts in coculture with MSCs as a spheroid. Similarly, HSPCs expanded in the 2D coculture contained remarkably more granulocyte/macrophage progenitors and produced significantly higher total colony numbers. The hanging drop coculture was only slightly superior in the content of erythroid and mixed progenitors. To summarize, the respective culture conditions supported distinct hematopoietic progenitors, and direct MSC contact apparently plays a different role in HSPC differentiation than in HSPC proliferation.

For a more authentic reproduction of the niche *in vitro*, supplement of additional bone marrow cells such as endothelial cells may be required. Recently, transplantable units isolated from mouse bone marrow with mesenchymal and hematopoietic stem cell properties were shown to be frequently associated with blood vessels [58]. However, incorporation of additional cell types will unavoidably increase the complexity of every model and hamper its realization due to restricted material availability.

## 5. Conclusions

The presented 3D hanging drop model of MSCs and HSPCs provides evidence that 3D culture is not always superior

to 2D conditions. For HSPC expansion especially, coculture with a MSC monolayer was more efficient than with a MSC spheroid. Our findings imply that direct contact of both cell types is required for HSPC expansion. Although the spheroid-forming MSCs are fully capable of synthesizing niche-specific ECM components, their strong homotypic interactions seem to prevent an extensive contact with HSPCs. MSC morphology, expression of surface molecules, and their interaction with HSPCs are different when MSCs are grown as a spread monolayer compared to the case when grown as a spheroid where the cells are of reduced volume and surface area. It appears that MSCs need a physical substrate in order to optimally exert their HSPC supportive functions, an important point that should be considered for *ex vivo* expansion protocols.

## Highlights

- (i) During MSC/HSPC coculture in hanging drops, MSCs segregate into tight spheroids.
- (ii) HSPCs are initially excluded from the MSC spheroids but replace MSCs at later stages.
- (iii) HSPC expansion in 3D culture is lower than in 2D coculture.
- (iv) The largest number of colony-forming units is found after 2D coculture.

## Conflict of Interests

The authors declare that there is no conflict of interests regarding the publication of this paper.

## Authors' Contribution

Olga Schmal has done conception and design, collection and/or assembly of data, data analysis and interpretation, and paper writing. Jan Seifert has done collection and/or assembly of data, data analysis, and interpretation. Tilman E. Schäffer has done data analysis and interpretation. Christina B. Walter has done provision of study material or patients, data analysis, and interpretation. Wilhelm K. Aicher has done provision of study material or patients, data analysis, and interpretation. Gerd Klein has done conception and design, data analysis and interpretation, and paper writing.

## Acknowledgments

The authors would like to thank the following members of the University of Tübingen: Tanja Abruzzese (Department of Urology) for technical support in MSC isolation, Eva Lohmann (Institute of Applied Physics) for her assistance in SEM analysis, and Dr. Christopher Shipp (Department of Medicine II) for critical reading of the paper. This work was supported by Contract Research "Adult Stem Cells II" of the Baden-Württemberg Stiftung, Germany (Grant no. P-LS-ASII/23). The authors acknowledge support by German

Research Foundation and Open Access Publishing Fund of University of Tübingen.

## References

- [1] E. A. Copelan, "Hematopoietic stem-cell transplantation," *The New England Journal of Medicine*, vol. 354, no. 17, pp. 1813–1826, 2006.
- [2] N. Kekre and J. H. Antin, "Hematopoietic stem cell transplantation donor sources in the 21st century: choosing the ideal donor when a perfect match does not exist," *Blood*, vol. 124, no. 3, pp. 334–343, 2014.
- [3] T. C. Lund, A. E. Boitano, C. S. Delaney, E. J. Shpall, and J. E. Wagner, "Advances in umbilical cord blood manipulation—from niche to bedside," *Nature Reviews Clinical Oncology*, vol. 12, pp. 163–174, 2015.
- [4] J. A. Schuster, M. R. Stupnikov, G. Ma et al., "Expansion of hematopoietic stem cells for transplantation: current perspectives," *Experimental Hematology & Oncology*, vol. 1, article 12, 2012.
- [5] R. Aggarwal, J. Lu, V. J. Pompili, and H. Das, "Hematopoietic stem cells: transcriptional regulation, ex vivo expansion and clinical application," *Current Molecular Medicine*, vol. 12, no. 1, pp. 34–49, 2012.
- [6] S. H. Orkin and L. I. Zon, "Hematopoiesis: an evolving paradigm for stem cell biology," *Cell*, vol. 132, no. 4, pp. 631–644, 2008.
- [7] L. D. Wang and A. J. Wagers, "Dynamic niches in the origination and differentiation of haematopoietic stem cells," *Nature Reviews Molecular Cell Biology*, vol. 12, no. 10, pp. 643–655, 2011.
- [8] A. Ehninger and A. Trumpp, "The bone marrow stem cell niche grows up: mesenchymal stem cells and macrophages move in," *Journal of Experimental Medicine*, vol. 208, no. 3, pp. 421–428, 2011.
- [9] S. J. Morrison and D. T. Scadden, "The bone marrow niche for haematopoietic stem cells," *Nature*, vol. 505, no. 7483, pp. 327–334, 2014.
- [10] L. M. Calvi, G. B. Adams, K. W. Weibrecht et al., "Osteoblastic cells regulate the haematopoietic stem cell niche," *Nature*, vol. 425, no. 6960, pp. 841–846, 2003.
- [11] L. Ding, T. L. Saunders, G. Enikolopov, and S. J. Morrison, "Endothelial and perivascular cells maintain haematopoietic stem cells," *Nature*, vol. 481, no. 7382, pp. 457–462, 2012.
- [12] O. Kollet, A. Dar, S. Shvitiel et al., "Osteoclasts degrade endosteal components and promote mobilization of hematopoietic progenitor cells," *Nature Medicine*, vol. 12, no. 6, pp. 657–664, 2006.
- [13] B. Sacchetti, A. Funari, S. Michienzi et al., "Self-renewing osteoprogenitors in bone marrow sinusoids can organize a hematopoietic microenvironment," *Cell*, vol. 131, no. 2, pp. 324–336, 2007.
- [14] J. Zhang, C. Niu, L. Ye et al., "Identification of the haematopoietic stem cell niche and control of the niche size," *Nature*, vol. 425, no. 6960, pp. 836–841, 2003.
- [15] T. M. Dexter, T. D. Allen, and L. G. Lajtha, "Conditions controlling the proliferation of haemopoietic stem cells in vitro," *Journal of Cellular Physiology*, vol. 91, no. 3, pp. 335–344, 1977.
- [16] S. Gartner and H. S. Kaplan, "Long-term culture of human bone marrow cells," *Proceedings of the National Academy of Sciences of the United States of America*, vol. 77, no. 8, pp. 4756–4759, 1980.
- [17] S. Méndez-Ferrer, T. V. Michurina, F. Ferraro et al., "Mesenchymal and haematopoietic stem cells form a unique bone marrow niche," *Nature*, vol. 466, no. 7308, pp. 829–834, 2010.
- [18] S. Pinho, J. Lacombe, M. Hanoun et al., "PDGFR $\alpha$  and CD51 mark human nestin<sup>+</sup> sphere-forming mesenchymal stem cells capable of hematopoietic progenitor cell expansion," *Journal of Experimental Medicine*, vol. 210, no. 7, pp. 1351–1367, 2013.
- [19] M. S. V. Ferreira, W. Jahnen-Dechent, N. Labude et al., "Cord blood-hematopoietic stem cell expansion in 3D fibrin scaffolds with stromal support," *Biomaterials*, vol. 33, no. 29, pp. 6987–6997, 2012.
- [20] I. Leisten, R. Kramann, M. S. Ventura Ferreira et al., "3D co-culture of hematopoietic stem and progenitor cells and mesenchymal stem cells in collagen scaffolds as a model of the hematopoietic niche," *Biomaterials*, vol. 33, no. 6, pp. 1736–1747, 2012.
- [21] A. Raic, L. Rödling, H. Kalbacher, and C. Lee-Thedieck, "Biomimetic macroporous PEG hydrogels as 3D scaffolds for the multiplication of human hematopoietic stem and progenitor cells," *Biomaterials*, vol. 35, no. 3, pp. 929–940, 2014.
- [22] M. B. Sharma, L. S. Limaye, and V. P. Kale, "Mimicking the functional hematopoietic stem cell niche in vitro: recapitulation of marrow physiology by hydrogel-based three-dimensional cultures of mesenchymal stromal cells," *Haematologica*, vol. 97, no. 5, pp. 651–660, 2012.
- [23] M. M. Cook, K. Futrega, M. Osiecki et al., "Micromarrows—three-dimensional coculture of hematopoietic stem cells and mesenchymal stromal cells," *Tissue Engineering Part C: Methods*, vol. 18, no. 5, pp. 319–328, 2012.
- [24] A. P. D. N. de Barros, C. M. Takiya, L. R. Garzoni et al., "Osteoblasts and bone marrow mesenchymal stromal cells control hematopoietic stem cell migration and proliferation in 3D in vitro model," *PLoS ONE*, vol. 5, no. 2, Article ID e9093, 2010.
- [25] I. Kurth, K. Franke, T. Pompe, M. Bornhäuser, and C. Werner, "Extracellular matrix functionalized microcavities to control hematopoietic stem and progenitor cell fate," *Macromolecular Bioscience*, vol. 11, no. 6, pp. 739–747, 2011.
- [26] N. Di Maggio, E. Piccinini, M. Jaworski, A. Trumpp, D. J. Wendt, and I. Martin, "Toward modeling the bone marrow niche using scaffold-based 3D culture systems," *Biomaterials*, vol. 32, no. 2, pp. 321–329, 2011.
- [27] J. Lee and N. A. Kotov, "Notch ligand presenting acellular 3D microenvironments for ex vivo human hematopoietic stem-cell culture made by layer-by-layer assembly," *Small*, vol. 5, no. 9, pp. 1008–1013, 2009.
- [28] I. Pallotta, M. Lovett, D. L. Kaplan, and A. Balduini, "Three-dimensional system for the in vitro study of megakaryocytes and functional platelet production using silk-based vascular tubes," *Tissue Engineering—Part C: Methods*, vol. 17, no. 12, pp. 1223–1232, 2011.
- [29] M. Dominici, K. Le Blanc, I. Mueller et al., "Minimal criteria for defining multipotent mesenchymal stromal cells. The International Society for Cellular Therapy position statement," *Cytotherapy*, vol. 8, no. 4, pp. 315–317, 2006.
- [30] G. Klein, C. A. Müller, E. Tillet, M.-L. Chu, and R. Timpl, "Collagen type VI in the human bone marrow microenvironment: a strong cytoadhesive component," *Blood*, vol. 86, no. 5, pp. 1740–1748, 1995.
- [31] F. Wein, L. Pietsch, R. Saffrich et al., "N-cadherin is expressed on human hematopoietic progenitor cells and mediates interaction

- with human mesenchymal stromal cells,” *Stem Cell Research*, vol. 4, no. 2, pp. 129–139, 2010.
- [32] Y.-C. Gu, J. Kortessma, K. Tryggvason et al., “Laminin isoform-specific promotion of adhesion and migration of human bone marrow progenitor cells,” *Blood*, vol. 101, no. 3, pp. 877–885, 2003.
- [33] U. Siler, M. Seiffert, S. Puch et al., “Characterization and functional analysis of laminin isoforms in human bone marrow,” *Blood*, vol. 96, no. 13, pp. 4194–4203, 2000.
- [34] U. Siler, P. Rousselle, C. A. Müller, and G. Klein, “Laminin  $\gamma 2$  chain as a stromal cell marker of the human bone marrow microenvironment,” *British Journal of Haematology*, vol. 119, no. 1, pp. 212–220, 2002.
- [35] W. Vogel, L. Kanz, W. Brugger, A. Berndt, and H. Kosmehl, “Expression of laminin beta2 chain in normal human bone marrow,” *Blood*, vol. 94, no. 3, pp. 1143–1145, 1999.
- [36] M. Seiffert, S. C. Beck, F. Schermutzki, C. A. Müller, H. P. Erickson, and G. Klein, “Mitogenic and adhesive effects of tenascin-C on human hematopoietic cells are mediated by various functional domains,” *Matrix Biology*, vol. 17, no. 1, pp. 47–63, 1998.
- [37] G. Klein, S. Conzelmann, S. Beck, R. Timpl, and C. A. Müller, “Perlecan in human bone marrow: a growth-factor-presenting, but anti-adhesive, extracellular matrix component for hematopoietic cells,” *Matrix Biology*, vol. 14, no. 6, pp. 457–465, 1995.
- [38] M.-C. Giarratana, L. Kobari, H. Lapillonne et al., “*Ex vivo* generation of fully mature human red blood cells from hematopoietic stem cells,” *Nature Biotechnology*, vol. 23, no. 1, pp. 69–74, 2005.
- [39] A. Amann, M. Zwierzina, G. Gamerith et al., “Development of an innovative 3D cell culture system to study tumour—stroma interactions in non-small cell lung cancer cells,” *PLoS ONE*, vol. 9, no. 3, Article ID e92511, 2014.
- [40] A. Y. Hsiao, Y.-C. Tung, X. Qu, L. R. Patel, K. J. Pienta, and S. Takayama, “384 hanging drop arrays give excellent Z-factors and allow versatile formation of co-culture spheroids,” *Biotechnology and Bioengineering*, vol. 109, no. 5, pp. 1293–1304, 2012.
- [41] Y.-C. Tung, A. Y. Hsiao, S. G. Allen, Y.-S. Torisawa, M. Ho, and S. Takayama, “High-throughput 3D spheroid culture and drug testing using a 384 hanging drop array,” *Analyst*, vol. 136, no. 3, pp. 473–478, 2011.
- [42] J. H. Ylostalo, T. J. Bartosh, A. Tiblow, and D. J. Prockop, “Unique characteristics of human mesenchymal stromal/progenitor cells pre-activated in 3-dimensional cultures under different conditions,” *Cytotherapy*, vol. 16, no. 11, pp. 1486–1500, 2014.
- [43] T. J. Bartosh, J. H. Ylostalo, A. Mohammadipoor et al., “Aggregation of human mesenchymal stromal cells (MSCs) into 3D spheroids enhances their antiinflammatory properties,” *Proceedings of the National Academy of Sciences of the United States of America*, vol. 107, no. 31, pp. 13724–13729, 2010.
- [44] Y. Jing and Y. Jian-Xiong, “3-D spheroid culture of bone marrow mesenchymal stem cell of rhesus monkey with improved multi-differentiation potential to epithelial progenitors and neuron in vitro,” *Clinical & Experimental Ophthalmology*, vol. 39, no. 8, pp. 808–819, 2011.
- [45] W. Wang, K. Itaka, S. Ohba et al., “3D spheroid culture system on micropatterned substrates for improved differentiation efficiency of multipotent mesenchymal stem cells,” *Biomaterials*, vol. 30, no. 14, pp. 2705–2715, 2009.
- [46] G. Benton, J. George, H. K. Kleinman, and I. P. Arnaoutova, “Advancing science and technology via 3D culture on basement membrane matrix,” *Journal of Cellular Physiology*, vol. 221, no. 1, pp. 18–25, 2009.
- [47] C. S. Hughes, L. M. Postovit, and G. A. Lajoie, “Matrigel: a complex protein mixture required for optimal growth of cell culture,” *Proteomics*, vol. 10, no. 9, pp. 1886–1890, 2010.
- [48] T. D. Schreiber, C. Steinl, M. Essl et al., “The integrin  $\alpha 9 \beta 1$  on hematopoietic stem and progenitor cells: involvement in cell adhesion, proliferation and differentiation,” *Haematologica*, vol. 94, no. 11, pp. 1493–1501, 2009.
- [49] C. M. Verfaillie, “Adhesion receptors as regulators of the hematopoietic process,” *Blood*, vol. 92, no. 8, pp. 2609–2612, 1998.
- [50] G. B. Adams, K. T. Chabner, I. R. Alley et al., “Stem cell engraftment at the endosteal niche is specified by the calcium-sensing receptor,” *Nature*, vol. 439, no. 7076, pp. 599–603, 2006.
- [51] J. Holst, S. Watson, M. S. Lord et al., “Substrate elasticity provides mechanical signals for the expansion of hemopoietic stem and progenitor cells,” *Nature Biotechnology*, vol. 28, no. 10, pp. 1123–1128, 2010.
- [52] C. Lee-Thedieck, N. Rauch, R. Fiammengo, G. Klein, and J. P. Spatz, “Impact of substrate elasticity on human hematopoietic stem and progenitor cell adhesion and motility,” *Journal of Cell Science*, vol. 125, no. 16, pp. 3765–3775, 2012.
- [53] A. J. Engler, S. Sen, H. L. Sweeney, and D. E. Discher, “Matrix elasticity directs stem cell lineage specification,” *Cell*, vol. 126, no. 4, pp. 677–689, 2006.
- [54] G. M. Harris, M. E. Piroli, and E. Jabbarzadeh, “Deconstructing the effects of matrix elasticity and geometry in mesenchymal stem cell lineage commitment,” *Advanced Functional Materials*, vol. 24, no. 16, pp. 2396–2403, 2014.
- [55] J. Isern, B. Martín-Antonio, R. Ghazanfari et al., “Self-renewing human bone marrow mesospheres promote hematopoietic stem cell expansion,” *Cell Reports*, vol. 3, no. 5, pp. 1714–1724, 2013.
- [56] D. A. Breems, E. A. W. Blokland, K. E. Siebel, A. E. M. Mayen, L. J. A. Engels, and R. E. Ploemacher, “Stroma-contact prevents loss of hematopoietic stem cell quality during *ex vivo* expansion of CD34<sup>+</sup> mobilized peripheral blood stem cells,” *Blood*, vol. 91, no. 1, pp. 111–117, 1998.
- [57] K. Harvey and E. Dzierzak, “Cell-cell contact and anatomical compatibility in stromal cell-mediated HSC support during development,” *Stem Cells*, vol. 22, no. 3, pp. 253–258, 2004.
- [58] N. Ahmadbeigi, M. Soleimani, M. Vasei et al., “Isolation, characterization, and transplantation of bone marrow-derived cell components with hematopoietic stem cell niche properties,” *Stem Cells and Development*, vol. 22, no. 23, pp. 3052–3061, 2013.

## Review Article

# Stem Cell Models to Investigate the Role of DNA Methylation Machinery in Development of Neuropsychiatric Disorders

**K. Naga Mohan**

*Department of Biological Sciences, Birla Institute of Technology and Science, Pilani, Hyderabad Campus, Jawaharnagar, Hyderabad 500 078, India*

Correspondence should be addressed to K. Naga Mohan; [kommumohan@gmail.com](mailto:kommumohan@gmail.com)

Received 31 July 2015; Accepted 10 September 2015

Academic Editor: Malin Jonsson

Copyright © 2016 K. Naga Mohan. This is an open access article distributed under the Creative Commons Attribution License, which permits unrestricted use, distribution, and reproduction in any medium, provided the original work is properly cited.

Epigenetic mechanisms underlie differentiation of pluripotent stem cells into different lineages that contain identical genomes but express different sets of cell type-specific genes. Because of high discordance rates in monozygotic twins, epigenetic mechanisms are also implicated in development of neuropsychiatric disorders such as schizophrenia and autism. In support of this notion, increased levels of DNA methyltransferases (DNMTs), DNMT polymorphisms, and dysregulation of DNA methylation network were reported among schizophrenia patients. These results point to the importance of development of DNA methylation machinery-based models for studying the mechanism of abnormal neurogenesis due to certain DNMT alleles or dysregulated DNMTs. Achieving this goal is strongly confronted by embryonic lethality associated with altered levels of epigenetic machinery such as DNMT1 and expensive approaches in developing *in vivo* models. In light of literature evidence that embryonic stem cells (ESCs) are tolerant of DNMT mutations and advancement in the technology of gene targeting, it is now possible to introduce desired mutations in DNMT loci to generate suitable ESC lines that can help understand the underlying mechanisms by which abnormal levels of DNMTs or their specific mutations/alleles result in abnormal neurogenesis. In the future, these models can facilitate development of suitable drugs for treatment of neuropsychiatric disorders.

## 1. Introduction

During postblastocyst stage of mammalian development, the embryo undergoes implantation and the cells of the inner cell mass undergo lineage specification. As a result, cells of different lineages, despite being genetically identical, express unique set of genes that are lineage-specific while keeping the nonspecific genes silent. This difference in expression patterns is achieved due to the developmental cues in the embryo but is maintained in form of distinctive epigenetic patterns of the genomes. These epigenetic marks are heritable such that they are propagated in all the daughter cells within the lineage.

DNA methylation, histone modifications, and regulatory noncoding RNAs constitute the main epigenetic marks of mammalian genomes. Of these three, DNA methylation or covalent addition of methyl group at the fifth carbon of cytosines in genomic DNA is the earliest to be reported and most well studied in terms of its establishment, maintenance,

and erasure (e.g., see [1]). Most cytosines are methylated in CpG dinucleotides except in the CpG islands wherein in most cases unmethylated state has been positively correlated with gene expression [2–4]. Because of this inverse relationship with gene expression, DNA methylation and the machinery responsible for establishment/maintenance play an important role in differentiation. Whereas *de novo* methyltransferases DNMT3A and DNMT3B can impart new methylation marks on unmethylated DNA, DNMT1 is responsible for maintenance of DNA methylation throughout life [5]. These contrasting functions of *de novo* and maintenance DNMTs are reflected in their expression patterns: DNMT3A and DNMT3B are involved in epigenetic reprogramming and expressed mainly in the germline [6, 7], pluripotent, and adult stem cells [8] whereas DNMT1 is expressed in all developmental stages and in terminally differentiated tissues.

Because of their central role in creation and maintenance of DNA methylation patterns and the inverse correlation between DNA methylation and gene expression, DNMTs

TABLE 1: Effects of DNMT deficiency and overexpression in development/differentiation.

S. number	Type of the defect	Model system	Phenotype(s)	Reference
1	DNMT1 deficiency	Mouse (knockout)	Lethality at midgestation with imprinting and DNA methylation defects	[10]
		Mouse (conditional knockout in precursor cells in central nervous system)	Degeneration of neurons	[11]
		Mouse embryonic stem cells (ESCs)	Differentiated neurons do not survive, self-renewal is unaffected	[16]
		Hematopoietic stem cells (HSCs)	Poor retention in niches, deficient self-renewal, and defective hematopoiesis	[18]
2	DNMT3a deficiency	Mouse (knockout)	Failure to develop to term	[13]
		Mouse ESCs (knockout)	No effect on self-renewal, progressive loss of DNA methylation, and ability to differentiate	[19]
		Conditional knockout in hematopoietic lineage	Block in differentiation and expanded number of HSCs in bone marrow	[20]
3	DNMT3b deficiency	Mouse (knockout)	Death within four weeks after birth	[13]
		Mouse ESCs (knockout)	Self-renewal unaffected, progressive loss of DNA methylation, and ability to differentiate	[19]
		Conditional knockout in hematopoietic lineage	Defects are milder than in case of DNMT3a deficiency in HSCs; double mutants (deficient in both DNMT3A and DNMT3B) have more severe defects	[20]
4	DNMT3L deficiency	Mouse (knockout)	Females: stochastic imprinting patterns	[14]
			Males: low spermatogonia and wide-spread methylation defects	[15]
5	DNMT1 overexpression	Mouse (transgenic)	Lethality at midgestation due to imprinting defects	[12]
		Mouse ESCs (targeted knocking to increase the levels of DNMT1)	Abnormal neuronal differentiation with upregulated NMDA receptor activity	[21]
6	DNMT3a and DNMT1 overexpression	Schizophrenia and bipolar patients with psychosis	Aberrant hypermethylation and downregulation of REELIN and GAD67	[22]

have been the subjects of intense research. In particular, the role of DNMTs and the influence of their dysregulation on the process of differentiation or maintenance of differentiated state are becoming unraveled in the recent past. Recent studies also indicate that dysregulation of DNMTs may be a disease-causing mechanism among patients with schizophrenia and bipolar disorders. Epigenetic mechanisms have been proposed to be involved in pathophysiology of schizophrenia and autism because of high discordance rates between monozygotic twins [9]. Although these defective epigenetic mechanisms include machinery responsible for establishment and maintenance of histone modifications as well as DNA methylation, published literature to date suggests more evidence for dysregulation of DNMTs in schizophrenia [10].

Here, I will describe the central role of DNMTs in mammalian development, the embryonic stem cell- (ESC-) based *in vitro* and animal models developed by different investigators that have helped in gaining insights into the critical role of DNMTs in pluripotency and differentiation (Table 1). I will then describe the problems associated with

development of suitable animal models and propose that transgenic ESC models can help in understanding the mechanisms by which dysregulation of DNMTs or particular DNMT mutants/alleles influences neuronal differentiation. An understanding of these mechanisms would in turn help in determining the pathophysiology among those schizophrenia patients where there is dysregulation of DNMTs. Such information is also invaluable in identification of suitable drugs that help in correcting the abnormal neuronal phenotypes because of dysregulation of DNMTs.

## 2. Basic Functions of *De Novo* and Maintenance DNMTs

As mentioned above, DNMT3A and DNMT3B are the *de novo* methyltransferases whereas DNMT1 is a maintenance methyltransferase. In addition to these enzymes, DNMT3L is another DNMT family member which is catalytically inactive. DNMT3L interacts with DNMT3A and DNMT3B and is important for establishment of certain methylation marks in the germline. Once DNA methylation marks are

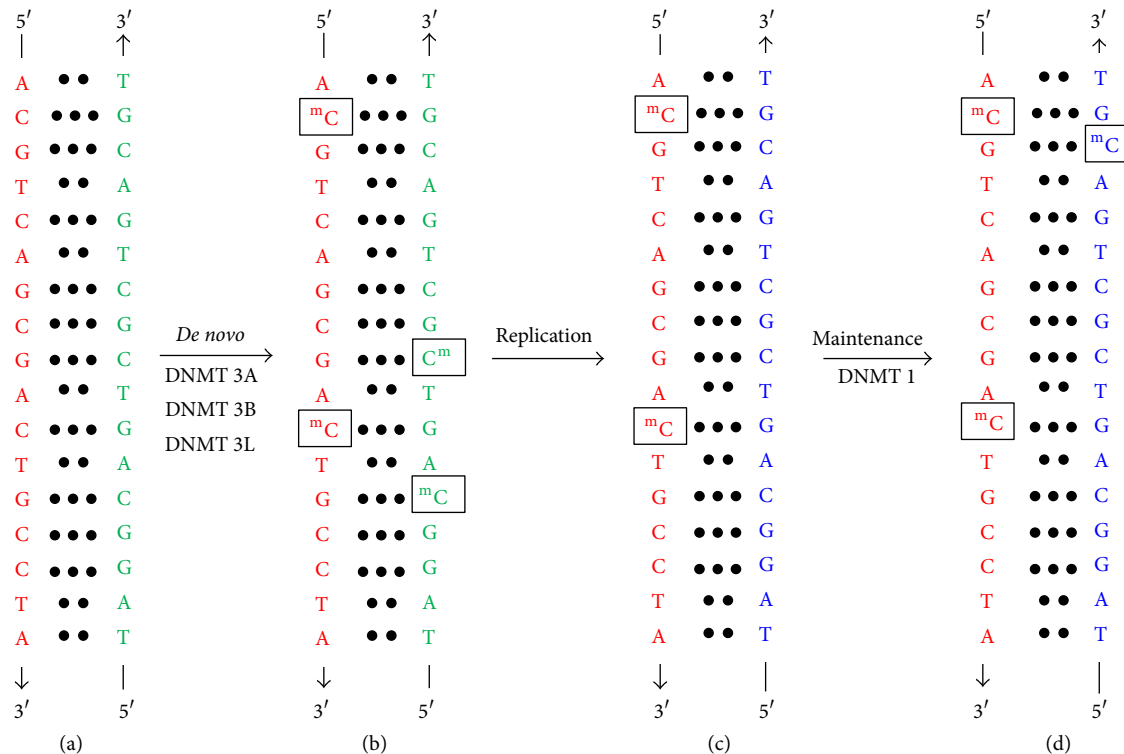


FIGURE 1: Specific roles of DNMTs in establishment and maintenance methylation in mammalian genomes. (a) Unmethylated DNA is acted upon by *de novo* methyltransferases DNMT3A and DNMT3B which methylated cytosines in the DNA molecule. The complementary strands are shown in green and red. This step also requires DNMT3L, the nonenzymatic member of DNMT family. (b) As a result of *de novo* methylation, methylated cytosines can be found in the context of both CpG and non-CpG dinucleotides. (c) After replication, the parental strand in each daughter DNA molecule serves as information for maintenance methylation. DNMT1 methylates cytosines in the daughter strand at positions that are exactly opposite to the methylated cytosines in the parent strand. (d) Because CpG dinucleotides are symmetric and exactly opposite in the daughter DNA, the maintenance methylation is highly efficient at CpG dinucleotides. Non-CpG dinucleotides do not contain cytosines at exactly the opposite positions in the two strands and therefore maintenance methylation in these dinucleotides is poor.

established on unmethylated DNA, they are maintained by DNMT1 in a postreplicative manner (Figure 1 [11]). When DNA is freshly replicated, the parental and daughter strands contain methylated and unmethylated cytosines and are said to be hemimethylated. DNMT1 is proposed to “read” these methylation marks and establish methylation on the opposite cytosines in the newly synthesized complementary strand. For this reason, CpG dinucleotide is best suited for heritability of methylation marks because the complementary strand also contains the same dinucleotide in exactly the same position. Because of the lack of this symmetry, non-CpG methylation is not efficiently maintained (Figure 1).

### 3. Essential Role of DNMTs in Mammalian Development

Indications that DNMTs are absolutely essential for development came from mouse transgenic studies. ESCs in which both alleles of *Dnmt1* were disrupted showed reduction in DNA methylation levels and normal growth rates and morphology, but embryos derived from them showed stunted growth and developmental delay and did not survive after

midgestation [12]. However, in mice carrying a conditional allele which results in loss of DNMT1 precursor cells of the central nervous system resulted in formation of hypomethylated neurons but these neurons quickly degenerated [13]. In subsequent studies in which the DNMT1 levels were altered, increased levels of DNMT1 also result in embryonic lethality around midgestation because of genomic hypermethylation aberrant regulation of imprinted genes (a class of genes that are expressed from only one of the two homologous chromosomes based on their parental origin) [14]. Similar to the results obtained with DNMT1 knockout embryos, absence of DNMT3A or DNMT3B affects normal development/survival. Whereas *Dnmt3B<sup>null/null</sup>* embryos fail to develop to term due to developmental defects, *Dnmt3A<sup>null/null</sup>* embryos survive to term but fail to survive beyond four weeks [15]. In contrast to lethality associated with deficiency of DNMT1 or DNMT3a or DNMT3b, *Dnm3L<sup>null/null</sup>* mice survive but their conceptuses have DNA methylation defects. *Dnmt3L<sup>null/null</sup>* females show stochastic imprinting patterns in their oocytes [16] resulting in a population of embryos that do not develop to term because of abnormal methylation patterns whereas *Dnmt3L<sup>null/null</sup>* males show loss of

spermatogonia with wide-spread DNA methylation defects that reduce the chances of survival of their progeny [17]. Taken together, these results suggest that optimal levels of DNMTs are essential for normal development and survival.

#### 4. DNMTs and Their Role Differentiation

The functional roles of DNMTs in the differentiation program were only established recently. Transgenic studies in which a catalytically inactive DNMT1 mutant was expressed in *Dnmt1<sup>cl/c</sup>* mouse ESCs that do not produce DNMT1 showed that in absence of DNMT1 ESCs do not lose their self-renewal capacity and their ability to initiate differentiation but the mutant cells do not survive differentiation [21]. For instance, loss of DNMT1 activity has been shown to be the sole reason for the inability of the *Dnmt1<sup>cl/c</sup>*-derived neurons to survive [19]. In another set of studies, mouse ESCs were genetically engineered to produce high levels of DNMT1 from the endogenous *Dnmt1* promoter [18]. These mutant ESCs showed normal morphology and growth patterns but produced abnormal neurons that showed extensive dendritic arborization, branching, and increased levels of NR1 subunit of N-methyl D-aspartate (NMDA) receptor [23]. This study has also shown that the levels of DNMT1 are tightly regulated during differentiation and, as a result, DNMT1 is maintained at low levels in embryoid bodies and neurons. This study also indicated that downregulation of DNMT1 is a general phenomenon associated with differentiation. Consistent with this indication, two pluripotency factors OCT4 and Nanog have been shown to bind to the *Dnmt1* promoter and enable the expression of DNMT1 in ESCs [20]. It is therefore plausible to expect that downregulation of OCT4 and Nanog results in lowering of DNMT1 levels during differentiation. Effects of DNMT1 loss of function have also been investigated in hematopoietic stem cells (HSCs) wherein specific absence of DNMT1 in the hematopoietic system results in poor retention of HSCs in their niches, deficient self-renewal, and multilineage hematopoiesis. These abnormalities were accompanied by enhanced cell cycling and dysregulated mature lineage gene expression in myeloid progenitor cells [24]. Taken together, it becomes evident that DNMT1 plays a crucial role in regulating the differentiation potential of pluripotent stem cells as well as adult stem cells.

Experiments using transgenic mice lacking DNMT3A and/or DNMT3B suggest that in addition to DNMT1, DNMT3A and DNMT3B also influence differentiation. For instance, in absence of DNMT3A and DNMT3B, ESCs retain their proliferative capacity and self-renewal but progressively lose DNA methylation [15]. Interestingly, these mutant cells also progressively lose their ability to differentiate [22]. Additional roles of DNMT3A and DNMT3B on self-renewal and differentiation of hematopoietic stem cells (HSCs) became evident from patients with DNMT3A mutations. About 20% of the individuals with DNMT3A mutations present with acute myeloid leukemia and myelodysplastic syndrome, characterized by abnormal differentiation or deficiency of hematopoietic lineages. Experimental data on mutant mice in which there is a loss of DNMT3A in hematopoietic stem

cells showed a block in differentiation and an expanded number of HSCs in bone marrow [25]. The molecular defect in the mutant HSCs is an increased expression of multipotency genes and a decreased expression of differentiation factors. Subsequent studies where either or both of DNMT3A and DNMT3B were conditionally knocked out in HSCs showed that double mutants show synergistic effects whereas DNMT3B mutants showed milder phenotypes [26]. In another set of experiments, DNMT3A expression in postnatal neural stem cells (NSCs) was observed to result in intergenic and gene body methylation of several regions, particularly in the gene bodies proximal to the promoters of neurogenic genes. Such methylation was shown to be required for expression of these genes to enable normal neuronal differentiation [27]. From the discussion above, a conclusion can be drawn that DNMT levels and their expression patterns determine the proliferative capacity and the differentiation potential of pluripotent and adult stem cells.

#### 5. Involvement of DNMTs in Neuropsychiatric Disorders

Because of their central role in the properties of pluripotent and adult stem cells, and their differentiation potential, abnormal regulation of DNMTs or their mutations are expected to cause a broad spectrum of human disease conditions. However, their essential requirement during embryogenesis makes many of the mutations in DNMTs unrecoverable due to embryonic lethality [28]. Mutations that are mild or those that occur in specific tissue types (somatic mutations) or tissue-specific dysregulation of DNMTs may present with clinically recognizable phenotypes. The only exception seems to be DNMT3B loss of function which results in immune deficiency, centromere instability, and facial abnormalities (ICF) syndrome [29]. Among recent investigations on disorders in which epigenetic mechanisms have been implicated, a relationship between dysregulation of DNMTs and schizophrenia has been observed. For instance, elevated levels of DNMT1 were observed in the interneurons of frontal cortex of schizophrenia and bipolar patients with psychosis. This overexpression of DNMT1 was correlated with hypermethylation and downregulation of GAD67 and REELIN [30]. Both GAD67 deficiency and REELIN deficiency have been shown to cause schizophrenia-like phenotypes [31]. Since DNMT1 cannot by itself establish new DNA methylation marks, it is reasonable to also expect dysregulation of *de novo* DNMTs in the brain samples with schizophrenia. Consistent with this expectation, overexpression of DNMT3A was also observed in GABAergic neurons of schizophrenia patients [32]. Mechanistically, the relationship between overexpression of DNMT1 and schizophrenia is not fully known although a recent study showed that DNMT1 binds to the promoters of *BDNF* and GABAergic genes. This finding is in support of the hypothesis that overexpression of DNMT1 downregulates both specific GABAergic and glutamatergic genes [33]. It is important to note here that the mechanistic basis by which DNMT1 is specifically targeted to promoters

such as those of *REELIN*, *BDNF*, *GAD67*, and the repressed GABAergic and glutamatergic genes is unknown. In addition to the reports that related overexpression of DNMT1 in brain samples from schizophrenia patients, certain alleles of *Dnmt1*, *Dnmt3A*, and *Dnmt3L* have been found to be associated with schizophrenia [34]. In summary, the findings described above indicate that dysregulation of DNMT expression and specific alleles of DNMTs may contribute to development of schizophrenia.

## 6. Stem Cell Models to Investigate the Role of DNMTs in Abnormal Neuronal Development

At present, there are no suitable *in vivo* models available to investigate the mechanistic basis by which overexpression of DNMTs or specific alleles of DNMTs cause phenotypes associated with schizophrenia. Animal models to investigate the mechanistic role of DNMT defects are very expensive as they require gene targeting experiments using conditional alleles that affect DNMTs in neuronal lineages. In addition, materials such as neuronal progenitors and neurons in early stages of differentiation are limited in their availability per animal and require multiple animals to be used in each study. *In vitro* models help address these problems because it is possible to genetically modify ESCs or neuronal progenitor cells, scale them up to required quantities, and induce differentiation into specific types of neurons, which in turn can be obtained in sufficient amounts. To this date, *Dnmt<sup>tet/tet</sup>* ESCs constitute the only cell line in which DNMT1 overexpression in ESCs results in abnormal neuronal differentiation. This transgenic cell line was obtained by inserting *tet-off* cassettes into the endogenous *Dnmt1* promoters of wild-type ESCs. As a result of transactivation mediated by the *tet-off* cassettes, the levels of DNMT1 in *Dnmt<sup>tet/tet</sup>* ESCs are five times higher than the wild-type cells [18]. These ESCs showed normal growth kinetics and morphological features but produced neurons that show abnormal dendritic arborization, branching as in case of patients with spontaneous limbic epilepsy, and hyperactive N-methyl-D-aspartate receptor due to overexpression of NR1 subunit [23]. Interestingly, the abnormal neurons do not overexpress DNMT1 anymore and in fact DNMT1 overexpression was lost immediately after induction of differentiation. Therefore, *Dnmt<sup>tet/tet</sup>* neurons appear to “remember” that DNMT1 was overexpressed in ESC stage and this memory results in abnormal neurogenesis. While there is an ESC model to investigate the role of DNMT1 overexpression in abnormal neurogenesis, the *Dnmt1<sup>tet/tet</sup>* neurons do not have elevated levels of DNMT1 in neurons and therefore do not represent the neurons of schizophrenia patients with psychosis.

From the description above, it is clear that there is an absolute need for development of suitable cell-based models to study the mechanisms by which elevated levels of DNMT1 and DNMT3A, or other DNMT family members, specific disease-associated DNMT alleles cause development of abnormal neurons. These models would then give us an opportunity to test whether the resultant neurons share any

molecular/phenotypic features of neurons from schizophrenia patients or from patients with other psychiatric disorders. The task of cell-based models to generate neurons that overexpress DNMTs or express specific schizophrenia-associated DNMT variants can be accomplished with relative ease because ESCs are tolerant to DNMT levels and even loss of methylation [35]. ESCs are also amenable to targeted gene modification, a method that can allow investigators to introduce specific DNMT alleles in place of wild-type alleles without altering the rest of the genome [36]. Technologies for achieving these goals are in practice for several years and are being constantly improved, especially in the recent five years. For example, CRISPR/Cas9 system is a recent technology that enables a high frequency replacement of wild-type alleles with the mutant alleles [37]. Using this system, it is possible to generate homozygous mutants that express only the mutant proteins (Figure 2). It is also possible to investigate specifically the functional role of a specific DNMT mutant by using DNMT-null ESCs to generate transgenic cell lines that only express the mutant proteins (Figure 2). To achieve constitutive overexpression of DNMTs, new generation expression vectors for ESCs are available with appropriate promoters that encode transcripts such that the transcript produced contains messages for both the gene of interest and a selection marker that confers resistance to an antibiotic such as geneticin, puromycin, and hygromycin (e.g., see [38]).

The possibility of development of ESC models offers certain advantages and disadvantages in their utility to understand the mechanistic basis by which dysregulation of DNMTs is associated with disorders such as schizophrenia. *In vitro* models offer a simple platform to investigate the disease-causing mechanisms because genetically altered ESC lines have well-defined mutations and, barring these specific changes, the remainder of the genome in each of these mutant cell lines is identical to the wild-type cells. As a result, the genotype-phenotype correlation would be clear and unequivocal. Following determination of the exact molecular defect, the *in vitro* models also become attractive tools for large-scale screening using potential drug targets to correct the abnormal neuronal phenotypes. Such high-throughput screens are difficult to perform with animal models. It is important to note that the details of affected cell types in the brain of schizophrenia patients are not well-established. In this context, *in vitro* differentiation of genetically altered ESCs might result in neuronal cell types that may not be representative of the cell types affected in schizophrenia. Although there is no complete picture, literature evidence suggests dysfunction of both GABAergic and Glutamatergic neurons in schizophrenia [39, 40]. In the light of this evidence, it is possible to “direct” differentiation of genetically modified ESCs to specifically glutamatergic and GABAergic lineages [41, 42]. In summary, genetically modified ESCs can help address the consequences of dysregulation of DNMT1 on development and function of either GABAergic or glutamatergic neurons but may not present the overall picture of abnormalities associated with a mixture of neurons and other supporting cells in the brains of schizophrenia patients.

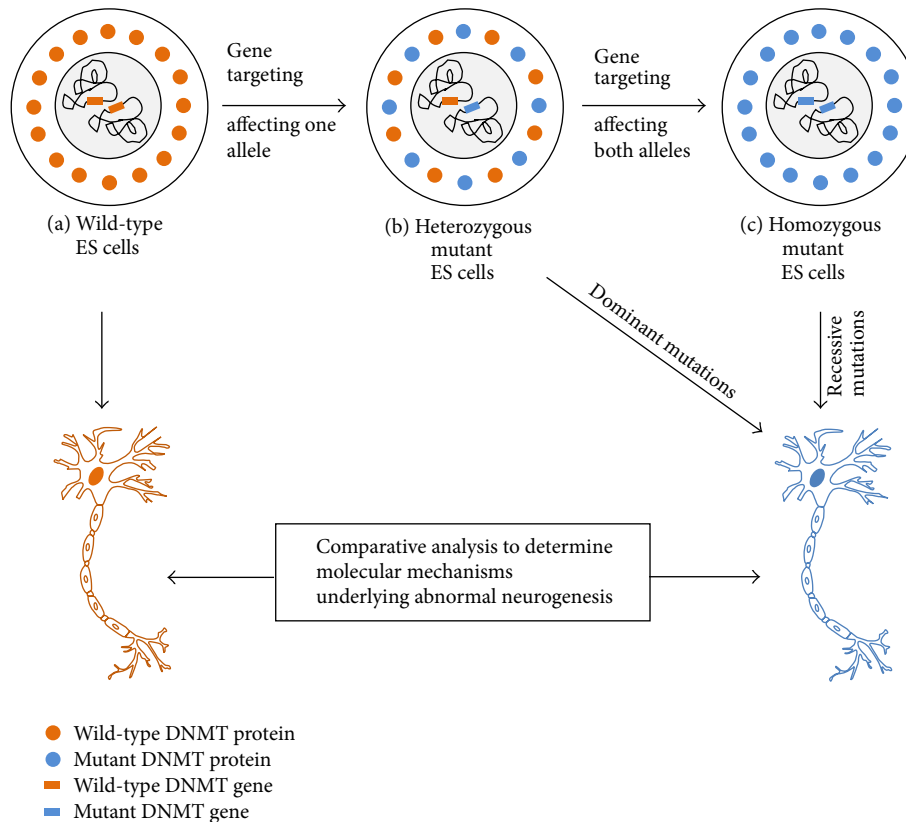


FIGURE 2: Schematic representation generation of embryonic stem cell-based models for studying the role of DNMT dysregulation on development of abnormal neuronal phenotypes. Desired mutations can be selected on the basis of literature evidence of mutations in DNMTs that are associated with neuropsychiatric disorders. Both alleles of DNMTs (*de novo* and maintenance) can be targeted to introduce desired mutations in the wild-type ES cells. First round of targeting results in heterozygotes which can then be used for a second round of targeting that results in homozygotes. Following gene targeting, homozygous ESCs (for recessive mutations) or heterozygous ESCs (for dominant mutations) can be differentiated into neurons. The resultant neurons can be used for detailed physiological and molecular-genetic studies to identify the molecular basis for abnormal neuronal phenotypes.

## 7. Conclusions

Research in the recent past by different groups has uncovered the important role of DNMTs in schizophrenia. It is also possible that, in the future, more DNMT alleles will be associated with other neuropsychiatric disorders. However, investigation of the mechanisms by which the dysregulation of DNMTs results in these disorders using animal models can be highly expensive and laborious. The availability of suitable knockout cell lines, advancements in the technology for targeted gene modifications, and constitutive expression of cDNAs in stem cells together provide a viable alternative option to animal models. Using this approach, elucidation of the mechanistic basis by which altered DNMT levels or specific DNMT alleles cause abnormal neuronal differentiation can pave the way in the future towards possible therapeutic interventions to neuropsychiatric disorders.

## Conflict of Interests

The author declares that there is no conflict of interests regarding the publication of this paper.

## Acknowledgments

Research in K. Naga Mohan's lab is supported by grants from the Department of Biotechnology and the Department of Science and Technology. The author thanks Swaminathan for critical reading of the paper and suggestions.

## References

- [1] H. Meng, Y. Cao, J. Qin et al., "DNA methylation, its mediators and genome integrity," *International Journal of Biological Sciences*, vol. 11, no. 5, pp. 604–617, 2015.
- [2] A. Breiling and F. Lyko, "Epigenetic regulatory functions of DNA modifications: 5-methylcytosine and beyond," *Epigenetics and Chromatin*, vol. 21, no. 8, article 24, 2015.
- [3] A. P. Wolffe and M. A. Matzke, "Epigenetics: regulation through repression," *Science*, vol. 286, no. 5439, pp. 481–486, 1999.
- [4] A. Blattler and P. J. Farnham, "Cross-talk between site-specific transcription factors and DNA methylation states," *The Journal of Biological Chemistry*, vol. 288, no. 48, pp. 34287–34294, 2013.
- [5] M. G. Goll and T. H. Bestor, "Eukaryotic cytosine methyltransferases," *Annual Review of Biochemistry*, vol. 74, pp. 481–514, 2005.

- [6] S. La Salle, C. Mertineit, T. Taketo, P. B. Moens, T. H. Bestor, and J. M. Trasler, "Windows for sex-specific methylation marked by DNA methyltransferase expression profiles in mouse germ cells," *Developmental Biology*, vol. 268, no. 2, pp. 403–415, 2004.
- [7] M. Okano, S. Xie, and E. Li, "Cloning and characterization of a family of novel mammalian DNA (cytosine-5) methyltransferases," *Nature Genetics*, vol. 19, no. 3, pp. 219–220, 1998.
- [8] R. P. Singh, K. Shiue, D. Schomberg, and F. C. Zhou, "Cellular epigenetic epigenetic modifications of neural stem cell differentiation," *Cell Transplantation*, vol. 18, no. 10–11, pp. 1197–1211, 2009.
- [9] J. E. Castillo-Fernandez, T. D. Spector, and J. T. Bell, "Epigenetics of discordant monozygotic twins: implications for disease," *Genome Medicine*, vol. 6, article 60, 2014.
- [10] E. Costa, E. Dong, D. R. Grayson, A. Guidotti, W. Ruzicka, and M. Veldic, "Reviewing the role of DNA (cytosine-5) methyltransferase overexpression in the cortical GABAergic dysfunction associated with psychosis vulnerability," *Epigenetics*, vol. 2, no. 1, pp. 29–36, 2007.
- [11] K. N. Mohan and J. R. Chaillet, "Cell and molecular biology of DNA methyltransferase 1," *International Review of Cell and Molecular Biology*, vol. 306, pp. 1–42, 2013.
- [12] E. Li, T. H. Bestor, and R. Jaenisch, "Targeted mutation of the DNA methyltransferase gene results in embryonic lethality," *Cell*, vol. 69, no. 6, pp. 915–926, 1992.
- [13] G. Fan, C. Beard, R. Z. Chen et al., "DNA hypomethylation perturbs the function and survival of CNS neurons in postnatal animals," *The Journal of Neuroscience*, vol. 21, no. 3, pp. 788–797, 2001.
- [14] D. Biniszkiwicz, J. Gribnau, B. Ramsahoye et al., "Dnmt1 overexpression causes genomic hypermethylation, loss of imprinting, and embryonic lethality," *Molecular and Cellular Biology*, vol. 22, no. 7, pp. 2124–2135, 2002.
- [15] M. Okano, D. W. Bell, D. A. Haber, and E. Li, "DNA methyltransferases Dnmt3a and Dnmt3b are essential for de novo methylation and mammalian development," *Cell*, vol. 99, no. 3, pp. 247–257, 1999.
- [16] P. Arnaud, K. Hata, M. Kaneda et al., "Stochastic imprinting in the progeny of Dnmt3L<sup>-/-</sup> females," *Human Molecular Genetics*, vol. 15, no. 4, pp. 589–598, 2006.
- [17] S. La Salle, C. C. Oakes, O. R. Neaga, D. Bourc'his, T. H. Bestor, and J. M. Trasler, "Loss of spermatogonia and wide-spread DNA methylation defects in newborn male mice deficient in DNMT3L," *BMC Developmental Biology*, vol. 7, article 104, 2007.
- [18] E. Borowczyk, K. N. Mohan, L. D'Aiuto, M. C. Cirio, and J. R. Chaillet, "Identification of a region of the DNMT1 methyltransferase that regulates the maintenance of genomic imprints," *Proceedings of the National Academy of Sciences of the United States of America*, vol. 106, no. 49, pp. 20806–20811, 2009.
- [19] M. Damelin and T. H. Bestor, "Biological functions of DNA methyltransferase 1 require its methyltransferase activity," *Molecular and Cellular Biology*, vol. 27, no. 11, pp. 3891–3899, 2007.
- [20] C.-C. Tsai, P.-F. Su, Y.-F. Huang, T.-L. Yew, and S.-C. Hung, "Oct4 and Nanog directly regulate Dnmt1 to maintain self-renewal and undifferentiated state in mesenchymal stem cells," *Molecular Cell*, vol. 47, no. 2, pp. 169–182, 2012.
- [21] H. Lei, S. P. Oh, M. Okano et al., "De novo DNA cytosine methyltransferase activities in mouse embryonic stem cells," *Development*, vol. 122, no. 10, pp. 3195–3205, 1996.
- [22] T. Chen, Y. Ueda, J. E. Dodge, Z. Wang, and E. Li, "Establishment and maintenance of genomic methylation patterns in mouse embryonic stem cells by Dnmt3a and Dnmt3b," *Molecular and Cellular Biology*, vol. 23, no. 16, pp. 5594–5605, 2003.
- [23] L. D'Aiuto, R. Di Maio, K. N. Mohan et al., "Mouse ES cells overexpressing DNMT1 produce abnormal neurons with upregulated NMDA/NR1 subunit," *Differentiation*, vol. 82, no. 1, pp. 9–17, 2011.
- [24] J. J. Trowbridge, J. W. Snow, J. Kim, and S. H. Orkin, "DNA Methyltransferase 1 is essential for and uniquely regulates hematopoietic stem and progenitor cells," *Cell Stem Cell*, vol. 5, no. 4, pp. 442–449, 2009.
- [25] G. A. Challen, D. Sun, M. Jeong et al., "Dnmt3a is essential for hematopoietic stem cell differentiation," *Nature Genetics*, vol. 44, no. 1, pp. 23–31, 2012.
- [26] G. Challen, D. Sun, A. Mayle et al., "Dnmt3a and Dnmt3b have overlapping and distinct functions in hematopoietic stem cells," *Cell Stem Cell*, vol. 15, no. 3, pp. 350–364, 2014.
- [27] B. Kadriu, A. Guidotti, Y. Chen, and D. R. Grayson, "DNA methyltransferases 1 (DNMT1) and 3a (DNMT3a) colocalize with GAD67-positive neurons in the GAD67-GFP mouse brain," *Journal of Comparative Neurology*, vol. 520, no. 9, pp. 1951–1964, 2012.
- [28] K. N. Mohan and J. R. Chaillet, "Emerging role of epigenetics in human neurodevelopmental disorders," in *Epigenetics in Human Disease*, pp. 153–173, Elsevier, 2012.
- [29] G.-L. Xu, T. H. Bestor, D. Bourc'his et al., "Chromosome instability and immunodeficiency syndrome caused by mutations in a DNA methyltransferase gene," *Nature*, vol. 402, no. 6758, pp. 187–191, 1999.
- [30] M. Veldic, A. Guidotti, E. Maloku, J. M. Davis, and E. Costa, "In psychosis, cortical interneurons overexpress DNA-methyltransferase," *Proceedings of the National Academy of Sciences of the United States of America*, vol. 102, no. 6, pp. 2152–2157, 2005.
- [31] K. Fujihara, H. Miwa, T. Kakizaki et al., "Glutamate decarboxylase 67 deficiency in a subset of GABAergic neurons induces schizophrenia-related phenotypes," *Neuropsychopharmacology*, 2015.
- [32] A. Zhubi, M. Veldic, N. V. Puri et al., "An upregulation of DNA-methyltransferase 1 and 3a expressed in telencephalic GABAergic neurons of schizophrenia patients is also detected in peripheral blood lymphocytes," *Schizophrenia Research*, vol. 111, no. 1–3, pp. 115–122, 2009.
- [33] E. Dong, W. B. Ruzicka, D. R. Grayson, and A. Guidotti, "DNA-methyltransferase 1 (DNMT1) binding to CpG rich GABAergic and BDNF promoters is increased in the brain of schizophrenia and bipolar disorder patients," *Schizophrenia Research*, 2014.
- [34] K. R. Saradalekshmi, N. V. Neetha, S. Sathyan, I. V. Nair, C. M. Nair, and M. Banerjee, "DNA methyl transferase (DNMT) gene polymorphisms could be a primary event in epigenetic susceptibility to schizophrenia," *PLoS ONE*, vol. 9, no. 5, Article ID e98182, 2014.
- [35] J. Liao, R. Karnik, H. Gu et al., "Targeted disruption of DNMT1, DNMT3A and DNMT3B in human embryonic stem cells," *Nature Genetics*, vol. 47, no. 5, pp. 469–478, 2015.
- [36] K. R. Thomas and M. R. Capecchi, "Site-directed mutagenesis by gene targeting in mouse embryo-derived stem cells," *Cell*, vol. 51, no. 3, pp. 503–512, 1987.
- [37] P. Mali, L. Yang, K. M. Esvelt et al., "RNA-guided human genome engineering via Cas9," *Science*, vol. 339, no. 6121, pp. 823–826, 2013.

- [38] K. N. Mohan, F. Ding, and J. R. Chaillet, "Distinct roles of DMAP1 in mouse development," *Molecular and Cellular Biology*, vol. 31, no. 9, pp. 1861–1869, 2011.
- [39] K. M. Spencer, P. G. Nestor, R. Perlmutter et al., "Neural synchrony indexes disordered perception and cognition in schizophrenia," *Proceedings of the National Academy of Sciences of the United States of America*, vol. 101, no. 49, pp. 17288–17293, 2004.
- [40] L. Volk, S. L. Chiu, K. Sharma, and R. L. Huganir, "Glutamate synapses in human cognitive disorders," *Annual Review of Neuroscience*, vol. 38, no. 1, pp. 127–149, 2015.
- [41] J. H. Reyes, K. S. O'Shea, N. L. Wys et al., "Glutamatergic neuronal differentiation of mouse embryonic stem cells after transient expression of neurogenin 1 and treatment with BDNF and GDNF: in vitro and in vivo studies," *The Journal of Neuroscience*, vol. 28, no. 48, pp. 12622–12631, 2008.
- [42] E. Shin, M. J. Palmer, M. Li, and R. A. Fricker, "GABAergic neurons from mouse embryonic stem cells possess functional properties of striatal neurons in vitro, and develop into striatal neurons in vivo in a mouse model of Huntington's disease," *Stem Cell Reviews and Reports*, vol. 8, no. 2, pp. 513–531, 2012.

## Research Article

# p53-Dependent Senescence in Mesenchymal Stem Cells under Chronic Normoxia Is Potentiated by Low-Dose $\gamma$ -Irradiation

Ines Höfig,<sup>1</sup> Yashodhara Ingawale,<sup>1</sup> Michael J. Atkinson,<sup>1,2</sup> Heidi Hertlein,<sup>1</sup>  
Peter J. Nelson,<sup>3</sup> and Michael Rosemann<sup>1</sup>

<sup>1</sup>Institute of Radiation Biology, Helmholtz Center Munich, German Research Center for Environmental Health, Ingolstaedter Landstraße 1, 85764 Neuherberg, Germany

<sup>2</sup>Chair of Radiation Biology, Technical University Munich, Ismaninger Straße 22, 81675 Munich, Germany

<sup>3</sup>Research Group Clinical Biochemistry, Medical Clinic and Polyclinic IV, Medical Center of the University of Munich, Schillerstraße 42, 80336 Munich, Germany

Correspondence should be addressed to Michael Rosemann; [rosemann@helmholtz-muenchen.de](mailto:rosemann@helmholtz-muenchen.de)

Received 31 July 2015; Accepted 2 November 2015

Academic Editor: Jane Synnergren

Copyright © 2016 Ines Höfig et al. This is an open access article distributed under the Creative Commons Attribution License, which permits unrestricted use, distribution, and reproduction in any medium, provided the original work is properly cited.

Mesenchymal stem cells (MSCs) are a source of adult multipotent cells important in tissue regeneration. Murine MSCs are known to proliferate poorly *in vitro* under normoxia. The aim of this study is to analyze the interaction of nonphysiological high oxygen and low-dose  $\gamma$ -irradiation onto growth, senescence, and DNA damage. Tri-potent bone marrow-derived MSCs from p53 wildtype and p53<sup>-/-</sup> mice were cultured under either 21% or 2% O<sub>2</sub>. Long-term observations revealed a decreasing ability of wildtype mMSCs to proliferate and form colonies under extended culture in normoxia. This was accompanied by increased senescence under normoxia but not associated with telomere shortening. After low-dose  $\gamma$ -irradiation, the normoxic wildtype cells further increased the level of senescence. The number of radiation-induced  $\gamma$ H2AX DNA repair foci was higher in mMSCs kept under normoxia but not in p53<sup>-/-</sup> cells. P53-deficient MSCs additionally showed higher clonogenicity, lower senescence levels, and fewer  $\gamma$ H2AX repair foci per cell as compared to their p53 wildtype counterparts irrespective of oxygen levels. These results reveal that oxygen levels together with  $\gamma$ -irradiation and p53 status are interconnected factors modulating growth capacity of BM MSCs in long-term culture. These efforts help to better understand and optimize handling of MSCs prior to their therapeutic use.

## 1. Introduction

Mesenchymal stem cells (MSCs) are multipotent with a life-long proliferation capacity in the adult organism. Their potential to generate precursors for osteoblasts, adipocytes, fibroblasts, and chondroblasts *in vitro* [1, 2] has prompted the idea that they could also be a reservoir for the regeneration of connective tissue after injuries and fractures or during normal cell loss [3]. Because of their multilineage differentiation capacity and long-term proliferation potential, they have received interest as vehicles for the treatment of chronic degenerative diseases and acute tissue injuries [4]. The relative ease of harvesting facilitates autologous transplantation of MSCs into a diseased target organ, usually after the cells have been expanded *ex vivo* [5]. Some of their therapeutic benefits are also found to be conferred by anti-inflammatory and immunomodulatory factors secreted

by the transplanted MSCs, rather than by the generation of viable cell progeny [6]. This may explain their reported efficiency as supplements in wound healing [7], bone marrow transplantation (to reduce graft-versus-host disease, GvHD) [8], and cardiac surgery [9].

At the time of writing, 529 clinical trials using MSCs are registered worldwide (<https://www.clinicaltrials.gov/>), with the majority intended to treat disorders of the CNS (12%), cardiac disease (10%), various types of autoimmune diseases (9%), joint and skeletal diseases (8%), metabolic disorders (7%), and GvHD (6%). Although the therapeutic procedures of autologous MSC transplantation are considered safe and more robust than allogenic transplantation protocols, the success of treatment in individual patients is variable [10]. To what extent transplanted MSCs proliferate and whether they are able to differentiate into fully functional cells capable of regenerating damaged tissue are usually not determined [11].

The mechanisms by which genetic, epigenetic, or environmental factors govern the efficiency of an MSC therapy are difficult to assess directly in patients but can be systematically studied in model organisms such as guinea pig, mice [12, 13], or minipig [14].

We are interested in the influence of genotoxic stress acting on MSCs both prior to and during *ex vivo* expansion, in particular by non-physiologically high oxygen levels and by ionizing radiation (IR). The sensitivity of eukaryotic cells to IR-induced cell killing depends on the presence of oxygen [15]. *In vitro* studies of cancer cell lines show that hypoxia confers radioresistance, which is associated with a lower level of DNA lesions in the nucleus [16]. MSCs in their normal physiological context reside in hypoxic niches [17, 18] and might therefore be relatively protected from radical oxygen species (ROS), which are generated by ionizing radiation. In the case of haematopoietic stem cells derived from bone marrow, exposure to atmospheric oxygen has been shown to trigger EPHOSS (for extraphysiologic oxygen shock or stress) that is linked to activation of the p53 pathway and mitochondria-mediated apoptosis [19]. Although our own studies indicate that apoptosis is, unlike in haematopoietic cells, not a common mechanism in MSCs during aging or after cytogenetic stress, a p53-mediated DNA damage response (DDR) could also impair their stem cell potency by premature senescence or differentiation. Since murine MSCs growing *in vitro* depend on a hypoxic environment [20], they are a suitable model to investigate the mechanisms of oxygen induced cellular stress both alone and also in combination with a low-dose radiation exposure.

We have examined the growth capacity, clonogenic potential, senescence induction, accumulation of DNA damage, and rate of telomere attrition of mMSCs grown under two different oxygen concentrations. Since the first findings suggested senescence induction and involvement of accumulating DNA damage, we tested this assumption by low-dose  $\gamma$ -irradiation of mMSCs comparing p53 wild-type with p53<sup>-/-</sup> cells.

## 2. Materials and Methods

**2.1. Cultivation of Primary Murine MSCs.** Female FVB/N p53wt/wt and C57BL/6 p53<sup>-/-</sup> mice, 3 to 12 months old, were originally supplied by Charles River Laboratories (Sulzbach, Germany) and maintained in a breeding colony at the Helmholtz Center Munich under specific pathogen-free conditions. To collect bone marrow MSCs, mice were sacrificed by CO<sub>2</sub> exposure, the hind limbs were aseptically dissected, and the femurs were cleaned from adherent tissues. One tip of each femur was removed and the bone marrow was collected by flushing with ice-cold PBS. After disaggregating larger clumps of bone marrow and allowing remaining cell clumps to sediment, the supernatant was centrifuged (5 min at 300 ×g), and the resulting cell pellet was washed again with PBS. Finally, bone marrow cells were plated at a cell density of 5,000,000 per 6-well plate in DMEM/F12 media containing 10% mesenchymal stem cell qualified FBS (Life Technologies, Carlsbad, CA). The cultures were kept in a humidified 5% CO<sub>2</sub> incubator at 37°C under 21% (normoxia) or 2%

(hypoxia) O<sub>2</sub>. After 4 h, 6 h, and twice a day for the following 3 days, supernatant containing nonadherent cells was aspirated and fresh complete medium was added. Adhering cells were grown for 7 days, detached for passaging with the StemPro Accutase Cell Dissociation Reagent (Life Technologies), and cell numbers were obtained using a Coulter Counter Analyzer (Beckman Coulter, Brea, CA). Growth medium was changed every 3.5 days and cells were passaged once a week.

**2.2. In Vitro Induction of Lineage Differentiation.** To verify the multilineage differentiation potential (Supplementary Figure 1 in Supplementary Material available online at <http://dx.doi.org/10.1155/2016/6429853>) the isolated mMSCs were plated at densities of 3,000 (osteogenic), 10,000 (adipogenic), or 80,000 (chondrogenic) cells per well in 96-well culture plates. For chondrogenic differentiation, cells were allowed to attach for 2 h before inducing the differentiation, using chondrogenic differentiation medium. In the case of osteogenic and adipogenic differentiation the cells were stimulated with appropriate differentiation medium only after 2 to 3 days. Remaining wells served as controls using normal MSC growth medium. All differentiation assays were performed under hypoxic conditions. Following lineage induction, cultures were stained and visualized on a Keyence BZ9000 microscope (Keyence, Neu-Isenburg, Germany).

**2.2.1. Alkaline Phosphatase Staining of Osteogenic Differentiation.** Murine MSCs were stimulated for up to 2 weeks in StemPro osteocyte/chondrocyte differentiation basal medium supplemented with StemPro Osteogenesis Supplement (Life Technologies). After fixation of the cells with 4% paraformaldehyde, alkaline phosphatase activity was revealed by SigmaFast BCIP/NBT chromogen staining (Sigma Aldrich, St. Louis, MO) according to PromoCell's application note for "osteoblast differentiation and mineralization" (PromoCell GmbH, Heidelberg, Germany).

**2.2.2. Oil Red O Staining for Adipogenic Differentiation.** Murine MSCs were stimulated for 2 weeks in StemPro Adipocyte differentiation basal medium supplemented with StemPro Adipogenesis Supplement (Life Technologies). After fixation of the cells with 4% paraformaldehyde, lipid vacuoles were stained for 45 min at room temperature with an Oil red O buffer solution (60% isopropanol with 3 mg/mL Oil red O (Sigma Aldrich), 40% H<sub>2</sub>O) and rinsed with water.

**2.2.3. Alcian Blue Staining for Chondrogenic Differentiation.** Murine MSCs were stimulated for 3 weeks in StemPro Osteocyte/Chondrocyte differentiation basal medium supplemented with StemPro Chondrogenesis Supplement (Life Technologies). After fixation of the cells with 4% paraformaldehyde, proteoglycan aggrecan in the cartilage extracellular matrix was stained by an Alcian Blue 8GX dye (Sigma Aldrich) according to PromoCell's application note for "chondrogenic differentiation and analysis of MSC" (PromoCell).

**2.3. Clonogenic Survival.** For the measurement of clonogenic survival, between 500 and 5,000 mMSCs per 75 cm<sup>2</sup> were

seeded in cell culture flasks under either normoxia or hypoxia. After 10 to 14 days, the colony formation capacity was assayed after ethanol fixation and Giemsa (Merck, Darmstadt, Germany) staining. Plating efficiency in percentage was calculated by the following formula: (number of colonies formed/number of seeded cells)  $\times$  100.

**2.4. Irradiation.** Irradiation of mMSCs was performed with a Cs-137 irradiator (HWM D-2000, Siemens, Germany) at a dose rate of 0.5 Gy/min. For irradiation doses lower than 0.5 Gy, a shielded lead box was used with an attenuation factor of 10%. Doses were administered at room temperature and control cells were sham-irradiated. During the entire irradiation procedure (about 20 min) the cell culture vessels were sealed with parafilm to reduce gas exchange.

**2.5. Senescence Analysis.** For assessment of senescence associated  $\beta$ -galactosidase activity 7 days after irradiation, subconfluent mMSCs in 96-well culture plates were washed with PBS, fixed with 4% paraformaldehyde, again washed with PBS, and stained for 12 h at 37°C with an X-gal buffer solution (40 mM Na<sub>2</sub>HPO<sub>4</sub>, 150 mM NaCl, 2 mM MgCl<sub>2</sub>, 5 mM K<sub>3</sub>Fe(CN)<sub>6</sub>, 5 mM K<sub>4</sub>Fe(CN)<sub>6</sub>·3H<sub>2</sub>O, and 1 mg/mL X-gal, pH 6). Multicolored microscope images were taken with a Keyence BZ9000 microscope.

**2.6. Analysis of p53 Stabilization and  $\gamma$ H2AX DNA Damage Repair Foci.** Murine MSCs were seeded on glass slides and grown in either hypoxia or normoxia for at least 24 h. Following irradiation, the cells were fixed at the indicated time points (methanol for p53 or 4% paraformaldehyde for  $\gamma$ H2AX). Fixed cells were washed in PBS, treated with 0.05% Saponin (40 min for p53) or 0.2% Triton-X (5 min for  $\gamma$ H2AX) in PBS, washed in PBS, and blocked with 10 mg/mL BSA and 1.5 mg/mL glycine in PBS for 1 h at room temperature. Cells were incubated with primary antibodies against phosphorylated  $\gamma$ H2AX (Upstate Biotechnology, Lake Placid, NY) diluted in antibody dilution solution (DCS, Hamburg, Germany) or against p53 (R19, Santa Cruz Biotechnology, Dallas, TX) in PBS for at least 90 min. For visualization goat anti-mouse Cy3-conjugated secondary antibody (GE Healthcare GmbH, Freiburg, Germany) diluted in antibody dilution solution or HRP-conjugated donkey anti-goat secondary antibody (Santa Cruz Biotechnology) was used after washing slides in PBS (and blocking peroxidases for 15 min with 0.2% H<sub>2</sub>O<sub>2</sub> for p53). For immunohistochemical staining of p53, SIGMAFAST DAB (3,3'-diaminobenzidine tetra hydrochloride, Sigma Aldrich) was added overnight. After a final PBS washing step slides were mounted in DAPI-containing mounting medium and analyzed with a Keyence BZ9000 microscope. The Keyence software counted nuclear foci in at least 50 cells. Appropriate negative controls were obtained by staining a replicate slide with the secondary antibody only.

**2.7. Telomere Length Determination.** Quantitative PCR of genomic DNA extracted from mMSCs was done to measure telomeric length [21]. For this purpose, qRT-PCR was set up using (TTAGGG)<sub>n</sub> primers detecting the telomere

sequence and primers for a genomic microsatellite marker (D14Miti192) for genomic DNA normalization in two separate reactions. Quantitative real-time amplification was done on a StepOne<sup>+</sup> device (Life Technologies), using the "Power Sybr-Green" master mix (including Rox-standard), 2 pmol of each primer, and 10 ng genomic DNA in a 20  $\mu$ L reaction volume. Relative telomeric length was calculated by the delta-delta CT method, with pooled newborn mouse skin DNA as a calibrator (set as 100 arbitrary units, AU).

**2.8. Triplex Assay to Quantify Viability, Cytotoxicity, and Apoptosis Induction.** Murine MSCs were seeded on 96-well plates, irradiated, and incubated in either hypoxia or normoxia for 7 days. Viability, cytotoxicity, and apoptosis were assessed in one well using the ApoTox-Glo Triplex assay (Promega, Madison, WI). In a first step, the cell-permeable substrate glycyLphenylalanyl-aminofluoro-coumarin (GF-AFC) is cleaved by live-cell protease activity to generate a fluorescent signal (400 nm excitation, 505 nm emission) proportional to the number of living cells. In parallel the nonpermeable substrate bis-alanylalanyl-phenylalanyl-rhodamine 110 (bis-AAF-R110; 485 nm excitation, 520 nm emission) is used to measure dead-cell protease activity, which is released from cells that have lost membrane integrity. In a second step, the addition of CaspaseGlo 3/7 reagent results in cell lysis, followed by caspase cleavage of the substrate and generation of luminescent signal produced by luciferase. Both fluorescence and luminescence signals were analyzed in a microplate reader (Infinite 200, Tecan, Männedorf, Switzerland). Positive controls for necrosis had cells exposed for 6 h to 100  $\mu$ M ionomycin, and positive controls for apoptosis had cells exposed to 100  $\mu$ M staurosporine for 6 h (both Sigma Aldrich), incubated under hypoxia.

**2.9. Statistical Analysis.** All experiments were performed with at least duplicate technical and biological replicates. Mean  $\pm$  standard errors of the mean (SEM) values are depicted unless stated otherwise. Results were statistically evaluated with indicated tests by the statistic software SigmaPlot (Systat Software Inc., San Jose, CA) and SPSS version 22 (IBM Corp, Armonk, NY). Statistical significance was accepted at the  $p < 0.05$  level.

### 3. Results

**3.1. Oxygen Concentration Affects Long-Term In Vitro Proliferative Potential of Murine MSCs.** In line with previously published studies [22], we observed increased proliferation of mMSCs in a 2% O<sub>2</sub> (hypoxic) environment as compared to the 21% O<sub>2</sub> (normoxic) environment. As the time in culture progressed, the total cell numbers in hypoxic cultures were significantly higher as compared to those in normoxic culture conditions. Representative images show long-term cultured hypoxic and normoxic mMSCs on day 32 after isolation (Figure 1(a)).

**3.2. Normoxic Culture Condition Reduces Colony Forming Ability of mMSCs.** The reduced cellularity of normoxia

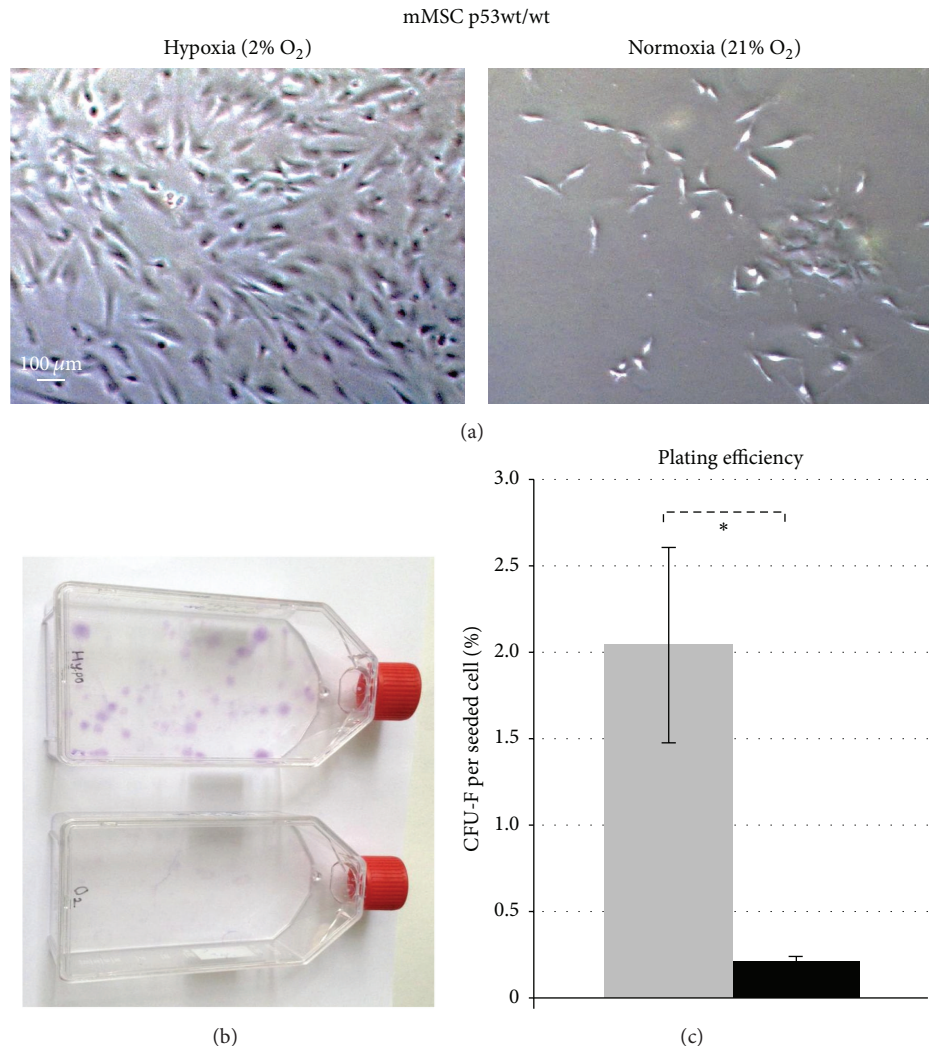


FIGURE 1: Effects of oxygen levels on long-term *in vitro* culturing and colony forming capacity of p53 wild-type mMSCs. (a) Proliferation and morphology of mMSCs p53wt/wt cultured in hypoxic conditions (2% O<sub>2</sub>, left) and in normoxic conditions (21% O<sub>2</sub>, right). Representative images show mMSCs cultured for 32 days. (b) Colony forming ability of mMSCs in hypoxic (upper) and normoxic (lower) atmospheres 14 days after plating 5,000 cells in a 75 cm<sup>2</sup> flask. (c) Plating efficiency calculated as mean values of fibroblast colony forming units (CFU-F) per plated cell ± standard error of the mean ( $n = 4$ ) in hypoxic (grey bar) and normoxic (black bar) conditions.

grown mMSC cultures was due to a reduced ability to form colonies. Thus, clonogenic assays of mMSCs revealed a tenfold higher number of colonies (2.04%) under hypoxia, as compared to growth under normal oxygen conditions (0.21%) (Figures 1(b) and 1(c)) ( $p = 0.03$ , one-tailed paired Student's *t*-test). These results prove that the clonogenicity of mMSCs is impaired in normoxic cultures.

**3.3. Normoxia Increases the Sensitivity of mMSCs towards Radiation-Induced Senescence.** We have not seen a relevant increase of necrotic or apoptotic cells using a multiplex assay with fluorescent GF-AFC/bis-AAF-R100 and luminescent caspase-3/-7 substrates (Supplementary Figure 2), neither after irradiation nor by normoxia. So we hypothesized that senescence is the key mechanism of decreased proliferative and loss of colony forming ability of mMSCs in cultures with ambient oxygen concentration (21% O<sub>2</sub>). To investigate the possible role of oxygen on senescence

induction, subconfluent mMSC cultures under hypoxic and normoxic conditions were stained for senescence-associated  $\beta$ -galactosidase (SA  $\beta$ -gal) activity. In sham-irradiated cells that were transferred to normoxic conditions, we observed a strong increase to  $54 \pm 1.2\%$  senescent cells, as compared to  $31 \pm 2.8\%$  in cells kept under hypoxic conditions for the same time (Figure 2(a)).

Ionizing radiation (IR) is known to generate oxidative stress in cells [23]. Therefore, we exposed mMSCs maintained in hypoxic and normoxic conditions to increasing doses of  $\gamma$ -irradiation (0.1 Gy, 0.2 Gy, 0.5 Gy, and 4 Gy). Cells irradiated with a dose as high as 4 Gy exhibited a change in the MSCs' typical spindle cell morphology, which might indicate cellular stress. There was also a much reduced cell growth of MSCs following 4 Gy irradiation, as measured by lower cell numbers after 7 days under both oxygen concentrations (Figure 2(a)). The combination of higher oxygen and IR significantly increased senescence in mMSCs ( $p = 0.003$ ,

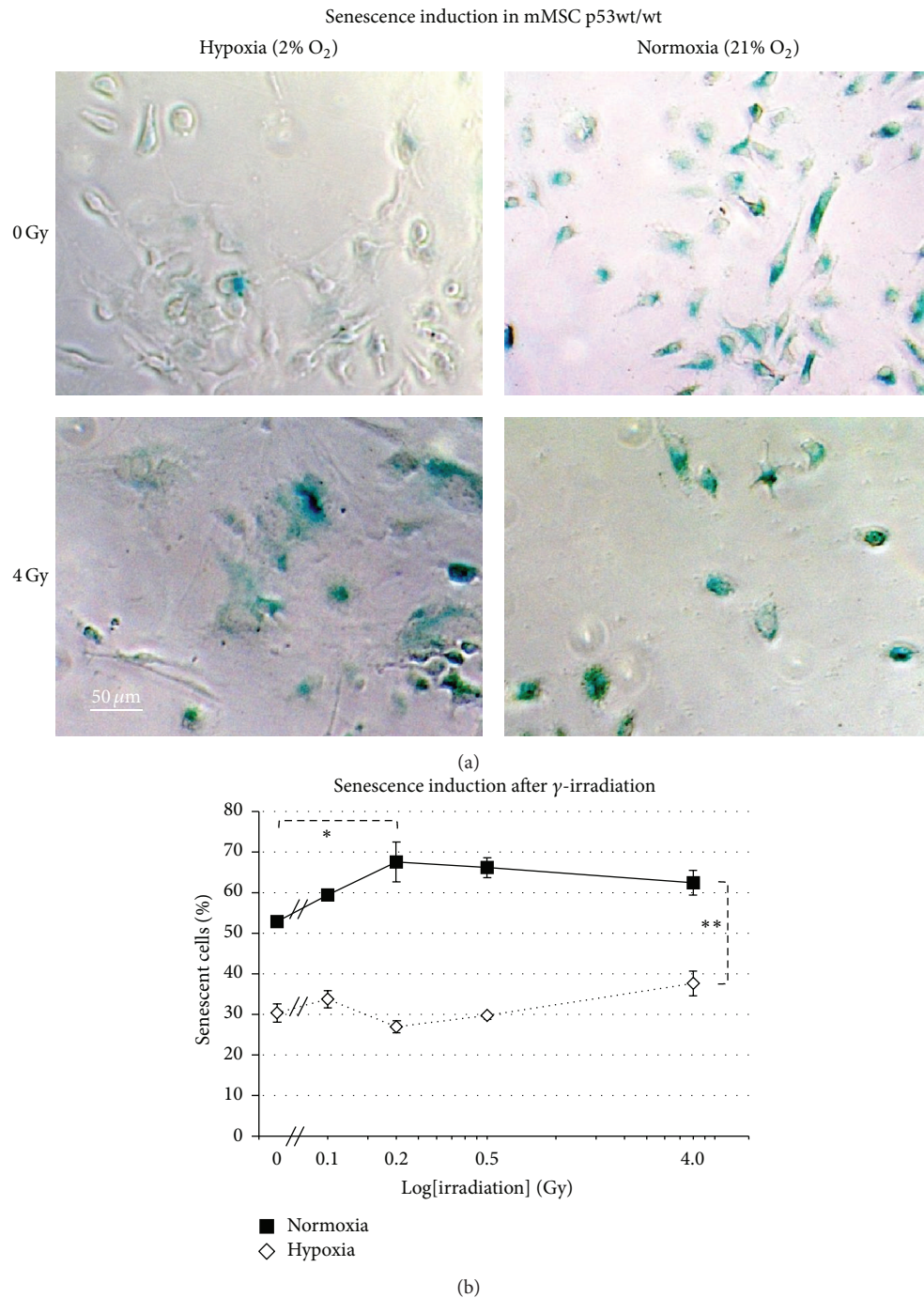
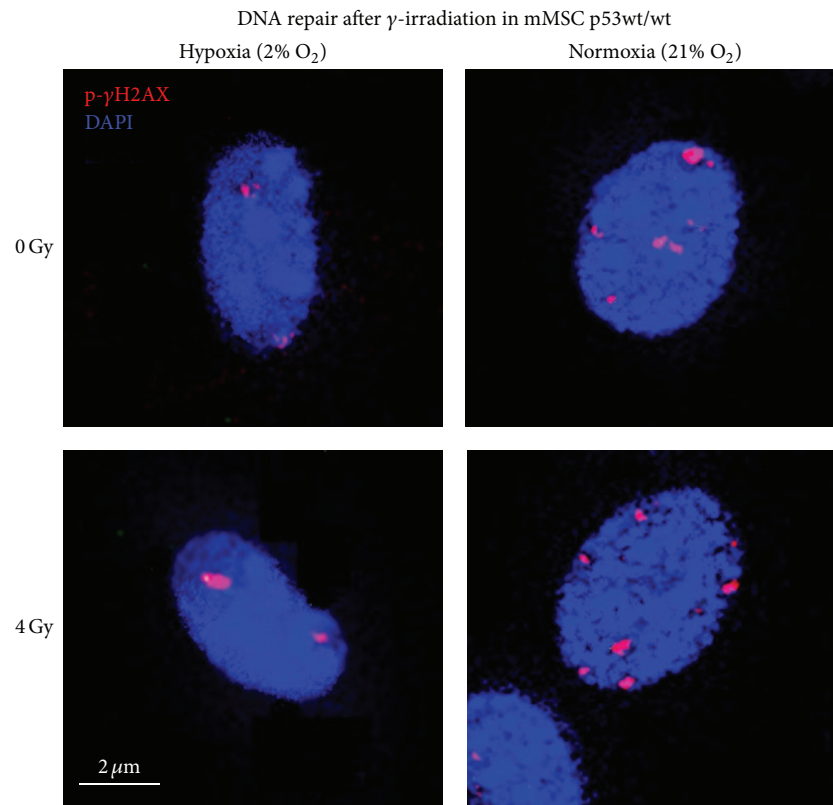


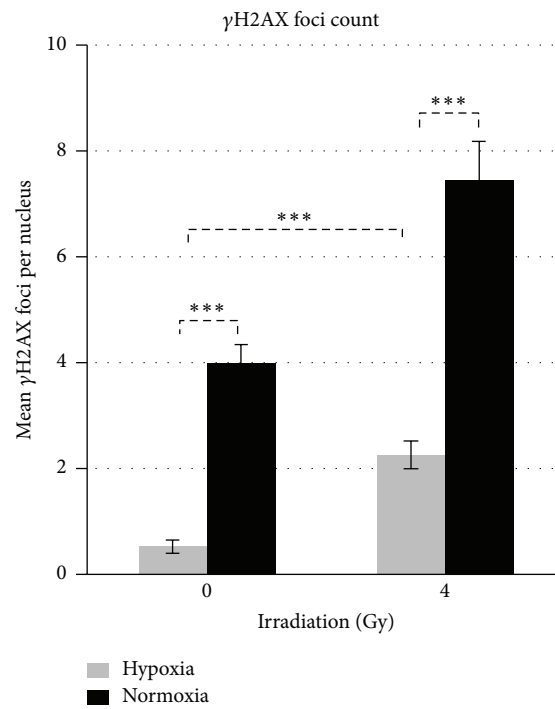
FIGURE 2: Effects of oxygen levels on sensitivity of p53 wild-type mMSCs for radiation-induced senescence. (a) Green SA  $\beta$ -gal positive mMSCs in sham-irradiated (0 Gy) hypoxic (upper left) and in normoxic cultures (upper right) and 7 days after exposure to 4 Gy  $\gamma$ -irradiation (hypoxia, lower left, and normoxia, lower right). (b) Percentage of cells undergoing senescence in hypoxic and normoxic conditions after increasing doses of  $\gamma$ -irradiation depicted as mean values  $\pm$  standard error of the mean (4 biological replicates), radiation dose on logarithmic scale.

ANOVA). Irradiation could independently cause mMSCs to undergo senescence ( $p = 0.031$ , ANOVA). Ambient oxygen concentration was also found to be a crucial factor responsible for increasing senescence in mMSCs ( $p = 3.2 \times 10^{-18}$ , ANOVA). All together this suggests that normoxia increases the sensitivity of mMSCs towards radiation-induced senescence.

**3.4. Murine MSCs Grown in Normoxia Have Higher Basal Levels of DNA Damage and Show a Greater Increase after  $\gamma$ -Irradiation.** In sham-irradiated mMSCs under hypoxia, most of the cells showed an absence of  $\gamma$ H2AX foci, with a mean value of 0.5 (range from 0 to 2) foci per nucleus (Figures 3(a) and 3(b)). The number and the size of the  $\gamma$ H2AX foci were significantly increased when cells were grown under



(a)



(b)

FIGURE 3: Effects of oxygen levels on the number of repair foci in sham-irradiated and 4 Gy irradiated p53wt/wt mMSCs. (a) Sham-irradiated (0 Gy)  $\gamma$ H2AX foci formation under normoxic cultures (right upper image) and hypoxic cultures (left upper image) and additionally 90 min after exposure to 4 Gy  $\gamma$ -irradiation (lower images). (b) Quantification of  $\gamma$ H2AX foci in 50 p53wt/wt mMSC nuclei depicted as mean values  $\pm$  standard error of the mean (3 biological replicates).

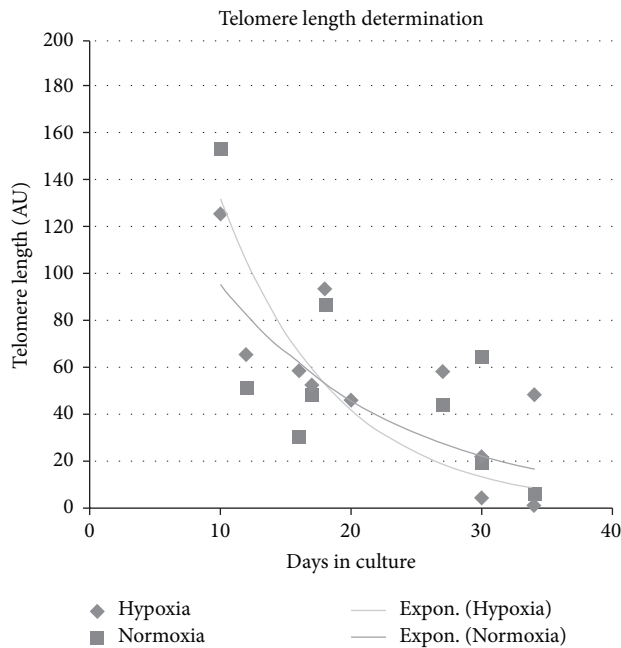


FIGURE 4: Effects of oxygen levels on telomeric length. Graph shows quantitative genomic PCR telomeric length determination performed with p53wt/wt mMSCs under hypoxic and normoxic conditions and with a pool of newborn mouse skin DNA as calibrator (set to 100 arbitrary units, AU). Fitted lines are exponential regression curves, and the differences are not significant.

normoxic conditions, reaching mean values of 4.0 (range from 2 to 6) foci per cell.

4 Gy irradiated mMSCs cultured under hypoxia increased the number of foci per cell to a mean value of 2.3 (range from 0 to 4) foci per nucleus (Figures 3(a) and 3(b)), indicating ongoing repair. 4 Gy irradiated mMSCs cultured under normoxia showed massive appearance of  $\gamma$ H2AX foci with a mean value of 7.5 per nucleus (range from 4 to more than 20 foci in some cells). These experiments indicate that normoxia increases the sensitivity of mMSCs towards DNA lesions when  $\gamma$ -irradiation is applied.

### 3.5. No Effect of Normoxia on mMSC Telomere Shortening.

DNA damage signaling can also be triggered by dysfunctional, eroding telomeres [24]. Therefore the relative telomere length of mMSCs growing under hypoxia and under normoxia was measured for 3 weeks in culture (Figure 4). At the beginning of the culture period, the telomere length in mMSCs was slightly longer (123 AU to 155 AU) than in the reference cells (new-born skin fibroblasts, set as 100 AU), but this declined during *in vitro* expansion. Within 24 days, telomere length had decreased to  $18 \pm 7$  AU (normoxia) or  $5 \pm 5$  AU (hypoxia), equivalent to a half-life time of about 7.8 days. Exponential fitting of the time course of telomere shortening did not yield significant differences in the kinetic parameter between the hypoxic and the normoxic curve.

### 3.6. Long-Term In Vitro Proliferative Potential of mMSCs Is Not Affected by Oxygen Conditions in the Absence of p53.

We found evidence of higher levels of senescence and DNA strand breaks to be present in mMSCs when kept under normoxia (21%  $O_2$ ). The transcription factor p53 regulates a variety of target genes affecting several cellular pathways, all involved in establishment of both senescence and DNA damage response [25, 26]. More prominent stabilization of p53 after irradiation was observed as a feature of mMSCs incubated under normoxia than under hypoxia (Supplementary Figure 3). Using MSCs from p53<sup>-/-</sup> mice, we found that *in vitro* proliferation was unaffected by normal oxygen concentration (Figure 5(a)). The plating efficiency as a measure of clonogenic potential of these cells was higher ( $28\% \pm 3\%$ ) than in the p53wt/wt cells ( $2\% \pm 0.6\%$ ) and it was unaffected by the oxygen concentration (Supplementary Figure 4 and Figure 5(b)).

### 3.7. Senescence and $\gamma$ H2AX Repair Foci Formation Are Reduced in p53<sup>-/-</sup> Irrespective of Oxygen Levels.

In p53-deficient mMSCs, the spontaneous frequency of senescence was significantly lower as compared to senescence in p53wt/wt mMSCs, both under hypoxic growth conditions ( $9.8\% \pm 1.5\%$ ), as well as in cells kept in normoxia ( $7.2\% \pm 1.8\%$ ) (Figure 6(a)). The difference of 2.6% ( $\pm 3.3\%$ ) in the senescence level between hypoxic and normoxic p53<sup>-/-</sup> mMSCs remained unaltered after additional  $\gamma$ -irradiation (0.2 Gy, 0.5 Gy and 4 Gy), despite the frequency itself being increased in a similar fashion as in normoxic p53wt/wt cells (Figure 2(b)).

The number of radiation-induced DNA double strand breaks ( $\gamma$ H2AX repair foci) under both hypoxic and normoxic conditions (0.4 foci per cell were similar to the results of p53wt/wt cells under hypoxia) is in line with our previous observations (Figure 6(b)). Basal levels of  $\gamma$ H2AX repair foci after sham-irradiation (0 Gy) were in the range of hypoxic p53 wild-type mMSCs, with mean values of  $0.4 \pm 0.08$  and  $0.5 \pm 0.08$  foci per nucleus in hypoxia and normoxic conditions, respectively. After  $\gamma$ -irradiation of 4 Gy, the number of  $\gamma$ H2AX repair foci after 90 min increased significantly to 1.1 (normoxia) or 1.4 (hypoxia) foci per nucleus, representing highly effective ongoing DNA repair compared to p53 wild-type mMSCs irrespective of oxygen conditions applied. These results show that p53 is a key factor in modulating both senescence induction and DNA repair efficiencies in mMSCs.

## 4. Discussion

Mesenchymal stem cells in their normal physiological state reside in a stem cell niche with low-oxygen pressure [17, 18]. Since they have a lower metabolic rate than the committed precursor cells and differentiated cells derived from them [27, 28], they are less dependent on high oxygen supply. Considering that their main function is the long-term regeneration of precursor cells of different lineages and hence the maintenance of a stable genome, a reduction of radical oxygen species (ROS) in a tissue environment with lower oxygen pressure and low metabolic activity could be beneficial. This protective hypoxic environment is compromised when MSCs are isolated and expanded *ex vivo* but also by exposure to any

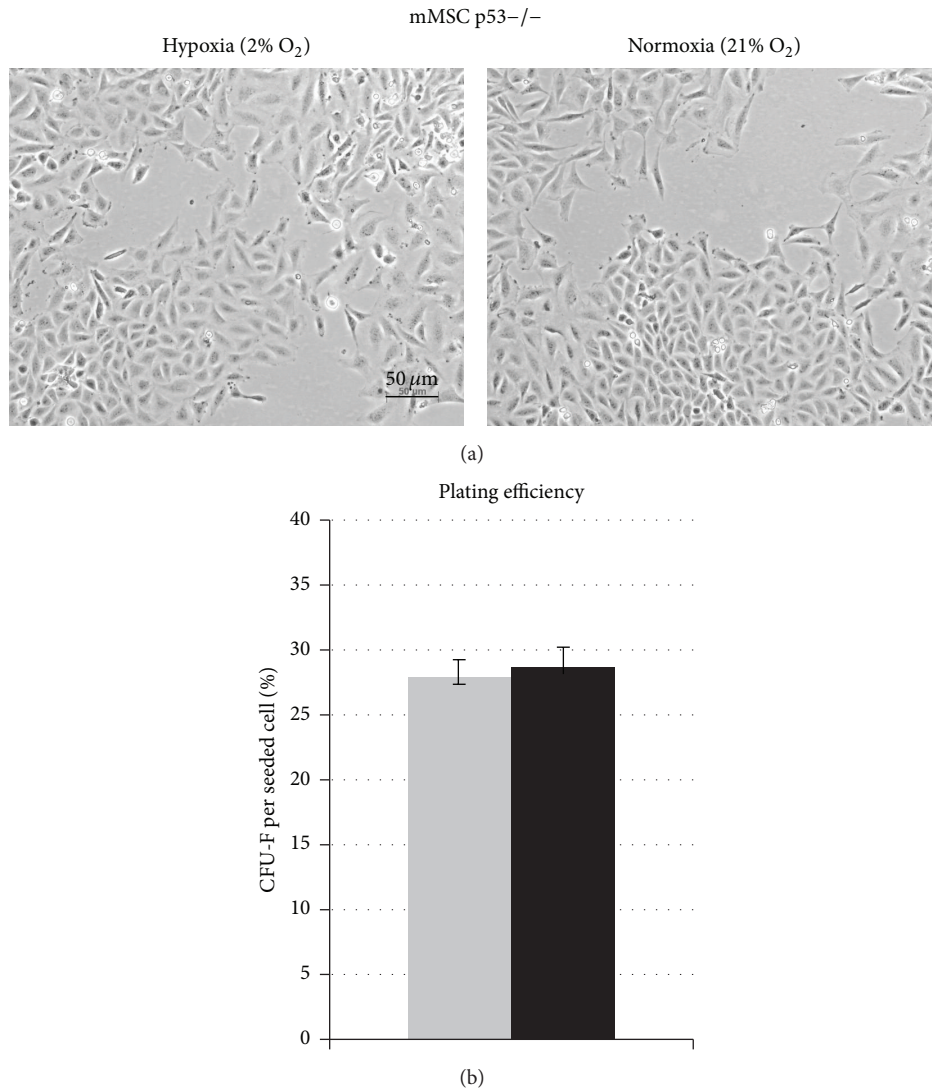


FIGURE 5: Impact of p53 status on oxygen effect of long-term *in vitro* culturing and colony formation capacity of mMSCs. (a) Morphology of mMSCs p53<sup>-/-</sup> cultured in hypoxic conditions (left image) and in normoxic conditions (right image). Representative images show mMSCs p53<sup>-/-</sup> cultured for 20 days. (b) Colony forming ability of mMSCs p53<sup>-/-</sup> after 14 days in hypoxic (grey bar) and normoxic (black bar) cultures calculated as mean values of fibroblast colony-forming units (CFU-F) per plated cell (3 biological replicates).

kind of ionizing radiation (IR) *in vivo* or *in vitro*. IR has the capacity to generate ROS- and OH-radicals from intracellular water, thereby bypassing the otherwise protective hypoxic stem cell niche [29].

We have shown that growth under ambient oxygen levels (i.e., 21%) compromises MSC proliferation when compared to growth under hypoxia (i.e., 2%). This is in line with observations by others, who suggested using reduced oxygen cell culture systems [22, 30]. In a therapy model, it has been shown that transient maintenance of human MSCs in hypoxia prior to autologous therapy increased their efficacy in the treatment of idiopathic pulmonary fibrosis, and that this was accompanied by enhanced survival of the grafted mMSCs [31].

We have shown here that the impairment of MSC proliferation under normoxia was associated with an increase

in cellular senescence. Senescence would not only preclude further stem cell expansion but also would hamper the differentiation capacity of the already existing cells [32]. Senescence can be triggered by various cellular signals: shortened telomeres that bring dividing cells close to the Hayflick limit [33], accumulated DNA damage [34], or activated oncogenes [35]. Measuring the average telomere length in the proliferating MSCs over several weeks in culture showed a clear reduction with time but no difference between cells grown under normoxia or low oxygen. We can therefore exclude that telomere shortening is involved in the oxygen sensitivity of MSCs.

There was, however, a striking increase in the level of DNA damage as detected by  $\gamma$ H2AX repair foci in cells that stopped growing after two weeks in normoxia. We tested the assumption that DNA lesions are causing senescence in MSCs

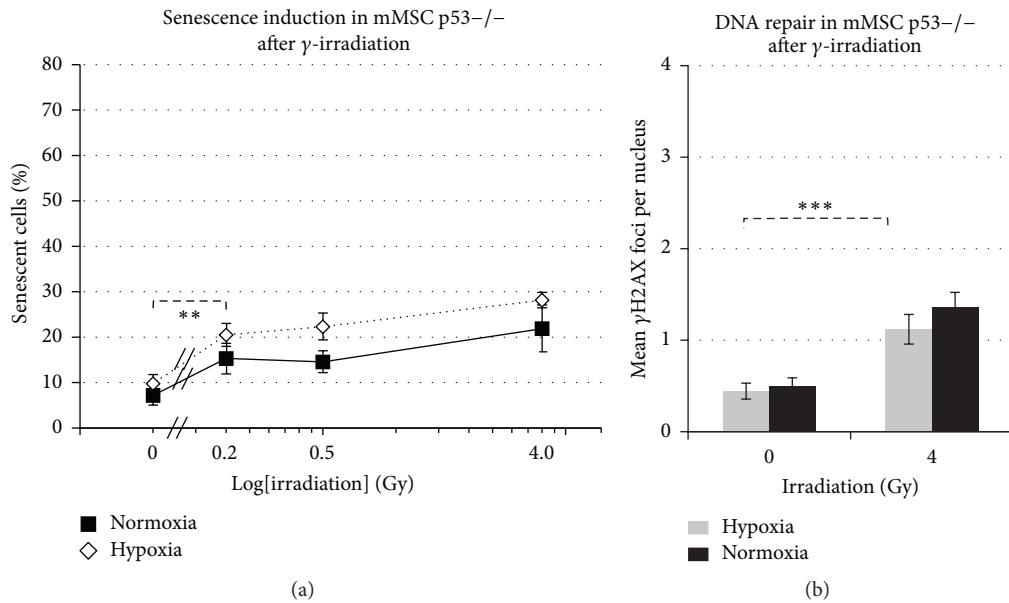


FIGURE 6: Impact of p53 status on senescence induction and number of DNA repair foci. (a) Graph shows percentage of p53<sup>-/-</sup> mMSCs undergoing senescence in hypoxic and normoxic conditions after exposure to  $\gamma$ -irradiation (sham-irradiated = 0 Gy, 3 biological replicates), radiation dose on logarithmic scale. (b) Quantification of p- $\gamma$ H2AX foci in 50 p53<sup>-/-</sup> mMSC nuclei depicted as mean values  $\pm$  standard error of the mean (3 biological replicates).

by subjecting cells in hypoxia and in normoxia to various doses of Cs-137  $\gamma$ -irradiation. With 500 mGy, we observed a significant increase in the frequency of senescent cells grown in normoxia compared to cells grown under hypoxic conditions. A radiation dose of this range could be delivered to long-living stem cells by 25 repeated computer tomography exposures (20 mGy each) and should warrant *ex vivo* expansion of MSCs collected from parts of the human body that might have been exposed to repeated radiation doses in the past. MSCs kept at 2% low oxygen exhibit signs of senescence only in 31% of cells as compared to 53% in normoxic cells. MSCs grown under reduced oxygen not only exhibit a lower percentage of senescent cells but also responded much less severe to  $\gamma$ -irradiation. Up to a dose of 500 mGy, the relative number of senescent cells did not increase above the control level, and we had to expose the cells with 4000 mGy to see a slight increase in senescence to 39%. This shows that the detrimental effects of ionizing radiation on MSCs proliferation are dependent on a non-physiologically high oxygen atmosphere (EPHOSS [19]) during *ex vivo* growth, which should be avoided while explanting as well as *ex vivo* expanding of MSCs in particular from patients who might have accumulated radiation-induced DNA damage in their MSCs prior to an autologous therapy.

*In vitro* expanded hMSCs treated with ROS-inducing chemical were found to exhibit an increased number of 53BP1-stained DNA repair foci, which in part could be rescued by adding an antioxidant [36]. This shows that the potential for induction of damage to the genomic DNA is greater under high oxygen levels but does not exclude other cellular targets (such as membranes or mitochondria) as potential mediators of the effect.

The suggestion that DNA damage induced by non-physiologically high oxygen and/or ionizing radiation can act synergistically in causing premature cell senescence was strengthened by the observation that MSCs with a homozygous deletion in the p53 gene (i.e. the main signal transducer for DNA damage response) grow considerably faster than wild-type MSCs, both under normoxia and under hypoxia. It is interesting to note that p53<sup>-/-</sup> mice do not show any defect in the growth or regeneration of mesenchymal tissue, rather an increased rate of tumors derived from cells of all germ layers [37]. This suggests that p53 is dispensable for the normal physiological function of MSCs. On the other hand, it was shown that hMSCs expanded for a prolonged time in *in vitro* hypoxia exhibit a change in their gene expression profile, in particular for three transcription factors (c-MYC, p53, and HIF1) that are frequently amplified, mutated, or overexpressed in cancer [38] and that this led to a higher transformation frequency after exposure of the cells to NiSO<sub>4</sub>. One suggestion from this observation was that genomic instability could be the result of forced proliferation and hypoxia. Our data show, however, that MSCs under hypoxia rather exhibit less spontaneous DNA strand breaks, therefore excluding the possibility that hypoxia per se is genotoxic. But it might be that premature senescence triggered by non-physiologically high oxygen indeed prevents a malignant progression, albeit on the expense of reduced cell proliferation.

## 5. Conclusions

We have shown that impaired growth of MSCs under a normoxic atmosphere *ex vivo* is associated with accumulated DNA damage but not with additional telomere attrition. This

impaired growth causes not only a reduced cell number but also, due to increased senescence, a loss of stem cell potency. The observation that radiation-induced DNA damage and high oxygen atmosphere seem to act synergistically advises caution not to explant MSCs from regions of the body that might have been radiation-exposed earlier in life, as for diagnostic X-ray imaging or therapeutic purposes. It might even be an option to store MSCs from tissues easily available early in life, thus sparing them from excess radiation exposure and having them available as a repository for autologous organ regeneration later in life.

## Conflict of Interests

The authors declare that there is no conflict of interests regarding the publication of this paper.

## Authors' Contribution

Ines Höfig and Yashodhara Ingawale contributed equally to this work.

## Acknowledgments

The authors would like to acknowledge the contribution of Daniela Hladik from the Institute of Radiation Biology at the Helmholtz Center Munich, Germany. This work was supported by the EU Euratom Project 323267 (RISK-IR).

## References

- [1] M. Owen and A. J. Friedenstein, "Stromal stem cells: marrow-derived osteogenic precursors," *Ciba Foundation Symposium*, vol. 136, pp. 42–60, 1988.
- [2] A. J. Friedenstein, "Marrow stromal fibroblasts," *Calcified Tissue International*, vol. 56, article S17, 1995.
- [3] A. M. DiMarino, A. I. Caplan, and T. L. Bonfield, "Mesenchymal stem cells in tissue repair," *Frontiers in Immunology*, vol. 4, article 201, 2013.
- [4] M. Griffin, S. A. Iqbal, and A. Bayat, "Exploring the application of mesenchymal stem cells in bone repair and regeneration," *The Journal of Bone & Joint Surgery—British Volume*, vol. 93, no. 4, pp. 427–434, 2011.
- [5] K. Bieback, S. Kern, A. Kocaömer, K. Ferlik, and P. K. Bugert, "Comparing mesenchymal stromal cells from different human tissues: bone marrow, adipose tissue and umbilical cord blood," *Bio-Medical Materials and Engineering*, vol. 18, pp. S71–S76, 2008.
- [6] C. Ménard and K. Tarte, "Immunoregulatory properties of clinical grade mesenchymal stromal cells: evidence, uncertainties, and clinical application," *Stem Cell Research & Therapy*, vol. 4, no. 3, article 64, 2013.
- [7] Y. Qi, D. Jiang, A. Sindrilaru et al., "TSG-6 released from intradermally injected mesenchymal stem cells accelerates wound healing and reduces tissue fibrosis in murine full-thickness skin wounds," *Journal of Investigative Dermatology*, vol. 134, no. 2, pp. 526–537, 2014.
- [8] M. E. Castro-Manreza and J. J. Montesinos, "Immunoregulation by mesenchymal stem cells: biological aspects and clinical applications," *Journal of Immunology Research*, vol. 2015, Article ID 394917, 20 pages, 2015.
- [9] Y.-H. Choi, A. Kurtz, and C. Stamm, "Mesenchymal stem cells for cardiac cell therapy," *Human Gene Therapy*, vol. 22, no. 1, pp. 3–17, 2011.
- [10] K. Bieback, P. Wuchter, D. K. Besser et al., "Mesenchymal stromal cells (MSCs): science and f(r)iction," *Journal of Molecular Medicine*, vol. 90, no. 7, pp. 773–782, 2012.
- [11] E. H. Javazon, K. J. Beggs, and A. W. Flake, "Mesenchymal stem cells: paradoxes of passaging," *Experimental Hematology*, vol. 32, no. 5, pp. 414–425, 2004.
- [12] E. A. Luria, M. E. Owen, A. J. Friedenstein, J. F. Morris, and S. A. Kuznetsow, "Bone formation in organ cultures of bone marrow," *Cell and Tissue Research*, vol. 248, no. 2, pp. 449–454, 1987.
- [13] K. Fukuda and J. Fujita, "Mesenchymal, but not hematopoietic, stem cells can be mobilized and differentiate into cardiomyocytes after myocardial infarction in mice," *Kidney International*, vol. 68, no. 5, pp. 1940–1943, 2005.
- [14] T. J. Heino, J. J. Alm, N. Moritz, and H. T. Aro, "Comparison of the osteogenic capacity of minipig and human bone marrow-derived mesenchymal stem cells," *Journal of Orthopaedic Research*, vol. 30, no. 7, pp. 1019–1025, 2012.
- [15] P. A. Riley, "Free radicals in biology: oxidative stress and the effects of ionizing radiation," *International Journal of Radiation Biology*, vol. 65, no. 1, pp. 27–33, 1994.
- [16] M. E. Lomax, L. K. Folkes, and P. O'Neill, "Biological consequences of radiation-induced DNA damage: relevance to radiotherapy," *Clinical Oncology*, vol. 25, no. 10, pp. 578–585, 2013.
- [17] H. Kofoed, E. Sjøtoft, S. O. Siemssen, and H. P. Olesen, "Bone marrow circulation after osteotomy: blood flow,  $po_2$ ,  $pCO_2$ , and pressure studied in dogs," *Acta Orthopaedica Scandinavica*, vol. 56, no. 5, pp. 400–403, 1985.
- [18] R. Das, H. Jahr, G. J. V. M. van Osch, and E. Farrell, "The role of hypoxia in bone marrow-derived mesenchymal stem cells: considerations for regenerative medicine approaches," *Tissue Engineering Part B: Reviews*, vol. 16, no. 2, pp. 159–168, 2010.
- [19] C. R. Mantel, H. A. O'Leary, B. R. Chitteti et al., "Enhancing hematopoietic stem cell transplantation efficacy by mitigating oxygen shock," *Cell*, vol. 161, no. 7, pp. 1553–1565, 2015.
- [20] S. V. Boregowda, V. Krishnappa, J. W. Chambers et al., "Atmospheric oxygen inhibits growth and differentiation of marrow-derived mouse mesenchymal stem cells via a p53-dependent mechanism: implications for long-term culture expansion," *Stem Cells*, vol. 30, no. 5, pp. 975–987, 2012.
- [21] N. J. O'Callaghan, V. S. Dhillon, P. Thomas, and M. Fenech, "A quantitative real-time PCR method for absolute telomere length," *BioTechniques*, vol. 44, no. 6, pp. 807–809, 2008.
- [22] H. Ren, Y. Cao, Q. Zhao et al., "Proliferation and differentiation of bone marrow stromal cells under hypoxic conditions," *Biochemical and Biophysical Research Communications*, vol. 347, no. 1, pp. 12–21, 2006.
- [23] W. W.-Y. Kam and R. B. Banati, "Effects of ionizing radiation on mitochondria," *Free Radical Biology & Medicine*, vol. 65, pp. 607–619, 2013.
- [24] A. Beliveau and P. Yaswen, "Soothing the watchman: telomerase reduces the p53-dependent cellular stress response," *Cell Cycle*, vol. 6, no. 11, pp. 1284–1287, 2007.
- [25] A. Rufini, P. Tucci, I. Celardo, and G. Melino, "Senescence and aging: the critical roles of p53," *Oncogene*, vol. 32, no. 43, pp. 5129–5143, 2013.

- [26] J. Zhang, L. Shen, and L. Q. Sun, "The regulation of radiosensitivity by p53 and its acetylation," *Cancer Letters*, vol. 363, no. 2, pp. 108–118, 2015.
- [27] C.-T. Chen, Y.-R. V. Shih, T. K. Kuo, O. K. Lee, and Y.-H. Wei, "Coordinated changes of mitochondrial biogenesis and antioxidant enzymes during osteogenic differentiation of human mesenchymal stem cells," *Stem Cells*, vol. 26, no. 4, pp. 960–968, 2008.
- [28] A. D. Hofmann, M. Beyer, U. Krause-Buchholz, M. Wobus, M. Bornhäuser, and G. Rödel, "Oxphos supercomplexes as a hallmark of the mitochondrial phenotype of adipogenic differentiated human MSCs," *PLoS ONE*, vol. 7, no. 4, Article ID e35160, 2012.
- [29] I. M. Allan, A. T. M. Vaughan, A. E. Milner, J. Lunec, and P. A. Bacon, "Structural damage to lymphocyte nuclei by H<sub>2</sub>O<sub>2</sub> or gamma irradiation is dependent on the mechanism of OH radical production," *British Journal of Cancer*, vol. 58, no. 1, pp. 34–37, 1988.
- [30] I. Berniakovich and M. Giorgio, "Low oxygen tension maintains multipotency, whereas normoxia increases differentiation of mouse bone marrow stromal cells," *International Journal of Molecular Sciences*, vol. 14, no. 1, pp. 2119–2134, 2013.
- [31] Y. W. Lan, K. B. Choo, C. M. Chen et al., "Hypoxia-preconditioned mesenchymal stem cells attenuate bleomycin-induced pulmonary fibrosis," *Stem Cell Research & Therapy*, vol. 6, article 97, 2015.
- [32] J. Campisi and L. Robert, "Cell senescence: role in aging and age-related diseases," *Interdisciplinary Topics in Gerontology*, vol. 39, pp. 45–61, 2014.
- [33] Y. Jung and A. S. Brack, "Cellular mechanisms of somatic stem cell aging," *Current Topics in Developmental Biology*, vol. 107, pp. 405–438, 2014.
- [34] A. Insinga, A. Cicalese, and P. G. Pelicci, "DNA damage response in adult stem cells," *Blood Cells, Molecules, and Diseases*, vol. 52, no. 4, pp. 147–151, 2014.
- [35] G. Cavalli, R. Biavasco, B. Borgiani, and L. Dagna, "Oncogene-induced senescence as a new mechanism of disease: the paradigm of Erdheim-Chester disease," *Frontiers in Immunology*, vol. 5, article 281, 2014.
- [36] H. Alves, A. Mentink, B. Le, C. A. van Blitterswijk, and J. De Boer, "Effect of antioxidant supplementation on the total yield, oxidative stress levels, and multipotency of bone marrow-derived human mesenchymal stromal cells," *Tissue Engineering—Part A*, vol. 19, no. 7-8, pp. 928–937, 2013.
- [37] L. A. Donehower, M. Harvey, B. L. Slagle et al., "Mice deficient for p53 are developmentally normal but susceptible to spontaneous tumours," *Nature*, vol. 356, no. 6366, pp. 215–221, 1992.
- [38] S. W. Crowder, L. W. Horton, S. H. Lee et al., "Passage-dependent cancerous transformation of human mesenchymal stem cells under carcinogenic hypoxia," *The FASEB Journal*, vol. 27, no. 7, pp. 2788–2798, 2013.